



# Towards In-process Inspection of Additive Manufacturing using Laser Ultrasonics

By Don Milesh Pieris, MEng

November 2021

A thesis submitted to the University of Nottingham  
for the degree of Engineering Doctorate

#### Academic Supervisors:

Prof. Matt Clark

Prof. Adam Clare

Dr. Richard Smith

Dr. Rikesh Patel

Dr. Wenqi Li

#### Industrial Supervisor:

David Wright

# Abstract

This thesis investigates the capabilities of two laser ultrasonic (LU) non-destructive evaluation (NDE) techniques to carry out an in-process inspection of additive manufacturing (AM) process.

Following a review of a wide range of AM processes, selective laser melting (SLM) is chosen due to its ability to manufacture complex geometries with internal features suitable for the aerospace industry. A variety of NDE techniques capable of carrying out an in-process inspection of SLM processes are reviewed. Due to their ability to detect the key performance variables (KPV) in SLM, such as changes to the scan strategy, laser power, scan speed, hatch spacing, surface defects, subsurface defects and changes to the part microstructure, the two LU techniques known as spatially resolved acoustic spectroscopy (SRAS) and laser induced phased arrays (LIPA) are chosen.

Using prepared AM samples, the capability of SRAS to detect, size and classify surface defects are initially explored. This is followed by several methods that can be used to detect changes in the microstructure of AM samples. Changes to the part geometry were used to force changes to the scan strategy which varied the part microstructure. A seed crystal was used to encourage epitaxy growth within an SLM component which was detected using SRAS. This work was progressed to the as-deposited surface of AM samples using a system specifically designed for the inspection of rough surfaces.

An alternate approach to the in-process inspection of AM was explored by carrying out a LIPA inspection on the underside of an SLM component. This sample was designed with several internal features with varying diameters positioned at increasing depths. The LIPA data demonstrated the ability to detect and locate the nested features within the SLM component. Using a combination of XCT and LIPA data, it was clear that the information extracted from a LIAP inspection had value from both an NDT and a metrology perspective.

Several challenges in carrying out an in-process inspection of AM using LU were identified. These included the effect of surface temperature and the complex effects of surface texture, which were divided into the effect of surface form, waviness and surface roughness. This was followed by a theoretical calculation of the time taken to carry out a full volumetric SRAS inspection. Finally, due to the similarities between a SRAS and a LIPA system, a hybrid system design was discussed.

# Acknowledgements

Firstly I would like to thank Steve Sharples and Adam Clare for giving me the opportunity to work on this engineering doctorate. I like to think that it was their initial seeds of wisdom that grew over the last five years into this thesis. I would also like to thank Matt Clark and Richard Smith who took me on as a student in 2017. Their guidance over the past few years brought me to the place I am today. The next two members of the UoN supervision team I would like to thank are Rikesh Patel and Wenqi Li. They thought me everything from the most basic things around the lab to some life lessons that I will never forget. I would also like to thank David Wright, my industrial supervisor from Rolls-Royce, for keeping me on track with this EngD.

I would like to thank Tony Gachagan at Strathclyde who gave me a blank sheet of paper, asked me whom I wanted to work for and then put me in touch with UoN, Rolls-Royce and the RNDE. I would like to Keith Newton, Nina Hancock and Peter Thayer from the RCNDE for supporting me and all the other EngD students through our projects.

Next, I would like to thank Paul who started his EngD at the same time as me and helped me with a lot of things throughout my EngD. We worked side by side over the last five years, made a lot of mistakes but more importantly learnt a lot of lessons together. I would like to thank Naomi for being the closest person I have to a mentor. I would also like to thank Teti from Strathclyde for involving me in her work when she was at Nottingham which then went on to form a significant part of my EngD.

I would like to thank all my friends from rowing, cycling and scuba diving who were just a wonderful bunch of people with whom I chose to spend my free time. My coaches from rowing and cycling also formed an important part of the team that got me through this. The discipline and rigour they instilled in me outside of academia along with the mental health benefits of the sports I love, gave me a welcome distraction and got me across the tough parts of this journey. I would like to thank Bill for his final proofreading of this thesis along with the many other bits of life advice along the way.

This journey started with me forwarding an email to Katie asking if I should apply for one of the RNCD EngDs advertised at Strathclyde. She said “go for it” and she has stood by me from that point on. She has proofread everything I have ever written including every word in this thesis. She was there for me through the highs, the lows and when everything went sideways. I could not have gotten through this without you.

# Contents

Abstract .....	i
Acknowledgements.....	ii
Contents .....	iii
List of Publications .....	vi
Nomenclature .....	ix
Chapter 1 Introduction .....	1
1.1. Industry Motivation.....	1
1.2. Research Motivation .....	9
1.3. Aims .....	10
1.4. Scope .....	10
1.5. Thesis Organization .....	11
Chapter 2 Literature Review and Background.....	12
2.1. Additive Manufacturing.....	12
2.2. Selective Laser Melting (SLM) .....	17
2.3. AM Structural Defects .....	22
2.4. Key Performance Variables .....	28
2.5. NDE within AM .....	30
2.6. NDE Review .....	34
2.7. Microstructure within AM.....	45
2.8. Ultrasonics .....	48
2.9. Laser Ultrasonics (LU) .....	56
2.10. Controlled Convergence Matrix .....	68
2.11. NDE Selection and Conclusion.....	69
Chapter 3 Spatially Resolved Acoustic Spectroscopy .....	73
3.1. Introduction.....	74

3.2. The Concept.....	75
3.3. Instrumentation.....	79
3.4. Fabrication and Preparation.....	92
3.5. SRAS Experiments.....	94
3.6. Conclusion .....	124
3.7. Future work .....	126
<b>Chapter 4     Laser Induced Phased Arrays .....</b>	<b>129</b>
4.1. Introduction.....	129
4.2. Literature Review of Laser Ultrasonic Phased Arrays .....	130
4.3. The concept .....	132
4.4. Instrumentation.....	135
4.5. Methodology .....	136
4.6. Results .....	139
4.7. Discussion .....	141
4.8. Conclusion .....	146
4.9. Future work .....	147
<b>Chapter 5     Challenges of In-Process Inspection.....</b>	<b>149</b>
5.1. Temperature.....	150
5.2. Surface Texture .....	152
5.3. Time .....	171
5.4. Integration .....	175
5.5. Conclusion .....	176
<b>Chapter 6     Conclusions .....</b>	<b>179</b>
<b>Bibliography .....</b>	<b>186</b>

“We choose to go to the moon in this decade and do the other things, not because they are easy, but because they are hard”

— John F. Kennedy

# List of Publications

The work carried out during this EngD has been published in a variety of journal and conference papers. These publications are listed below followed by a list of conferences and meeting where some of this work was presented.

## Journal papers

Pieris, D., Stratoudaki, T., Javadi, Y., Lukacs, P., Catchpole-Smith, S., Wilcox, P. D., Clare, A., & Clark, M. (2020). Laser Induced Phased Arrays (LIPA) to detect nested features in additively manufactured components. *Materials and Design*, 187, 108412.

<https://doi.org/10.1016/j.matdes.2019.108412>

**Winner, University of Nottingham Advanced Manufacturing Technology Showcase 2020**

Pieris, D., Patel, R., Dryburgh, P., Hirsch, M., Li, W., Sharples, S. D., Smith, R. J., Clare, A. T., & Clark, M. (2019). Spatially Resolved Acoustic Spectroscopy Towards Online Inspection of Additive Manufacturing. *Insight - Non-Destructive Testing and Condition Monitoring*, 61(3), 132–137. <https://doi.org/10.1784/insi.2019.61.3.132>

Brown, M., Pieris, D., Wright, D., Crawforth, P., M'Saoubi, R., McGourlay, J., Mantle, A., Patel, R., Smith, R. J., & Ghadbeigi, H. (2021). Non-destructive detection of machining-induced white layers through grain size and crystallographic texture-sensitive methods. *Materials and Design*, 200, 109472. <https://doi.org/10.1016/j.matdes.2021.109472>

Dryburgh, P., Pieris, D., Martina, F., Patel, R., Sharples, S., Li, W., Clare, A. T., Williams, S., & Smith, R. J. (2019). Spatially resolved acoustic spectroscopy for integrity assessment in wire–arc additive manufacturing. *Additive Manufacturing*, 28(April), 236–251.

<https://doi.org/10.1016/j.addma.2019.04.015>

Oyelola, O., Jackson-Crisp, A., Crawforth, P., Pieris, D. M., Smith, R. J., M'Saoubi, R., & Clare, A. T. (2020). Machining of directed energy deposited Ti6Al4V using adaptive control. *Journal of Manufacturing Processes*, 54, 240–250.

<https://doi.org/10.1016/j.jmapro.2020.03.004>

Patel, R., Hirsch, M., Dryburgh, P., Pieris, D., Achamfuo-Yeboah, S., Smith, R., Light, R., Sharples, S., Clare, A., & Clark, M. (2018). Imaging material texture of as-deposited selective laser melted parts using spatially resolved acoustic spectroscopy. *Applied Sciences (Switzerland)*, 8(10), 1991. <https://doi.org/10.3390/app8101991>

Bai, L., Velichko, A., Clare, A. T., Dryburgh, P., Pieris, D., & Drinkwater, B. W. (2020). The effect of distortion models on characterisation of real defects using ultrasonic arrays. *NDT and E International*, 113(March). <https://doi.org/10.1016/j.ndteint.2020.102263>

Fuentes-Domínguez, R., Yao, M., Colombi, A., Dryburgh, P., Pieris, D., Jackson-Crisp, A., Colquitt, D., Clare, A., Smith, R. J., & Clark, M. (2021). Design of a resonant Luneburg lens for surface acoustic waves. *Ultrasonics*, 111. <https://doi.org/10.1016/j.ultras.2020.106306>

Clark, M., Clare, A., Dryburgh, P., Li, W., Patel, R., Pieris, D., Sharples, S., & Smith, R. (2019). Spatially resolved acoustic spectroscopy (SRAS) microstructural imaging. *AIP Conference Proceedings*, 2102, 020001. <https://doi.org/10.1063/1.5099705>

Dryburgh, P., Patel, R., Pieris, D. M., Hirsch, M., Li, W., Sharples, S. D., Smith, R. J., Clare, A. T., & Clark, M. (2019). Spatially resolved acoustic spectroscopy for texture imaging in powder bed fusion nickel superalloys. *AIP Conference Proceedings*, 2102(May), 020004. <https://doi.org/10.1063/1.5099708>

Speidel, A., Su, R., Mitchell-Smith, J., Dryburgh, P., Bisterov, I., Pieris, D., Li, W., Patel, R., Clark, M., & Clare, A. T. (2018). Crystallographic texture can be rapidly determined by electrochemical surface analytics. *Acta Materialia*, 159, 89–101. <https://doi.org/10.1016/j.actamat.2018.07.059>

Chaplain, G. J., De Ponti, J. M., Colombi, A., Fuentes-Dominguez, R., Dryburg, P., Pieris, D., Smith, R. J., Clare, A., Clark, M., & Craster, R. V. (2020). Tailored elastic surface to body wave Umklapp conversion. *Nature Communications*, 11(1). <https://doi.org/10.1038/s41467-020-17021-x>

## Conference Talks

Optics & Photonics Group Research Seminar 11/05/2017  
Non-Destructive Evaluation of Additive Layer Manufactured Component Microstructure

Optics and Ultrasound IV, University of Strathclyde 22/11/2017  
Non-Destructive Evaluation of Additive Layer Manufactured Component Microstructure  
**Winner, Physical Acoustics Group, Best Student Presentation Prize**

Rolls-Royce EngD Conference, Derby, 14/12/2017  
Non-Destructive Evaluation of Additive Layer Manufactured Component Microstructure

RCNDE Technology Transfer Event, London, 29/01/2018  
Observing Defects and Microstructure in Additively Manufactured Components

Optics and Photonics Showcase Event, University of Nottingham, 23/03/2018  
Observing Defects and Microstructure in Additively Manufactured Components

RCNDE CDT Conference, Manchester, 01/05/2018  
Assessing the capability of the current state of NDE for the In-Line inspection of Additive Layer Manufacturing

BINDT NDT 2018 Conference, Nottingham, 12/09/2018  
Spatially Resolved Acoustic Spectroscopy - Additive Manufacturing - Towards Online Inspection  
**Winner, W E Gardner prize for the best paper by an early-stage researcher**

46th Annual Review of Progress in Quantitative Non-destructive Evaluation, Portland  
15/07/2019  
LIPA Inspection of Additive Manufacturing for Geometrical Accuracy

International Congress on Ultrasonics, Bruges, 03/09/2019  
LIPA Inspection of Additive Manufacturing for Geometrical Accuracy  
**Honourable Mention R.W.B Stephens Prize**

Rolls-Royce Doctorate Network Seminar, Virtual, 29/07/2020  
Laser Ultrasonics for the in-process inspection of Additive Manufacturing

Rolls-Royce ALM Forum, Virtual, 17/11/2020  
Towards In-process inspection of Additive Manufacturing using Laser Ultrasonics

RCNDE Early Career event, Virtual, 25/11/2020  
Towards In-process inspection of Additive Manufacturing using Laser Ultrasonics  
**Winner, 1st prize for flash talks**

Rolls-Royce Doctorate Network Conference, Virtual, 11/12/2020  
Towards In-process inspection of Additive Manufacturing using Laser Ultrasonics.

Optics and Photonics Showcase Event, University of Nottingham, 25/03/2021  
Towards In-process inspection of Additive Manufacturing using Laser Ultrasonics.

RCNDE CDT Conference, Virtual, 20/05/2021  
Towards In-process inspection of Additive Manufacturing

# Nomenclature

Abbreviation	Description
<b>AM</b>	Additive Manufacturing
<b>ASTM</b>	American Society for Testing and Materials
<b>CAD</b>	Computer-Aided Design
<b>CCD</b>	Charge-Coupled Device
<b>CCM</b>	Controlled Convergence Matrix
<b>CFD</b>	Computational Fluid Dynamics
<b>CMM</b>	Coordinate Measurement Machine
<b>CW</b>	Continuous-Wave
<b>DLP</b>	Digital Light Processing
<b>DOF</b>	Depth Of Field
<b>EBM</b>	Electron Beam Melting
<b>EBSID</b>	Electron Backscatter Diffraction
<b>EMDA</b>	East Midlands Development Agency
<b>FAA</b>	Federal Aviation Administration
<b>FFT</b>	Fast Fourier Transform
<b>FMC</b>	Full Matrix Capture
<b>HIP</b>	Hot Isostatic Pressing
<b>IR</b>	Infrared
<b>JEEP</b>	Joint Engineering, Environmental, and Processing
<b>KED</b>	Knife Edge Detector
<b>KPV</b>	Key Performance Variables
<b>LCF</b>	Low Cycle Fatigue
<b>LIPA</b>	Laser-Induced Phased Arrays
<b>LU</b>	Laser Ultrasonic
<b>MTR</b>	Micro-Textures Region
<b>NA</b>	Numerical Aperture
<b>NDE</b>	Non-Destructive Evaluation
<b>NDT</b>	Non-Destructive Testing
<b>O-SAM</b>	All-Optical Scanning Acoustic Microscope
<b>PAUT</b>	Phased Array Ultrasonic Testing
<b>PBF</b>	Powder Bed Fusion

<b>RCNDE</b>	Research Centre for Non Destructive Evaluation
<b>RGB</b>	Red Green Blue
<b>SAFT</b>	Synthetic Aperture Focusing Technique
<b>SAW</b>	Surface Acoustic Wave
<b>SEM</b>	Scanning Electron Microscope
<b>SKED</b>	Speckle Knife Edge Detector
<b>SLE</b>	Scanning Laser Epitaxy
<b>SLM</b>	Selective Laser Melting
<b>SLS</b>	Selective Laser Sintering
<b>SMC</b>	Selective Matrix Capture
<b>SNR</b>	Signal to Noise Ratio
<b>SRAS</b>	Spatially Resolved Acoustic Spectroscopy
<b>TFM</b>	Total Focusing Method
<b>WAAM</b>	Wire Arc Additive Manufacturing
<b>XCT</b>	X-ray Computed Tomography

# **Chapter 1 Introduction**

This thesis aims to identify and further investigate the capabilities of non-destructive evaluation (NDE) techniques capable of carrying out an in-process inspection of additive manufacturing (AM).

This chapter introduces the industry motivation for the use of advanced manufacturing techniques such as AM within the aerospace industry. It then discusses some applications of AM within the industry followed by the need for NDE of AM processes. Finally, the research aims of this engineering doctorate are presented along with an outline of this thesis.

## **1.1. Industry Motivation**

The term “*Power By The Hour*” was invented by Rolls-Royce and trademarked in 1962 to support their Viper engine which was used on the De Havilland / Hawker Siddeley 125 business jet [1]. This was a pioneering approach where a jet engine was sold to a customer – an airline operator – for a fixed cost per flying hour. According to Rolls-Royce “*These programs provide the operator with a fixed engine maintenance cost over an extended period of time. Operators are assured of an accurate cost projection and avoid the costs associated with unscheduled maintenance actions*” [2]. This moved the responsibility of maintaining and repairing the engine from the customer over to the supplier – Rolls-Royce.

The arrangement before was known as a “*Cost Plus contract*” which meant that the supplier sold the engine to the operator and the supplier serviced and repaired the product whilst charging the customer a premium rate. This was beneficial for the supplier and provided few to no incentives for them to reduce the price of service, repair and maintenance.

With a “*power by the hour*” arrangement, the risks and incentives are more balanced between the supplier and operator. This means it is in the supplier’s best interest to increase the overall lifespan of their product and even more important to increase the time between maintenance. This is directly linked to the quality and the initial manufacturing of their product followed by the ability to rapidly and dynamically maintain their products in operation.

As manufacturing processes such as AM evolve from being used for rapid prototyping to a more common process in the manufacturing industry, they are perfectly positioned to provide the high-value industries such as aerospace with the rapid and versatile manufacturing solution they need [3]. AM is defined by the American Society for Testing and Materials (ASTM) as a manufacturing process of joining materials to make objects from 3D model data, usually, layer upon layer [4]. This manufacturing process allows the component to be designed with nested features and complex external geometry. The strength, stiffness and microstructure of these parts can be tailored using different materials, infill patterns and scan strategies [5]. AM processes such as powder bed fusion (PBF) can manufacture complex components which could not be produced using conventional methods such as milling and casting [6]. Due to the layer-by-layer nature of AM, they only use the material required to build the part and provide a huge cost saving compared to subtractive methods such as milling. This also removes the need for traditional tooling, used in processes such as casting. AM instead allows the manufacturer to dynamically adapt their production to meet demand. This ability to adapt one build platform removes the need to hold inventory of a wide range of tooling and moulds to manufacture various parts. The combination of the benefits outlined above makes AM an ideal candidate for high-value industries such as aerospace.

### 1.1.1. Applications of AM in aerospace

Singamneni et al. link the capabilities unique to AM and their benefits within the aerospace industry [7]. The capability for AM to manufacture parts with complex geometries allows the designers to optimise the parts in ways they previously couldn’t. This allows them to consolidate several assemblies in one part, which in turn increases part functionality and reduces weight. This results in better performance and fuel efficiency when considered within the aerospace industry. The layer-by-layer nature of AM reduces the need for tooling and makes it easy to deploy at a new location. This, in turn, aids just in time manufacturing and repair by making the production facility available locally. The final result of this is a reduction in overall build time and unit cost by reducing the length and complexities of the supply chain.

The path to integrating AM components within current generation systems is illustrated in Figure 1 using three stages [8].

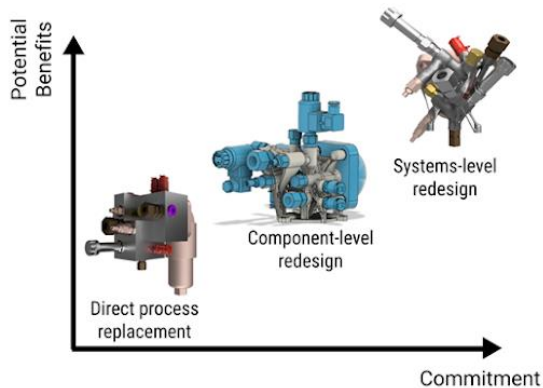


Figure 1 Illustrative graph showing the potential benefit vs commitment of implementing AM processes for manufacturing parts within industries such as aerospace [8].

- **Direct Replacement** is where a like-for-like component is manufactured using AM to replace an existing component. This requires minimal commitment and provides no tangible benefit apart from the fact that the replacement can be manufactured locally.
- **Component-level Redesign** allows the part to be optimised within the constraints of the original design – defined by the existing infrastructure such as connections and fixings – for weight using processes such as generative design, for optimal flow using computational fluid dynamics (CFD) and finally for cost both in terms of part consolidation and or reduced material cost [9]–[11]. This is what is typically carried out on current generation systems, where an existing part is replaced with an optimised AM version of the same part.
- **System-level Redesign** removes the design constraints from the original design where the part was designed to be manufactured using traditional processes. Instead, it fully utilises the benefits of AM in terms of weight reduction, flow optimisation and cost reductions, found as part of the component-level redesign. This also opens the pathway to further optimise various other systems around the part being considered. This is well suited for next-generation systems where AM is considered a viable manufacturing process from the early design stage. As shown in Figure 1, this provides the greatest potential benefit but also requires the most commitment.

In early 2014 GE aerospace planned to open a new assembly plant to produce the first Federal Aviation Administration (FAA) approved AM part to fly on a passenger aircraft [12].

This was to be a fuel spray nozzle built using PBF. Nineteen of these flue spray nozzles were used inside the new-generation LEAP engine which was initially designed to power the Airbus A320 neo but evolutions of which went on to power the Boeing 737 MAX and Comac C919. This single assembly consolidated twenty individual parts that previously required twenty-five welds and brazes. Moving to AM reduced this to five welds and reduced the weight of the nozzle by 25% [13]. The use of AM to produce this part gave the designers the freedom to incorporate complex nested features which previously could not be incorporated when using subtractive processes. On the 19<sup>th</sup> of May 2015, the new-generation LEAP engine took flight for the first time powering an Airbus A320 neo [14]. This engine achieved a 15% reduction in fuel burn along with CO<sub>2</sub> and NO<sub>x</sub> emissions which were 50% below the current standard. This was the world's first AM component to power a commercial passenger aircraft and was an example of a component-level redesign.

Rolls-Royce followed this with the world's largest 3D-printed aero-engine component. On the 5<sup>th</sup> of November 2015, the Trent XWB-97 engine became airborne on the wing of an Airbus A380 testbed aircraft [15]. The Trent XWB-97 engine's front bearing housing contained 48 aerofoil-shaped guide vanes manufactured using AM as seen in Figure 2 and Figure 3. The engine was designed to power the first flight of the Airbus A350-1000 which took place on the 24<sup>th</sup> of November 2016 [16]. This bearing housing was developed by Rolls-Royce in partnership with the Manufacturing Technology Centre (MTC) in Coventry, Sheffield University and 3D printing specialist Arcam [17]. Rolls-Royce previously used additive processes to repair components, but this served as a significant landmark in the journey of AM as it was the first complete component to be built using AM which replaced a part that was previously manufactured using more traditional manufacturing processes. This again was an example of a component-level redesign for AM, where a part manufactured using traditional methods was replaced using a more optimised AM component.

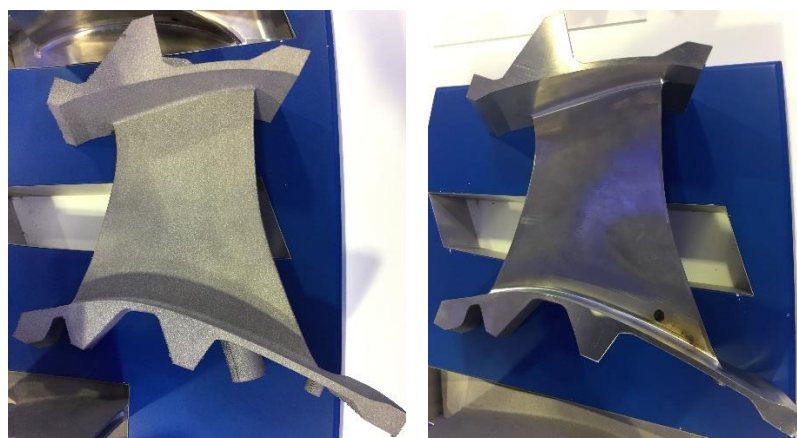


Figure 2 Photographs of as-built AM guide vane (Left) post-processed AM guide vane (Right)

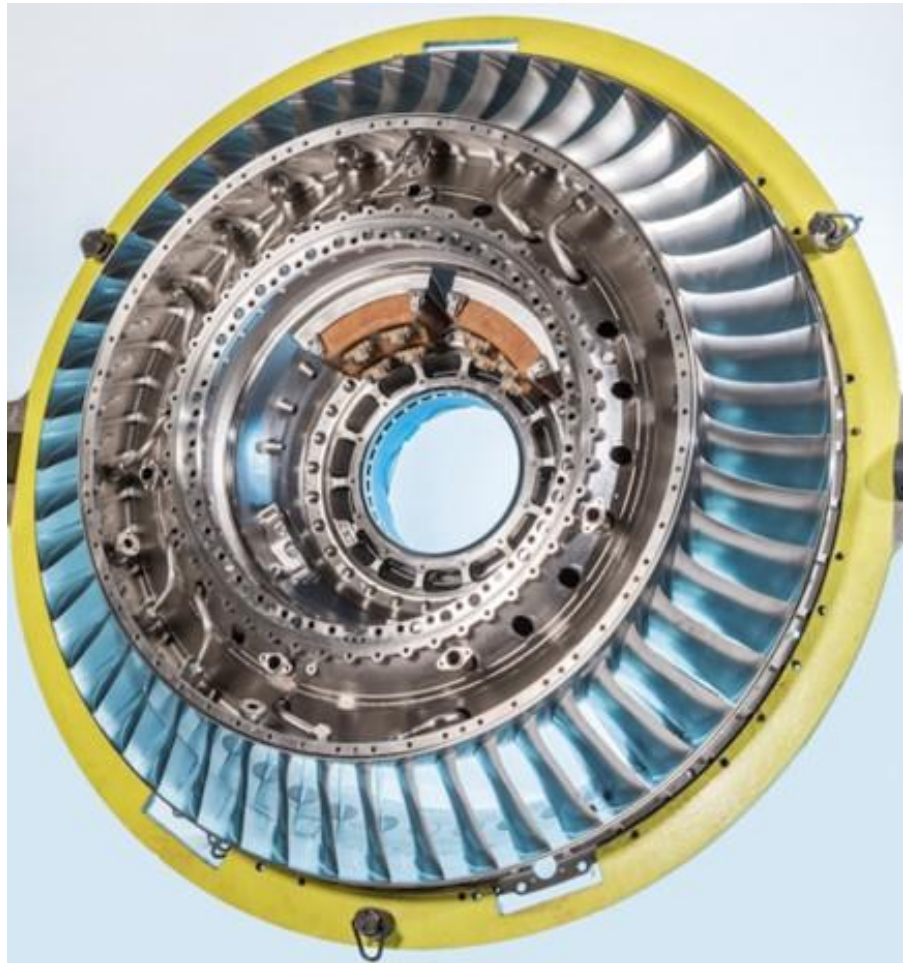


Figure 3 Photograph of XWB-97 engine's front bearing housing with guide vanes made using AM [17].

The applications of AM within the aerospace industry are not just limited to engines. Modern aircraft are extremely complex with various systems all working in unison to keep them airborne. Current-generation aircraft are fly by wire, where the pilot's inputs are electronically transferred to hydraulic actuators which move the control surfaces. Hydraulic manifolds are well suited for AM due to their complexity and potential for flow improvements, part consolidation and mass reduction. The MTC and Gen3D – a company that provides software for AM processes – collaborated on a project to redesign a hydraulic manifold used in aerospace to be manufactured using AM. The first iteration of this involved a component-level redesign. At this stage, the fluid channels remained at the same locations as the original design but internal fluid channels were smoothed to improve the flow and reduce turbulence around 90° corners – modelled using CFD. Following this generative design was used to optimise the part geometry. Here the geometry of the pipes and mounting points were preserved whilst the rest of the volume was optimised to minimise weight and provide the required strength. The final part following this component level redesign is shown in the middle of Figure 4.



Figure 4 Pictures illustrating the original manifold machined down from a billet of steel (left), followed by a photograph of the component-level redesigned part manufactured using Ti6Al4V powder (middle) and finally the system-level redesigned part (right) [8].

Based on the methodology in Figure 1, the component-level redesign was followed by a system-level redesign. As seen in Figure 4 right, this version was more compact than the previous version. This instantly provided a reduction in material use and less space was required. At this stage, specific considerations were also given to the additive processes used to build the part. The length of the fluid channels was reduced to allow line of sight to facilitate excess powder removal. The larger fluid channels were modified to a diamond shape to reduce the stock material used and teardrop shapes were added to the fluid channels to minimise the need for support material. The redesign of this one component stood as an example of the changes AM process can bring to next-generation components, where the use of AM is considered from an early stage of the part design.

The three components discussed above illustrated how AM processes are poised and ready to support the future generations of aerospace systems, engines, airframes and a wide range of other applications. This is due to the flexibility which AM processes provide at the design stage, the ability to incorporate several assemblies into one, reductions in part weight, the savings in material cost and reduction in build time.

### 1.1.2. Need for NDE in aerospace

Aviation is commonly known to be one of the safest modes of transportation. This is due to the relatively large numbers of people using commercial aviation and travelling much greater distances when compared to other methods of transport [18]. Due to the inherently increased risk of purely being thousands of feet in the air, the aviation industry is very cautious and safety-focused. The industry is constantly monitored, all accidents are thoroughly investigated, lessons learnt are well communicated and commonly result in improvements of systems and protocols to improve the safety of the industry as a whole. The current example of this is the two fatal crashes of the Boeing 737 MAX which resulted in a

grounding of the global fleet until a solution was found and implemented to the satisfaction of all of the various national aviation authorities [19].

Over the 100+ year history of aviation, the modern turbofan engine only came into use in the late 1950s. Over these 70 years, several air disasters were caused by engine failures. On the 19<sup>th</sup> of July 1989, the No2 Engine of United Airlines Flight 232 failed. The aircraft was a McDonnell Douglas DC10 with three GE CF6-60 high bypass ratio turbofan engines. The engine failure was followed by a complete loss of all three hydraulic systems onboard, disabling all of the pilot's flight controls [20]. The pilots were able to have a very small amount of control over the aircraft by varying the thrust of the remaining two engines. This, however, was not easy as the badly damaged aircraft had no flaps and the crew were only able to make right-hand turns. The pilots made an emergency landing at Sioux City airport where the aircraft broke into three pieces. 111 passengers and 1 flight attendant lost their lives, 184 people survived.

The loss of hydraulics was due to hydraulic lines around the tail from all three systems being severed. Close inspections of the severed sections showed traces of titanium. Upon recovery of sections of the titanium fan disk, it was found that the root cause of No2 engine failure was the fracturing of the fan disk, which scattered shards of titanium radially away from the tail-mounted engine and severed the hydraulic lines. The metallographic analysis showed that the reason for the fan disk failure was a hard alpha inclusion within the fan disk. This relatively brittle inclusion acted as an initiation point for a crack, which grew over time. This crack was missed during a routine inspection and eventually grew up to 13 mm in length before it failed in flight.

Another more recent engine failure occurred on the 30<sup>th</sup> of September 2017 on an Air France Airbus A380 which planned to fly from Charles de Gaulle international airport in France to Los Angeles International Airport. When flying over Greenland the No4 engine failed. The pilots shut down the No4 engine and landed the aircraft safely at Goose Bay, a Canadian Airforce base [21]. Once on the ground, pilots saw that the entire front section of the engine nacelle which held the fan casing was missing along with the fan. The initial investigation of the remaining fan hub section showed no microstructural or chemical composition anomalies and so it was unable to identify the cause of the failure. An initial theory of tool damage during maintenance was considered but then discounted due to a lack of supporting evidence. A search was launched in Greenland alongside information from ballistic simulations to recover the section of the fan hub that was detached during the flight. The

third phase of the search was able to find the ejected section of the fan hub under several feet of ice.

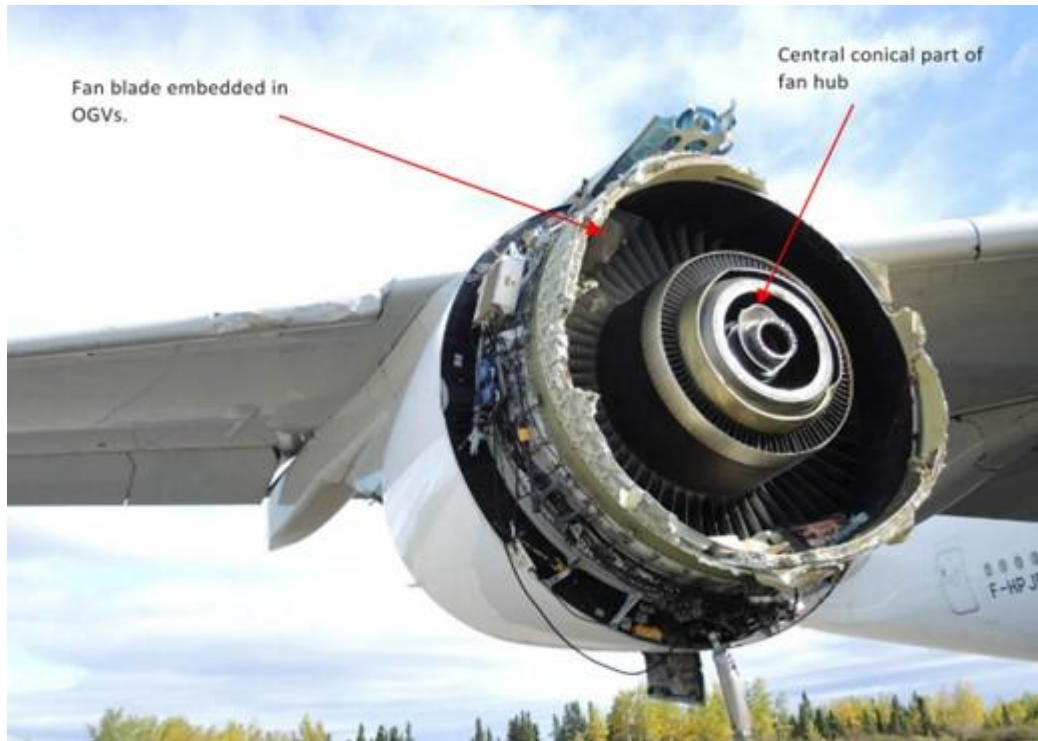


Figure 5 Image of engine No4 taken from the incident report of the Air France A380 showing the damage caused to the nacelle and the small remaining section of the fan hub [22].

Investigation of the recovered fan hub section showed that the failure was caused by low cycle fatigue (LCF) cracking which was initiated within the part [22]. The origin of the crack was at the bottom of slot No10, 14 cm behind the front face and 1.4 mm below the top surface. Scanning electron microscope (SEM) analysis of the region between the crack initiation point and the inner face of the fan hub showed striations that were characteristic of LCF crack progression. Electron backscatter diffraction (EBSD) analysis of the crack initiation region showed that it was predominantly basal-oriented alpha grains, which were positioned perpendicular to the hoop stress within the fan hub. The engine manufacturer stated that this micro-texture region (MTR) was larger and more intense than the mean values for such components. The investigation concluded that the crack originated in this macro-zone as the orientation of the grains were unfavourable with respect to the maximum hoop stress direction.

The two engine failures above were a result of unfavourable microstructure being present within relatively large components. Ultimately Sioux City incident was due to human factor limitations which led to the crack not being detected. The cause of the crack however could have been detected if the internal microstructure of the part was known. Similarly, although

the MTR caused the LCF cracking in the Air France engine, the route to the final failure started early on in the supply chain where the titanium was formed into a billet. Knowing the internal microstructure and having the ability to detect internal cracks within such a large component could have prevented both of these failures. This illustrates the need for NDE to be embedded into the manufacturing process of components to be used in safety-critical industries such as aerospace.

## 1.2. Research Motivation

When compared to processes such as investment casting which could be traced back to 5000BC, AM is relatively new and does not have as much of a knowledge base [5], [23]. Due to this lack of knowledge and maturity, a wide range of defects are commonly found in AM components. For this reason, assurances around part integrity are required to push AM as a whole forward.

Conventionally manufactured parts using milling and casting processes are typically inspected after the components are complete. In some cases - curved surfaces - the part is specially machined for inspection with flat surfaces. Following the inspection, the part is machined down to its final shape. This method does not allow for any remedial action to be taken if the part does not conform to the specifications outlined for the part at the design stage. The layer-by-layer nature of AM, however, provides a unique opportunity for an intermediate layer inspection to be carried out as the component is being built. This provides information in terms of any mechanical and microstructural properties from within the part as it is being built. The collection of these layer-by-layer inspection data sets can be used to construct a digital twin of the component, which could follow the part throughout its product lifecycle. These inspections also provide a unique opportunity for some remedial action to be taken in a situation where the part does not conform to the design specification, or in some cases they can provide sufficient information for the build to be abandoned, where the part cannot be recovered, to reduce the overall material waste [24]. Furthermore the ability to carry out an in-process inspection of AM components provides evidence of the repeatability of the process. This paves the way for AM to mature into a robust and agile manufacturing process.

The motivation for this engineering doctorate comes from a combination of factors. The industrial motivation discussed in section 1.1 showed the need for advanced manufacturing processes such as AM in the aerospace industry. This was reinforced by the applications of AM within the aerospace industry in section 1.1.2. The safety-critical nature of aerospace

combined with the lack of maturity meant that NDE was necessary for the successful deployment of AM within aerospace. For these reasons, the research within this engineering doctorate is focused on identifying and developing NDE techniques capable of carrying out an in-process inspection of AM processes.

### 1.3. Aims

- Identify one or more NDE solutions capable of carrying out an in-process inspection of industry-relevant additive processes such as selective laser melting (SLM).
- Demonstrate the capabilities of these NDE solutions and progress them towards an in-process inspection.
- Use NDE to add value to the component being manufactured using information from the NDE data.
- Provide information and insights into AM components during the build process that cannot be obtained post-manufacture.
- Address some of the challenges around carrying out an in-process inspection of an AM process such as SLM.

### 1.4. Scope

The scope of this thesis is limited to the industry-relevant AM process known as SLM. This is due to its current use within the aerospace industry to manufacture high-value components. This was also a guide from the sponsors of this engineering doctorate, Rolls-Royce.

Key performance variables (KPV) of SLM were used to assess the capability of the NDE techniques. These were limited to process parameters available in a typical use case – the variables a user on the shop floor can change.

Other AM processes such as wire arc additive manufacturing (WAAM) are used to illustrate further capabilities and challenges for the in-process inspection of AM.

In line with the aims above, the scope is limited to NDE solutions that can be implemented as part of an in-process inspection. NDE used for the post-manufacture inspection of AM is discussed and primarily used as a validation for the potential in-process NDE solutions.

NDE solutions not applicable for the inspection for AM and have no potential to be implemented as part of an in-process inspection are considered to be outside the scope of this thesis.

## 1.5. Thesis Organization

This thesis consists of four main chapters.

- **Chapter 2** discusses the following areas: AM, NDE and the need for NDE as part of an in-process inspection of AM. It then goes on to discuss the theory behind and review a wide range of NDE techniques used for the inspection of AM. The reviewed NDE solutions are ranked against KPV of SLM, which is used to select the most suitable NDE techniques for further investigation.
- **Chapter 3** presents the laser ultrasonic (LU) NDE technique known as spatially resolved acoustic spectroscopy (SRAS). It discusses the various experiments designed to demonstrate the capability of SRAS to detect the presence of surface defects and changes to AM component microstructure. This combined with the inspection of the as-deposited surface of AM samples is an initial step towards the in-process inspection of AM.
- **Chapter 4** presents the LU NDE technique known as laser-induced phased arrays (LIPA). It demonstrates the capability of such a system to provide information regarding nested features within an AM component and how it is more comparable to a metrology inspection instead of pure NDE.
- **Chapter 5** addresses some of the challenges around implementing the two LU NDE techniques discussed in chapters 3 and 4 as part of an in-process inspection. It initially covers the effect elevated temperatures due to the build have on the inspection. It then goes on to discuss the effect of surface roughness and various methods in which the system could be designed to cope with this. It also discusses the amount of time required for an in-process inspection and its effect on the overall build time. Finally, it discusses a design of a hybrid system capable of carrying out a SRAS and LIPA inspection, providing both surface and cross-sectional information about an AM component.
- **Chapter 6** summarises the previous chapters. It goes over the various experiments carried out to demonstrate the capabilities of SRAS and LIPA and how they can contribute towards an in-process inspection of AM.

# **Chapter 2 Literature Review and Background**

Following on from the industry motivation for the use of AM outlined in chapter 1, this chapter discusses the wide range of AM processes available and focuses on those suitable for the aerospace industry. It then goes on to discuss the various defects found within AM components and their causes. This is followed by an outline of the KPV of SLM used to rank various NDE techniques. NDE is then discussed within the context of AM and how it can provide assurances around part integrity which are required to push AM as a whole forward.

A wide range of NDE techniques used for in-process and post-manufacture inspection of AM is reviewed along with the relevant theory. Each NDE technique is then ranked based on its ability to detect the KPV of SLM using a controlled convergence matrix (CCM). This is used to identify the most suitable NDE techniques for further investigation in the following chapters.

## **2.1. Additive Manufacturing**

As previously discussed in section 1.1 ASTM define AM as “a process of joining materials to make objects from 3D data, usually layer upon layer, as opposed to subtractive manufacturing methodologies” [4]. The 3D data here typically refers to computer-aided design (CAD) models of the part to be manufactured. AM processes deposit material using one of the various methods discussed below (Figure 7) onto a build plate. The build plate is then translated vertically by a pre-defined layer height and a new layer is deposited. Some processes keep the part and build plate static and move the deposition head instead.

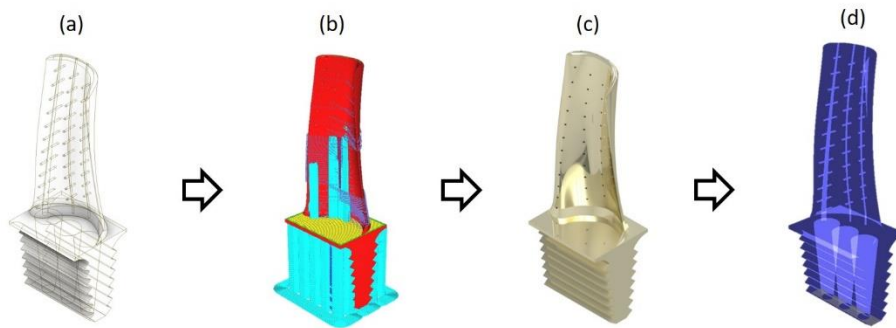


Figure 6 Diagram illustrating the current AM workflow where the CAD model of the part (a) is sliced using a slicing software. This is used to generate the tool paths for the AM platform and is typically exported in G code (b). The machine executes this G code and builds the part (c). The part is inspected using various NDE techniques (d).

The current AM workflow in Figure 6 illustrates how the CAD model (a) of a given component is imported into a slicing software. This slices the CAD geometry into individual build layers and generates the tool paths (b). These tool paths are exported to the AM build platform in the form of G code and are used to build the part layer by layer (c). Finally, the completed part is inspected for any defects (d). This is currently a linear process with no feedback loop, which results in any errors during the slicing or defects that occur during the build going unnoticed until the final post-manufacture inspection of the part.

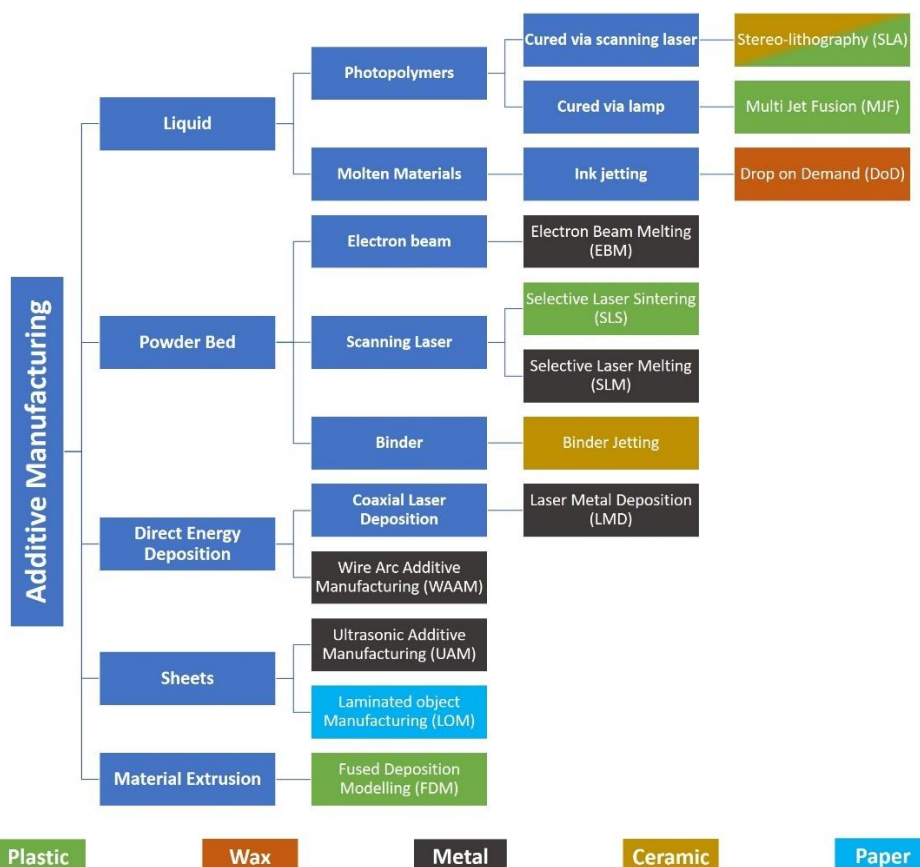


Figure 7 Flowchart of AM processes where they are separated using the form of material and then the energy source or material delivery method used to fuse the material. The various colours are used to denote the types of materials used.

AM is capable of processing a variety of materials in a variety of forms. Figure 7 illustrates this and has initially separated the AM processes into categories based on the form of the material used, then where applicable, the energy source used to fuse the material. Finally, the coloured boxes are used to separate the processes based on the materials they use. The following section discusses the various AM processes based on how they are categorised in Figure 7. Due to SLM being a primary focus within this thesis, it is discussed in greater detail than the other AM processes in section 2.1.11.

### 2.1.1. Stereolithography (SLA)

SLA was developed in 1988 and was primarily used for rapid prototyping [25]. It is still one of the processes with the highest accuracy when it comes to manufacturing polymer and ceramic parts. SLA use a photocurable liquid monomer onto which the individual layer cross-sections are traced using a laser or light projector (high-resolution LCD panel). Based on the material used this can either be ultraviolet light or visible light (daylight). In a “Top-down” system a laser is scanned across the surface of the vat of liquid and the build plate is lowered into the vat as the part is completed. In a “Bottom-up” system the light is projected through the vat of liquid onto the surface and the part is lifted out of the vat. Due to the high melting point of ceramics, the energy of the beam used is not sufficient to fully fuse the ceramic particles. The ceramic liquids used are typically mixed with a polymer which during the build fuses and binds the component together. This is removed during a de-binding and sintering process.

### 2.1.2. Multi Jet Fusion (MJF)

MJF is a powder-based high-speed sintering process [26]. The entire powder bed is heated to a near-sintering temperature and a radiation-absorbing ink is selectively deposited across the powder bed. This ink absorbs more heat than the non-exposed powder. As an IR lamp is moved across the surface, the powder particles in the inked regions absorb more heat and are fused together. The powder bed is lowered, a new layer of powder is deposited, and the process is repeated. Unlike other plastic AM processes which typically require supports, the powder-based nature of MJF removes the need for supports. The ability to vary the ink used allows MJF parts to be manufactured in various colours with high accuracy and so the process is well suited for rapid prototyping.

### 2.1.3. Drop on Demand (DoD)

In a similar manner to an inkjet printer, the ‘print head’ of DoD processes moves across the required areas and deposits the material using a thermal or piezoelectric approach [27]. The

head moves across the horizontal plane to deposit the required geometry layer by layer. The layer is then allowed to cool, and UV light is used to cure or harden the deposited layers. The build plate is lowered and the process is repeated to build a 3D part.

#### 2.1.4. Electron Beam Melting (EBM)

EBM is a metal powder-based process where an electron beam is translated across a powder bed which is maintained at a vacuum in a similar to an SEM [28]. EBM was primarily developed for processing resistant materials such as tantalum, niobium, molybdenum, tungsten, vanadium, hafnium, zirconium, titanium and their alloys [29]. This makes it well suited for high-speed manufacturing of high-value, precision parts for industries such as aerospace.

#### 2.1.5. Selective Laser Sintering (SLS)

SLS is a laser-based powder bed AM process where a laser beam is used to sinter or partially sinter the top surface of the powder bed [25]. This process is typically used for plastics and ceramics, however, it can also be used for metallic powders. Due to the high melting point of ceramics, the fast-moving laser beam is not able to fully fuse the ceramic particles. For this reason, the ceramic powders are mixed with a low-temperature binder or an inorganic binder. This mixture is partly sintered during the build process. The binder is then burnt off during the de-binding and final sintering processes. The powder-based nature of this process removes the need for support structures giving the manufactured parts a uniform finish on all surfaces [30].

#### 2.1.6. Binder Jetting (BJ)

BJ is another powder bed-based AM process where a binder is injected onto the surface using an inkjet head [30]. This process is typically used for ceramics, where once the build is complete the ceramic powder is only held together by the strength of the binder and the part is classified as ‘green’. Following this, the parts are de-binded in an oven and sintered in a furnace. Primarily used for ceramics, BJ can be used for the manufacture of some metallic components.

#### 2.1.7. Laser Metal Deposition (LMD)

This process is also referred to as blown powder because of how the power is delivered to the melt pool. A laser is focused on the workpiece or build plate and a continuous flow of powder is fed to this area either co-axially or off-axis into the melt pool [31]. The powder is blown onto the area using an inert gas which acts as a shielding gas for the melt pool/weld

taking place. Some of the main advantages of LMD processes are the high precision and limited heat effect to the surrounding area. This makes it an ideal candidate for the repairing of complex high-value components [32]

### 2.1.8. Wire Arc Additive Manufacturing (WAAM)

WAAM utilises a welding torch and a wire feed system to deposit individual weld beads to build large components. WAAM differs drastically from previously discussed AM processes. In WAAM the build plate is kept static and the deposition head is moved as the part grows. This process utilises a seven-axis robotic system to manipulate the welding torch [33]. This allows WAAM to manufacture relatively large structures at high deposition rates when compared to other AM processes. The open architecture of WAAM allows for a wide range of combinations of robotic systems and welding platforms to be used. This also provides the opportunity for the straightforward integration of NDE of the parts as discussed by Dryburgh et al. [34].

### 2.1.9. Laminated Object Manufacturing (LOM)

Typically known as sheet lamination, this process fuses sheets of material and uses a laser to cut the desired shape [30]. This process can be advanced further by infusing colour into the individual sheets to create vivid patterns on the final components. This process is not capable of manufacturing any structural components but instead was geared more towards manufacturing promotional material and prototypes.

### 2.1.10. Ultrasonic Additive Manufacturing (UAM)

This process uses metallic sheets of material that are layered on top of each other and precision cut to the required 2D shapes. Using either ultrasonic consolidation, diffusion bonding, laser welding and resistance welding, each of the layers are consolidated together to build up the 3D shape [30]. In some cases, the individual sheets are machined post adhesion. Due to the way they are manufactured, these components do not work well under shear and tensile loading.

### 2.1.11. Fused Deposition Modelling (FDM)

FDM is one of the most widely used AM processes and has become commonplace in a lot of small workshops for the rapid manufacture of prototypes and functional parts. This is a material extrusion-based process where a plastic filament is extruded through a heated nozzle [35]. The nozzle is translated across the surface of the build plate where the beads of material are deposited in a 2D form. This process is then repeated layer by layer to build up

a 3D shape. Due to its popularity, FDM printers have drastically come down in price and are becoming more and more affordable. Although not suitable for high load applications, FDM came into the world's spotlight during the COVID-19 outbreak where hobbyist FDM printers were used to rapidly manufacture a huge number of plastic head braces for face shields [36].

## 2.2. Selective Laser Melting (SLM)

Patented in 1997, SLM was developed from its predecessor SLS - briefly discussed in section 2.1.5 [37]. A high energy laser is used to selectively melt and fuse regions of a metallic powder bed. A thin layer of powder is initially deposited across the surface of the build plate using the recoater blade. Galvanometer mirrors are used to translate the build laser beam across the surface (in the X Y plane) of the powder bed, this selectively melts the cross-section of the part being built. Once a layer is completed the build plate is lowered by a pre-defined layer height in the Z direction and a new layer of powder is deposited. This process is repeated until the 3D part is complete [38]. To minimise oxidation during the melting process, the atmosphere within the build chamber is tightly controlled. It is typically filled with inert gases such as argon or nitrogen. The build volume of SLM platforms are limited by the build plate size and Z height, this ranges from ~50 to 400 mm cubed. Sanchez et al. present a comprehensive review of the literature regarding the mechanical properties and microstructure of nickel-based superalloys manufactured using PBF processes such as SLM [39].

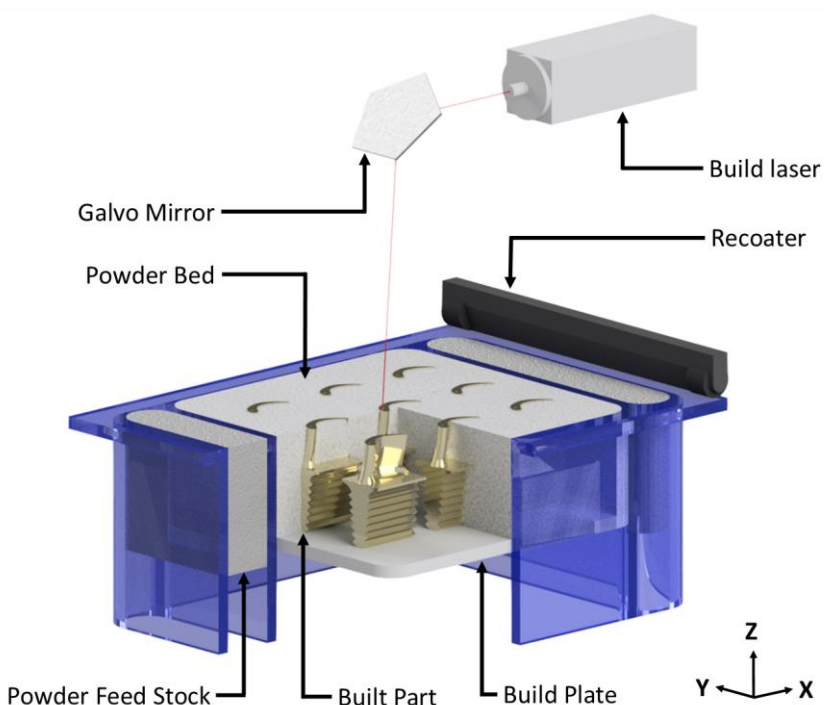


Figure 8 Rendered image of a simplified SLM build platform illustrating the build laser, galvo mirror, recoater blade, feedstock, with a cut-out of the powder bed showing the built parts and the build plate.

Over 50 individual process parameters can be varied when controlling the SLM build process [40]–[42]. These can be divided into several categories: Laser scan parameters; powder bed parameters; build environment and powder feedstock [43].

- **Laser scan parameters** are the parameters of the SLM build laser which is typically a pulsed IR (1064 nm). The peak power of these lasers ranges from 300 W to 1 kW where power incident on the powder bed can be varied. Similarly, the laser spot size, scan speed, hatch spacing and scan strategy can be varied. Parameters such as the pulse width, wavelength, repetition rate and intensity profile are specific to each laser so cannot be varied - these parameters are generally brand and model-specific e.g. Renishaw, Realizer, EOS, etc.
- **Powder bed**, the user has relatively less control over. Parameters such as the layer height can be varied between ~20 and 100 µm. The power distribution can be controlled indirectly by controlling the pressure and translation speed of the recoater blade. Most other parameters such as powder bed waviness cannot be controlled but are known to have an effect on the build taking place.
- **Build environment** temperature and atmosphere are two parameters that can be directly controlled within the build chamber. The temperature is affected by a wide range of factors such as the interactions between the build laser and the powder bed, alongside any heating within the chamber. The build chamber atmosphere can be controlled by the mix of purge gasses used inside the chamber.
- **Powder feedstock** has a very large influence over the entire build process. Parameters such as the bulk density, thermal conductivity, specific heat capacity, melting temperature, melt pool viscosity, coefficient of thermal expansion, diffusivity, particle size distribution and foreign particle inclusions are all under the control of the powder suppliers.

### 2.2.1. Materials

The materials used and discussed within this thesis were chosen as they are materials used in the manufacture of gas turbine engine components. These range from aluminium alloys used in lightweight structural components; titanium alloys used in the relatively cold sections of the engines (upstream of the combustion chamber), and nickel alloys used in the hot sections of engines (such as the combustion chamber and turbines). A further constraint within this project was the suitability of a material for AM processes and its availability in

powder form. Existing research showed that pure metals were not well suited for AM process [44]. This was due to their somewhat limited mechanical, poor anti-oxidisation and poor anti-corrosion properties. Pre-alloyed powders based on aluminium, titanium and nickel have been shown to yield good results in high energy density AM processes such as SLM. For these reasons the following alloys were chosen when manufacturing samples throughout this engineering doctorate.

### 2.2.1.1. AlSi10Mg

Aluminium alloys are typically used in applications that require thin-walled structures - such as heat exchangers - but also in complex structural sections which require a material with a high strength-to-weight ratio, corrosion resistance and thermal properties [45]. Using aluminium alloys in AM processes yields parts with high mechanical properties due to their fine microstructure [46].

Table 1 Nominal weight % composition of AlSi10Mg [47]

	<b>Weight %</b>
<b>Aluminium</b>	87 Balance
<b>Magnesium</b>	0.45
<b>Nitrogen</b>	0.2
<b>Titanium</b>	0.15
<b>Manganese</b>	0.1
<b>Copper</b>	0.05

	<b>Weight %</b>
<b>Silicon</b>	11
<b>Iron</b>	0.25
<b>Oxygen</b>	0.2
<b>Zinc</b>	0.1
<b>Nickel</b>	0.05
<b>Lead</b>	0.02

### 2.2.1.2. Ti-6Al-4V (Ti 64)

The titanium alloy Ti6Al4V is made up primarily of titanium with about 6% Aluminium, 4% Vanadium and trace amounts of other metals. For this reason, it is commonly referred to as Ti64 [48]. Its low density, high strength, corrosion resistance and high fracture toughness make it the most commonly used titanium alloy, occupying about half of the market share of titanium components used to date [49]. Developed in the 1950s for use in heavily loaded lightweight aircraft structural components, this alloy is a good candidate for relatively cold sections of gas turbine engines such as the compressor (~600°C [50]).

Table 2 Nominal weight % composition of Ti 64 [51]

	<b>Weight %</b>
<b>Titanium</b>	89 Balance
<b>Aluminium</b>	6.42
<b>Vanadium</b>	4.02
<b>Oxygen</b>	0.19

	<b>Weight %</b>
<b>Iron</b>	0.15
<b>Carbon</b>	0.06
<b>Nitrogen</b>	0.0055
<b>Hydrogen</b>	0.0031

### 2.2.1.3. Hastelloy X

Hastelloy X is a nickel super alloy developed and used to manufacture the pressure-actuated trailing edge flaps of the Pratt & Whitney J58 engine used on the Lockheed SR-71 Blackbird [52], [53]. The SR-71 - designed by Clarence "Kelly" Johnson and first flown in 1964 - was a long-range, high-altitude strategic reconnaissance aircraft capable of flying at Mach 3.2 at an altitude of 85,000 feet. Nickel superalloys such as Hastelloy X are widely used to this day in high-temperature aero-engine components such as afterburners, combustor cans, flame holders and transition ducts due to their high strength to weight ratio and temperature resistance [54].

Table 3 Nominal weight % composition of Hastelloy X [54].

	<b>Weight %</b>
<b>Nickel</b>	47 Balance
<b>Chromium</b>	22
<b>Iron</b>	18
<b>Molybdenum</b>	9
<b>Cobalt</b>	1.5
<b>Tungsten</b>	0.6

	<b>Weight %</b>
<b>Carbon</b>	0.1
<b>Manganese</b>	1 Max
<b>Silicon</b>	1 Max
<b>Niobium</b>	0.5 Max
<b>Aluminium</b>	0.5 Max
<b>Titanium</b>	0.15 Max

### 2.2.1.4. Inconel 718

Due to the operating temperatures of the J58 engine reaching over 538°C, the engine was almost entirely made of Waqsaloy which was one of the strongest materials available at the time [55]. Over several cycles, however, the diffuser case welds were prone to strain-age cracking and Inconel 718 was chosen as a replacement. This was based on its unique balance of mechanical properties, its weldability and the fact that it can be processed as both wrought and cast. Following this, it was also used in a variety of other engine components such as turbine exhausts, stator assemblies, variable guide vanes and diffusor cases.

Table 4 Nominal weight % composition of Inconel 718 [56]

	<b>Weight %</b>
<b>Nickel</b>	52 Balance
<b>Iron</b>	19
<b>Chromium</b>	18
<b>Niobium + Tantalum</b>	5
<b>Molybdenum</b>	3
<b>Cobalt</b>	1 Max

	<b>Weight %</b>
<b>Titanium</b>	0.9
<b>Aluminium</b>	0.5
<b>Carbon</b>	0.05
<b>Manganese</b>	0.35 Max
<b>Silicon</b>	0.35 Max
<b>Boron</b>	0.004

## 2.2.2. Physics of Melting

The fundamental concepts around the laser melting process within an SLM system have been around for a long time and are well understood. The process essentially uses a moving heat source to melt and solidify a given section of material, similar to most welding processes.

When a laser is incident on the surface of a given section of material, the energy is initially absorbed within a few nanometers of the surface via a process now as Fresnel Absorption [57]. Due to the high energy density (see section 2.4.7) some of the material is vaporised and a small depression forms on the surface. This depression deepens and turns into a keyhole. Further Fresnel Absorption occurs along the walls of the keyhole which increases the energy coupled deeper into the material. Some energy is converted into plasma vapour within the keyhole. The combination of gravity and surface tension forces the molten material to close the hole, whilst the plasma vapour helps keep it open. As the laser moves across the surface, the tail of the melt pool cools and allows the material to solidify and fresh material is melted at the head of the melt pool. This process is extremely violent and ejects particles at a velocity between 0.44-4.7 m/s [58]. This contributes to some of the defects discussed in section 2.3.

A Rosenthal's solution for temperature distribution of a moving heat source across a semi-infinite plate is shown in Equation 1 [59]. This relatively simple solution is used within this thesis to understand the change in temperature on a part being built (see section 5.2). Mackwood et al. reviewed wide a range of methods used to thermally model laser welding and related processes [60]–[63]. More detailed multi-physics models have been considered in the literature but are seen to be outside the scope of this thesis [64].

$$T - T_o = \frac{q}{2\pi kR} e^{-\frac{v(w+R)}{2a}} \quad \text{Equation 1}$$

For a moving heat source with velocity  $v$   $w = (x - vt)$  Equation 2

$T$  = Temperature

$T_0$  = Initial Temperature

$q$  = Laser power

$k$  = Thermal conductivity

$R$  = Distance to the centre of the arc

$v$  = Laser scanning speed

$w$  = Distance in the x direction

$a$  = thermal difusivity

### 2.2.2.1. Epitaxy Growth

In the casting of directionally solidified or single-crystal turbine blades, the use of a seed crystal helps govern the microstructure of the part being built. This concept was not well utilised in the AM industry. Scanning Laser Epitaxy (SLE) is a specific AM process developed

to produce components with equiaxed, directionally solidified microstructure. SLE works similarly to SLM where a 1064nm 2kW Nd: YAG laser is fired at a powder bed and controlled using a galvanometer scanner [65]. The primary difference is the fact that SLE focuses the beam down to a much larger spot size ~1.5 mm compared to SLM of ~50  $\mu\text{m}$ .

Bansal et al. investigated this technique and the effect the substrate used to manufacture the component had on the morphology of the component being manufactured [66]. The substrate used was a cast rectangular section of single-crystal CMSX-4. The powder used was also CMSX-4 with a particle size ranging from 85-150 $\mu\text{m}$ . The results presented illustrate the growth of dendrites from the substrate into the melted powder section. This type of microstructure was not normally seen in AM processes. There was, however, a sharp step change in the dendrite size. The deposited section was found to have dendrites ~15 times finer than the substrate. Relative to the substrate the columnar grains in the deposited section had little to no angular misorientation, this was due to the higher temperature gradient present in the SLE process. Some drastic changes in orientation were observed along the deposited section of material. This was due to the change in temperature gradient as the substrate increased in temperature. The next observation in terms of microstructure was the transition of the grain growth from columnar to equiaxial. This was due to the decrease in thermal gradient and increase in isothermal velocity near the surface. This caused the formation of undercooled zones near the surface. An important observation was the lack of porosity and cracking in these samples. This was uncharacteristic of AM processes. This phenomenon was investigated further within the context of SLM in section 3.6.2.1.

## 2.3. AM Structural Defects

The defects found in AM components are commonly caused by the process parameters used and variations in the powder feedstock itself, including how the powder was stored and prepared. Grasso et al. review a wide range of defects seen in PBF processes [67]. They categorize the defects observed into one of the following: pores; cracks; delamination; balling; geometric defects; reduced mechanical properties; unmelted powder; inclusions and microstructural variations. The following section focuses on these defect categories - what causes them and how they can be detected and categorized.

### 2.3.1. Pores

The existence of pores within a component impacts fatigue performance by acting as a crack initiation point. They also aid crack growth, where cracks bridge across several pores over time [67]. Pores are commonly caused by the following processing parameters:

- Beam scanning and/or deflection system [68]
- Build chamber environmental control [40]
- Powder handling and deposition system [68]

Detecting a pore is relatively straightforward using any NDE method as a drastic contrast can be observed between the bulk material and a pore. This is due to the bulk material typically being more dense (solidified powder) than pores which tend to be full of air or unsolidified powder. Classification of a pore is very important as it can provide information as to what caused the pore to form. The following two equations can be used to classify a pore based on its geometry [69], [70]. The circularity of a pore  $P_{circ}$  can be calculated using the pore area  $A$  and the perimeter  $p$  whereas the aspect ratio  $P_{aspect}$  can be calculated using the major axis length  $d_{max}$  and minor axis length  $d_{min}$ .

$$\text{Pore circularity } P_{circ} = \frac{4\pi A}{p^2} \quad \text{Equation 3}$$

$$\text{Pore aspect ratio } P_{aspect} = \frac{d_{min}}{d_{max}} \quad \text{Equation 4}$$

Sharat et al. stated that the more spherical a pore was the more likely it was to be a gas pore [71]. This was caused by the powder itself due to the gas atomization process used to manufacture the powder. Gas pores can also be due to poor control of the build environment where oxidization can occur. Non-spherical porosity is more likely caused by instabilities in the melt pool and/or a lack of fusion due to insufficient energy density. Lower energy densities cause molten balls to form on the surface, whereas higher energy densities effectively drill into the surface of the component. Recognising the cause of such defects that occur during the build process can aid in the prevention of them in subsequent layers and builds.

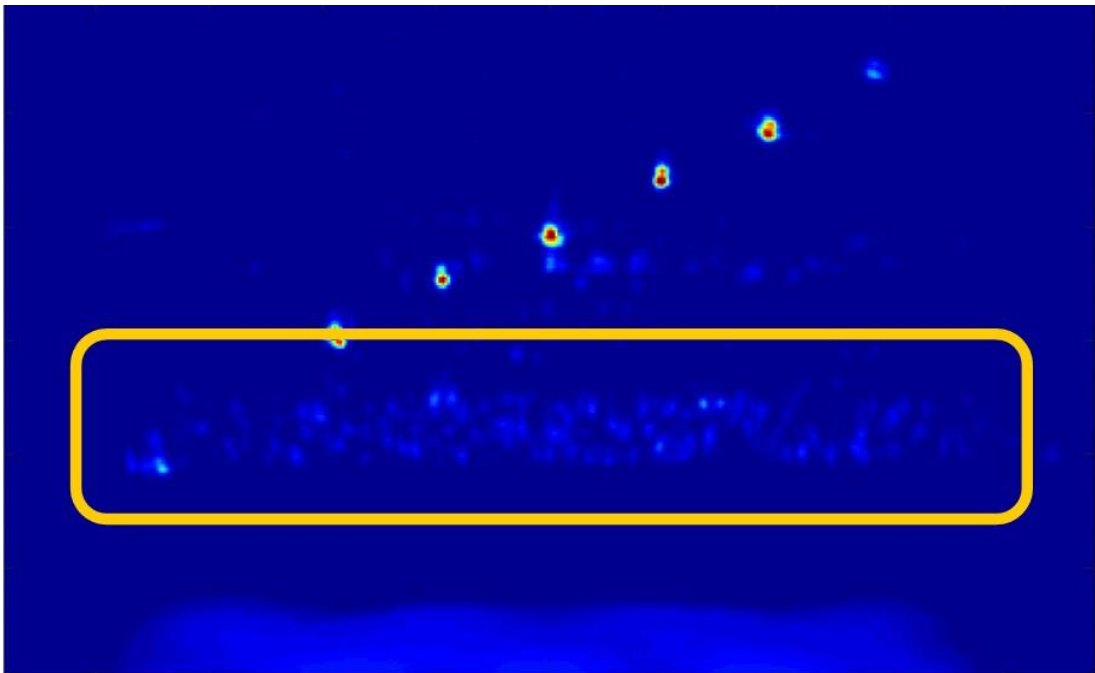


Figure 9 Conventional ultrasonic phased array (see section 2.8.4) dataset showing microporosity in the region between the build plate and the AM part. This is due to the steep thermal gradients that occur during the build process. This SLM sample was 40 x 20 mm.

### 2.3.2. Cracks

Cracks are usually caused by residual stress in the material [72]. This is due to high thermal gradients that occur during the build process, especially during the cool-down phase [67]. Cracks found on the surface are caused due to residual stress across the surface [73]. Equation 3 and Equation 4 can be used to identify a crack, where for a crack the aspect ratio would be high and circularity would be low.

### 2.3.3. Delamination

Delaminations are a specific case of cracking where cracking that forms on the outer edge of a component spreads into the component as a separation between two adjacent layers [67]. Delaminations are also caused when the residual stress in the top layer of a part exceeds the binding strength between the two layers [74].

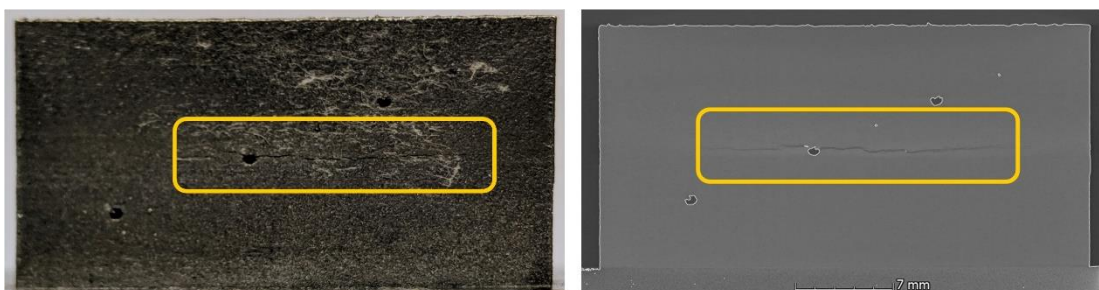


Figure 10 Photograph and X-ray computed tomography slice (see section 2.6.5) of an AM sample outlining some delamination that took place during the build. This SLM sample was 40 x 20 mm.

### 2.3.4. Balling

Balling is primarily caused during the build process when particles of unmolten material are dislodged from the melt pool and shot across the surface. Once cooled, they form spheres or balls on the surface [75]. This is due to low heat input and a lack of melting. Balling is commonly caused by either high scan speeds where the energy density (discussed further in section 2.4.7) is not sufficient for melting the powder or low scan speed and hatch spacing, where the energy density is too high for a given region. In-process optical NDE techniques have the capability of detecting balling. The presence of balling increases the external surface roughness of the finished component.

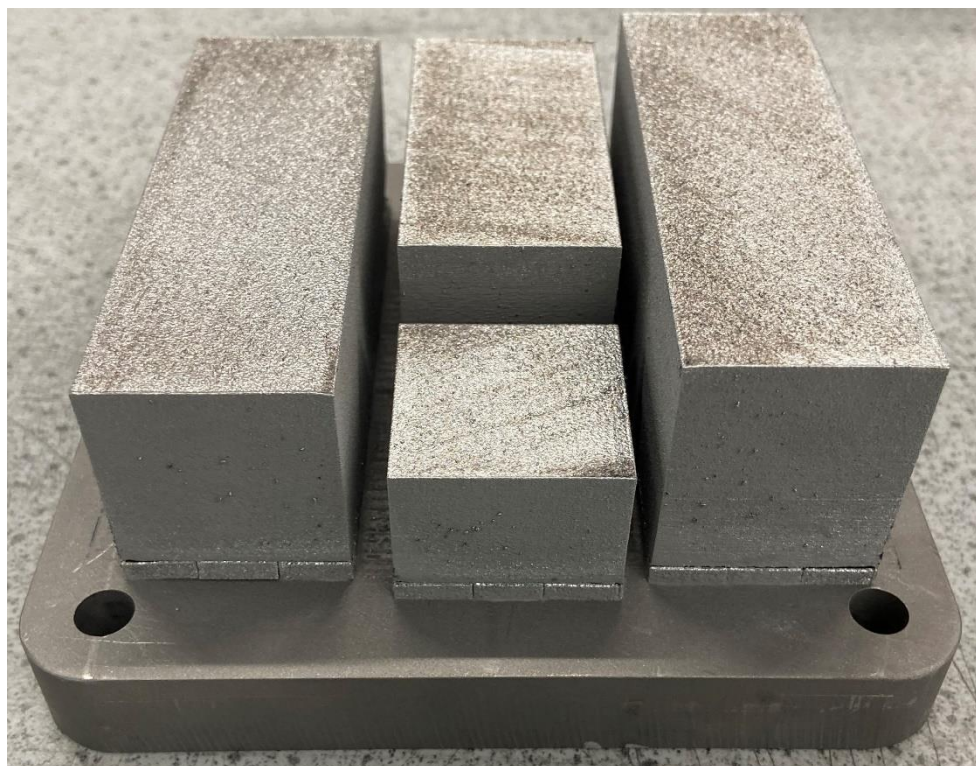


Figure 11 Photograph of AM samples showing evidence of balling that occurred during the build along the vertical walls of the part as small spheres. These SLM samples sit on a 125 x 125 mm build plate.

### 2.3.5. Geometrical Defects

Geometrical defects are commonly seen as shrinkage or oversizing of the final component. This is typically detected by comparing the measured geometry post-manufacture to the designed CAD geometry [76]. Such an inspection would typically be considered post-manufacture metrology. The capability to detect such changes in-process, however, would cross the boundary between metrology and NDT depending on the techniques used. Geometrical defects can be detected in-situ using simple optical NDT methods and corrected using a feedback loop. This is a good example of the line between NDE and metrology being blurred.



Figure 12 Photograph of an AM sample warped from the build plate causing a geometrical defect. This sample was manufactured using SLM and its dimensions were 90 x 30 x 35 mm.

### 2.3.6. Reduced Mechanical Properties

Changes to mechanical properties – such as yield strength and ductility – of a component cannot be directly measured in-process using typical NDE techniques. Instead, they are usually found using destructive methods post-manufacture. The cause of reduced mechanical properties in AM components could be caused by a wide range of detectable defects such as porosity, cracking, delamination and microstructure. By detecting these defects during the build and using tighter process control, the mechanical properties of the final component could be improved. Tsopanos et al. demonstrated the effect changing the build laser power had on part density and thereby the elastic modulus and yield stress [77].

### 2.3.7. Inclusions

Inclusions typically manifest as impurities in the powder feedstock used to build the part and are detected using XCT in the form of a change in contrast due to their difference in density. In AM components Inclusions tend to limit service life due to reduced structural strength, impact toughness and corrosion resistance [78].

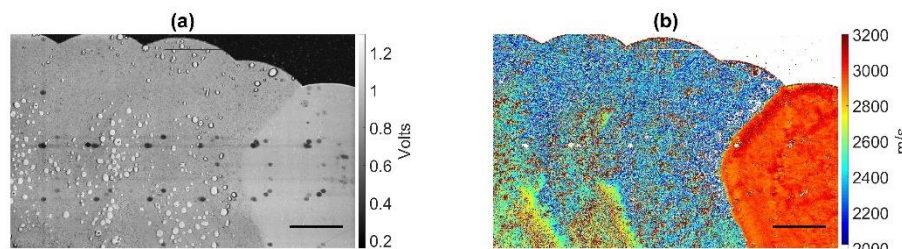


Figure 13 Optical (a) and surface wave velocity (b) data collected using the SRAS technique (see chapter 3) from a titanium sample with tungsten inclusions. These inclusions stand out as white patches on the optical data and red segments of high velocities in the velocity data. The black scale bar represents 1 mm.

### 2.3.8. Unmelted Powder

This can be caused by an irregular melt pool, where pockets of unmelted powder remain within the solidified region of the bulk component. They tend to be spherical in a similar manner to gas pores but resemble a lower contrast to the parent material when detected using NDE methods [79].

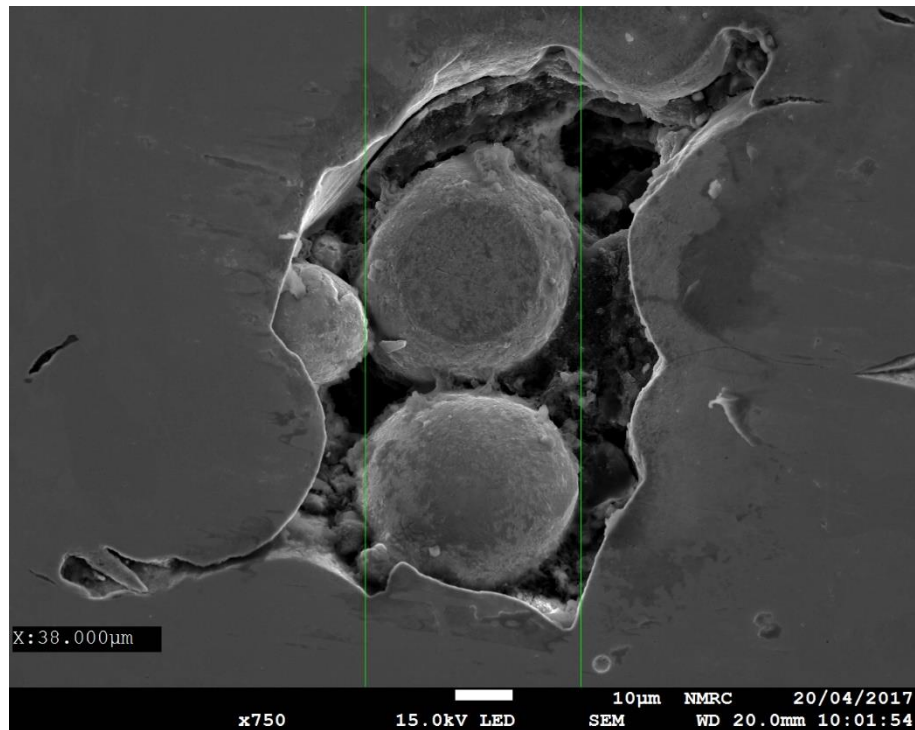


Figure 14 SEM image of the surface of an AM sample showing unmelted powder particles entrapped within a pore.

### 2.3.9. Microstructure variations

Although the microstructure of a component is not classed as a classical defect, it directly affects the material properties of the final component. If the component does not have the mechanical properties that it was designed for, it could be defective and that could be due to differences between the manufactured and assumed microstructure at the design stage of the component. AM component microstructure and grain orientation are commonly measured using prepared cross-sections of built components using destructive techniques such as etching and EBSD. Section 2.7 discusses this in greater detail within the context of AM and NDE.

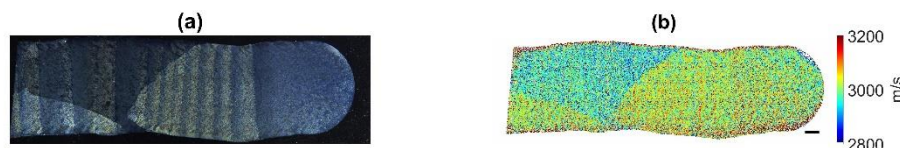


Figure 15 Microscope image of etched surface (a) and surface wave velocity (b) data obtained using the SRAS technique (see chapter 3) of a Ti64 WAAM sample. The black scale bar represents 1 mm.

## 2.4. Key Performance Variables (KPV)

As discussed in section 2.2 within the context of SLM there was a wide range of parameters that could be varied to meet the specification of the part being manufactured. Section 2.3 illustrated a wide range of defects found within AM components which can be avoided by varying the appropriate build parameters. The build environment, the powder feedstock and the powder bed itself were outside the scope of this thesis, due to them not being controllable by a user on the shop floor. Properties such as the wavelength, beam quality, repetition rate, pulse width and intensity profile were defined by the laser used within the SLM systems and so could not be changed. For this reason, they were not considered within the context of this thesis.

The work within this thesis focuses on identifying NDE techniques that can detect changes to KPV that directly influenced the parts manufactured using SLM. These were split into several categories such as the capability to detect surface and sub-surface defects and the ability to detect changes to build parameters such as the scan strategy, laser power, scan speed, hatch spacing and energy density [43]. The following sections discussed these processing parameters as KPV within this thesis. The capability to detect these KPVs was then used to evaluate the various NDE techniques reviewed.

### 2.4.1. Surface and External Defects

The typical defects found within AM components were discussed in greater detail as part of section 2.3. Detecting and classifying surface defects such as cracks (see section 2.3.2) and pores (see section 2.3.1) was considered a KPV within the context of in-process inspection of AM.

### 2.4.2. Subsurface Defects – Internal Features

In a similar manner to surface defects, the detection of subsurface defects was also considered a KPV within the context of in-process inspection of AM. Furthermore, detecting and sizing internal features within AM components provided useful information from a metrology point of view as this type of information was typically only achievable post-manufacture.

### 2.4.3. Scan strategy

The scan strategy refers to the path the build laser takes across the surface of the sample as it melts the powder. Kruth et al. discussed the effect various varied strategies had on the AM part being built, its effect on the part density and final mechanical properties [80]. Catchpole-

Smith et al. utilised fractal scan strategies on ‘unweldable’ nickel superalloys and were able to minimise cracking and increase part density when compared to the island scan strategy used by Kruth [81]. This showed the importance the scan strategy had on the components being built and so was identified as a KPV within this thesis.

#### 2.4.4. Laser Power

The power envelope of the build laser is defined by the specific laser selected for each build platform. Within this envelope, the power used to manufacture individual parts can be varied. The power itself can be measured as peak power  $P_{peak}$  which is the maximum power per pulse (for the pulsed laser) and the average power  $P_A$  which is more representative of the heat added to the part. Two other parameters that affect the power are the frequency or repetition rate of the laser  $R_r$  and the pulse width  $PW$ . Equation 5 can be used to combine all these terms to calculate the peak power output of a given laser [43]. The power of the build laser directly impacts the parts being built and so was identified as another KPV within this thesis.

$$P_{peak} = \frac{P_A}{PWR_r} \quad \text{Equation 5}$$

#### 2.4.5. Scan Speed

The scan speed  $V_s$  refers to the speed at which the build laser is moved across the surface. The scan speed is directly coupled to the build rate and to common AM defects such as balling (discussed in section 2.3.4). The scan speed also defines the energy density and so was chosen as a KPV within this thesis.

#### 2.4.6. Hatch Spacing

The hatch spacing  $H_s$  refers to the space between individual scan lines used when manufacturing AM components. Increasing the hatch spacing increases the build rate but reduces the energy density of the region being melted. Sharratt discusses the effect of hatch spacing within the context of surface defects [71]. As the hatch spacing increases, due to the lack of energy density lines of porosity form throughout the build. Conversely, decreasing the hatch spacing increases the energy density across a given area, which can also lead to defects as discussed in section 2.3.1. The hatch spacing can be used to strike a compromise between the build rate and the energy density used to manufacture a part. For this reason, it was chosen as another KPV within this thesis.

### 2.4.7. Energy Density

The energy density  $E_{d3D}$  was a representative value of the total energy forced into the material being melted. This has a direct impact on the material properties of the parts being manufactured and can be expressed as a function of the average laser power  $P_A$ , scan speed  $V_s$  and hatch spacing  $H_s$ . By taking into account the layer thickness  $t_s$  we can calculate the energy supplied to a volumetric unit of unmelted powder using Equation 6 [82].

$$E_{d3D} = \frac{P_A}{V_s H_s t_s} \quad \text{Equation 6}$$

## 2.5. NDE within AM

A wide range of NDE techniques have been used in the past for the inspection of AM components. The point at which this inspection is carried out, however, has a significant impact on the relative value of the data obtained. At this stage, it is important to understand the various terminologies used in the context of the NDE used for the in-process inspection of AM.

The current AM workflow discussed in section 2.1 and illustrated in Figure 6 relies on post-manufacture inspections to ensure part integrity. To truly utilise the advantages of AM, some form of in-process NDE is required. This would also allow for the implementation of closed-loop feedback for part optimisation and to obtain a digital twin as discussed in the research motivation in section 1.2. In-process inspections as a whole can be split into three separate categories as illustrated in Figure 16; Off-line, On-line and In-line.

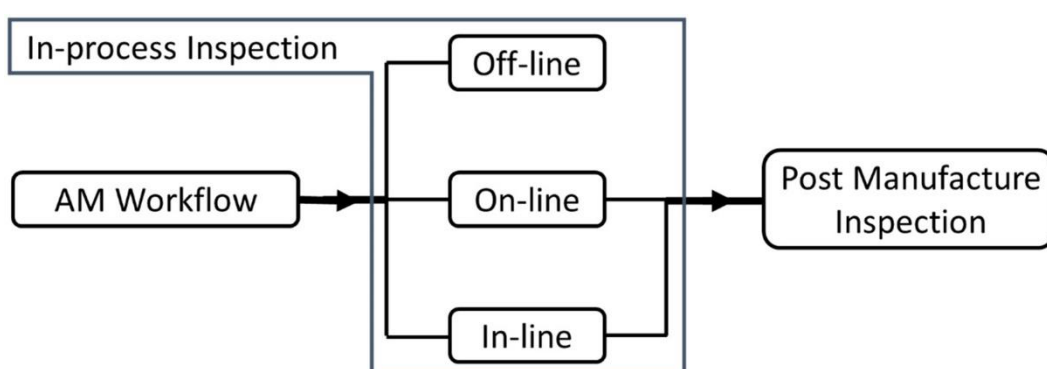


Figure 16 Diagram illustrating the various stages throughout an AM workflow at which an inspection could take place.

- **Off-line** inspections are commonly used in large-scale industries where from a production line individual parts are removed for inspection. Established processes used for large-scale manufacturing, this provides a good representation of the components being manufactured and helps maintain quality control. In the relatively

smaller manufacturing volume of individual AM parts, where the identical parts across one build could vary significantly, this is less representative. Instead, off-line inspections are more applicable for the raw materials (powders, filaments, liquids and sheets) used in AM where a small sample of the material can represent the quality of the entire batch.

- **On-line** inspections refer to inspection that has no impact on the build taking place. They are performed in parallel to the build and require inspection rates comparable to or faster than the build rate [83]. Such inspections are what is required within AM platforms to achieve goals such as 100% inspection of a given component, closed-loop feedback for real-time process control and to build an accurate digital twin of built parts.
- **In-line** inspections refer to inspections carried out in between the build process. Here the build and inspection happen sequentially [83]. This means that the overall build time of a given component is a sum of the build time and inspection time (Figure 17), which inherently is longer than the time required to build a component with no in-process inspection whatsoever.

At this stage, it is also important to define the subtle differences and discuss the similarities between NDE and metrology.

- **NDE** on its own is commonly used as an umbrella term for a range of concepts such as testing, inspection and evaluation [84].
- **Testing** is where experiments are used to quantitatively or qualitatively determine the characteristics of a given object based on its response to various physical fields such as radiation, electromagnetism, light and sound.
- **Inspection** is when the compliance of a given component is tested against a predetermined standard.
- **Evaluation** refers to a quantitative assessment of specific characteristics of an object and tends to overlap with metrology.
- **Metrology** is defined as the science of measurement and its applications [85]. This primarily refers to the measurement of the external or internal surfaces or features of a given component.

The development of modern NDE techniques and their capabilities to not only detect the presence of defects but also locate and size them gives NDE an increasing presence in the field of metrology. Although pure metrology – the measurement of a component against its reference geometry – is classically a post-manufacturing process, there are cases in the literature where a classically NDE system is used to obtain metrology information [76].

It is worth considering that for real-world components such as those discussed in section 1.1.1 the total time between the start of the build and the part being cleared for service, was a sum of the manufacturing time and the inspection time as illustrated in Figure 17 - post-build inspection. This was worth considering when assessing the time capabilities of any in-process NDE solution used within the context of AM.

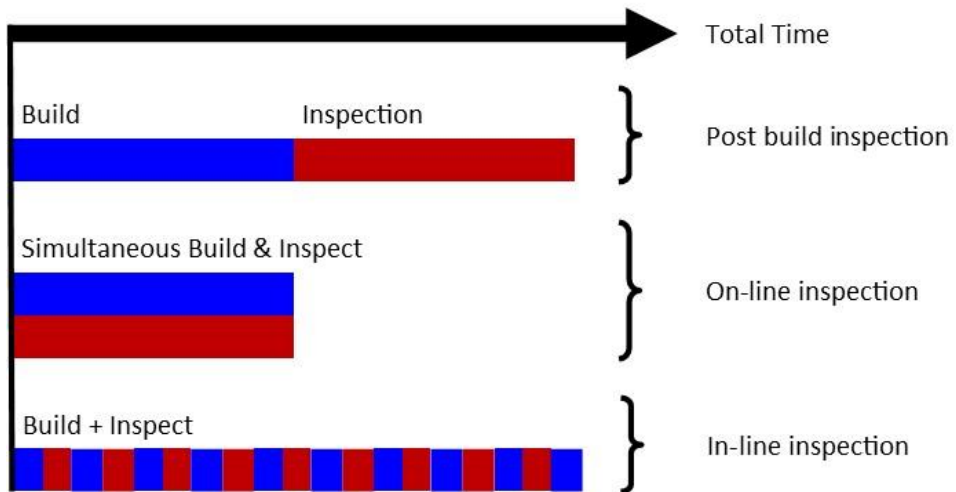


Figure 17 Diagram illustrating the difference in total time required for carrying out an inspection post-build, on-line and in-line.

As Figure 17 illustrates, the ideal solution would be an on-line inspection, to obtain data from a build taking place. However, in a situation where an on-line solution was not available, the total times compared should be between the in-line inspection timeline and the post-build inspection timeline. Comparing an in-line inspection timeline to a pure build timeline would be an unfair comparison, as at the end of a pure build timeline a post-build inspection would be required to obtain a similar amount of data. It is also worth considering that the time required for a vast majority of NDE techniques is directly related to the resolution of the data obtained. This is discussed in greater detail has part of section 5.4.

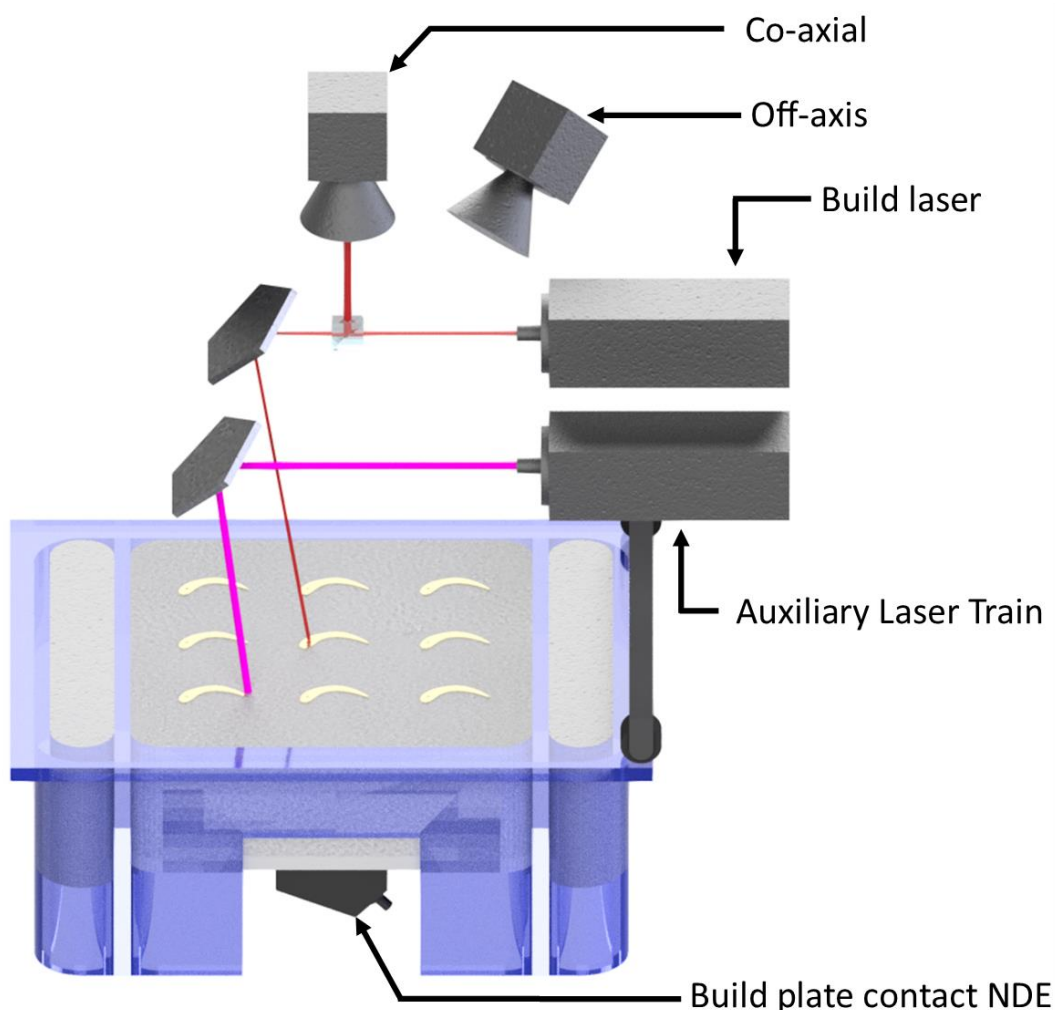


Figure 18 Rendered image of an SLM build platform illustrating several methods in which NDE can be implemented into an SLM build platform.

When considering an in-process inspection for AM, there are several avenues of inspection that can be explored as illustrated in Figure 18. Contact NDE solutions such as phased array UT or thermocouples could be embedded within the build plate to monitor the initial conditions and continuously monitor the build as it progresses. Optical NDE solutions could be implemented off-axis to continuously monitor the build volume using a wide field of view or focus specifically on the powder bed and melt pool. A variety of other optional NDE solutions could be implemented as part of a co-axial system that utilises the same optical train as the build laser. Such a co-axial system in an on-line context could be used to continuously monitor the melt pool and the surrounding area. Whereas if the inspection and build were to be carried out sequentially, (in-line) the auxiliary laser train can be used to inspect the entire powder bed independent of the build laser.

The following section reviews the literature around a wide range of NDE techniques that can be used for the in-process inspection of AM, implemented using the methods discussed

above. It also goes on to review several post-manufacture NDE techniques due to their potential to be implemented as part of an in-process inspection and or as a verification.

## 2.6. NDE Review

This section discusses the theory behind various NDE techniques used for the post-manufacture and in-process inspection of AM components. The field of NDE is vast and based on the material, manufacturing process and inspection environment a combination of complementary techniques can be used to detect and classify various defects. As the scope of this study is limited to metallic AM, only NDE techniques suitable for the inspection of metallic AM components are discussed below. Ahead of reviewing the existing literature, it is worth making a distinction between direct and indirect NDE.

- **Direct NDE** refers to the capability to directly measure various properties of a given material. An example of this would be the measurement of the speed of sound through a given material or the measurement of the time of a known ultrasonic wave (travelling at a known speed).
- **Indirect NDE** refers to the measurement of the state of a given parameter to infer a specific property or state of the material. An example of this would be thermography where typically the amount of IR light reflected is calibrated and used to infer the temperature of a given component.

The following sections lay out the theory behind some metrology techniques followed by optical, thermal and X-ray NDE techniques. It then discusses ultrasonic NDE and focuses on LU techniques as they are the primary methods used within this engineering doctorate. Techniques such as eddy current, die penetrant, magnetic particle inspection and radiography were seen to be outside the scope of this study and were not considered. This is due to these techniques not having the potential to be integrated as part of an in-process inspection and there being very little evidence in the literature of them being used for the inspection of AM.

### 2.6.1. Metrology

It is worth noting that the line between the fields of NDE and metrology is constantly being blurred. This is due to both NDE and metrology being used side by side as they provide complementary measurements. For this reason, some metrology techniques are reviewed as part of this section. Surface metrology, for example, provides a useful insight into the challenges faced by LU NDE techniques and is discussed further in section 5.3.

Metrology is defined as the science of measurement and its applications [83]. This primarily refers to the measurement of the external or internal surfaces or features of a given component. Contact probes along with coordinate measurement machines (CMM) are some of the most commonly used tools within the field of metrology. Laser line scanners are also used with CMM where a laser line is projected across the surface of an object and its position in space is recorded using triangulation [86]. Data from contact probes, CMM and laser line scanners can be used to reconstruct the object in 3D space [87]. As these techniques measure the true dimensions of the part in question, they can be considered to be direct measurements.

### Structured light or fringe projection

This works on the principle of projecting a known light pattern on the surface of a component and then capturing it from a known angle [88]. Zhang et al. presented an in-situ surface topography measurement system that used a commercial digital light processing (DLP) projector with a customised projection system [89]. This was mounted at the top of the build chamber looking down at the build plate at 35° through an anti-reflection coated glass. The heightmap obtained of the surface of the build provided a rich stream of information regarding the fusion process. The boundary of the fusion region was a feature that could not easily be seen using other optical sensors. This could then be processed using edge detection and used as part of a geometrical analysis application. Similarly, the average height of the fused surface was measured and tracked for each layer. This data was modelled by taking into account factors such as the layer thickness, the powder shrinkage ratio, powder density and metal density. The average height was used as an indication of the thermal growth of the chamber or drift in the build platform. This was due to the average height of a layer being a function of the distance between the fringe projector and the camera.

More abrupt changes in height were also observed within the fused region alongside small peaks observed in the unfused region. These were assumed to be due to splatter caused by the fusion process. Finally, a parameter that was unique to this process was the powder bed waviness. The height difference here was measured to be about 28µm and was assumed to be caused by the vertical motion of the recoating blade. In some cases, fused metal protruding above the new layer was detected using this process. In this case, the height or waviness of the powder bed could be considered a direct measurement, whereas measuring the drift of the chamber overall would be considered an indirect measurement.

### Photogrammetry

This technique uses the principle of optical triangulation, where measurements are extracted from multiple projections by rotating the component or manipulating the imaging system. Common points are identified from each image and using optical triangulation the geometry of the component is reconstructed and a 3D point cloud is generated [90].

The combination of structured light and photogrammetry can optically measure all external features of a given component to a very high level of accuracy. Although pure metrology was considered outwith the scope of this project it was worth reviewing and understanding the work carried out in the metrology field, as they could provide useful insights into workflows that could be implemented within the field of NDE.

Afazov et al. presented a novel distortion compensation method to address the shrinkage that occurs when additively manufacturing metallic, ceramic or polymer components [91]. This shrinkage or distortion was due to the various thermal gradients that occur across the component. In the specific case of ceramics, the shrinkage occurred during the de-binding and sintering process where the polymers used to bind the ceramics were burnt away. Due to the complex nature of the components being manufactured, this distortion was difficult to model. Instead, Afazov et al. propose a novel distortion compensation method where the part was first built and then 3D scanned using a combination of photogrammetry and structured light. The measured points were aligned to the reference CAD and checked against a predetermined tolerance (Figure 19 top row). If the part was above or below the tolerance, the measured difference was inverted and applied to the reference CAD. This pre-distorted part (Figure 19 bottom left) was built and the process was repeated. The authors showed that a tolerance of  $\pm 65 \mu\text{m}$  can be achieved using powder bed fusion and that the entire methodology was at a TRL level of 5-6. It was worth noting that the authors only presented this methodology applied to external features. It was however noted that with the use of XCT, the same methodology can be applied to internal features.

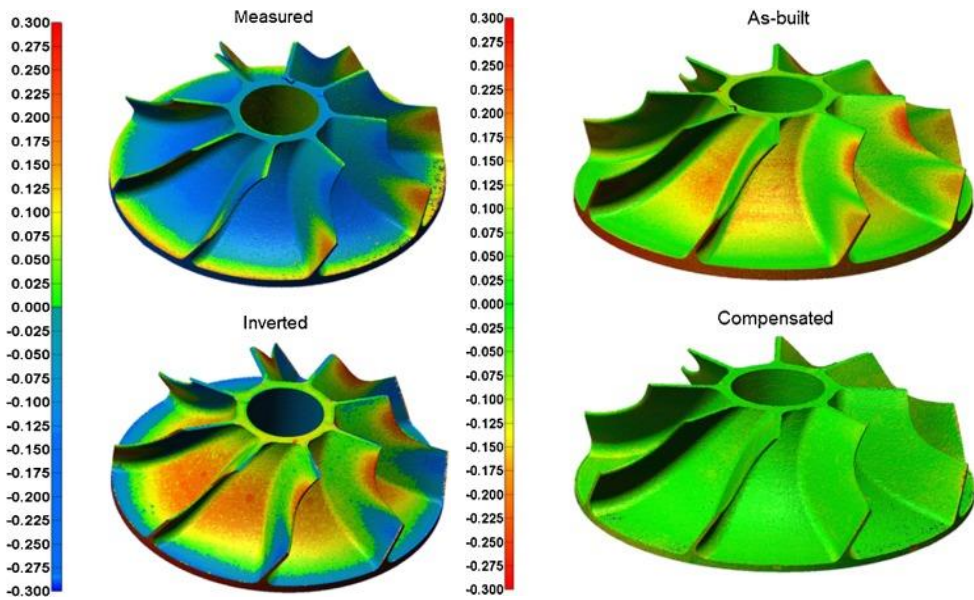


Figure 19 3D measurement data for an impeller where the measured surface of the built part is presented relative to its original CAD in the top left and the same data is presented using a different colourmap in the top right. The bottom left figure shows the inverted 3D data used to print the 2<sup>nd</sup> iteration and the bottom right figure shows the compensated part measured against the original CAD. All measurements are in mm [91].

Although the in-process implementation potential of photogrammetry based techniques was low, the overall methodology served as a good example to demonstrate the potential a closed-loop feedback NDE solution would have on the final part.

### 2.6.2. Surface metrology

Although the pure subject of surface metrology was outside the scope of this EngD, it was important to understand how the measurements were taken and how the surface roughness changed across components manufactured using AM processes such as SLM. This was because to carry out an in-process inspection, the surface texture – discussed in greater detail as part of section 5.3 – was one of the main challenges. Surface metrology is a subset of metrology, where the variation in surface texture is measured. Based on the vertical variation in height of the sample, various mechanical and optical techniques can be used.

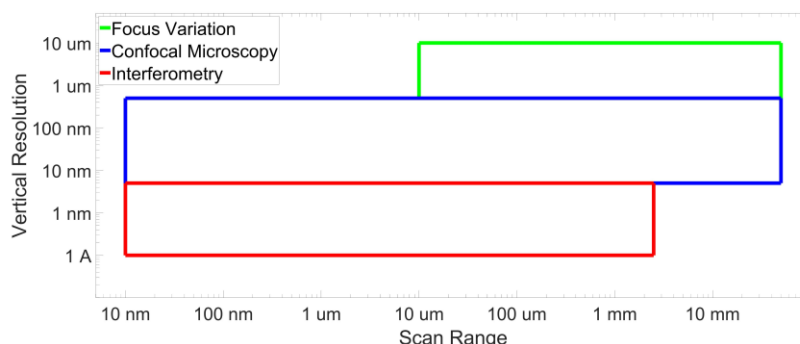


Figure 20 Figure illustrating the various vertical resolutions and scanning ranges in terms of linear distance for three surface metrology techniques: focus variation, confocal microscopy and interferometry. Reconstructed using the data from Sensofar Metrology technology [92].

### Focus Variation

A small depth of focus optical system is used here in conjunction with a vertical stage to collect information as the focus is varied [93]. The small depth of focus results in only small regions of the object being sharply in focus. Once an entire stack of images is captured across the vertical translation of the optics, an algorithm is used to convert the gathered data into 3D information. This builds a true colour image with the true depth of field of the area being inspected.

### Confocal Microscopy

This uses a point source light focused on the sample being measured [94]. Using a pinhole, only the information in focus is captured. As the height of the sample is varied, a height map of the sample is constructed using only the data that is in focus. This is typically used for the inspection of surfaces deemed too rough for interferometer-based techniques but those not rough enough for focus variation.

### Coherence Scanning Interferometry (CSI)

This technique is used for the measurement of surface variations in the nanometer range [94]. This works on the principle of interfering two beams of coherent light. One which reflects off a reference mirror and the other which reflects off the surface being measured. The change in phase of the interference pattern is used to calculate the change in height of the surface being measured [95]. White light is used here instead of monochromatic light due to its shorter coherence length, which gives greater accuracy.

### Profilometry

Surface Profilometry or Stylus Profilometry uses a small stylus that drags along the surface of a given component to measure its surface roughness. The disadvantage of this contact technique is the aliasing effect that occurs due to the diameter of the scanning probe head. Due to their non-contact nature and the wavelengths of light used, optical surface metrology techniques provide much more accurate measurements and can scan a much larger area.

Strano et al. manufactured a truncheon sample with sloping surfaces between 0° and 90° to the vertical with horizontal increments of 5° [96]. Using profilometry the authors were able to measure surface roughness of ~9 µm Ra on the vertical faces and ~13 µm Ra on the top (as deposited) surface of the sample. The authors observed increased surface roughness values – above the ~13 µm Ra – on the angled surfaces. Through closer analysis, it was understood that this was due to discontinuities on the stepped edges of each layer where particles were ejected due to balling (see section 2.3.4).

### 2.6.3. Optical

Within the wider field of NDE, optical is the simplest form. It involves visually inspecting built components and parts. Spaces that are difficult to access are inspected using a mirror. A somewhat more complicated visual inspection is carried out as part of the manufacture of single-crystal turbine blades [97]. Here the cast nickel blades are etched and visually inspected by highly trained and experienced inspectors. This is to ensure the entire blade consists of one grain and does not contain any secondary grains. Such inspections, however, are limited to post-manufacture inspections as they are limited by the speed and accuracy of the human eye. In-process applications of high throughput systems such as production lines and AM require faster visual inspection systems able to process and store large quantities of data. For this reason, the following optical sensors were required.

Kanko et al. used an Inline Coherent Imaging (ICI) system to directly analyse the melt pool and indirectly infer the morphology of the surrounding area during the build [98]. An ICI system consisted of a low-power broadband light source, a high-speed spectrometer and a fibre-based Michelson interferometer. The light was captured by the sampling arm of the fibre and compared to a reference beam. The reference beam passed through a fibre polarization controller and dispensation matching elements, this was to correct for the polarization changes caused by the use of a single-mode fibre and depressions caused by optical elements along the sampling fibre. A commercial ICI system (setup 1) and a custom build ICI system (setup 2) were used. These were used as part of two setups: the first of which used an XY translation stage for the sample and the second used a galvanometer (similar to those used in SLM systems) to move the beam across the sample surface. The impact of changes to the melt pool geometry due to changing process parameters such as laser power, scan speed, layer thickness and overhanging structures were investigated.

Ocylok et al. employed a coaxial optical inspection system as part of a blown powder manufacturing process [31]. The melting laser (976nm wavelength) was collimated and then reflected down to the build plate using a dichroitic mirror. The collimated beam was then focused down to the build plate using an optical system. A reflection of the melt pool travelled back along this optical train, passed through the dichroitic mirror, through a coloured filter and onto the CMOS camera. This setup was used to directly measure the width and length of the melt pool and infer how they were impacted by changes in build parameters. It was also observed that an increase in the feed rate, negatively impacted the size of the melt pool. Whereas an increase in laser power caused an increase in the size of

the melt pool. A similar but less drastic correlation was observed when the temperature of the base plate was changed.

Finally, unlike the retrofitted inspection systems discussed above, Keaveney et al. discussed the use of the InfiniAM spectral monitoring system in Figure 21, fitted to Renishaw AM500 [99]. This consisted of two independent systems known as LaserView and MeltView that monitored the build laser (1) and the melt pool (18) [100]. The LaserView module (10) was placed behind the first mirror (11) along the beam path of the build laser. This provides a direct measurement of the power output of the build laser which was used to melt the material within the build chamber. The MeltView system (2) consisted of two separate photodiodes, where one was for visible light (4) and the other for infrared (5). Via a series of mirrors, reflected light from the melt pool was focused on these two detectors. This module provided an indirect data stream of what was going on during the build. InfiniAM combines the data from LaserView and MeltView along with the part geometry to present a 3D representation of the data collected during the build process.

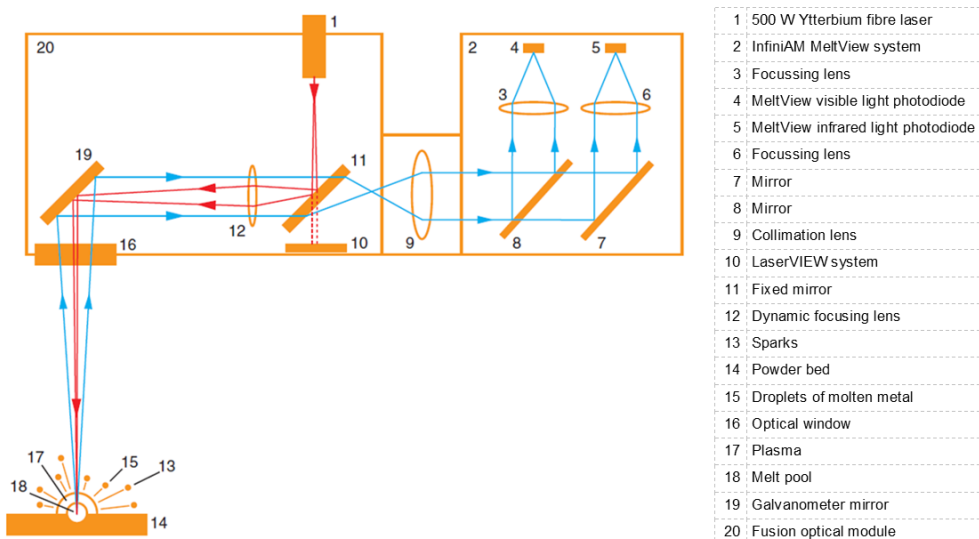


Figure 21 Schematic of the InfiniAM spectral monitoring system fitted to Renishaw AM500 [99].

Keaveney et al. demonstrated how the raw data obtained using the InfiniAM system could be used to detect regions where powder particles had been redeposited and thereby led to defects during the build process [99]. The Renishaw AM500 with its InfiniAM spectral monitoring system was one of the few commercially available AM platforms with inbuilt process monitoring. This showed the future potential a wide range of in-process AM inspection techniques could have if they were to be fully integrated into the AM system.

### 2.6.4. Thermography

Infrared (IR) thermography, commonly referred to as thermography is widely used in NDE due to it being a non-contact method that works in real-time. In very simple terms “Infrared thermography is a graphical representation of heat” where the temperature of an object is imaged and used to deduce some information about its condition [101]. Thermography is a good example of an indirect NDE technique. It works on the principle that any object that exists above absolute zero emits electromagnetic radiation which can be characterised by its wavelength and intensity [102]. This emitted radiation can be used to interpret the temperature of an object.

Thermography typically uses an IR camera or pyrometer to detect the emitted radiation. Based on the way the component is heated thermography is split into two categories: active and passive [103]. Active thermography uses an external energy source to heat the object being inspected. Based on the method in which the energy is applied, active thermography can be separated into several subcategories. Pulsed thermography utilises heat sources such as pulsed lasers, heat guns and flash lamps to heat the sample. This specifically focuses on the heating process, where the inspection is focused on the increase in temperature. Long-pulse thermography uses a continuous heat source and focuses more on the cooling process/the rate at which heat is lost from the component. Finally, passive thermography requires no external heat source and instead purely measures the infrared radiation emitted by the object. This is well suited for the in-process inspection of a manufacturing process.

Islam et al. used a pyrometer alongside a CMOS camera with an external illumination laser to inspect the melt pool, heat-affected zone and build the surface [104]. As the pyrometer measurement diameter was about 15mm it was seen to be much larger than a typical SLM melt pool. This meant that the temperature information retrieved was from the heat-affected zone. Two setups were used and the results were compared to each other. Setup A was a simple processing chamber with a 200 W IPG fibre laser and mechanical powder spreading system. Setup B used a commercially available research system similar to the EOS M270. The combination of the pyrometer and camera provided a set of thermal and optical results at different laser energy inputs for both setups. A similar variation in temperature was detected at the same volumetric energy input across the two setups. Different to other studies, Islam et al. also presented the difference in the cooling rate between the two setups which could have an impact on the microstructure of the final component. Finally, combining the thermal data with the optical data provided a correlation between the input energy and

balling phenomena discussed in section 2.3.4. Using this information an optimal energy input of 1400 to 1700 J/mm<sup>3</sup> was identified for these setups.

Krauss et al. used a microbolometer detector as an off-axis sensor to cover 30% of the EOS M270 build plate at a 45° angle [105]. The detector was used to measure the irradiance in and around the melt pool. It was also capable of measuring the melt pool area, circularity and aspect ratio similar to Kanko et al. [98]. The effect of scan velocity, laser power, hatch distance, scan vector length and layer thickness on the melt pool characteristics mentioned above was investigated. Artificial cylindrical defects several layers high were manufactured into the components and then covered with a sealing layer. A thermogram of the heat-affected zone showed an increase in irradiance around the flaw. Following this, results were presented as to how this could be used to size manufactured defects below a solidified surface ranging from 40µm to 500µm. The temporal evolution of a sub-surface defect was also presented.

### 2.6.5. X-ray

Commonly used in the medical industry, X-ray inspection forms a key aspect of industrial NDE. X-rays refer to high energy, low wavelength electromagnetic rays which are typically used to obtain 2D projections of internal structures such as bones in the human body and cracks or voids in industrial applications. X-ray inspections use a point source and project high-energy rays through the item being inspected onto a 2D detector or radiation-sensitive film [106]. The distance between the X-ray source, the part and the detector is varied to obtain the required magnification. The amount of energy required (governed by the voltage supplied to the filament) varies based on the density of the part, whereas more dense parts require more energy for the X-rays to penetrate. These individual projections show changes in density as changes in detected energy intensity due to the energy lost by the X-rays travelling through the component. This is an example of a direct NDE technique where the X-rays passing through the part are used to visualise changes in the part density.

X-ray computed tomography (XCT) is a volumetric measurement technique that is achieved by incrementally rotating the part and obtaining a range of individual 2D projections. These are combined using reconstruction algorithms to build a 3D grayscale image of the part [107]. The resolution of the final 3D data set was defined by the pixel size within the detection array, the size of the array and the magnification. For example, a small part could be positioned close to the X-ray source which provides a large magnification as a small region of the part is imaged on more pixels on the detector. This makes XCT a very good NDE technique for

imaging extremely small details embedded within a component. The requirement to manipulate the sample combined with the amount of shielding required around the system and the prohibitive cost make it impractical to implement XCT as part of an in-process inspection.

Mireles et al. presented a study where data obtained from an in-situ IR thermography system was compared to post-manufacture XCT data [108]. Three identical samples were manufactured containing seeded defects in the form of spheres, triangular prisms, cubes and cylinders ranging from 100 to 2000 µm using an Arcam EBM system using Ti64 powder. The system was equipped with a Flir SC645 IR camera used for the in-situ inspection. One of the samples was kept in its original as-built state, the next was put through a hot isostatic pressing (HIP) cycle and the third one went through a re-melt cycle. The XCT dataset of the as-built part showed the presence of the seeded defects larger than 600 µm. The part that was put through the post-manufacture HIP cycle showed no visible evidence of the seeded defects in the XCT data, this included the 2000 µm cubes. Finally, the re-melted parts showed no evidence of the seeded shapes in the in-situ thermography data which was confirmed using the post-manufacture XCT.

Kim et al. presented the use of XCT data obtained from an SLM sample used from a metrology analysis of the internal features within three different components [109]. The first was a 10 mm diameter cylinder containing a 5 mm cube in the centre, orientated diagonally to the build direction. The second was a 6 mm diameter cylinder with a 2 mm cube in the centre, aligned to the build direction. The third was a 5 mm diameter cylinder with 6 spheres ranging from 2 - 0.2 mm in diameter aligned in the centre of the cylinder in a line. The metrology grade XCT data obtained from a Nikon XT H 225 ST system was compared to the CAD of the three parts. The difference in internal volume relative to the CAD was the lowest in the large cube at 2.3% and then 8.8% for the small cube. This trend was also observed in the spheres where the large 2 mm sphere had a difference of 12% and the smaller 0.4 mm sphere had a difference of 49.2%. The comparison between the CAD and XCT showed that the majority of the shrinkage occurred on the top overhanging surface of the internal features.

Due to the nature of XCT discussed above, it was clear that was difficult to implement as part of an in-process inspection. Leung et al. used a synchrotron X-ray system aimed at the cross-section of an I12: Joint Engineering, Environmental, and Processing (JEEP) system beamline [110]. The authors were able to produce exceptionally detailed figures and movies of the laser melting process as it happened in real-time. It was observed how throughout the

melting of a single laser track, how unmelted powder was entrapped within the scan track (see section 2.3.8), how ejected particles from the melt pool contribute to spatter and balling (see section 2.3.4) and how dissolved gasses within the powder forms pores within the solidified section and surface (see section 2.3.1). It was also observed during the melting of a second layer how part of the first layer was remelted and gas bubbles were drawn in between the two layers. Although this was a small step taken toward an in-process inspection using a simplified version of the problem, it provided useful insight into the physics of what goes on during the melting process (see section 2.2.2) and showed the value of such in-process inspections.

### 2.6.6. Electron backscatter diffraction (EBSD)

The mechanical properties of most materials are closely linked to their microstructure. For this reason knowing, understanding and being able to control the microstructure of an AM component is critical when building a component to perform under high mechanical loads and temperatures [111]. EBSD is an SEM-based technique used to obtain crystallographic data from a given material [112]. An SEM works on the principle of firing a beam of low-energy electrons at a given sample surface. This beam is steered across the surface and focused onto the sample using electromagnets. The emitted photons and electrons from the near-surface of the sample are detected using various detectors. EBSD utilises this by tilting the sample to 70° which focuses the diffracted electron cone from each point onto a phosphor screen. The Kikuchi diffraction patterns obtained from the phosphor screen are unique to the various crystal orientations of a given material and are used to identify them [113]. EBSD requires a well-polished, extremely flat surface with no contaminants. For this reason, it's only used in a laboratory environment for detailed analysis of materials.

The true potential of EBSD within the context of AM was presented by Polonsky et al. where Tri-Beam femtosecond laser ablation system was used inside the SEM [114]. An AM sample was placed within this chamber and after an EBSD data set was obtained the top layer was ablated. This process was repeated to obtain 204 slices of EBSD data with a spatial and layer step size of 1.5 µm to form square pixels. This was off a 100x40x40 mm sample manufactured using an Arcam S12 EBM machine and Inconel 718 powder. A columnar grain structure with a preferred [001] orientation was observed along the build direction. The authors also showed how the presence of a large lack of fusion defect affected the columnar grain structure in the sample. In the layers following this defect, the columnar growth restarted due to the presence of fresh powder. This direct measurement of the crystal orientation across the full volume of a given sample showed the potential for the in-process inspection of AM. The

negative here was the fact that each layer of the sample was ablated to obtain this data. Where in the case of a layer-by-layer inspection of an AM component, the volumetric data would exist alongside the built sample.

## 2.7. Microstructure within AM

The majority of the existing literature analyzed a cross-section of AM components in the XZ and YZ planes, where Z referred to the build direction (see Figure 8). This is due to the columnar grain structures commonly observed in the build direction [115]. As outlined in sections 2.3 and 2.3.9, it was clear that the speed and power of the heat source had a significant influence on the build. It also affected the thermal gradient  $G$  and the liquid-solid interface velocity  $R$  of the melt pool [111]. Based on the theory found in the literature using  $G$  and  $R$  it was possible to calculate the transition region between equiaxed and columnar grains for various AM processes as shown in Figure 22 [116]. Applying this to a range of materials provided the end-user control over the microstructure of the components being built.

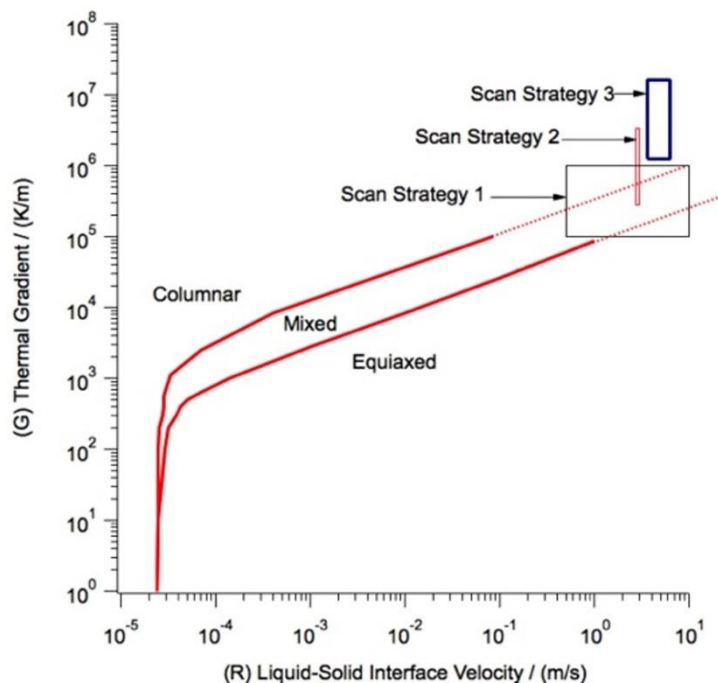


Figure 22 EBM Solidification map for Inconel 718 with thermal gradient  $G$  plotted against the liquid-solid interface velocity  $R$  for obtaining columnar, mixed and equiaxed microstructure [117]. The overlaid scan strategies are used to manufacture the site-specific microstructure in Figure 23.

Sames et al. illustrated how the scan speed and power should be linked to several other factors such as the edge effect, scan strategy, part geometry and the thickness of the powder bed within the scan area [111]. These parameters had a significant impact on the initial conditions and the boundary conditions of the heat transfer and thereby the component

microstructure. Considering an edge of a sample, the heat source could pass over it and return before the heat could dissipate. Similarly, a smaller part could reach an overall higher temperature compared to a larger part due to the lack of material to dissipate the heat. Due to the powder having a lower thermal conductivity compared to a solidified component, an unsupported overhanging section could again reach a higher temperature (overheat) and thereby have more defects compared to the solid component.

Carter et al. manufactured two batches of samples using CM247LC powder (a nickel-base superalloy developed for high-temperature directionally solidified turbine blades) on a Concept Laser M2 using SLM platform [73]. One batch of samples used a simple ‘back and forth’ scan strategy and the second used an ‘island’ scan strategy where the 2D surface of the sample was divided into small ~ 5 mm squares and the scan direction was changed by 90° for each adjacent square. When inspected using EBSD, it was clear that compared to the back and forth scan strategy, the island scan strategy provided highly textured samples. This was due to the relatively localised heat flow during the solidification of each of the layers. The authors showed how using EBSD throughout the Z height of the sample the island boundaries had a more fine-grained chaotic nature, whereas the regions within the islands had a strong [001] orientation. Using MicroCT they also demonstrated that clusters of cracks formed close to high-angle grain boundaries.

Körner et al. discuss the effect changes to the scan speed and hatch spacing have on the growth of columnar grains and equiaxed grains within EBM samples [115]. The authors showed how a relatively slow scan speed of 4.5 m/s and large hatch spacing of 100 µm resulted in columnar grain structure, compared to a faster scan speed of 8.8 m/s and smaller hatch spacing of 37.5 µm resulted in equiaxed grains in the build direction.

Dehoff et al. used proprietary EBM scan strategies which varied scan speed and beam path to manufacture several samples [118]. This allowed the beam to change between a point source and a line source. The EBSD data presented from three of these samples showed how authors were able to achieve control over manufacturing samples with equiaxed and columnar grains with a strong [001] orientation aligned to the build direction. They were also able to show the capability to manufacture samples with a strong [001] orientation in the transverse direction.

Raplee et al. progressed this further by installing an IR camera aimed at the build plate of an ARCAM S12 EBM system [119]. In a similar manner to Dehoff, Raplee manufactured a component using a combination of line and point melt strategies across various sub-regions

of the same part. The thermographic data showed how the point melt strategy maintained an elevated temperature for longer compared to the line scans. When inspected using EBSD, the two sub-regions showed an equiaxed grain structure for the point melt strategy and large columnar grains in the build direction for the line scan regions.

Finally, as a demonstration of their capability to control the microstructure within a component using EBM, Dehoff et al. manufactured a 25.4mm x 12.7mm x 25.4mm block using Inconel 718 powder [117]. The plan view as shown in Figure 23 contained the letters ‘DOE’ across the full depth of the sample. This was achieved using 3 different scan strategies on effectively 3 passes across the surface highlighted in Figure 22. On the first pass using a beam current of 10 mA, a scan speed of 800 mm/s and a spot melt strategy was used to melt the boundaries of the letters. On the second pass using a line melting strategy with a beam current of 15 mA and a scan speed of 4530 mm/s was used to melt the background. Finally, on the 3<sup>rd</sup> pass, the same spot melt strategy as the first pass was used to fill in the letters. The sample was polished and inspected using EBSD to obtain the data shown in Figure 23.

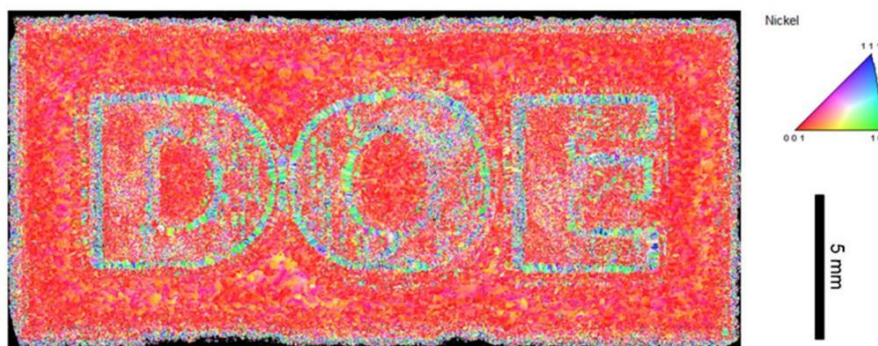


Figure 23 EBSD orientation map of the plan view of a nickel part manufactured using EBM. Three passes of different scan strategies were used to 1) melt the boundaries of the letters using a spot melt strategy 2) melt the rectangular outer region using a line melt strategy 3) fill in the letters using a spot melt strategy [117].

In all of the studies above, the authors demonstrated the effect changes to the scan strategy had on the component microstructure. Section 1.1.2 at the start of this thesis illustrated using two air disasters the consequences of unfavourable microstructure and thereby the need for NDE capable of detecting microstructure within the aerospace industry. The existing literature primarily focused on post-manufacture inspections for detecting changes in component microstructure. This shows that there is a distinct lack of research into in-process techniques capable of detecting AM component microstructure. For this reason, when selecting NDE techniques for further study as part of this engineering doctorate, the ability to detect component microstructure is considered alongside the KPV (see section 2.4) as part of the CCM in section 2.10.

## 2.8. Ultrasonics

Human hearing ranges from about 20 Hz to 20 kHz, anything above this range is considered to be ultrasound (discovered by Lazzaro Spallanzani in 1790) [120]. Dogs, cats and bats can hear up to 50, 60 and 120 kHz respectively. Ultrasonics uses the concept that energy can propagate as acoustic waves. As these waves propagate through a material they are sensitive to a wide range of features such as material thickness, surface defects, sub-surface defects and changes in material properties.

Ultrasonics as a whole refers to a broad range of techniques used in sectors such as marine, health care and NDE. They typically propagate ultrasound into a given medium and listen for the echoes. Information from these echoes in the form of amplitude and frequency is used to understand the properties of the medium in which the wave is being propagated. Transverse and longitudinal waves are the most common in ultrasonic inspections but several other wave modes exist. Before World War II, sonar was developed to send ultrasonic waves into water and listen for any reflected sound, also known as echoes. These echoes can be used to understand the distance, size and shape of items of interest beneath the surface such as the seabed and other submarines.

### 2.8.1. Acoustics

Sound travels in waves. The simplest visualisation of the properties of a wave would be dropping a stone into a still pond and watching the waves propagating radially away from the point that the stone hit the water [120]. This demonstrates two key properties of waves: they originate from some form of motion (the stone falling into the still water) and they have a direction of travel (away from where the stone hit the water). This wave also has other properties such as period, wavelength, amplitude and speed. The following equation can be used to illustrate relationships between the frequency  $f$ , period  $T$ , wave speed  $v$  and wavelength  $\lambda$ .

$$f = \frac{1}{T} \quad \text{Equation 7}$$

$$v = f\lambda \quad \text{Equation 8}$$

Waves can be classified into various categories based on their particle motion. Sound is a longitudinal wave that requires a medium such as liquid, solid or gas to travel through. The pressure difference caused by the resonating membrane of a speaker travels across the room using air as a medium, to your eardrum. It is worth noting that sound cannot travel if there

is no medium for the sound wave to propagate through. This is why in space, no one can hear you scream.

### longitudinal or pressure waves

If a repeating force was applied to the top surface of the particles in Figure 24, the up-down motion of this force generates a pressure wave into the material, causing the particles to move in an up-down motion as the wave travels down. This parallel motion of the particles to the direction of the wave classifies it as a longitudinal wave. They are also known as pressure waves as they are made up of individual segments of high and low pressure in the direction of travel [121].

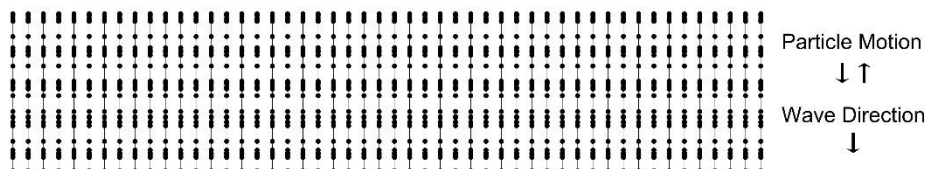


Figure 24 Schematic illustrating the up-down motion of particles as a longitudinal wave travels down.

longitudinal waves are the fastest waves used in ultrasonic NDE and travel at  $\sim 5900$  m/s in steel [122]. The Longitudinal wave speed  $V_L$  for a given material can be calculated using Equation 9, where  $\rho$  is the density,  $\lambda_c$  is Lame's first constant,  $\mu$  is the shear modulus,  $E$  is Young's modulus and  $\sigma$  is the Poisson's ratio [123].

$$V_L = \sqrt{\frac{\lambda_c + 2\mu}{\rho}} = \sqrt{\frac{E(1 - \sigma)}{\rho(1 + \sigma)(1 - 2\sigma)}} \quad \text{Equation 9}$$

### Shear or transverse wave

If a shear force was applied to the top surface of the particles in Figure 25, the left-right motion would generate a shear wave into the material, causing the particles to move in a left-right motion as the wave travels down. This perpendicular motion of the particles relative to the direction of the wave classifies it as a transverse wave. This wave is also known as a shear wave in the context of ultrasonics [121].

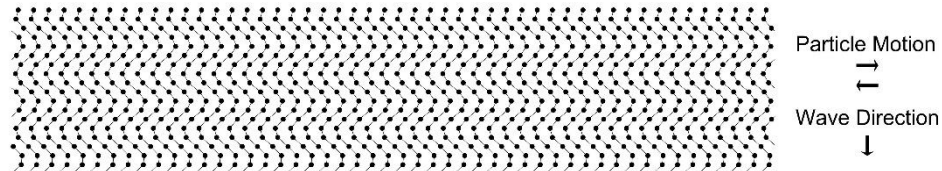


Figure 25 Schematic illustrating the left-right motion of particles as the shear wave travels down.

Shear waves require an acoustically solid material to propagate and are relatively weak. They are relatively slower and travel at a speed of  $\sim 3200$  m/s in steel [122]. The transverse wave speed  $V_T$  can be calculated using equation Equation 10, where  $\rho$  is the density,  $\mu$  is the shear modulus,  $E$  is Young's modulus and  $\sigma$  is the Poisson's ratio [123].

$$V_T = \sqrt{\frac{\mu}{\rho}} = \sqrt{\frac{E}{2\rho(1+\sigma)}} \quad \text{Equation 10}$$

### Surface or Rayleigh waves

Surface waves also known as Rayleigh waves are named after the British physicist Lord Rayleigh who mechanically proved their existence. They travel along the vacuum/air interface and penetrate deep into the material (typically quoted as one wavelength) [124]. The surface wave decayed in amplitude as the dept increased, illustrated in Figure 26. Surface waves are made up of a combination of longitudinal and transverse waves. Their particle motion forms an ellipse whose major axis is aligned perpendicular to the surface and the minor axis is aligned to the direction of travel of the wave. Surface waves are generated at the point of intersection of a longitudinal wave and the surface of a component. Because they travel on the surface of a given material they are sensitive to surface defects along with other surface material properties and can be used for the inspection of curved surfaces with very little attenuation.

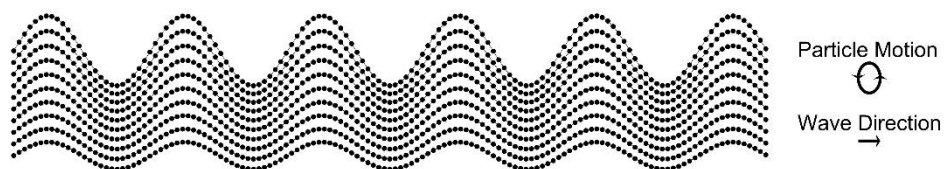


Figure 26 Schematic illustrating elliptical motion of particles as the surface wave moves from left to right. The surface wave amplitude decreases as the depth increases.

Surface waves travel at a velocity that 87-95% of the shear wave velocity which is  $\sim 2900$  m/s in steel. The surface wave speed  $V_R$  can be calculated using equation Equation 11, where  $V_T$  is the shear wave speed and  $\sigma$  is the Poisson's ratio [123].

$$V_R = V_T \frac{0.862 + 1.14\sigma}{1 + \sigma} \quad \text{Equation 11}$$

### Plate waves

These are similar to surface waves but are generated in thin, plate-like regions. Lamb waves are a subset of plate waves and are complex vibration waves that travel along a surface within

the thickness of the material [125]. Symmetrical Lamb waves move symmetrically away and from a central plane of the thin plate-like material. Asymmetrical Lamb waves have a large part of their motion perpendicular to the plate.

### 2.8.2. Flaw Detection & Material Characterisation

The oldest method of flaw detection using sound involves gently hitting or tapping an object and listening to the sound it makes. Looking at a mug for example, and you tap it gently with your fingernail and it makes a clear high pitched sound, it could be assumed that it had no flaws. If it makes a dull sound, this could be seen as an indication of a flaw. The modern equivalent of this test involves an ultrasonic source used to generate ultrasonic waves into a material and a receiver used to detect the ultrasonic waves [126]. The two primary methods of ultrasonic flaw detection are pulse-echo and pitch-catch using longitudinal waves.

Pulse-echo ultrasonics uses a single transmit/receive transducer to generate and detect ultrasonic waves. The most common use of this is thickness measurement where the transducer is placed on top of a section of material or pipe. A baseline measurement is taken by measuring the time between the initial pulse and the back wall echo. As the thickness of the material decreases over time due to corrosion or erosions, the measured time decreases and can be correlated to a reduction in wall thickness. Pulse-echo can also be used for the detection of flaws within the bulk of a given piece of material. The presence of a flaw is detected in the form of a small reflection which appears before the back wall echo or the complete lack of a back wall echo, in which case all the energy is reflected away from the transducer.

Pitch-catch utilises two separate transmit and receive elements. In this arrangement, the ultrasound can be transmitted into the material at an angle, skipped off the back wall and onto the receiving element. This can be used to target specific regions of interest, such as the root of a weld or an angled section of plate. It can also be used for a thorough transmission inspection of a given component where the transmit and receive elements are placed on opposite sides of the part.

Ultrasonic waves can also be propagated across the surface of a component as a surface acoustic wave (SAW) and used to detect surface breaking flaws and other changes in material properties [127]. Although sensitive to changes deeper within the material, as illustrated in Figure 26 SAWs are typically used within NDE for the inspection of a depth equal to its wavelength.

The sensitivity of ultrasonics to variations in material properties can be used to help obtain an understanding of the material being inspected. Changes to the velocity of an acoustic wave travelling through a material can be correlated to a wide range of material properties such as porosity, residual stress, microstructure or coating thickness.

### 2.8.3. Conventional Ultrasonic Transducers

For the inspection of materials and their properties using the ultrasonic waves discussed above, we require a means by which to generate and detect ultrasound within a given material. The most common method for this within NDE is a piezoelectric transducer. When a time-varying electrical potential is applied to a piezoelectric material, the material expands and contracts along with the electrical signal. This property of piezoelectrics can be used to manufacture elements for the generation of ultrasound within materials. Due to the large difference in impedance between the piezoelectric element and air, some form of liquid couplant is required for the efficient generation of ultrasound within a given material. Another property of piezoelectrics is that if the material is contracted or expanded due to an external force, a time-varying electrical potential is generated. This property can be used for the detection of ultrasonic waves.

The frequency noted on a transducer is its centre frequency. Typically low frequencies between 0.5-2.25 MHz provide greater energy and can penetrate deep into the material. Due to their bigger wavelength of  $\sim$ 11.8-2.6 mm in steel for a longitudinal wave, they are not sensitive to small defects. High-frequency transducers between 15-25 MHz have a reduced penetration depth but are more sensitive to small defects. This is due to their much smaller wavelength of  $\sim$ 0.4-0.2 mm in steel for a longitudinal wave.

### 2.8.4. Conventional Phased Array Ultrasonic Testing (PAUT)

Phased array transducers take the concept of individual transducer elements a step further by combining several of them. Compared to a single element transducer that emits a beam in a fixed direction, a PAUT probe can steer and focus its beam within the component. This is carried out by individually firing the elements within the probe to obtain the desired beam path. Phased array probes allow the user to carry out more complex inspections covering a wider field of view.

To fully utilise the signals obtained from the entire array, all the transmit-receive pairs of time-domain signals are collected in a process referred to as full matrix capture (FMC) [128].  $N$  number of generation and  $M$  number of detection elements in an array, this creates an

$N \times M$  matrix. When it comes to processing this data, various ultrasonic array imaging algorithms exist. The total focusing method (TFM) was seen to be the gold standard in this area due to how robust it was and its ability to detect various types of defects [129], [130].

### Total Focusing Method (TFM)

This is an ultrasonic array imaging algorithm that uses all the elements in the  $N \times M$  matrix from FMC to produce a 2D image where all points in the plane are in focus [128]. The focal laws are calculated for each point in the 2D image and the recorded signals are time-shifted accordingly before they are summed for point. A more detailed description of this method can be found in the literature [131]. This is also discussed further within the context of LIPA in section 4.4.2.

#### 2.8.5. Data Presentation

The data obtained using an ultrasonic system can be presented in various methods. The simplest method is an A-scan where the acoustic amplitude detected is displayed against time. In a pulse-echo or pitch-catch application discussed above, this method can be used to measure the time-of-flight between the initial pulse and the back wall echo or received signal. The difference in time between the initial signal and the back wall echo or detected signal in conjunction with the speed of the wave can be used to calculate material thickness or the location of a defect. Figure 27 illustrates an A-scan of a SAW generated and detected using the LU technique known as SRAS discussed in chapter 3. This snapshot of information however only represents one point in space across the sample being inspected.

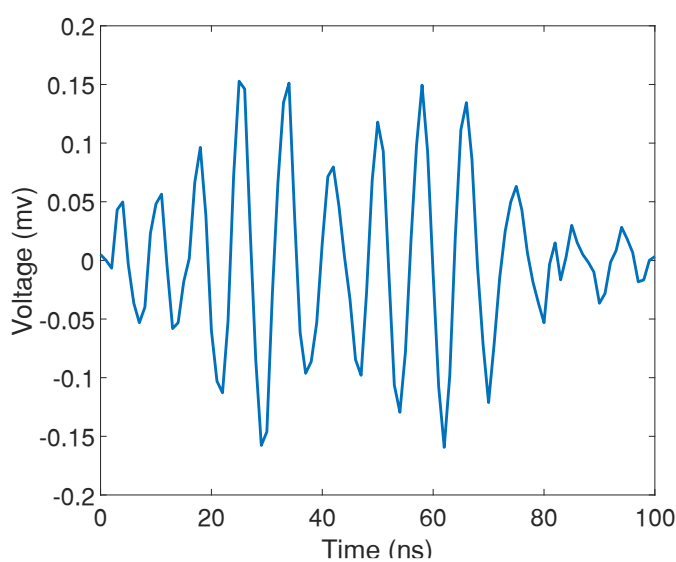


Figure 27 Voltage vs Time graph showing an A-scan of SAW packet generated and detected using the smooth surface SRAS system discussed in chapter 3.

The next level in which information can be presented is a B-scan where the effective 2D dataset is presented as the generation and detection elements are translated across the surface. A typical B-scan plot would consist of one axis displaying time (in terms of the signal) and the other either presenting distance – recorded using an encoder – or time (in terms of global time) as the probe is moved across the sample surface. The signal amplitude in this case is presented using a colour bar or grayscale. B-scans are typically used to present information from the cross-section of a given part in the case of time-of-flight. This gives the person viewing this data an understanding of the size and position of any defects or features within the part. In the case of a SRAS dataset, the B scan presented in Figure 28 (a) represents the SAW packets obtained from a line across the surface of a given sample. The signal amplitude in millivolts is presented using the colour scale. A Fast Fourier Transform (FFT) is performed on the SAW data to obtain the frequency data in Figure 28 (b) where the amplitude is presented using a colour bar.

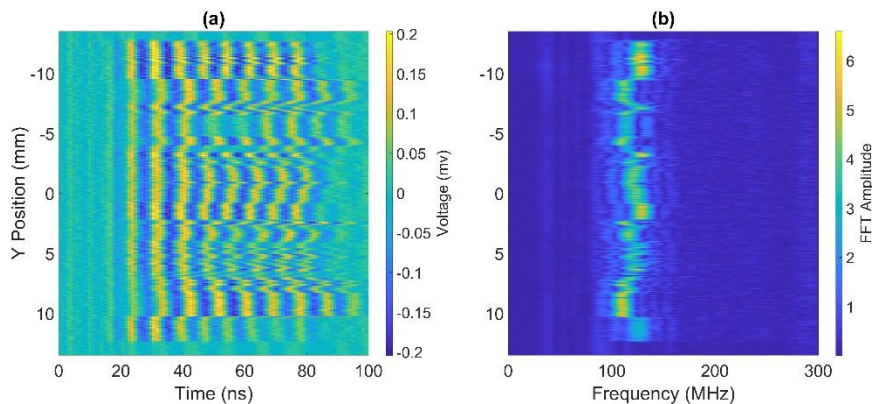


Figure 28 B-scan figures showing the position vs time plot from 1080 points (a) and position vs frequency plot showing frequency peaks between 120-130 MHz (b).

The final method in which acoustic data is presented is a C-scan. Here the probe is scanned across a 2D surface of the component and plotted using an XY coordinate system. The signal intensity in a similar manner to a B-scan is presented using a grayscale or colour map. This method is used to present information from the surface of a given component which makes measuring the position and size or surface area of a defect relatively straightforward. Typically the data presented is gated in the time domain of each signal, this effectively limits the depth sensitivity of the C-scan image being presented. By either changing the window position or increasing the width of the window, the sensitivity to the defect or region of interest can be varied in the final picture presented. Using a SRAS dataset as an example, the FFT amplitude can be presented as a C-scan as shown in Figure 29 (a). This can be taken further as discussed in section 3.3 using the wavelength  $\lambda$  and peak frequency  $f$  to calculate

the SAW velocity using Equation 8. A 2D plot of the changes to the SAW velocity is presented in Figure 29 (b).

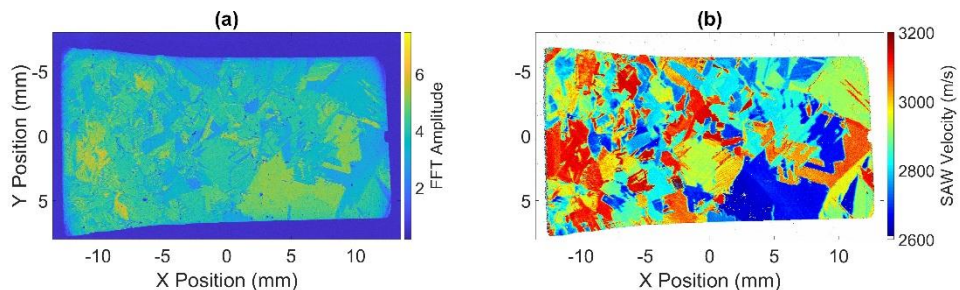


Figure 29 C-scan figures showing FFT amplitude across the sample surface (a) and SAW velocity (b).

### 2.8.6. Ultrasonics on AM

Rieder et al. used an unfocused 10 MHz ultrasonic transducer to generate longitudinal waves into an AM sample being built [132]. This was permanently fixed to the underside of an AM build plate. Their experiment aimed to detect information on the fusion of each layer as the component was built up. Another aim was to detect a seeded defect within the component. The experiment was carried out on a 20 mm diameter cylinder which was 10 mm tall. The cylinder was manufactured using SLM with a 40  $\mu\text{m}$  layer height. The component also contained a spherical (2 mm in diameter) seeded defect full of un-melted powder. The in-line ultrasonic data showed an indication of the manufactured defect. This methodology was used again with different laser powers as the component was built, going from, 100%, 50%, 100%, 25% and finally 100%. This generated more promising results, where effectively a back wall was created as the laser power changed from 100% to 50%. This was visible on the A-scans presented. Due to the lack of mechanical coupling at the 25% to 100% laser power interface, a large back wall echo was observed. This experiment, however, was only sensitive to a very small region of the sample as the data could only be acquired from the sample/material directly above the transducer.

The above work progressed further by comparing the time-of-flight data to XCT data from the same sample [133]. It was clearly shown how the change in laser power to 50% resulted in a band of 3% porosity and the step down to 25% laser power resulted in a region of 30% porosity. This was followed by the manufacture of a semi-cylindrical SLM test block seeded with cylinders ranging from 2-4 mm in diameter at depths of 10, 20 and 30 mm. Using a 5 MHz linear phased array probe, the authors were able to detect all the seeded features and the back wall echo from 50 mm away from the probe.

Chabot et al. presented the potential of PAUT from the in-process inspection of WAAM [134]. On a calibration block manufactured using WAAM, the authors presented the ability to detect side-drilled holes with diameters between 1.2-0.8 mm at a depth of 10 mm. When inspecting a multi-layer aluminium WAAM sample, the authors detected two pores at 11.75 and 4.8 mm from the surface. PAUT was used to estimate these to be ~0.6 mm in diameter. XCT was used to measure the pores to be 0.69 mm and 0.88 mm in diameter.

Javadi et al. presented the use of a PAUT probe for the in-process inspection of WAAM [135]. A PAUT probe was attached to a robotic arm and run alongside the robotic arm used for welding. The open architecture of the WAAM process allowed this type of inspection to be easily integrated into the build process. The authors demonstrated the ability to detect the presence of a 2.6 mm diameter tungsten rod which was placed in the weld to simulate an inclusion. Similarly, a crack was intentionally manufactured into the weld and detected using the PAUT data. The growth of this crack was monitored and measured over the following hours. Some of the limitations of PAUT was the fact that it required a smooth surface and acoustic coupling to generate and detect ultrasound within the part.

Kim et al. used measurements of ultrasonic phase velocity in three (X, Y and Z) directions to obtain an understanding of the porosity, pore aspect ratio and texture within several stainless steel AM samples [136]. These samples were manufactured using a Concept Laser Mlab 100R Cusing SLM platform and 316L stainless steel powder. Each of the samples had a different hatch spacing varying from 50 µm up to 150 µm, whilst all other parameters such as laser power, scan speed and layer thickness were kept constant. The phase velocity measured using ultrasonics was compared to the phase velocity calculated using EBSD estimated anisotropic elastic constants and Christoffel equation. The authors demonstrated how as the hatch spacing was varied, a relationship between the average ultrasonic phase velocity and the part density measured using XCT could be observed. Finally, the authors demonstrated the effect hatch spacing had on the yield strength, ultimate tensile strength and elongation of the samples.

## 2.9. Laser Ultrasonics (LU)

Similar in practice to conventional ultrasonics, LU uses lasers instead of physical probes to both generate and detect ultrasonic waves. The following subsections discuss the various methods of generation and the detection of ultrasound using lasers.

### 2.9.1. Generation

Unlike transducers which require to be in contact with the surface, lasers are capable of remotely generating ultrasound on a given surface. When a laser beam is focused on the surface of a sample, some energy is absorbed by a thin layer of material close to the surface, and some energy is reflected. The absorbed energy is converted into ultrasonic waves via either the ablation regime or the thermoelastic regime. The amount of energy absorbed into the sample is dependent upon the laser power, laser repetition rate and the absorptivity of the sample [137].

In the ablation regime, the energy from the laser source is focused on the sample surface and forms a plasma. This plasma ejected from the surface creates a net recoil which produces a bulk wave, a large component of which is perpendicular to the surface of the sample. For this reason, the ablation regime is most suitable for carrying out bulk measurements using LU. Due to the ablation of the surface, this is considered to be a destructive process.

In the thermoelastic regime, the energy focused on the sample surface is less than that of the damage threshold of the material. This energy is absorbed within the skin depth of the material which causes thermal expansion. This primarily generates acoustic waves parallel to the surface with a small amount of energy being dispersed into the sample. This is a completely non-destructive process and is used in a wide range of NDE applications.

The method in which the energy is incident upon the surface can further define the way energy is propagated across or into the material being inspected. For example, a laser spot propagates energy into the material in the shape of a hemisphere; whereas a line would have a more directed energy distribution, where a majority of the energy is propagated in a radial pattern perpendicular to the line. This was discussed further by Aindow et al. [138]. The effect of the generation laser shape and directivity is discussed further concerning the specific set of experiments in section 4.4

Another difference compared to conventional ultrasonics (which tend to provide a narrowband excitation), LU generation is typically a broadband excitation. The excitation frequency for a given laser is primarily defined by its laser pulse width. Using Equation 7 for given laser pulse width, the maximum frequency is calculated. It is, however, worth noting that this is a theoretical ‘maximum’ frequency and that the actual frequency content will be lower. A better method for visualising this is by plotting the pulse shape of a given laser and then using an FFT to plot the frequency spectrum from that laser. This was carried out for the various SRAS systems and discussed further in section 3.4.1.1.

Finally, the material being inspected has a significant effect on how efficient a given laser is for generation or detection. Typical engineering materials that are silver in colour such as aluminium, nickel and titanium reflect green (532 nm) and absorb IR (1064 nm) more efficiently. Whereas materials such as copper, brass and gold absorb green and reflect IR. For this reason, the lasers chosen should be considered based on the materials being inspected to maximise the absorption for generation and reflection for detection.

### Types of lasers

There are two types of lasers used in LU: pulsed and continuous-wave (CW) [137]. Pulsed lasers are commonly used as generation lasers due to their higher energy densities and the ability to induce rapid temperature changes that generate stress and elastic waves within the material [139]. The pulse width of the laser also affects the frequencies of ultrasound it can generate (see Figure 38). The emitted wavelength and power tend to vary based on the lasing medium used within the cavity. Pulsed lasers themselves can be separated into several subcategories based on their mode of operation.

The simplest type operates by energising a flash tube, these generate pulses within the range of 100  $\mu$ s – 1 ms. These pulses tend not to be uniform and consist of several spikes which ride on top of the overall energy profile lasting about a microsecond. Although capable of producing high-energy pulses, these lasers are not suitable for LU applications due to the long pulse width.

Q-switched lasers produce pulses in the 1-100 ns range [139]. These lasers store energy within a cavity with mirrors on either end to build up the energy per pulse and so can create much higher energy peaks and shorter pulses. The Q (i.e. quality) factor of a cavity resonator is calculated by dividing the energy stored in the cavity by the energy lost by the cavity in each cycle. This means that when the Q factor is low, the oscillations are suppressed and the energy stored within the cavity builds up. When the Q factor is high the cavity can support oscillation using energy from the lasing medium. This switching from low to high Q results in the rapid extraction of energy from the laser cavity. Q switches are typically made up of an element with a variable absorption that is inserted in between the mirrors.

Finally, mode-locked lasers are capable of producing pulses in the picosecond range. These work using a saturable dye as their Q switch. The non-linear nature of the dye mixes several modes within the cavity effectively locking them. This produces a regular train of mode-locked pulses which physically correspond to a single pulse travelling around the cavity.

## 2.9.2. Detection

Laser detection of ultrasound has similar advantages when compared to laser generation of ultrasound, where the detection element does not require to be in contact with the surface being inspected. Instead, laser detection relies on a beam of light reflecting off the surface of a sample and being focused onto a detector. Here the detector measures one of a variety of changes in the incident beam. The phase, intensity or displacement both in-plane or out of plane relative to the detector surface. In this case, the laser detection system is a combination of a detection laser and LU detector. When considering LU detection systems, they can be split into two categories, those that are based on an interferometer, and those that aren't [140].

### Types of lasers

Detection lasers tend to be CW lasers with a lower intensity when compared to the pulsed generation lasers. As discussed in the section above they tend to be green (532 nm) when used with typical engineering materials that are silver in colour, to maximise reflection. As an example, aluminium has a reflectance of 0.92 at 532 nm compared to Gold which has a reflectance of 0.70. This meant that aluminium reflects a 532 nm light more efficiently when compared to Gold [141]–[143]. For this reason, the lasers chosen should be considered based on the materials being inspected to maximise the absorption for generation and reflection for detection.

### 2.9.2.1. Interferometric

Interferometric techniques work by interfering two coherent beams of light - one reference beam and a second reflected or time-delayed beam - to obtain a signal. Based on the implementation, various types of interferometric techniques can be used for the detection of a wide range of vibrations and displacements.

#### Michelson Interferometer

A Michelson interferometer is one of the simplest interferometers which uses a 50/50 beam splitter to split the input laser beam into two paths. One of these beams - the reference beam - is reflected off a reference mirror. The second beam is reflected off the sample surface and so is affected by changes to the surface such as small displacements due to acoustic waves or surface texture. Both beams are recombined at the beam splitter and focused on to a photodetector. By interfering the sample beam with the reference beam, this technique is sensitive to small changes in the amplitude and phase. This technique is sensitive to changes in the order of ångströms or a frequency range between ~50 kHz and several hundreds of

MHz. This type of interferometer requires an optically flat surface for detection. For this reason, it is not suitable for rough and dirty shop floor environments. Instead, it is more suitable for extremely precise measurements carried out in a laboratory environment. This simple principle however is very relevant and a majority of the following detection techniques utilise this.

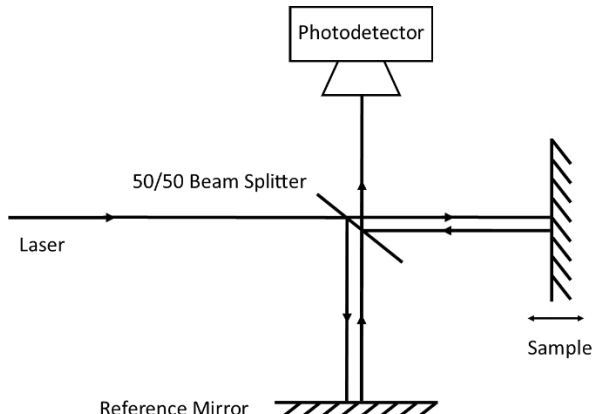


Figure 30 Schematic of how a Michelson Interferometer works.

### Two-wave Mixing

This technique addresses the pitfalls of typical interferometric systems and their inability to take measurements off rough surfaces. In a similar manner to an interferometer, a single beam of light is split into two beams using a polarising beam splitter. The reference beam is reflected off a reference mirror into a photorefractive crystal. The sample beam is reflected off the sample and back into the same photorefractive crystal. A photorefractive crystal can alter its refractive index, in this case, based on the voltage provided to it [144]. The dynamic refractive index within this crystal is used to diffract the reference beam to the propagation direction of the signal beam. Both the transmitted signal beam and diffracted reference beam are focused onto a photodetector that can demodulate them and obtain the vibration signal from the sample.

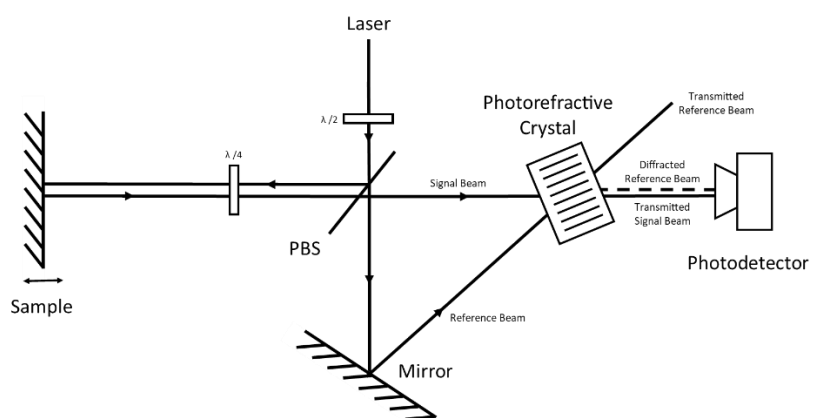


Figure 31 Schematic of how a two-wave mixing interferometer works.

### Quadrature Demodulation

The base principles behind a Quadrature interferometer are the same as the interferometers discussed above: where a coherent light source is split into two beams, one to the sample and one to the reference arm. The primary difference is when it comes to detection [137]. The combined sample and reference arms of the interferometer are split into two channels using a beam splitter. Each channel then uses a combination of a quarter-wave plate, polarising beam splitter and two separate detectors working at a  $90^\circ$  phase shift. As illustrated in Figure 32, this effectively works as 4 separate interferometers. The signals from the phase-shifted beams are then combined using a differential amplifier to obtain the signal from one channel. The two separate channels can then be combined to obtain a signal using displacement-square demodulation or displacement demodulation discussed to a greater detail by Pouet et al. [145]. Furthermore, the authors demonstrated how the use of a detection array can effectively combine several interferometers where each element in the array collects a small amount of light. A greater number of detectors also provide a greater optical étendue making this system more robust and suitable for industrial workshop based applications.

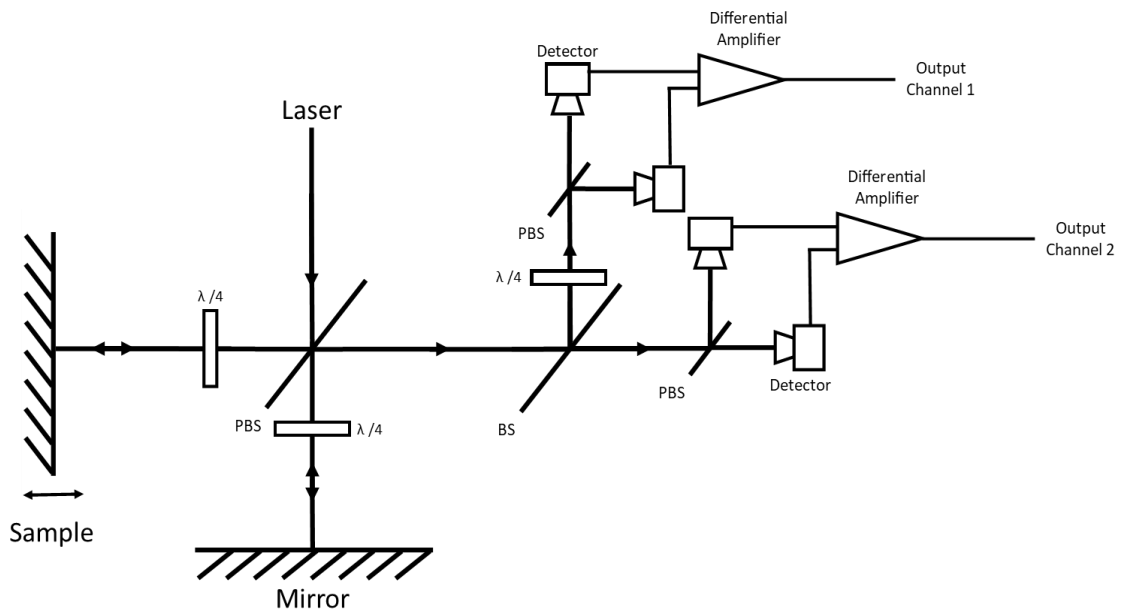


Figure 32 Schematic of quadrature detection interferometer.

### Heterodyne detection

This is a subtopic under interferometric detection and is used in some interferometers as a method of extracting information encoded in the phase or frequency within the wavelengths of visible and infrared light [139]. Here the signal beam is compared to a reference beam known as the “local oscillator” which has a known, fixed offset in frequency and phase in the

instance where the signal beam carried no information. The term heterodyne refers to more than one frequency, compared to homodyne which refers to one frequency. The two beams (reference and signal) are combined on the face of a photodetector which typically has a linear response. The frequencies of the two beams are typically very similar which makes their beat frequency in the region of microwave bands. Where the signal beam does carry some information this can be extracted using the known offset via conventional electronics.

Most commercially available vibrometers operate in a similar principle to an interferometer and use heterodyne detection. A single beam of light is split into two beams using a beam splitter. One reference beam and the second sample beam. The reference beam is reflected using a mirror and 2<sup>nd</sup> beam splitter (used to combine the reference and sample beam). The reference beam has a known frequency  $f_o$ . The sample beam is passed through an acousto-optic modulator or Bragg cell. This introduces a frequency shift  $f_b$  (a career frequency) to the sample beam. The motion or vibration of the sample introduces a Doppler shift to the sample beam  $f_d$ . This sample beam is then combined with the reference beam and focused onto a photodetector. The career frequency can then be removed using electronics to obtain the beat frequency which is that off the surface of the sample.

### 2.9.2.2. Non-interferometric

These detection systems are based on the principle of reflecting a beam of light off the surface of a sample onto a detector. This translates the up-down motion of the surface due to the acoustic waves into a side to side motion on the surface of the detector. The following techniques are defined based on the detector and technique used.

#### Knife-edge Detection

A knife-edge detector (KED) is a form of amplitude variation detector. Here the reflected beam is focused on-to a single photodetector. As illustrated in Figure 33 a knife-edge is used to block half the light, which allows for a greater intensity change to be measured off a single photodetector [146]. In practice, two photodetectors are used instead of a knife-edge along with a differential amplifier to measure the beam displacement across the surface of the detector [147]. The current generation of KED are limited to ~200 MHz due to electronics within the current generation PCB design.

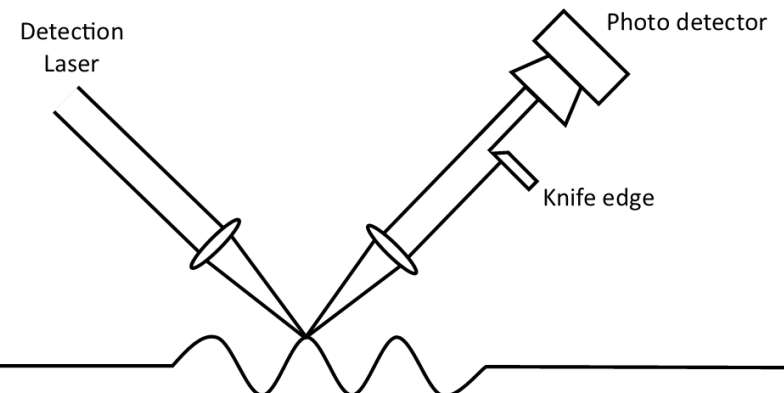


Figure 33 Schematic diagram of how a knife-edge detector works. Illustrating the surface wave travelling across the sample and how the detection laser is reflected off the sample surface and onto the photodetector. This translates the up-down motion of the sample surface into a side to side motion across the face of the detector.

### Speckle Knife Edge Detector

The speckle knife-edge detector (SKED) is an evolution of the KED which was developed at the University of Nottingham to detect acoustic waves off optically rough surfaces [147]. Here the primary difference or “problem” is speckle caused by the surface roughness instead of the single beam of light reflected off a smooth polished surface (see section 5.3.1.3). To cope with the speckle, an array of photodetectors are used where the electronics can identify the individual points of speckle and split them in half to a right and left channel. These two separate channels in a similar manner to a KED can then be used with a differential amplifier to obtain a signal.

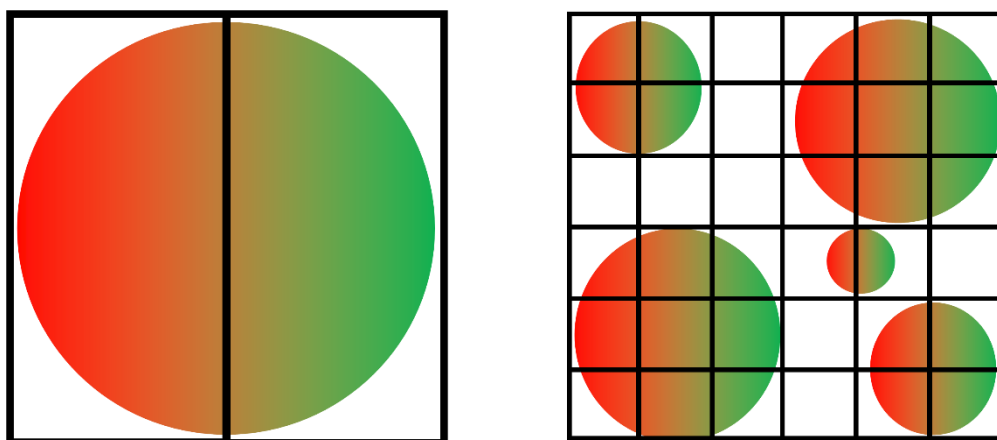


Figure 34 A schematic of how both a KED and SKED work. (left) A single beam of light on the surface of a split photodiode (how a KED works in practice) is split into two channels denoted by the red and green half circles. (right) When a speckle pattern is reflected onto the surface of a SKED, each speckle is split into the two channels denoted by the red and green half circles.

### 2.9.3. Laser Ultrasonics on AM Review

Davis et al. presented a method for integrating an ultrasonic slit mask into an AM component [148]. A slit mask in this context referred to an optical mask (typically a series of lines) used to block part of the light incident on the sample. The spacing of these lines was set to a

specific acoustic wavelength (0.4 mm in this case). When used in conjunction with an IR laser the mask provided a narrowband excitation. An interferometer with a bandwidth of 125 MHz was used to detect the ultrasonic waves. The authors utilised the non-destructive and non-contact nature of LU to demonstrate the capability of a permanently installed slit mask to successfully generate and detect A0 and S0 modes within a 0.8 mm thick aluminium part manufactured using AlSi2 powder. Although a different approach to conventional flaw detection, this was an interesting concept where part of the laser-based ultrasonic NDE system was simplified. Based on prior knowledge of the component life cycle a permanently installed slit mask could provide a targeted inspection to be carried out over time and provide information about the condition of the part.

Everton et al. presented data from an AM component using a 1046 nm pulsed IR laser as a broadband excitation source [149]. The detection system used was an Optech AIR-1550-TWM adaptive interferometric receiver which was equipped with a 1550 nm CW detection laser. The sample inspected contained several 200 µm seeded voids at depths of 200 µm and 500 µm below the surface. It was manufactured using Ti-6Al-4V powder on a Realizer SLM50. The most dominant waves generated were SAW along with longitudinal and shear waves. The generated bulk waves penetrated the component, similar to conventional ultrasound. The B-scan results presented, showed an indication of the presence of the seeded defects within the component but could not be used to size or quantify them. This was confirmed using XCT but also showed how due to the nature of the SLM process some of the seeded defects could have self-healed and could not be detected.

Millon et al. in a similar manner to Everton used an LU system in a pitch-catch configuration [150]. In this case, however, the generation laser was a pulsed 532 nm laser whilst the detection laser was a pulsed 1064 nm laser. The detector used was a two-wave mixing interferometer equipped with a photorefractive crystal. The authors elegantly demonstrated the simulated directivity of a line generation source versus a spot. This showed how more energy propagated away from a line source in the perpendicular direction, whereas a spot had a more isentropic energy distribution. Using this experimental setup the authors demonstrated the ability to detect machined notches, between 0.05-0.3 mm wide and between 0.1-0.5 mm deep. The AM sample inspected was manufactured using blown powder using 316L stainless steel powder. The second part inspected was forged using 316L stainless steel and used as a comparison for the data obtained from the AM sample. The results showed the capability to detect the surface breaking notches on both the AM and forged samples. It was clear that the SNR from the forged sample was greater than that of

the AM sample. This was assumed to be due to the attenuation caused by the internal grain structure of the AM samples.

Smith et al. presented how SRAS was used to detect pores and subsurface defects on SLM samples manufactured using Ti-6Al-4V powder [151]. Unlike other systems, the IR laser here was used for the narrowband excitation of SAWs. Using this technique the authors were able to identify changes in the microstructure of the samples manufactured. This SRAS system equipped with a KED required a surface roughness less than  $\sim 100$  nm Ra compared to typical SLM components which had a surface roughness of  $\sim 10$   $\mu\text{m}$  Ra. Hirsch et al. discussed how SRAS was used to detect “Meso-scale” defects on components manufactured using ‘un-weldable’ nickel superalloys such as CM247 [152]. The authors demonstrated how SRAS was capable of detecting the average change of texture along the island boundaries within the scan strategy. This based on previous measurements and mathematical models of nickel superalloys was linked to the change in crystallographic orientation. This work was progressed further by the author to demonstrate the capability of SRAS to carry out an off-line inspection and perform a targeted repair [24]. A more detailed review of the SRAS technique and its use within the field of AM can be found in section 3.3.1.

Stratoudaki et al. artificially synthesise a laser phased array on the underside of an AM component to carry out a remote ultrasonic inspection [153]. The LIPA results presented showed the capability to detect nested features as deep as 26 mm and as small as 0.5 mm in diameter. This technique and its potential within the field of AM are discussed further in chapter 4 of this thesis.

Zhang et al. presented the use of an IR laser as a broadband excitation source for SAWs on the surface of several AM samples [154]. For detection, the authors used a Quartet that worked on the principle of Quadrature Demodulation discussed in section 2.9.2.1. This allowed the authors to inspect the as-deposited surface of AM components and detect artificially positioned notches on the samples. The size of the notches ranged from 50-100  $\mu\text{m}$  at depths between 1-3 mm. The authors showed how the measured size of the defects on the as-deposited surface was consistently larger than their actual dimension and the defects on the polished surfaces. This demonstrated the potential capability of an in-process LU inspection within an SLM system, to detect surface defects.

Singh et al. presented a different view on the inspection of AM components [155]. The authors presented a novel framework by including a shape optimisation as part of the design process so that the post-manufacture inspection considerations were included as part of the

design. It was shown using a TFM simulation of a point scatterer how the shape optimised component provided a better estimate of 3.9 mm of the 3 mm defect compared to the initial estimate of 7.4 mm. It was also shown how the ultrasonic sensitivity factor was improved by two for an I beam that was designed using this framework. This was a promising concept to provide better scope for the post-manufacture inspection of AM components.

#### 2.9.4. Industrial Laser Ultrasonics

The non-contact and nondestructive nature of LU makes them an extremely useful NDE solution in an industrial environment due to their ability to carry out unobtrusive inspections on components and manufacturing processes. Within this context, it is important to understand the various other criteria and limitations this type of inspection brings with it [145].

##### 2.9.4.1. Cost

The cost of an inspection within any setting tends to be one of the most important factors. In the context of NDE, this can be broken down into three areas: equipment, integration and operation cost [145]. Out of these three, the initial equipment cost tends to be the highest. This is due to lasers themselves being more expensive than conventional ultrasonic transducers. Furthermore, the nature of LU typically requires a generation and detection laser, alongside several optical elements, detectors and signal condition equipment. The integration cost compared to the equipment itself tends to be relatively low due to the system being non-contact and only needing line of sight to the component or process being inspected. The operation cost would be relatively low compared to more conventional processes. This is because the nature of laser inspections meant that they tend to require mechanical stages, fixed sample positions and well-aligned beam paths. This removes the need for a human operator. Also from a laser safety point of view, humans are usually not present in the proximity of a laser inspection. Finally, the reason for selecting a laser-based system in most cases tends to be because the environment is not suited for humans.

##### 2.9.4.2. Optical Etendue

The capability of an optical device to collect scattered light or speckle is referred to as its etendue or throughput [145]. The etendue is defined by the product of the systems entrance aperture area and the solid angle limited by the rays of maximum inclination going through the centre of the entrance aperture. On a laboratory-based device geared for smooth surfaces such as a Michelson interferometer or KED, the etendue is of the order of the square of its optical wavelength. Practically this focuses the return beam of light into one speckle.

On an industry-focused device designed to work on rough surfaces such as those that incorporate two-wave mixing or quadrature demodulation, they tend to have a large optical etendue to collect as much light as possible.

#### 2.9.4.3. Sensitivity

The sensitivity of a given system is defined by its ratio of the change in the output to the change in signal or displacement [156]. At a high sensitivity, a large change is observed in the output relative to a small displacement, and at low sensitivity, a small change is observed in the output relative to a large displacement. Within this context, it's also worth considering the ambient noise, as if the noise is greater than the system output it cannot be detected. This detection limit of a given system can be increased by either increasing the sensitivity, reducing the noise floor or averaging.

#### 2.9.4.4. Depth of field

The depth of field (DOF) refers to the amount of change in sample position – in and out of focus – a system could cope with whilst maintaining its sensitivity. This could also be seen as a range of acceptable sharpness. Within the context of interferometers, the DOF is defined as the sample position at which the signal is reduced by half compared to when the sample is in focus [145]. When a large collection aperture is used to increase the sensitivity, the DOF decreases. A larger detector could be used to increase the depth of field, but this comes with a reduction in sensitivity and increase in shot noise, so a compromise needs to be found when designing systems for industrial applications.

Commonly confused with depth of field, depth of focus refers to the range of movement behind the lens. The depth of focus of a system is the range in which the image sensor could be moved to still capture an image that is in focus.

#### 2.9.4.5. Integration

Integrating an LU system into an existing manufacturing system can be challenging. This is both from a mechanical and software/control point of view. Mechanically the laser system either requires a significant amount of space in/close to the manufacturing process. Or a majority of the system needs to be placed elsewhere and the lasers delivered to the build area via optical fibres. As discussed above the system would also require some noise suppression to maximise its output signal. In terms of software, both the LU system and manufacturing system require seamless integration.

Patel et al presented an SLM-integrated SRAS system where the LU system was built on top of the framework used by a Renishaw SLM platform [157]. The authors demonstrated the capability to measure the SAW velocity off the as-deposited surface of an AM sample. The final optical element used to steer the LU beams across the sample surface were galvanometer mirrors, which were also used by the SLM system to steer the build laser. This was an important first step in the journey towards an in-process inspection from SRAS. The use of glavo mirrors here provided the opportunity for a step up in the inspection speed for SRAS, previous generation of which used mechanical stages to translate the sample.

Although not an LU system the Renishaw InfiniAM was a good example of the integration between build and NDE, both from a mechanical point of view and software [100].

## 2.10. Controlled Convergence Matrix

The wide range of NDE techniques reviewed in the sections above required to be compared and contrasted against their capability to detect changes to the KPV discussed in section 2.4. This section aims to develop an objective scoring methodology to find the most suitable NDE techniques for the in-process inspection of AM processes such as SLM.

Based on the literature reviewed, each NDE technique was scored within the CMM in Table 5 against the KPV discussed in section 2.4. This was carried out in a simple binary fashion where the ability to detect scan strategy, laser power, scan speed, hatch spacing, surface defects and subsurface defects each scored one point. A sum of the detected KPV contributed to the final score.

Following this, each NDE technique was scored out of four based on its current level of integration into an AM system.

- **On-line** scored four points in the CMM. If a new layer could be built whilst the inspection was taking place or if data could be collected as a layer was being deposited/melted.
- **In-line** scored three points in the CMM. If the inspection took place between build layers.
- **Off-line** scored two points in the CMM. If the component was removed from the build chamber to carry out the NDE and then was returned or in a condition to be returned to the build chamber.

- **Post-manufacture** scored one point in the CMM. If the component was removed from the build and any post-manufacture treatment – be it grinding, polishing and heat treatment – was carried out before the NDE.

Section 1.1.2 stressed the importance of the ability to detect component microstructure within the aerospace industry and in conjunction with this section 2.5 reviewed the current work being carried out within the field of AM to detect changes to the component microstructure. In line with this, the ability to detect AM component microstructure was included in the CCM as a special category and contributed five points to the total score.

The total score calculated in the CCM was initially the sum of the KPV multiplied by the level of integration to which an extra five points were added if the NDE technique demonstrated the ability to detect component microstructure. The total score calculated here was not perfect but was used as a guide to select the most suitable NDE techniques for further investigation within this engineering doctorate.

## 2.11. NDE Selection and Conclusion

Based on the information collated in the CCM in Table 5 it was clear that the thermographic NDE techniques scored higher than the others, even without the ability to directly detect variations in the component microstructure. This is due to a lot of literature already demonstrating the capacity for on-line and in-line inspections to detect changes in the scan strategy, laser power, scan speed hatch spacing, surface and subsurface defects. Furthermore, the data presented by Raplee et al. demonstrated the ability of thermographic NDE to infer component microstructure [119]. This however left very little room for further research in this area.

Considering then the NDE techniques with the potential for further development towards an in-process inspection, SRAS came out as one of the leading techniques due to the literature having shown its ability to detect changes in scan strategy, laser power, surface defects and component microstructure. The work presented by Hirsch et al. demonstrated the off-line potential of SRAS to aid in targeting repair strategies to help close the loop within AM as a whole [24]. Chapter 3 in this thesis aims to take the existing capabilities of SRAS as an off-line inspection technique and develop it further to be used as an on-line inspection. This chapter primarily focuses on prepared AM samples. Some data from as-deposited surfaces are presented at the end of chapter 3. The specific challenge – to laser-based inspections – of surface roughness, is addressed in chapter 5 alongside several other challenges such as inspection temperature and inspection time.

When taking a close look at the high-scoring NDE techniques in the CCM there was a clear gap in the capability to detect subsurface defects and nested features within AM components. This was primarily due to most of the NDE techniques with this capability needing either contact – in the case of PAUT – or large-scale investment and space – in the case of XCT – to carry out a subsurface inspection. The LIPA technique presented by Stratoudaki et al. combined the advantages of LU with the data quality of PAUT to inspect the cross-section of an AM component [153]. Chapter 4 in this thesis explores the LIPA technique further and demonstrates its capability to detect nested features within AM components. It is also used to extract positional information of the detected features whilst touching on the value of this technique from a metrology perspective. Upon closer inspection of the system schematics of both the LIPA and SRAS systems, various similarities were observed. Chapter 5 elaborates on this further and explores the concept of a hybrid system design. The aim here was to combine the surface capabilities of SRAS with the subsurface capabilities of LIPA to demonstrate the full potential of an in-process inspection of AM.

Table 5 CCM used to score a wide range of NDE techniques based on theirs ability to detect KPV combined with the current level of integration and ability to detect microstructure.

Inspection Capability	Type of NDE	Inspection of	Method of Integration	Ability to Detect Changes to KPV								Ability to Detect Microstructure	Total Score	Ref	
				Scan Strategy	Laser Power	Scan Speed	Hatch Spacing	Surface Defects	Subsurface Defects	KPV Sum	Level of Integration				
Distortion compensation	Photogrammetry + Structured light	Final part	-					1		1	1		1	Afazov et al. 2017	[91]
Surface defects - time of flight	Laser Ultrasonic	Final part	-					1		1	1		1	Millon et al. 2018	[150]
Post Manufacture PAUT	PAUT	Final part	-						1	1	1		1	Chabot et al. 2020	[134]
Internal defects - time of flight	Laser Ultrasonic	Final part	-						1	1	1		1	Everton et al. 2016	[149]
Metrology, internal features	XCT	Final part	-						1	1	1		1	Kim et al. 2016	[109]
Post processing & in-situ correction	XCT	Final part	-						1	1	1		1	Mireles et al. 2015	[108]
Surface roughness	Profilometer	Final part	-					1		1	1		1	Strano et al. 2013	[96]
2D Cross-section data	Laser Ultrasonic - LIPA	Final part	-						1	1	1		1	Stratoudaki et al. 2018	[153]
Component condition monitoring	Laser Ultrasonic	Final part	-					1	1	2	1		2	Davis et al. 2019	[158]
Post Manufacture PAUT	PAUT	Final part	-		1				1	2	1		2	Rieder et al. 2016	[133]
As deposited surface defects	Laser Ultrasonic	Final part	-					1		1	2		2	Zhang et al. 2020	[154]
Ultrasonic phase velocity	Ultrasonic	Final part	-				1		1	2	1		2	Kim et al. 2021	[136]
In-process PAUT for WAAM	PAUT	Build plate	Build plate						1	1	4		4	Javadi et al. 2020	[159]
Post processing & in-situ correction	Thermography - IR camera	Build plate	Off-axis						1	1	4		4	Mireles et al. 2015	[108]
Coaxial, Melt pool geometry	CMOS camera	Melt pool	Co-axial		1					1	4		4	Ocylok et al. 2014	[31]

Inspection Capability	Type of NDE	Inspection of	Method of Integration	Ability to Detect Changes to KPV								Ability to Detect Microstructure	Total Score	Ref	
				Scan Strategy	Laser Power	Scan Speed	Hatch Spacing	Surface Defects	Subsurface Defects	KPV Sum	Level of Integration				
On-line UT	UT	Build plate	Build plate						1	1	4		4	Rieder et al. 2014	[132]
Temperature profile	Thermography - Pyrometer	Build plate	Off-axis		1			1		2	3		6	Islam et al. 2013	[104]
Powder bed waviness	Structured light	Build plate	Off-axis		1			1		2	3		6	Zhang et al. 2016	[89]
Volumetri EBSD	EBSD	Final part	-						1	1	1	1	6	Polonsky et al. 2018	[114]
2D microstrucre control	EBSD	Final part	-	1						1	1	1	6	Dehoff et al. 2015	[118]
Varying build parameters	Laser Ultrasonic - SRAS	Final part	-		1			1		2	1	1	7	Smith et al. 2016	[151]
Transducer in build plate	Ultrasonic	The build	Build plate		1				1	2	4		8	Rieder et al. 2014	[132]
Scan strategy influence on microstructure	EBSD	Final part	-	1			1	1		3	1	1	8	Carter et al. 2014	[73]
Scan strategy influence on microstructure	Laser Ultrasonic - SRAS	Final part	-	1	1			1		3	1	1	8	Hirsch et al. 2017	[152]
Scan strategy influence on microstructure	EBSD	Final part	-		1	1	1			3	1	1	8	Körner et al. 2014	[160]
Renishaw InfiniAM	Photodiodes	Melt pool	Co-axial		1			1		2	4		8	Keaveney et al. 2020	[99]
Infer microstructure on-line	Thermography + EBSD (Post)	Build plate	Off-axis	1						1	4	1	9	Raplee et al. 2017	[119]
Off-line targeted repair	Laser Ultrasonic - SRAS	Final part	-	1	1			1		3	2	1	11	Hirsch et al. 2018	[24]
Melt pool geometry	Inline coherent imaging	Melt pool	Off-axis	1	1	1				3	4		12	Kanko et al. 2016	[98]
Thermography Heat affect zone	Thermography - Microbolometer	Build plate	Off-axis	1	1	1	1			4	4		16	Krauss et al. 2012	[105]

# **Chapter 3   Spatially Resolved Acoustic Spectroscopy**

This chapter introduces SRAS – an LU NDE technique used for material characterisation initially proposed by Sharples et al. [161]. It discusses the basic concepts behind this technique, followed by a review of its use within the field of AM. It then goes on to present the work carried out through this engineering doctorate to move SRAS towards an on-line inspection solution for AM. The work published by the author in the March 2019 issue of *Insight - Non-Destructive Testing and Condition Monitoring*, by the British Institute of Non-Destructive Testing forms the core results of this chapter [162]. Further details about the instruments used and experimental methodologies are presented. This is followed by several new experiments on smooth and as-deposited surfaces.

## **3.1. Contributions to the Knowledge**

This chapter contributes to the knowledge helping to progress SRAS towards an in-process inspection by individually addressing several areas within the wider engineering problem of carrying out an in-process inspection of AM:

- Mechanical defects are detected using SRAS data and linked to AM process parameters.
- Changes to component microstructure detected using SRAS are linked to further changes in the processing parameters and scan strategies.
- Methodologies are developed for extracting microstructural information from current generation and future generation SRAS instruments.

- The initial effects of inspecting as-deposited AM surfaces are identified.
- The potential for future generations of high-resolution SRAS systems is showcased using the large grains seen on WAAM components.

## 3.2. Introduction

SRAS is an LU (see section 2.9) NDE technique, capable of measuring the SAW velocity of a wide range of engineering materials. This can be used to image the microstructure of such materials and provide an understanding of their crystal orientation. Based on the CMM in section 2.10, compared to a wide range of other NDE techniques, it was clear that the ability of SRAS to detect changes to a wide range of KPV (see section 2.4) made it an ideal candidate for the in-process inspection of AM. An in-process inspection capable of mapping the microstructure and surface defects can contribute to the AM workflow from both process control and a part performance points of view.

From a process control point of view, the combination of a constantly moving energy source such as a laser or electron beam; variable part geometry; the relatively large thermal mass of the build plate; the thermal conductivity of the part; and surrounding powder bed makes the thermal gradients which occur within AM builds difficult to predict and model [163], [164]. The effect temperature gradients have on the microstructure forming within the part being built is well understood and documented in the literature [165]. These variations in microstructure combined with the tendency of the current generation of AM build platforms to manufacture parts with high levels of structural defects (see section 2.1), lead to parts with unpredictable and often inferior mechanical performance compared to those manufactured using more traditional methods such as milling and casting. The early detection of such defects and deviations can help improve the process control within AM. An in-process inspection can close the loop by aiding repair strategies and reducing the parts that get scrapped following a post-manufacture inspection.

From a part performance point of view, the relationship between the mechanical properties of superalloys and their performance at elevated temperatures and loads, in high-performance applications such as gas turbine engines is well understood [166]. Ahead of the utilisation of AM parts in such high-performance applications, assurances will be required around part integrity. The presence of a traceable set of inspections carried out throughout the build process will: aid the certification process of AM parts for use in aerospace applications; reduce the requirements for post-manufacture inspections; provide

information to maintain a digital twin of the component and follow it through its product life cycle. The capability to understand and quantify the mechanical properties of a part being built then opens the window for the part to be specifically tailored for the application.

Within this chapter, the potential of SRAS for the in-process inspection of AM is explored further. The capability of SRAS to detect various defects discussed in section 2.3 is used to classify and obtain an understanding of the causes of such defects within AM components. Methods of detecting variations in the microstructure are discussed and used to improve the information obtained from SRAS acoustic data. This is followed by the inspection of the as-deposited surface of AM samples manufactured using SLM and WAAM.

### 3.3. The Concept of SRAS

The concept of SRAS evolved from the all-optical scanning acoustic microscope (O-SAM) developed by Steve Sharples in 2003 as part of his PhD thesis [167]. A Q-switched mode-locked laser with an acoustic frequency of 82 MHz and a mean power output of 2W was used as a generation source. This was reflected off a spatial light modulator which projected a series of concentric arcs onto the sample. The spacing of these arcs was varied to maximise the signal amplitude. Current generation SRAS systems achieve this by imaging a fixed grating pattern onto the surface of a sample using a broadband IR generation laser [168]. The spacing of the grating pattern defines the acoustic wavelength  $\lambda$  of the SAW being generated. The velocity of the SAW is defined by the material properties of the region directly below the generation patch. The frequency  $f$  of this SAW is measured using a green detection laser reflected off the surface of the sample onto a photodetector. The perturbation of the surface of the sample is proportional to that of the detection laser beam on the photodetector. The SAW velocity  $v$  is then calculated using Equation 12.

$$v = f\lambda \quad \text{Equation 12}$$

A SAW velocity map of a given material is useful for understanding the change in crystal orientation across its surface. Obtaining crystal orientation using SRAS was a somewhat more involved process. A three-way relationship exists between the elastic constants, SAW velocity and crystal orientation. If two of these elements are known, the third can be found. First, the elastic constants of a given material are used to calculate the expected SAW velocity, for all crystal orientations. This is carried out using the forward model discussed by Li in the literature [169]. Following this, using a SRAS system the SAW velocity can be measured in all propagation directions in one plane. Using data from the smooth surface SRAS system

discussed in section 3.4.2.1, Figure 35 (a) illustrates how by rotating the generation patch, and the detection spot, the SAW propagation direction can be changed to measure the SAW velocity in various directions. Finally, by cross-referencing the measured SAW velocity profile with the calculated velocity profiles, the crystal orientation of that grain can be obtained. This process is described to a much greater detail by Li et al. in the literature [170]. The image in the centre of Figure 35 (a) shows the crystal orientation obtained using SRAS and Figure 35 (b) shows the EBSD data from the same region.

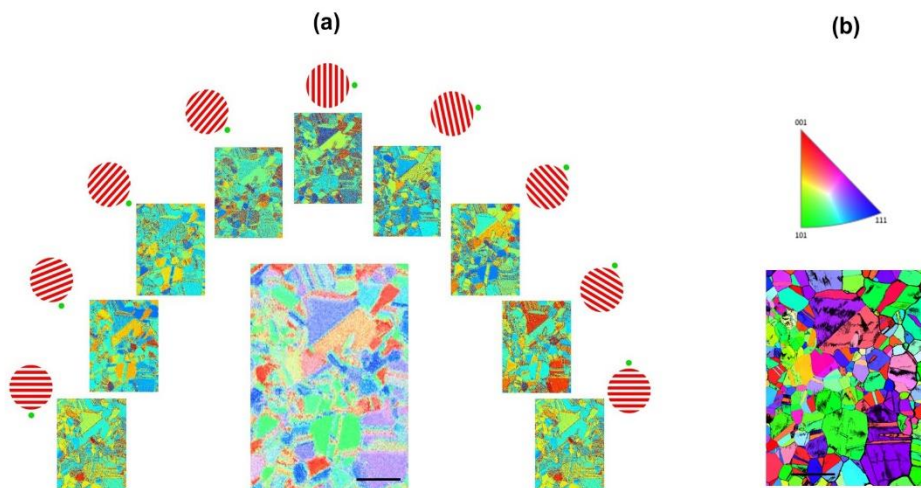


Figure 35 SRAS data illustrating an orientation map of a nickel sample obtained using SRAS, surrounded by velocity maps of SAW propagated in various directions (a) and EBSD data of the same region where the colours represent the crystal orientation (b). The black scale bar represents 1 mm.

EBSD has a much higher spatial resolution compared to SRAS. As discussed in section 2.6.6 however, EBSD is still a laboratory-based technique that requires samples with a well-polished surface. SRAS on the other hand is a relatively fast and mechanically robust technique with the potential for implementation as part of industrial manufacturing systems.

Measuring the SAW velocity in two orthogonal directions and combining them in a vector image provides a method of distinguishing between grains with different crystal orientations but the same velocity in one direction. This can provide some understanding of the crystal orientation in situations where full orientation mapping cannot be carried out. As illustrated in Figure 36, this is useful in the case where a rapid inspection is required or the resolution is not good enough to image individual grains. This is also very useful in a situation where the time available is not sufficient to carry out a full orientation inspection. This entails measuring the SWA in up to 9 or 18 directions (in  $20^\circ$  or  $10^\circ$  increments), modelling the SAW in all directions and cross-correlating the two datasets. Instead, a vector map can be created following two SRAS inspections in orthogonal directions.

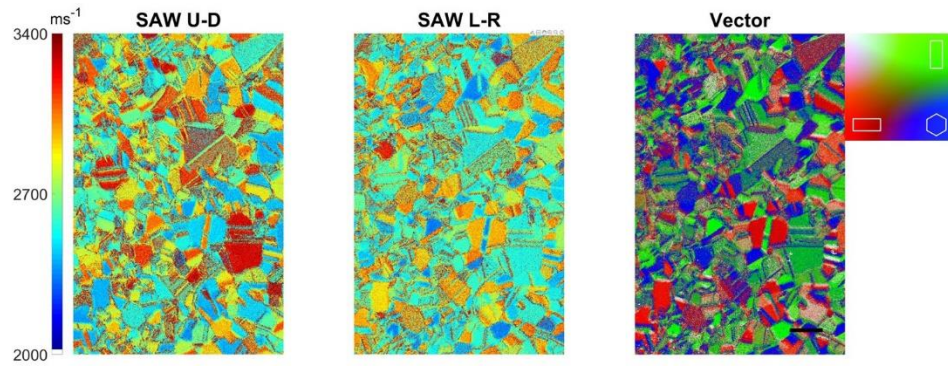


Figure 36 Orthogonal velocity maps (with the SAW travelling up-down and left-right) next to the vector map of a nickel sample, the RGB colours provide some idea of the crystal orientation. Where green represents the hexagonal crystal orientated vertically, red is the crystal orientated horizontally and blue is the top of the crystal. The black scale bar represents 1 mm.

Within the context of an AM in-process inspection, however, there were several challenges to overcome before obtaining the crystal orientation. These are discussed further in chapter 5. The majority of the work in this chapter is focused on exploring and improving the quality of information extracted from measuring the SAW velocity in one propagation direction. This is initially carried out on the smooth, prepared surface of AM samples followed by the as-deposited surface of AM samples.

### 3.3.1. Literature Review of SRAS

This section reviews the literature published since the early iterations of SRAS and its use for the inspection of samples manufactured using AM processes.

Sharples et al. presented O-SAM in 2003 as an LU method of detecting material defects by correcting for the distortion in the ultrasonic waves propagating through grains [171]. The O-SAM system was utilised by Clark et al. to carry out inspections on blown powder and wire-based AM components [172]. These early experiments showed the capability of the O-SAM system to detect the change in amplitude of acoustic waves. This corresponded to a lack of consolidation and voids in the Ti64 wire-based AM sample and the grain boundaries in the MERL 76 blown powder sample. Sharples et al. presented SRAS as a method of directly and quantitatively imaging the SAW velocity on materials such as titanium alloys in 2006 [161]. This SRAS system was used to measure the changes in SAW velocity across MERL 76 blown powder and Ti 64 wire-based AM samples in 2011 [172].

Smith et al. used a re-engineered SRAS instrument described in section 3.4.2.1 to inspect a range of prepared AM samples manufactured using SLM [151]. The authors demonstrated a relationship between the mean SAW velocity and laser power used to build eleven cubes using Ti64 powder. As the laser build power increased, an increase in the mean SAW velocity

was measured. This study also gave a useful insight into how an in-process SRAS inspection could provide closed-loop feedback to improve the SLM process as a whole. When specifically considering pores, the authors showed that alongside detecting, counting and sizing the surface pores, they were also able to detect subsurface pores. This was in the form of a drastic change in the SAW velocity by  $\sim 200$  m/s, where in the thin plate-like region above the pores, the SAW transformed into a Lamb wave. The presence of these subsurface pores were confirmed using an XCT slice of the same region.

Hirsch et al. manufactured four 10 mm cubes using a nickel superalloy power (CM247LC) on a Realizer SLM machine [152]. The aim here was to understand the capability of SRAS to detect changes to the scan strategy used. The cubes were made up of four small 5 mm square islands similar to those discussed by Carter et al [73]. In this work, the authors used one sample as a control ( $0^\circ$ ) and rotated the islands in the other three samples relative to the previous layer. The rotation angles were set to  $15^\circ$ ,  $30^\circ$  and  $45^\circ$  across the three samples. Using SRAS data and verified by optical microscopy the authors were able to identify trends between the crack and pore distributions on the surface of these samples. Furthermore, the authors were able to identify the island boundaries of the samples in the form of a distinct drop in the group SAW velocity. This was consistent with the changes along island boundaries observed and verified using EBSD by Carter et al. [73].

Dryburgh et al. manufactured a triangular sample similarly to Hirsch et al. using islands to further investigate the effect of changing scan lengths and part geometry on crystal orientation and SAW velocity [173]. Using SRAS velocity data the authors observed that in the region close to the tip of the triangle, as the scan line shortened and the build laser spent more time in a small region, the SAW velocity on average was measured to be higher. When inspected using EBSD the tips of the triangle were seen to have an [001] orientation. The authors carried this analysis further by calculating the velocity gradient across the sample. As discussed by Mark et al. this gradient related to the stiffness of the material and was again verified using EBSD [174].

As an initial step towards closed-loop feedback for AM, Hirsch et al. utilised SRAS optical data to inform several repair strategies on a sample manufactured using SLM [24]. Although the resolution of the SRAS system used and discussed in section 3.4.2.1 was quoted as  $100\text{ }\mu\text{m}$  for the acoustic data, its optical resolution was much higher than this at  $\sim 10\text{ }\mu\text{m}$ . Following some image processing, the centroid and aspect ratio dimensions for each defect was used to target the rework strategies used. A remelt area of 150% of the identified defect size was

used to ensure sufficient material was remelted to reduce the final defect size. The authors demonstrated the feasibility of the methodology developed by achieving a 50% reduction in defect depth and a change in the defect morphology. This allowed the next layer of powder to more easily backfill the existing surface pores which could help improve the overall part density and reduce porosity.

The literature reviewed until this point utilised a smooth surface SRAS system. The inspection capability of this system was limited to  $R_a < 100$  nm due to the detector used (discussed further in section 3.4.2.1). The next challenge for SRAS as a technology was the development of a system capable of measuring as-deposited AM surfaces.

Patel et al. addressed this by using a prototype SRAS system equipped with a detector specifically designed to be used on rough surfaces. This system was capable of carrying out measurements on an as-deposited SLM sample with a surface roughness of  $S_a \sim 6 \mu\text{m}$  [157]. The SRAS measurements on these rough surfaces were made possible by the use of a SKED [147], [175]. This was a 32x32 pixel array of photodetectors that was able to adapt on the fly to the speckle pattern created due to the surface roughness of the sample being inspected (see section 2.9.2.2). The AM sample inspected was manufactured using a Renishaw AM250 and Ti64 powder. Its surface was measured using an Alicona infinite focus microscope to have a surface roughness of  $6.11 \mu\text{m} S_a$ . The as-deposited surface of these samples was inspected at an acoustic wavelength of  $200 \mu\text{m}$ . This work was progressed further by integrating the prototype system discussed above into an SLM build chamber. It was also worth noting that the generation and detection laser beams were translated across the surface of the sample using galvanometer mirrors. This was another leap in technology compared to previous SRAS configurations where the laser beams were kept static and the sample was translated using linear stages.

The work carried out as part of this thesis builds upon the literature reviewed to progress SRAS towards becoming a useful and robust candidate for the in-process inspection of AM. Due to its versatility, there are several SRAS instruments in existence with various configurations. The following section focuses on these instruments.

### 3.4. Instrumentation

This section initially breaks down a typical SRAS system into its base elements and discusses the considerations within the context of the aim of the inspection taking place. It then discusses some further points such as signal processing and SNR that need to be considered

when designing a system. The second half of this section discusses the details of the SRAS systems used within this engineering doctorate.

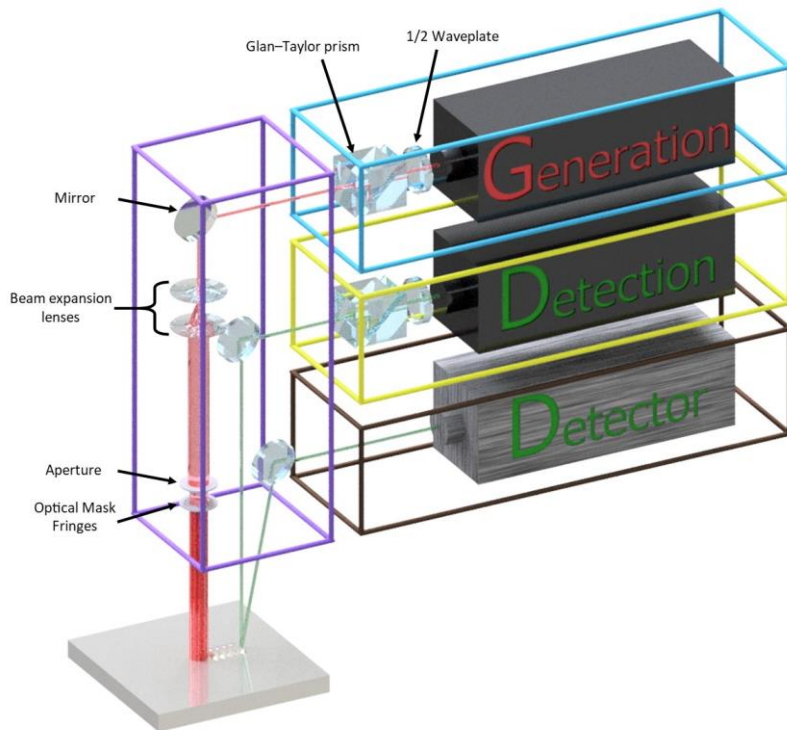


Figure 37 Schematic block diagram of a SRAS system where the generation laser block was outlined in blue, the detection laser block was outlined in yellow, the system optics block was outlined in purple and finally, the detector block was outlined in brown.

### 3.4.1. Base Elements

As outlined in the previous section the basic concept of SRAS is relatively straightforward. The fact that it is not a time-of-flight technique makes it a robust NDE technique for the characterisation of materials. This also makes it easy to adapt towards the main aim of the inspection taking place, ranging from speed, portability, rough surface or an in-process inspection. For this reason, several SRAS systems were used throughout this engineering doctorate. Between these systems, items such as generation lasers, detections lasers and LU detectors varied but the overall block diagram introduced in Figure 37 stayed consistent.

#### 3.4.1.1. Generation Laser

The generation laser block typically contains a pulsed IR (1064 nm) laser along with any required power control and collimation optics. The choice of a pulsed laser here was due to its ability to induce a rapid change in temperature which generates stress and radiates elastic waves into the material [139]. The short pulse lengths also provide a higher energy density compared to CW lasers. This increased energy is required for the generation of ultrasonic waves on the surface of the sample being inspected. The pulsed lasers used were typically a

Q-switched laser that built up the energy within a cavity over a short time and, when released produced a pulse with a much higher peak power value [137].

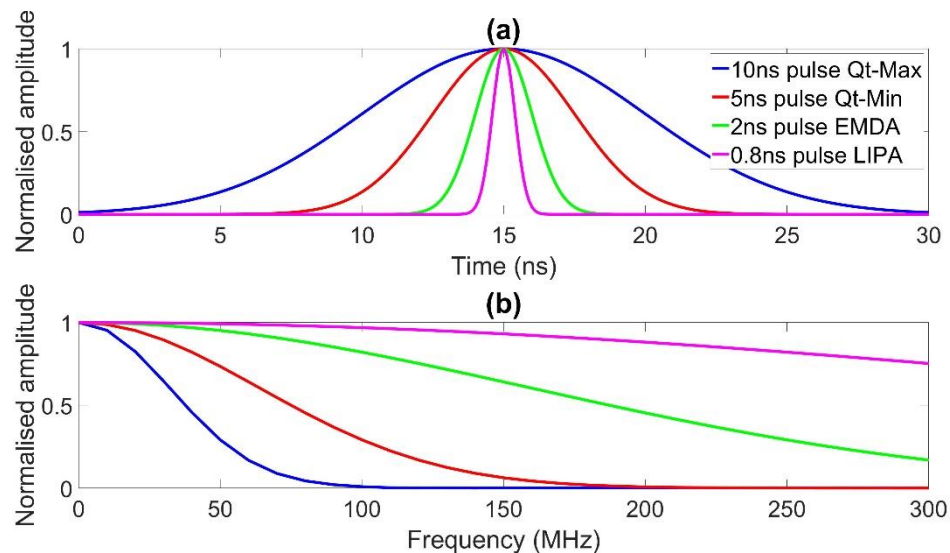


Figure 38 Simulated image showing the effect of laser pulse width (a) and ultrasonic frequency content (b) for several lasers used in the experimental systems within this engineering doctorate.

The theory and reasoning behind the selection of generation lasers are detailed further in section 2.9.1. The pulse width of the laser was an important factor. Figure 38 illustrates the relationship between the pulse width and ultrasonic frequency content of the generation lasers used as part of the experimental systems used as part of this engineering doctorate. Lasers with shorter pulse widths provide more ultrasonic frequency content compared to lasers with longer pulse widths. Although a laser with the shortest pulse width would suit most situations, other considerations such as laser power and repetition caused the pulse width of each laser to vary based on its specific application. As each SRAS system presented in section 3.4.2 was optimised for various inspection cases such as speed or surface texture, the lasers used varied.

### 3.4.1.2. Detection Laser

The detection laser block typically consisted of a green (532 nm) CW laser along with any power control required. Unlike the generation laser, the aim of the detection laser was to be reflected off the surface of the sample. For this reason, a 532 nm laser was chosen as it was reflected well by materials that were silver in colour. As an example, at 532 nm, gold had a reflectivity of 0.70 compared to aluminium which had a reflectivity of 0.91.

Similarly, the detection laser required relatively less power on optically smooth surfaces when compared to the generation laser as the aim here was to project a reflection of the surface perturbation of the sample onto the face of the detector. If required some optics

were used to shrink the beam diameter down. This was to ensure the detection beam diameter was less than half of the SAW acoustic wavelength in line with the Nyquist sampling criterion. LU detection was discussed to a greater detail in section 2.9.1.

#### 3.4.1.3. Detector

The detector block typically only contained the photodetector and any optics required. It is worth noting that in the case where commercial detectors were used, the detection laser and the detector were physically in one sealed box, and so were considered as one block. The detector used in the SRAS system was a critical component and defined the performance envelope of the system. The detection beam travelled through the imaging optics and was focused onto the surface of the photodetector. The aim here was to reflect the perturbation of the sample surface onto the photodetector so that it could then be measured. LU detection was discussed further in section 2.9.1. Based on the specific application, be it a smooth surface or a rough surface, the appropriate detection system was chosen.

#### 3.4.1.4. General Optics

The general optics of any SRAS system consisted of all the optics required to facilitate the SRAS inspection. The generation laser beam path initially consisted of some beam expansion optics. Here the relatively narrow beam directly from the laser head was expanded to illuminate the relative larger optical mask (~5 mm in diameter). The beam expander consisted of two lenses as illustrated in Figure 37. This also distributed the energy from the laser across a larger area reducing the energy density incident on the sample. The optical mask consisted of several dark fringes that were used to block some of the IR light to create alternating dark and bright fringes on the sample surface. The spacing of these fringes varied between ~1-10 µm. Based on the imaging lenses along the generation path, this was imaged onto the sample to provide a fringe spacing between ~10-100 µm.

The Gaussian beam profile generated by lasers if uncontrolled provided soft (un-focused) edges around the IR patch. For this reason, an aperture was used to provide a sharp edge to the IR patch which controlled the spatial resolution of the system (Figure 39). The apertures used varied between ~0.1-1 mm to control the generation patch size in combination with the system magnification.

The green laser beam path in some cases required beam reduction optics, which worked similarly to the beam expansion explained above but to reduce the beamwidth. Mirrors were then used to position and steer the detection laser spot relative to the generation patch so that it was able to pick up the surface perturbation caused by the SAW.

In most SRAS systems, the generation and detection beam paths were combined. A dichroic mirror was used in this case to combine the IR and green beams. Based on the chosen dichroic mirror it either reflected the IR and transmitted green – short pass as they transmitted the shorter wavelengths – or transmitted IR and reflected green – long pass as they transmitted the longer wavelengths. Both the IR generation patch and green detection lasers typically used the same final imaging optics, where the generation patch and detection spot were imaged onto the sample surface as illustrated in Figure 39. In some cases, an objective lens was used to achieve the desired working distance and or magnification. The reflected green detection beam returned through the imaging optics and was reflected onto the photodetector.

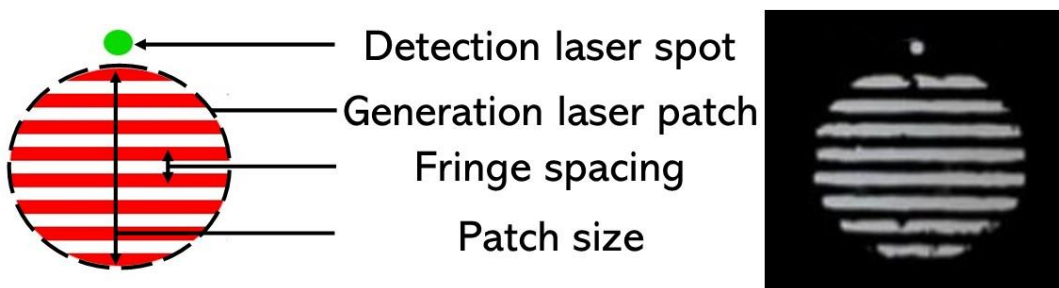


Figure 39 Annotated diagram of the generation laser patch and detection laser spot (left) and an optical image off the surface of a prepared sample (right) obtained from the smooth surface SRAS system. Here the bright fringes within the generation patch were  $\sim 24 \mu\text{m}$  apart and the entire generation patch was  $\sim 200 \mu\text{m}$  in diameter. The detection laser spot was  $\sim 10 \mu\text{m}$  in diameter and was positioned close to the generation patch.

The patch size illustrated in Figure 39 defined the spatial resolution of the acoustic data obtained from the SRAS system. This was due to the frequency of the SAW generated being directly influenced by the material properties of the region beneath the generation patch where the energy was absorbed. In the smooth surface SRAS system, the patch size was  $\sim 200 \mu\text{m}$  in diameter. This provided an effective spatial resolution – for the acoustic data – of  $\sim 100 \mu\text{m}$  as this patch was translated across the sample surface [176].

The acoustic wavelength  $\lambda$  of the SAW was governed by the fringe spacing illustrated in Figure 39. This was defined by the optical mask used further up the generation laser path and any magnifying optics used downstream of this to image the mask. For this reason, to obtain a true measurement of the acoustic wavelength, a calibration was required. Although the magnification of the system was known, there was some uncertainty in this due to the positioning of the various optical elements. The calibration process discussed in section 3.6.1.1 accounted for this by calculating the generation wavelength based on a known SAW velocity. In the smooth surface SRAS system, the acoustic wavelength was typically  $\sim 24 \mu\text{m}$ .

As illustrated in Figure 40, the number of fringes affected the width and height of the frequency spectrum obtained using an FFT and thereby the velocity resolution. The greater number of fringes provided a higher frequency peak above any noise in the system. This, however, increased the generation patch diameter and thereby reduced the spatial resolution. This meant the number of fringes used, was a compromise between the spatial resolution and the velocity resolution. This was discussed further and shown experimentally in the literature [168]. The smooth surface SRAS system typically worked using 8 fringes (seen Figure 39).

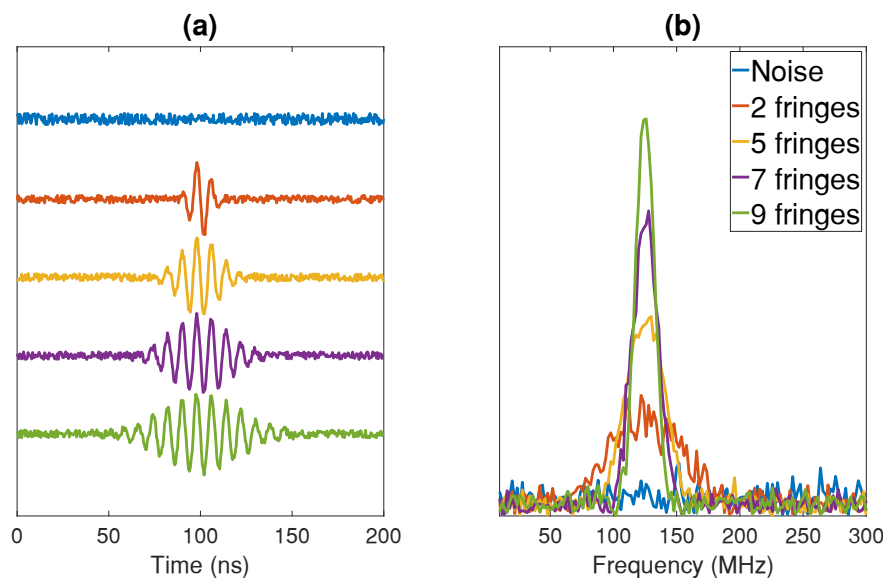


Figure 40 Simulated image illustrating the effect the number of fringes used had on the SAW packet (a) next to the width and peak of the frequency spectrum obtained using an FFT(b).

The detection spot was sized considering the Nyquist sampling criterion where its width is required to be less than half the acoustic wavelength being measured. Furthermore the smaller the detection spot was the more sensitive it was to the gradient of the SAW. A larger spot would measure an average of this change across its diameter. This was  $\sim 10 \mu\text{m}$  in diameter for the smooth surface SRAS system and  $\sim 30 \mu\text{m}$  for the rough surface SRAS system.

The distance between the generation patch and detection spot, in theory, had no impact on the measurement taking place due to SRAS not being a time-of-flight measurement. There was however some attenuation of the SAW, especially on rough surfaces. For this reason, the detection spot was positioned as close as possible to the generation patch. Due to the detection spot being much smaller than the generation patch, the spatial resolution of the optical data was relatively higher than that of the acoustic data.

### 3.4.1.5. Signal Processing

Typically in LU, signals tend to be low in amplitude and contain a lot of noise – compared to conventional ultrasonics. For this reason, some signal conditioning is required. The smooth surface SRAS system discussed in section 3.4.2.1 as a baseline contained the following elements for signal conditioning downstream of the detector:

- 0.1-500 MHz low noise powered amplifier
- 6 dB attenuator
- 0.1-1000 MHz low noise powered amplifier
- 90-2000 MHz high pass filter

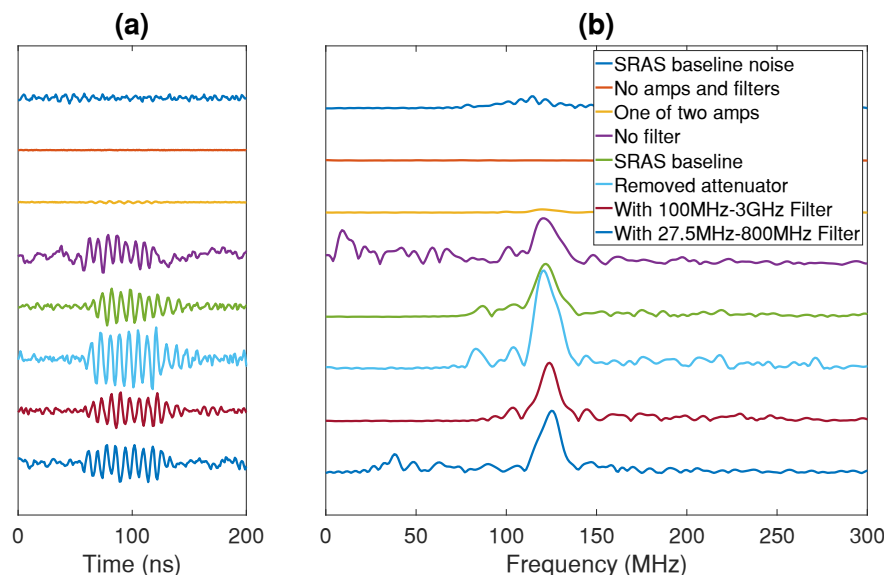


Figure 41 Collection of digitised SAW waveforms (a) and frequency response (b) of a ~125 MHz signal illustrating the effect various elements in the signal processing chain had. Each of the individual waveforms was staggered vertically to aid in the comparison being made.

With these elements in place, a typical SAW packet had a peak-to-peak signal amplitude of over 600 mV illustrated using the green line in Figure 41 and Figure 46 (a), compared to the baseline noise which was less than 100 mV illustrated using the blue line. The two amps used here amplified the relatively small (10-20 mV) signal. When the amps were completely removed from the signal chain, the peak amplitude was in the region of 10 mV illustrated using the orange line, and with one amp in place, this increased to 20 mV illustrated using the yellow line. This showed the need to use two amps. The purple line illustrated the effect removing the inline 90-2000 MHz high pass filter had on the signal, where some low-frequency peaks appeared on the frequency response. The light blue line illustrated the effect removing the attenuator had where the effective amplitude increased. It was difficult to visualise here, but the reason for the attenuator was to not saturate the 2<sup>nd</sup> amplifier, and

it was in place as part of the baseline signal chain. Finally, the last two maroon and dark blue lines illustrated the effect two different inline filters had on the signal and frequency response. These could be used when carrying out experiments that required focussing on different frequency bands.

### Averaging

On top of the signal processing discussed above, another method of improving the SNR of a given signal was averaging. Using the rough surface SRAS system discussed in section 3.4.2.2 the data presented in Figure 42 illustrates the effect the number of averages taken had on the data collected. The system in this case was inspecting the as-deposited surface of an AM sample. The waveforms illustrated in Figure 42 (a) were using 16000-5 averages. The frequency spectrum in Figure 42 (b) illustrates how between 16000-1000 averages, the most dominant frequency was ~35 MHz. The greater number of averages although improving the signal amplitude, came at the cost of time. For these reasons, the number of averages used needs to be a compromise between the SNR and the total time taken. This point was discussed further in section 5.4.

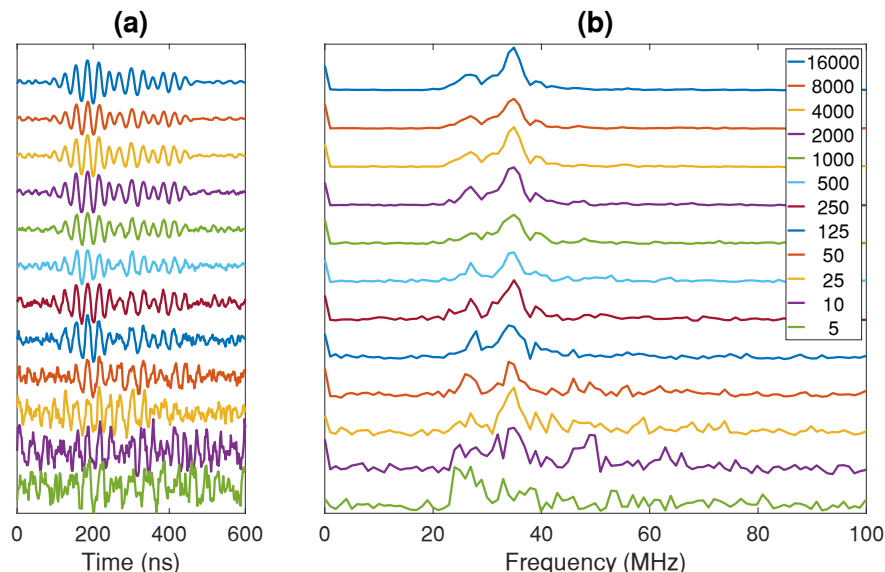


Figure 42 Collection of digitised SAW waveforms (a) obtained from the as-deposited surface of an AM sample (rough) using the rough surface SRAS system and frequency response (b) for a 35 MHz signal.

The number of averages used started from 16000 and was halved every time down to 5. This illustrates how the noise in the waveform increased as the number of averages decreased.

### Masking/ Thresholding

Another method of filtering SRAS data was using either the optical or acoustic amplitude as a mask for the velocity data. This was carried out by creating a binary data set of the optical or acoustic amplitude when it was above a predetermined threshold. The velocity data was then multiplied by this binary dataset and any data points below the threshold were

discounted. If the optical amplitude was below the threshold, not enough light returned to the detector. If the acoustic amplitude was below the threshold, the peak of the FFT was indistinguishable from the noise (Figure 42 (b), green and purple lines for 5 and 10 averages).

### Digitisation

When digitising the signals, the sampling frequency was typically set to over double that of the maximum frequency being measured. This was again similar to the detection spot, in line with the Nyquist sampling criterion. This allowed enough points to be captured for the signal to be accurately reconstructed digitally.

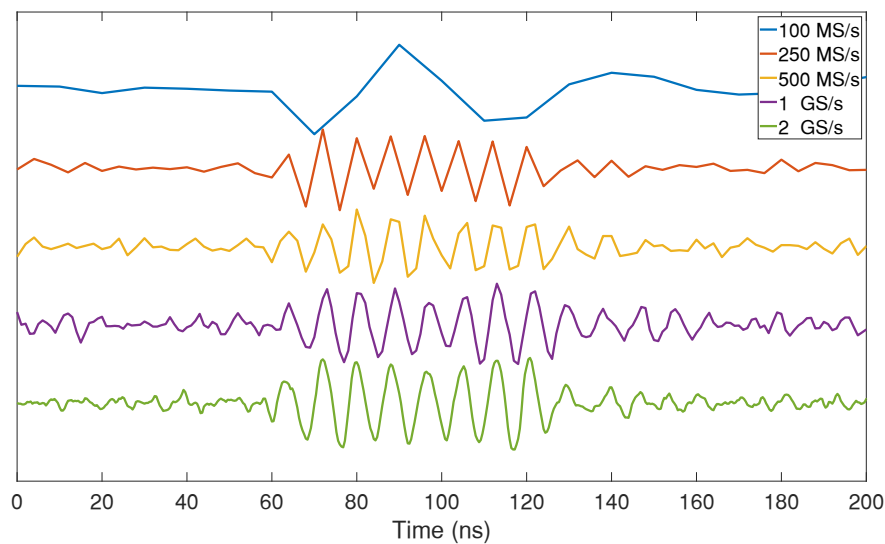


Figure 43 Collection of digitised SAW waveforms of a ~125 MHz signal using various sampling frequencies between 100 MS/s and 2 GS/s. This illustrated the effect an inadequate (below double the signal frequency) had on the signal being digitised, followed by the diminishing return of higher sampling frequency.

The effect of changing the sampling frequencies on a SAW packet of ~125 MHz is illustrated using Figure 43. This shows that at 100 MS/s there were not enough points to successfully digitise the signal, whereas at 250 MS/s – which was exactly double the frequency of the signal – there were just enough points to capture the peaks of the signal. There was some benefit to increasing the sampling frequency further, such as obtaining a smoother signal, accounting for higher frequencies and changes in phase. There was, however, a diminishing return from increasing the sampling frequency. More data per signal and an increase in overall file size, for not a lot of increase in signal quality. For this reason, a compromise was required between the quality of a signal and storage space.

### 3.4.2. SRAS Systems

This section focuses on the two SRAS systems used within this engineering doctorate. Each system was designed around a specific use case, and so had various engineering compromises.

#### 3.4.2.1. Smooth Surface – EMDA

This system was designed and built for the rapid imaging of material microstructure and crystal orientation on optically smooth (mechanically polished) surfaces [168]. The build of the system was partly funded by the east midlands development agency (EMDA) and so was named and referred to as the EMDA system.

The generation block in this system used a 1064 nm Q-switched Nd:YAG laser from AOT lasers (AOT-YAG-10Q), which worked at a repetition rate of 2 kHz. The 1-2 ns pulse width provided good frequency content up to 150 MHz as illustrated in Figure 38. The power out of the laser was 1150 mW and pulse energy of 575 µJ. Once going through all of the optics within the system, the IR laser power incident on the sample was ~60 mW. The damage threshold for aluminium is ~150 kW/mm<sup>2</sup> which meant that this was still within the non-destructive regime [177].

The detection laser in this system was physically separated from the rest of the system. It was brought into the system via an optical fibre. In cases where space and size were a consideration, this type of fibre-coupled laser can be used to reduce the overall size of the instrument. The EMDA system used a CW Quantum Torus 532 nm laser with an output power of 420 mW. After going through the fibre and arriving at the system, this was reduced to ~220 mW, at the sample, this was further reduced to ~110 mW and finally, when reflected back to the detector, it was down to ~60 mW.

The detector used in this system was KED as discussed in section 2.9.2.1. This was specifically chosen due to its speed and relatively high upper-frequency limit of ~ 200 MHz. In this case, the KED used was a split photodiode, which added to the simplicity of this system and allowed it to achieve real-time scanning. The simplicity of the KED/split photodiode used however also limited this system to work on smooth mechanically polished surfaces ( $R_a \sim 100$  nm). The detector was mounted in a rotation stage which allowed it to be used for measuring SAW velocities in all propagation directions. This was required for obtaining crystal orientation from SRAS as described in section 3.3.

The generation laser train used a combination of a tube lens with a focal length of 100 mm and a Mitutoyo Plan APOCHROMAT  $\times 10$  objective lens with a working distance of 30.5 mm. This imaged the aperture and mask onto the sample with a 5:1 reduction. The use of a 1 mm aperture gave a generation patch a diameter of 200  $\mu\text{m}$  as shown in Figure 39. The effective generation wavelength on the sample was 24  $\mu\text{m}$ . Another unique element to this system was the fact that the optical mask was mounted on a rotation stage. This allowed the mask to be rotated and generate SAW waves in all directions. This was required for obtaining crystal orientation from SRAS as described in section 3.3.

The detection laser train used a polarising beam splitter along with a quarter waveplate. This separated the outgoing beam going to the sample and the returning beam from the sample, which was focused on the detector. A steering mirror was used to steer the detection laser spot across the surface of the sample independently of the generation laser patch. A long pass dichroic mirror was placed between the tube lens and objective to bring the detection beam in line with the generation beam. This allowed the final section of both the beam paths to be delivered using the same objective lens onto the sample.

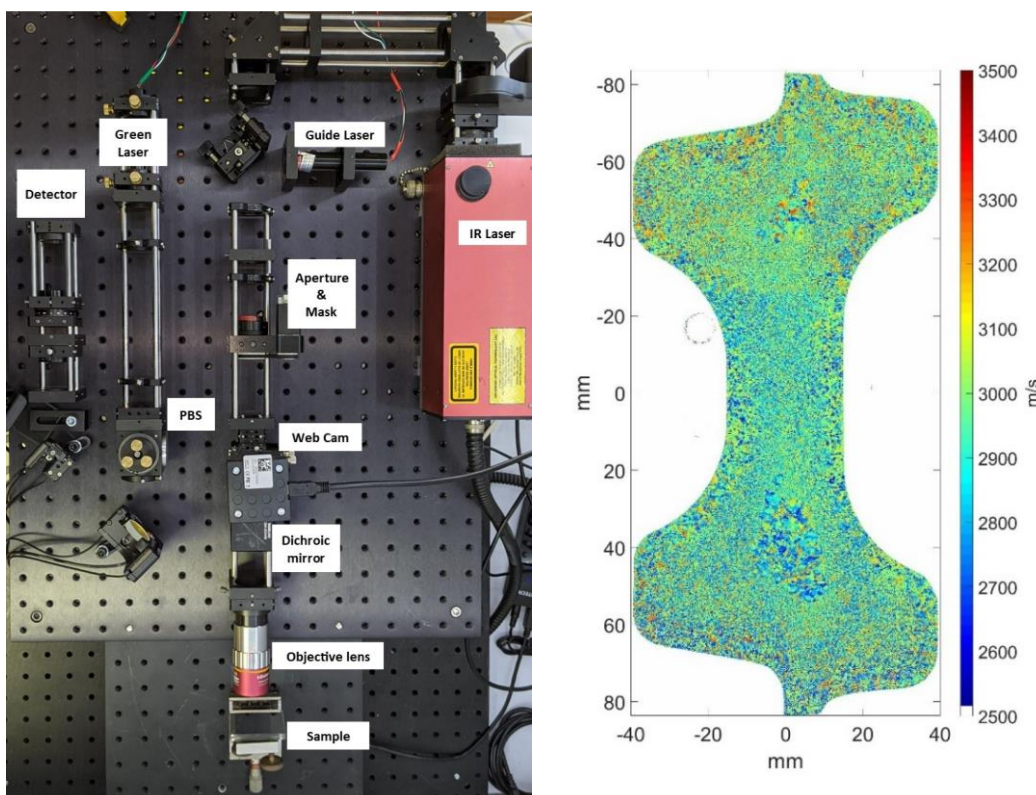


Figure 44 Picture of the EMDA system which was designed and built for the rapid imaging of material microstructure and crystal orientation on smooth, polished surfaces (left). SRAS velocity map of large titanium sample ~16 cm x 8 cm with changing grain sizes across the sample, where the colours represent the change in SAW velocity (right).

Unlike a majority of other experimental LU systems, the EMDA system in Figure 44 was first designed and optimised for speed. It was also built to demonstrate the relatively small footprint required for a functional SRAS system, illustrated in Figure 44 as the region outlined using the yellow tape. It is also worth noting that almost half of this region was taken up by the generation laser (red box to the right). This meant that if the generation laser was fibre coupled similar to the detection laser this footprint could effectively be halved.

One of the mechanisms used to optimise this system for speed was that the entire system was synchronized and driven by a signal generator. Here a 2 kHz pulse was used to trigger the generation laser. The oscilloscope used this same trigger to capture a segment of data. These individual segments were captured as the stage moved (the sample was in motion) and synchronised with the 2 kHz laser repetition rate of the laser. Here the speed of the stage was defined by the product of the step size ( $\mu\text{m}$ ) and the laser repetition rate (points per second). A group of these segments (limited to 5000 by the memory on the scope used) were captured as the sample moved in one direction, and transferred across to the PC as the sample moved back, minimising downtime and making the system as fast and efficient as possible.

#### 3.4.2.2. Rough surface – SRAS-Qt

This system was specifically designed around the need to inspect industry-relevant components with optically rough surfaces as seen in Figure 45. With this consideration, all of the optics of the system were built up around the central column which contained the detection system head.



Figure 45 Composite image made up of a photograph of an as-deposited SLM sample and rough surface SRAS velocity data obtained using the SRAS-Qt system. This SLM sample was 60 x 24 mm.

The Sound & Bright Quartet (formally known as Bossa Nova Technologies) is a commercially available industrial LU detection system – referred to as the Quartet within the context of this thesis. This was the reason for the “Qt” designation in the naming of this SRAS system.

### 3 | Spatially Resolved Acoustic Spectroscopy

With reference to Figure 37, the Quartet effectively contained both the detection laser and the detector inside one sealed enclosure. The detection laser within the Quartet was a CW Cobolt Samba 532 nm laser with a maximum power of 1.5 W. This was much greater than the 200 mW of the EMDA system but was required for the inspection of optically rough surfaces. The detection system within the Quartet used the principle of Quadrature Demodulation which was explained in section 2.9.2.1. The detection laser was delivered from the sealed enclosure to the SRAS central optics column via the optical fibre which terminated in a 2-inch adjustable collimation adapter (SM2F) from Thorlabs. This formed the start of the central optics column on to which the IR generation laser was coupled using a short pass dichroic mirror. The reflected green light was focused back along the central optics column into the optical fibre.

The generation laser used in this system was a TECH-1053 Advanced 1053 nm pulsed laser with a maximum power of 3.2 W. This resulted in 800  $\mu\text{J}$  on the surface of the sample. The laser had a 5 ns pulse width in its specification but in reality, was in the region of 10 ns as illustrated in Figure 38. It operated at a 4 kHz repetition rate which was double that of the EMDA system and provided an improvement in scan speed. This laser was also fibre coupled into the system, which minimised the size of the SRAS instrument. In this case, the “SRAS system” purely consisted of the central optics block with respect to Figure 37.

Unlike the EMDA system which rotated the individual elements (the mask and KED) to measure the SAW velocity in all directions, this system rotated the entire central optics block around the central axis (defined by the Quartet head). This meant that if a specific point of interest was chosen, a full 180° measurement with fine radial resolution could be taken to obtain its crystal orientation, without mechanically translating the sample.

Table 6 Comparison between the smooth surface EMDA and rough surface Qt system.

	<b>EMDA</b>	<b>SRAS-Qt</b>
<b>Generation patch size</b>	200 µm	1000 µm
<b>Acoustic spatial resolution</b>	100 µm	500 µm
<b>Generation wavelengths</b>	12-48 µm	80 µm
<b>Detection spot size</b>	10 µm	30 µm
<b>Optical spatial resolution</b>	10 µm	30 µm
<b>Laser ultrasonic detector</b>	Knife Edge Detector	Quartet
<b>Acoustic signal bandwidth</b>	up to 200 MHz	up to 60 MHz*
<b>Generation Laser power</b>	1150 mW	3.5W
<b>Detection laser power</b>	420 mW	1.5 W
<b>Maximum surface roughness</b>	0.1 µm Ra	3.2 µm Ra
<b>Optimised for</b>	Optically smooth surfaces High spatial resolution Large sample orientation measurement	Optically rough surfaces High radial resolution Orientation measurement of specific areas
*New model goes up to 100 MHz		

The rough surface capability, however, came with its compromises. The generation wavelength of this system was 80 µm and used 12 fringes. As discussed in section 3.3.1.1, illustrated using Figure 40 this provided a higher and sharper frequency peak but reduced the spatial resolution because the generation patch was ~1 mm (which was 5 times greater than that of the EMDA system). Similarly, as discussed in section 3.3.1.5, illustrated using Figure 42, when inspecting rough surfaces, some averaging was required.

Table 6 lists the various specifications and parameters of both the SRAS systems discussed above. In this case, it is clear that although both the systems work on the basic principles outlined in section 3.2 they are specifically designed for two very different purposes and so are optimised differently.

### 3.5. Fabrication and Preparation

The following section initially discusses AM build platforms/processes used to manufacture the samples within this engineering doctorate, followed by the sample preparation procedures. It goes on to discuss the design and the reasoning behind the various samples manufactured. This is followed by the methodology behind the various experiments designed to demonstrate the capability of SRAS as a candidate for the in-process inspection of AM.

A majority of the samples were manufactured using a Realizer SLM50 system equipped with a 100 W CW laser at a wavelength of 1064 nm. This machine consisted of a circular build plate that had a usable build area of ~60 mm in diameter and was screwed into the machine

[178]. Throughout manufacture, the build chamber was purged and continuously flushed with argon to ensure a working atmosphere of less than 500 ppm of O<sub>2</sub>. The build plate was heated and maintained at 200 °C, a commonly used technique to reduce the build-up of thermal stresses during manufacture. Outside of an academic research environment, a system like this would primarily be used for the manufacture of small but complex metallic components such as dental implants or bespoke pieces of jewellery.

As part of the as-deposited surface SRAS experiments carried out, the WAAM samples used were manufactured by the Welding Engineering and Laser Processing Centre at Cranfield University. These samples were manufactured using a Ti–6Al–4V welding wire feedstock which was melted using a pulsed gas tungsten arc welding torch, with argon shielding [34]. After each layer was cooled a 100mm diameter roller was passed over the top surface of the samples where a 50 and 100 kN load was applied to manufacture the two deformed samples. This process is discussed to a greater detail in the literature by Martina et al. [179].

### 3.5.1. Sample Preparation

The as-deposited surface of typical AM samples had a surface roughness of ~6 µm S<sub>a</sub> [157]. For this reason, part of the sample manufacturing process was getting them prepared for the smooth surface EMDA systems. In this case, the surface finish requirement of the smooth surface (EMDA) system was R<sub>a</sub> ~100 nm. This meant that some mechanical polishing was required. A standardised polishing procedure was developed for processing all AM samples inspected using SRAS and further prepared for EBSD which had even higher requirements specifically in sample cleanliness.

All samples were mounted in a 30 mm diameter thermosetting resin. Primarily driven by the requirements of the SEM for EBSD, the resin used was bakelite with carbon filler which made it conductive. The mounted samples were ground down starting at grit 200 down to 1200. The grinding paper was attached to a spinning disk and was continuously lubricated with water. Between every grinding paper, the sample was rinsed with water and rotated by 90° to ensure that the scratches from the previous grit paper had disappeared. After these stages, cleanliness started to become more of an important factor as it could introduce contaminants that cause more scratches on the samples. During the following stages, disposable gloves were used and changed after every stage, the samples were rinsed with water and then isopropyl alcohol to avoid any cross-contamination. The final stages of mechanical polishing for SRAS samples were on a 6 µm and 1 µm diamond paste lapping wheel. Here the sample was rotated in the opposite direction to the spinning wheel and

lubricated with white spirits, to avoid washing away the diamond paste. This for a majority of samples provided a surface with  $R_a \sim 100$  nm, which was acceptable for SRAS. EBSD however required two further levels of mechanical polishing using 0.1 and 0.06  $\mu\text{m}$  colloidal silica followed by some intense cleaning. These processes are explained to a greater detail in the web pages referenced [180], [181].

## 3.6. SRAS Experiments

This section initially outlines the experimental design, presents the results obtained and discusses the various SRAS experiments carried out as part of this project. It first describes the calibration process used by all SRAS systems followed by some data from large-grained Titanium samples. It then presents data from a prepared AM sample. This is followed by several mathematical methods used to extract more information regarding the defects and the microstructure of these samples. This is progressed further by using samples designed to encourage variations in the component microstructure.

As a transition to carrying out experiments on the as-deposited surface of AM samples, a surface roughness comparator is used. The first set of rough surface experiments are carried out on both the EMDA and SRAS-Qt systems. This is followed by data from the as-deposited surface of SLM samples. The final set of SRAS data presented is from the sidewall of a WAAM sample. This is used to illustrate the true rough surface potential of SRAS alongside the current generation capability to detect large changes to AM component microstructure.

### 3.6.1. Calibration

#### 3.6.1.1. Experiment Design

Firstly it was important to measure the generation wavelength of each of the systems being used. This was done using a calibration sample, which was a piece of dark glass coated with a thin layer of aluminium, which provided an isotropic piece of material. The SAW velocity of this sample was measured to be 2933 m/s using a different experiment and was considered a known and constant value within the confines of these experiments. A SAW was generated on the surface of this sample using the SRAS system being calibrated. The wavepacket travelling across the surface was measured. A FFT was used to extract the frequency spectrum of this wave packet. The frequency with the maximum amplitude  $f$  and the known velocity  $v$  of the calibration sample (2933 m/s) was used in Equation 12 to calculate the wavelength of the system  $\lambda$ . This wavelength was used in all the following experiments to calculate the SAW velocity. Following this, a sample with a large grain size was scanned. This

was used to illustrate the capability of the smooth surface SRAS system to image the grains on the surface of a sample.

### 3.6.1.2. Results

The results presented in Figure 46 (a) illustrate a SAW packet obtained off the surface of the calibration sample. Using a FFT, the frequency response in (b) was obtained. The peak frequency was used in this case to calculate the system's wavelength. Once calibrated, this process was used (with the known wavelength) to calculate the SAW velocity for each point of a sample being inspected.

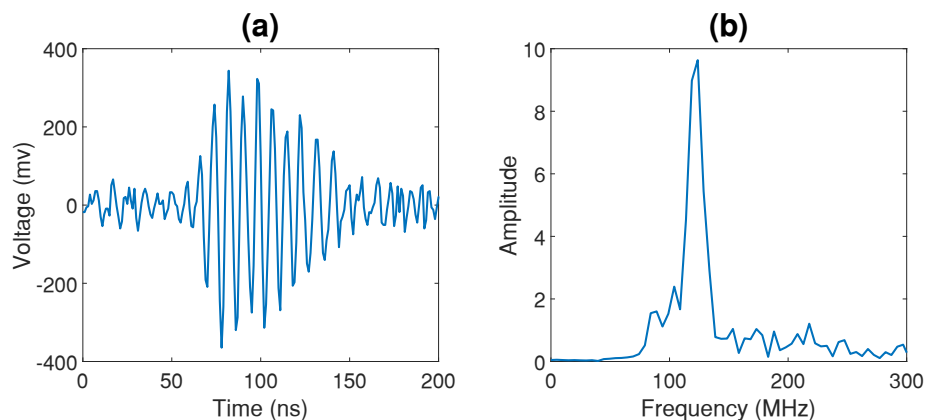


Figure 46 SRAS system calibration data showing (a) the raw SAW wavepacket and (b) the frequency spectrum used to pick up the frequency with the highest amplitude.

Table 7 SRAS Calibration scan results.

Known SAW velocity	Measured frequency peak	Calculated wavelength
$v=2933 \text{ m/s}$	$f=123.8 \text{ MHz}$	$\lambda=23.7 \mu\text{m}$

The following datasets are used to demonstrate the capability of SRAS on a prepared sample with large grains. The table below is used alongside all SRAS data sets presented to specify parameters around each experiment that took place.

Table 8 System specifications for large grain titanium sample

<b>Detector</b>	KED	<b>Spot size</b>	<10 $\mu\text{m}$
<b>Wavelength</b>	23.2 $\mu\text{m}$	<b>Patch size</b>	200 $\mu\text{m}$
<b>Step size (x)</b>	25 $\mu\text{m}$	<b>Step size (y)</b>	25 $\mu\text{m}$
<b>Sample size (x)</b>	10 mm	<b>Sample size (y)</b>	10 mm
<b>Segments (x)</b>	400	<b>Segments (y)</b>	400

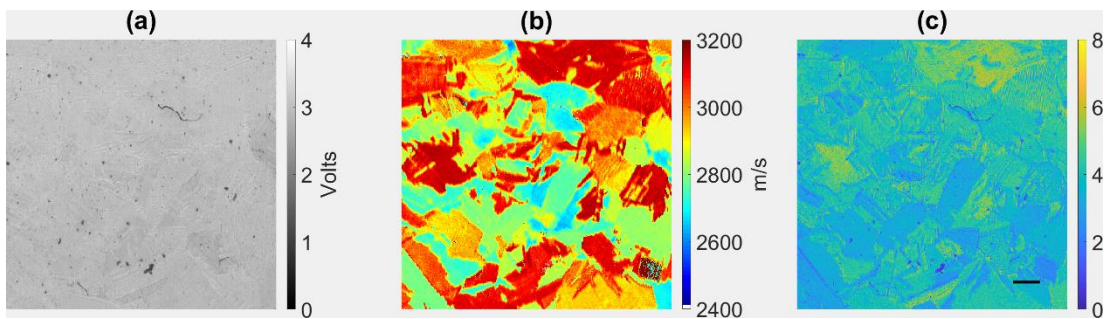


Figure 47 Images of SRAS data from a square titanium large grain sample, (a) optical data where the greyscale represented the detected optical amplitude (b) acoustic data where the RGB colour map illustrated the calculated SAW velocity and (c) the amplitude of the highest frequency in the FFT in arbitrary units. The black scale bar represents 1 mm

Figure 47 (a) illustrates the optical response from the surface of the sample. Here the amount of light returning to the detector was measured in volts and plotted using a grayscale. This was consistent throughout all SRAS optical data sets presented, as a grayscale was seen to be a good representation of optical intensity.

Figure 47 (b) illustrates the calculated SAW velocity from the surface of the sample. The jet colour map from MatLab was used here and in all SRAS velocity data sets presented. This was due to the good spread of primary colours across the range and several distinct bands of colours.

Finally, Figure 47 (c) illustrates the amplitude of the FFT, referred to from this point forward as the signal amplitude. The colours here represent the height of the peak frequency as shown in Figure 46 (b). This is presented in the parula colour map from MatLab so that it could be distinguished from the optical and velocity data. This data set is present with all SRAS data sets but not presented unless required.

The optical - in some cases the signal amplitude - datasets were used as a filtering mask for the velocity data. If the optical return was below a set threshold (2 Volts in the context of Figure 47) the data was not a true representation of the surface of the sample and so was discounted. Similarly, considering the velocity data, the expected velocity from titanium was between 2400 – 3200 m/s and so data above and below these values were not presented. Optical thresholding and limiting the velocity range was a common practice on all of the SRAS data presented within this thesis and was performed on top of the filtering and noise removal discussed in section 3.4.1.5.

### 3.6.1.3. Discussion

The calibration data set was used to illustrate the initial calibration process carried out on all SRAS systems to ensure the velocity being measured was correct, compared to a known constant value. This was necessary due to the SRAS systems used within this thesis being lab-

based systems where elements were occasionally changed to carry out various experiments. It also illustrated the basic principles behind how a SRAS system works and how although various elements – such as the generation, detection lasers and detectors – were different between the various systems the methodology used to obtain the data stayed the same. The calculated wavelength  $\lambda$  was reported for each set of results presented as it varied based on when and on which system the experiment took place.

Following this, the three datasets in Figure 47 illustrated the varied streams of data that can be acquired from a typical SRAS system. The first was the optical data in Figure 47 (a) which in this case had a spatial resolution of 10  $\mu\text{m}$ . This was due to the green detection spot being  $\sim 10 \mu\text{m}$  in diameter. The step size of 25  $\mu\text{m}$  for this dataset meant that each pixel in the results presented was  $25 \times 25 \mu\text{m}$ . Due to the effect of moving a 10  $\mu\text{m}$  spot across the surface with a 25  $\mu\text{m}$  step size, the optical resolution, in this case, was 25  $\mu\text{m}$ . If the step size was set to 5  $\mu\text{m}$ , then due to the detection spot being 10  $\mu\text{m}$ , the optical resolution would be 10  $\mu\text{m}$ . This dataset clearly showed, in the form of drops in optical return (volts), a few small scratches or cracks across the surface of the sample. This is due to there being no reflected light in these areas. For this reason, the optical data is used as a mask for the velocity data. If no optical data was present, the measured acoustic data was considered invalid – in this case, the acoustic data was primarily noise.

The velocity data presented in Figure 47 (b) illustrated the change in SAW velocity across the sample. This was due to the grains on the surface of the sample being at different crystal orientations to each other. This resulted in the SAW travelling at various speeds across them. Compared to the optical resolution, the acoustic spatial resolution was lower. This was governed by the generation patch size of 200  $\mu\text{m}$ . This meant that the spatial resolution of the optical data was 100  $\mu\text{m}$ .

Figure 47 (c) illustrated the amplitude of the FFT for each point across the surface of the sample. When compared to the optical (a) and velocity (b) data sets, the acoustic amplitude (c) was visually similar to the velocity data. This was due to various grains and thereby crystal orientations having varying efficiencies in the generation of SAW waves. Although not obvious in this data set, the acoustic amplitude can also be used in a similar manner to the optical data as a mask for the velocity data. If the acoustic amplitude is below a certain threshold, the data can be considered invalid – again in this case the acoustic data was primarily noise.

### 3.6.2. SRAS on Prepared AM

The prepared AM experiments aimed to lay out the procedures and demonstrate the future potential of SRAS as part of an in-process inspection of AM. As discussed in the literature review it was clear that SRAS was well-positioned to detect classic mechanical defects such as cracks and pores but also microstructural variations.

#### 3.6.2.1. Experiment Design

The following subsections discuss the various experiments carried out to demonstrate the capability of SRAS to detect and classify surface defects and changes to the microstructure of AM components. These experiments were carried out on the EMDA system which was specifically designed to work on optically smooth surfaces and optimised for fast scanning.

#### Mechanical Defect Detection and Classification

Mechanical defects found within AM were primarily cracks and pores as discussed in section 2.3. Such defects led to drastic reductions in the mechanical performance of the finished part. For this reason, the detection, classification and prevention of such defects were critical ahead of the use of AM in high-performance industries such as aerospace. The velocity and optical data obtained from a prepared AM sample manufactured on a Realizer SLM50 using Hastelloy X was used to demonstrate the capability of SRAS to detect and classify such mechanical defects.



Figure 48 Photograph of Hastelloy X 10x10 mm cube manufactured using a Realizer SLM50. The horizontal lines observed were due to the short vertical hatch pattern used. Each layer of the sample was manufactured using five rows of short vertical hatch lines. The swollen region diagonally across the sample was a defect that occurred during the build.

#### Detection

The SRAS optical and acoustic data obtained from AM samples such as this required some filtering to remove individual points of noise. As part of the data processing carried out after any SRAS scan, outlying points with excessively high or low velocity were removed from the data by limiting the plotted velocity range. Following this, a morphological operator was

used. Here the values of small sub-regions around each pixel were considered, and the size and geometrical shape of the region varied based on how much noise was required to be removed. The chosen sub-regions were dilated, here the output value was equated to the maximum pixel value within the sub-region. Following this, the data set was eroded, here the output pixel was set to the minimum value within the sub-region. This removed any further small regions of noise missed by the initial SRAS data processing. Following this, an optical threshold was used to generate a binary dataset containing the surface pores and combined with the acoustic data which would account for any subsurface pores. This was then converted into a binary dataset used for the detection and classification of pores.

### Classification

Further image processing was carried out on this binary dataset. Object analysis was used to individually identify each of the pores and their distinct properties. Properties such as the centroid, area, perimeter, major and minor axis lengths for each pore were extracted and used to classify each of the defects.

### Microstructural Classification

Another key aspect that defined the performance of a part, especially at elevated temperatures, was its crystal structure. As discussed in section 2.7 having some knowledge of the microstructure within the components being built aided the build process and helped predict the through-life performance of the part. SRAS has been used to map the microstructure of large grain materials such as nickel, titanium and silicon in the literature [170], [176], [182]. This study aims to explore the capabilities of SRAS to inspect the microstructure of AM components.

The SRAS acoustic data contained valuable information regarding global changes to the velocities and thereby the crystal orientation of the component. This was due to the individual grains of the AM components inspected being  $\sim 25 \mu\text{m}$  which was much smaller than the  $100 \mu\text{m}$  resolution of the smooth surface SRAS system.

Two mathematical methods were used to obtain a more global understanding of the SAW velocity across the sample. The aim here was to bring forward acoustic features which were previously drowned and difficult to resolve due to the surrounding peaks and troughs in the data.

The first method implemented a spatial filter by considering a mini matrix of dimensions  $m \times m$ . In this case,  $m$  was up to an order of magnitude smaller than the SRAS dataset in question, for example, for a square data set of 2000 data points “ $m$ ” would be in the region

of 200 data points. The mean value of this matrix was calculated and used to provide a more global representation of the variation in the SAW velocity and thereby microstructure across this smaller region. This process was repeated across the entire sample. The aim here was to remove any small sharp changes in the SAW velocity and enhance the global changes in the measured SAW velocity.

The next method investigated was a watershed transform. Inspired by how water collects in the low points of a landscape and flows away from the high points, this method helped identify various regions across the samples being inspected with similar SAW velocities. This method, unlike the spatial filter method above, conserved the spatial resolution of the velocity data and was more focused on identifying smaller clusters of similar velocities based on the velocity gradient between them.

#### Further Microstructural Classification and Verification

The next batch of samples were manufactured to explore the changes to the microstructure within AM samples. Changes to the part geometry were used to challenge the scan strategy (typically built up of square islands) to adapt and provide changes to the microstructure. This was due to the lack of granular control over AM build laser scan strategies. Simple geometrical shapes such as a trapezoid, triangle, square and circle were built. The different geometries of these samples were a step closer to the geometry of real engineering components when compared to the typical cube samples commonly used. These samples were manufactured using a Realizer SLM50 with Inconel 718 powder.

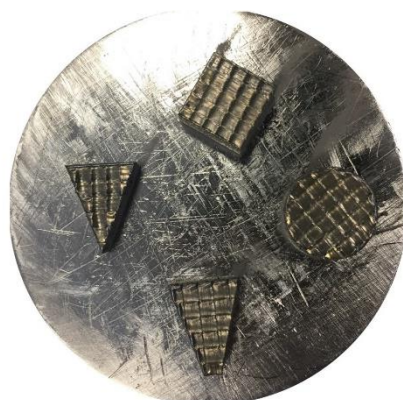


Figure 49 Photograph of four ~10x10 mm geometrical AM samples attached to the 70 mm diameter Realizer SLM50 build plate. The raised square boundaries show how each layer of the sample was manufactured using several small islands and how they were forced to adapt to the change in geometry.

#### Seed Crystal - Epitaxial growth

A final avenue explored was the effect of the substrate on the component being built. This was based on the finding within the literature review section 2.2.2.1 discussing epitaxial

growth within AM. An experiment was designed where a seed crystal was mechanically embedded within the build plate. A sample was manufactured on top of this seed crystal and the aim was for the built sample to replicate the crystal orientation from the seed crystal.

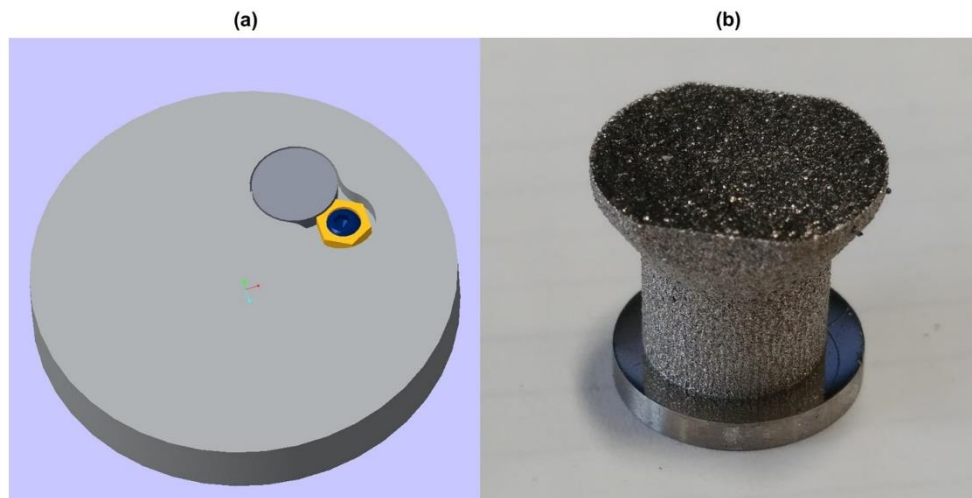


Figure 50 Image of CAD rendering of a 70 mm diameter Realizer build plate with a seed crystal insert, held in place with a specially designed nut (a) and photograph of finished seed crystal sample (b), where the structure was built on top of the nickel seed crystal.

### 3.6.2.2. Results

#### Mechanical Defect Detection and Classification

The two datasets below were obtained from an AM sample manufactured using SLM and Hastelloy X powder.

Table 9 System specifications for Hastelloy X sample

<b>Detector</b>	KED
<b>Wavelength</b>	23.2 $\mu\text{m}$
<b>Step size (x)</b>	5 $\mu\text{m}$
<b>Sample size (x)</b>	10 mm
<b>Segments (x)</b>	2000
<b>Spot size</b>	<10 $\mu\text{m}$
<b>Patch size</b>	200 $\mu\text{m}$
<b>Step size (y)</b>	5 $\mu\text{m}$
<b>Sample size (y)</b>	10 mm
<b>Segments (y)</b>	2000

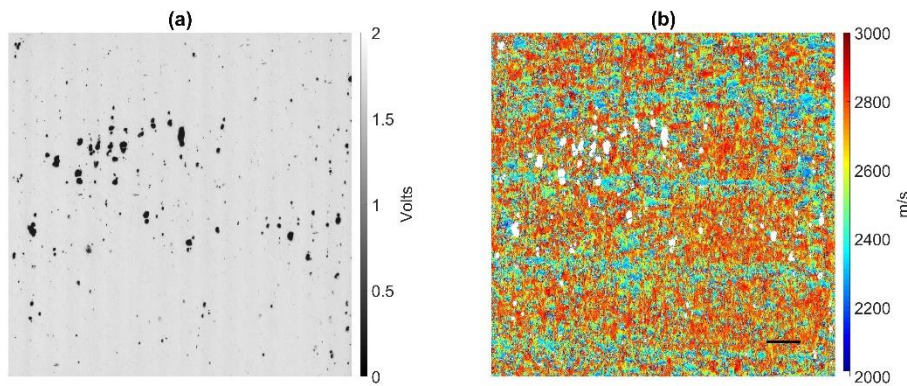


Figure 51 Images of SRAS data from a square AM sample (a) optical data where the greyscale reflects the amplitude and (b) acoustic data where the RGB colour map reflects the calculated SAW velocity. The black scale bar represents 1 mm.

Figure 51 (a) illustrates the optical response obtained from the EMDA system. This showed drops in DC voltage due to a drop in light reflected onto the detector, which was due to surface pores on the sample. Figure 51 (b) illustrates the velocity data from the EMDA system. This dataset showed subtle changes across the surface of the sample. Several horizontal bands of high and low velocities can be observed.

The data presented in Figure 51 was useful from a research and development point of view for understanding the machine behaviours within a development sandbox. For more mainstream implementation and as a useful tool from a shop-floor perspective, this data required further processing. The following steps aimed to take the data from the SRAS system presented above and convert it into useful information from a shop-floor perspective.

#### Defect Detection

The first step in this process was extracting the surface pores from the SRAS data and converting it into a binary dataset. Figure 52 (a) illustrates the surface pores extracted from both the optical and velocity data. Any surface pores are presented as black dots (zeros in the dataset) which made any further data processing straightforward. This was accompanied by Figure 52 (b) where the spatial filter method discussed above was used to identify regions with increased levels of porosity. The spatial filter matrix consisted of 250 elements square ( $1.25 \text{ mm}^2$ ). This data set effectively ignored small clusters and emphasised the presence of larger groups of defects.

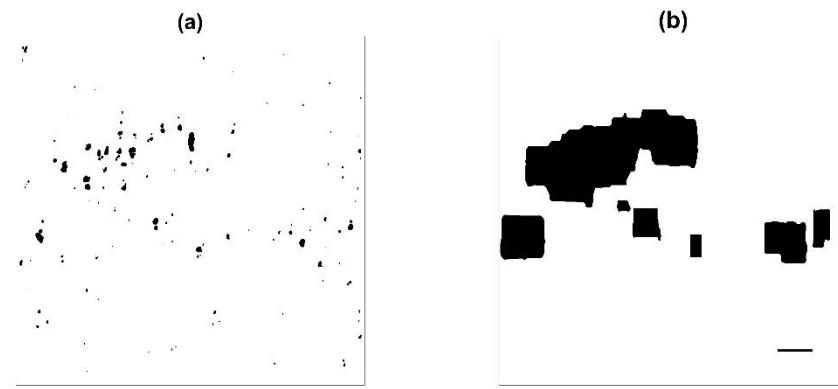


Figure 52 Image of optical data illustrating (a) surface pores where the data is filtered to remove any single-pixel noise and (b) identified regions of relatively higher porosity as an initial step towards closed-loop feedback. The black scale bar represents 1 mm.

#### Defect Classification

The extraction of a binary data set from the SRAS data, allowed image processing to be performed within Matlab. Using built-in functions such as ‘bwboundaries’ and ‘regionprops’ it was possible to initially isolate all the individual pores from their neighbours. Following this, individual properties such as the area, perimeter, centroid position, major and minor axis lengths were extracted. This provided a vast amount of data, an example of which is shown in Figure 53 (a) where the area of the detected pores values are presented in a histogram with 9 bins with a spread of  $100 \mu\text{m}^2$ . The ratio between the area and perimeter can be used to calculate the roundness followed by the major and minor axis lengths to calculate the aspect ratio. Figure 53 (b) presents the normalised roundness against the normalised aspect ratio which provides an understanding of the spread and shapes of the various defects.

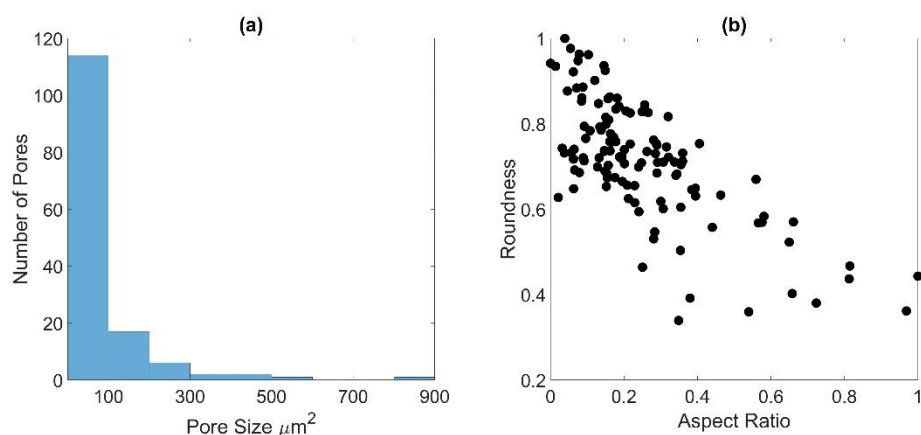


Figure 53 Plots showing the pore distribution where the bar chart (a) plotted the pore count against pore area and the scatter plot (b) plotted the normalised roundness against aspect ratio.

#### Microstructural Classification

The velocity data presented in Figure 51 (b) was difficult to understand if it was to be presented in a shop floor environment or as a part of a much larger dataset containing several

slices of SRAS acoustic data. For this reason, the SRAS velocity data was processed further to reveal more global changes across the surface of the sample. This was also akin to the data that could be obtained from a lower resolution SRAS system designed for inspecting as-deposited surfaces such as the SRAS-Qt system.

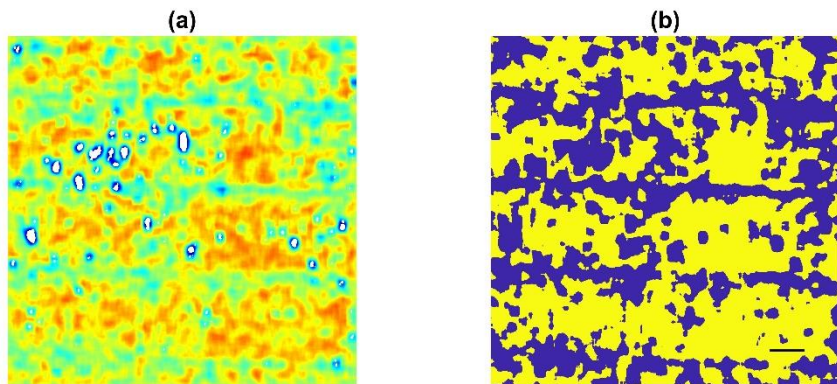


Figure 54 Images of SRAS velocity maps where (a) the spatial filter method was applied to emphasise the average change in the texture of the sample. A simple velocity threshold (b) brought forward the island boundaries in blue and central island regions in yellow. The black scale bar represents 1 mm.

The spatial filter method discussed above was used here with a matrix of 50 elements ( $0.25 \text{ mm}^2$ ). Figure 54 (a) illustrates the global changes to the SAW velocities with the thicker high velocities in red/orange and the lower thin lines of velocities in green/blue. This still requires some user interpretation and so some further processing was carried out. In this case, the mean velocity of the data set (2595 m/s) was used as a threshold for high and low velocities. Figure 54 (b) illustrated these as yellow for high and blue for low. This, however, is just an illustration. The filtered data could be separated into several more bands to extract more granular details regarding the spread of microstructure across the surface of the sample.

Following the global texture analysis above, the prospect of identifying small regions of similar SAW velocities and thereby individual crystal orientations was explored. A watershed transform was performed on the velocity dataset. Here the peaks (highs) and troughs (lows) in the velocity data were used to attempt to identify the smallest regions with the same SAW velocity. This was initially developed to identify individual grains on the surface of large-grained materials and so was applied to the dataset from Figure 47. The images in Figure 55 illustrate how although this method was able to identify some grain boundaries, it was too sensitive and in some cases, it misidentified boundaries that did exist and completely missed other more subtle grain boundaries. This showed that it required further optimisation for large-grained materials.

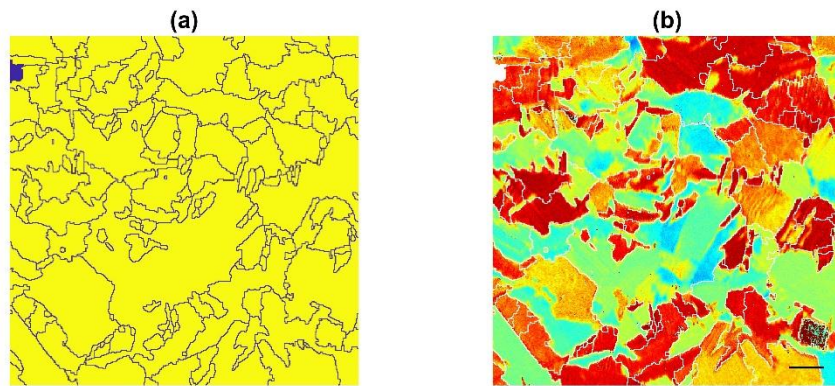


Figure 55 Images illustrating the results from applying the watershed method to the SRAS velocity data from a material with large grains. Here (a) illustrates the outlines drawn using the watershed method and (b) illustrates this method overlaid on the velocity map of the same area. The black scale bar represents 1 mm.

Following this, the watershed method was applied to the AM sample discussed above. Figure 56 (a) illustrates the identified borders in blue between the regions of similar SAW velocity. Figure 56 (b) illustrates a  $2.5 \times 2.5$  mm zoomed-in region of the boundaries accompanied by Figure 56 (c) which is matching velocity measurements from that region. This data set showed more promise than the large grain dataset. There were however some intermediate regions that were missed and so required some further optimisation.

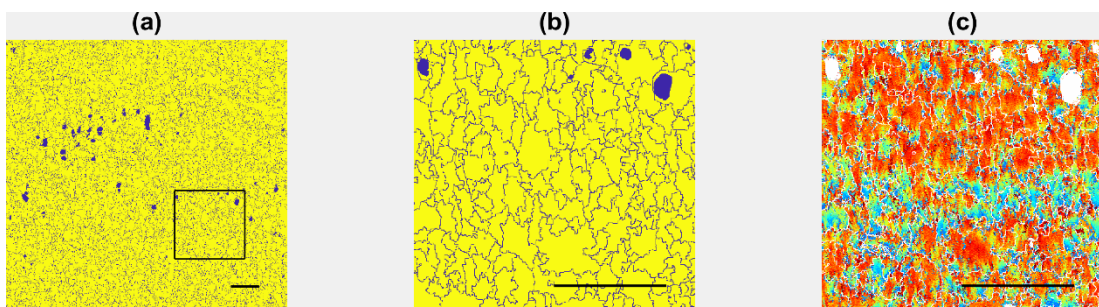


Figure 56 Images illustrating the results from applying the watershed method to the SRAS velocity data where (a) illustrates the outlines drawn using the watershed method, square box outlining the zoomed area. Image (b) illustrates the zoomed area and the outlines of the regions and (c) illustrates the zoomed velocity map with the watershed regions in white. The black scale bar represents 1 mm.

The identification of these boundaries provided the capability to carry out the same analysis as on the pore data above. If these were real grains on the surface of the sample they could be sized, counted and classified. Due to the current resolution limitations of SRAS, this was not performed as the outlined regions were still clusters of grains due to the effective averaging that happened when the data was acquired due to the small grain size of AM.

#### Further Microstructural Classification and Verification

As a different approach to detecting changes to AM component microstructure, another batch of samples were manufactured with different geometries using Inconel 718 powder on a Realizer SLM50. This attempted to mimic “real world” applications for AM which would be

used to build more challenging geometries and forced the scan strategies to adapt to the geometry. Out of the four geometrical shapes manufactured (Figure 49), the triangle sample in Figure 57 provided the most fruitful.

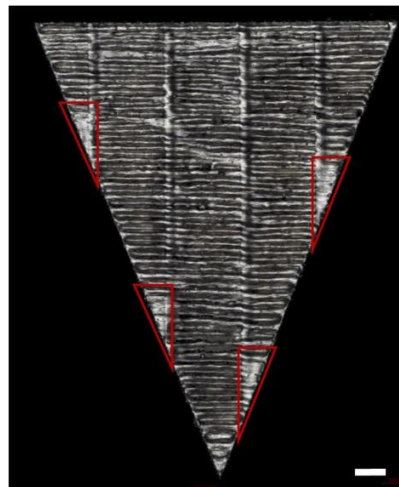


Figure 57 Image of the as-deposited surface of the triangle sample obtained using optical microscopy. Illustrating the tracks left behind by the build laser along with mini right-angle triangles (emphasized using the red triangles) where the surface appeared more smooth compared to the rest of the sample. The white scale bar represents 1 mm.

The optical microscopy image of the as-deposited triangle sample surface in Figure 57 illustrates similarly raised regions as seen in Figure 48 and Figure 49 but more importantly, the improved resolution shows the relatively smooth regions, outlined by the red triangles. Here due to the reducing (going from top to bottom) horizontal space, the scan lines got shorter and shorter. This resulted in the build laser spending more time in a small region increasing the energy density in that area. For further analysis using SRAS and EBSD, the surface of this sample was prepared as outlined in section 3.5.1.

Table 10 System specifications for Inconel 718 Triangle

<b>Detector</b>	KED	<b>Spot size</b>	10 $\mu\text{m}$
<b>Wavelength</b>	23.2 $\mu\text{m}$	<b>Patch size</b>	200 $\mu\text{m}$
<b>Step size (x)</b>	5 $\mu\text{m}$	<b>Step size (y)</b>	5 $\mu\text{m}$
<b>Sample size (x)</b>	13 mm	<b>Sample size (y)</b>	16 mm
<b>Segments (x)</b>	2000	<b>Segments (y)</b>	2000

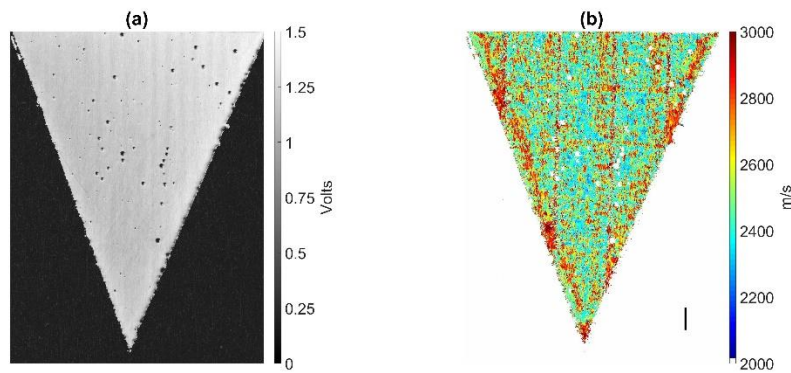


Figure 58 Images of SRAS data from the triangle AM sample where the optical return (a) presented in a greyscale shows the smooth flat surface with some porosity. The acoustic data (b) illustrates the clear square island boundaries at the top of the sample and large areas of high velocities (~3000 m/s) in the regions highlighted in Figure 57. The black scale bar represents 1 mm.

Figure 58 (a) demonstrates how following the sample preparation no indications of how the sample was manufactured were evident. The acoustic data in Figure 58 (b) however shows very clear indications of the square islands towards the top/flat section of the triangle. It also shows clusters of high velocities along the tapered sides of the triangle which correspond to the red triangles in Figure 57. This was explored further by inspecting the sample using EBSD. Another observation was the higher concentration of high velocities (red) towards the right-hand side of each of the square islands.

Table 11 SRAS System specifications for small area Inconel 718 Triangle

<b>Detector</b>	KED	<b>Spot size</b>	10 $\mu\text{m}$
<b>Wavelength</b>	23.2 $\mu\text{m}$	<b>Patch size</b>	200 $\mu\text{m}$
<b>Step size (x)</b>	1 $\mu\text{m}$	<b>Step size (y)</b>	1 $\mu\text{m}$
<b>Sample size (x)</b>	3 mm	<b>Sample size (y)</b>	3 mm
<b>Segments (x)</b>	2000	<b>Segments (y)</b>	2000

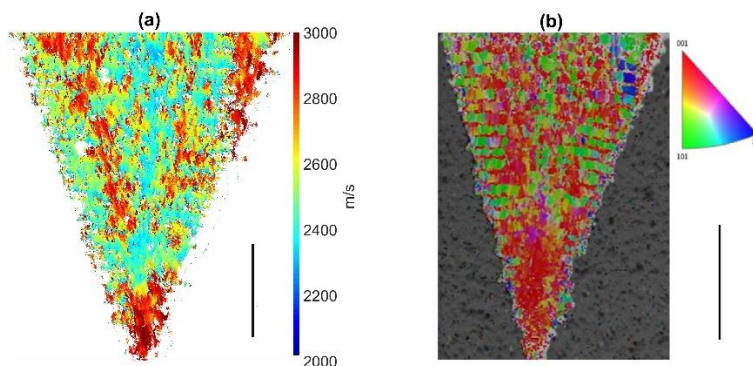


Figure 59 Image of SRAS acoustic data (a) of a smaller region close to the tip of the triangle alongside EBSD data from the same region (b). The EBSD data shows some clear green bands which are formed in a similar direction to the scan lines. The tip of the EBSD data shows a strong 001 orientation and is comparable to the high 3000 m/s regions observed in the SRAS data. The black scale bar represents 1 mm.

The two datasets from SRAS and EBSD in Figure 59 show complementary information about the same region. It was clear that the spatial resolution of the EBSD data was much higher than the SRAS data. Although SRAS was unable to resolve individual grains, the acoustic data provided a good indication of the changes to overall texture across the surface of the sample.

### Seed Crystal - Epitaxial Growth

In this case, the AM sample, manufactured using INC 718 powder was built on top of a 14 mm diameter disk of single-crystal CMSX-4 – a second-generation nickel-base superalloy [183] – referred to as the “seed crystal”. In an ideal situation, both the seed crystal and the build powder would be identical, however, due to the availability of materials, both being nickel-based superalloys were seen to be a good match for this experiment.

The results below were obtained from the cross-section of the AM sample, which was different from all of the other results discussed within this thesis. The reason for inspecting the cross-section of this sample was to explore in detail the interaction between the seed crystal used and the manufactured AM part. This was more akin to the results that could be obtained from an in-process inspection of AM processes that don't use a powder bed such as WAAM or blown powder.

Table 12 SRAS System specifications for large area seed crystal

<b>Detector</b>	KED	<b>Spot size</b>	10 µm
<b>Wavelength</b>	23.2 µm	<b>Patch size</b>	200 µm
<b>Step size (x)</b>	5 µm	<b>Step size (y)</b>	5 µm
<b>Sample size (x)</b>	14 mm	<b>Sample size (y)</b>	14 mm
<b>Segments (x)</b>	2000	<b>Segments (y)</b>	2000

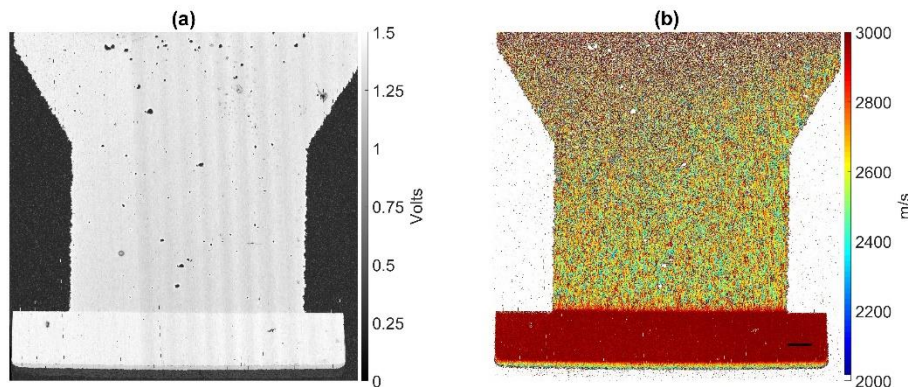


Figure 60 Images of SRAS optical data (a) and acoustic data (b) obtained from the cross-section of the seed crystal sample. The large flat region on the bottom was the seed crystal and the region above it was manufactured using AM. The black scale bar represents 1 mm.

The optical return in Figure 60 (a) illustrates how the seed crystal at the bottom of the image had a slightly higher optical return compared to the AM section of the sample. Whereas the AM section of the sample had a slightly lower optical return. This was due to the different wear rates of the seed-crystal and AM section. The seed crystal was better polished and therefore had a better reflection of the detection laser. The vertical striping observed in the optical data across half the sample was due to a problem with the green generation laser at the time. Due to an overheating issue, its power output was not consistent. This, however, had no impact on the acoustic data presented in Figure 60 (b).

The acoustic data presented in Figure 60 (b) illustrates how the seed crystal was isotropic and had a consistently high velocity (of ~3000 m/s). Whereas the AM section of the sample had a more stochastic distribution which reflected the random equiaxed microstructure typically found within AM components. No large changes to the AM component were observed, due to the seed crystal. The thin ~100 µm region, however, showed some influence due to the seed crystal. For this reason, that region was inspected further using both SRAS and EBSD.

Table 13 SRAS System specifications for small area seed crystal

<b>Detector</b>	KED	<b>Spot size</b>	10 µm
<b>Wavelength</b>	23.2 µm	<b>Patch size</b>	200 µm
<b>Step size (x)</b>	1 µm	<b>Step size (y)</b>	1 µm
<b>Sample size (x)</b>	3 mm	<b>Sample size (y)</b>	3 mm
<b>Segments (x)</b>	2000	<b>Segments (y)</b>	2000

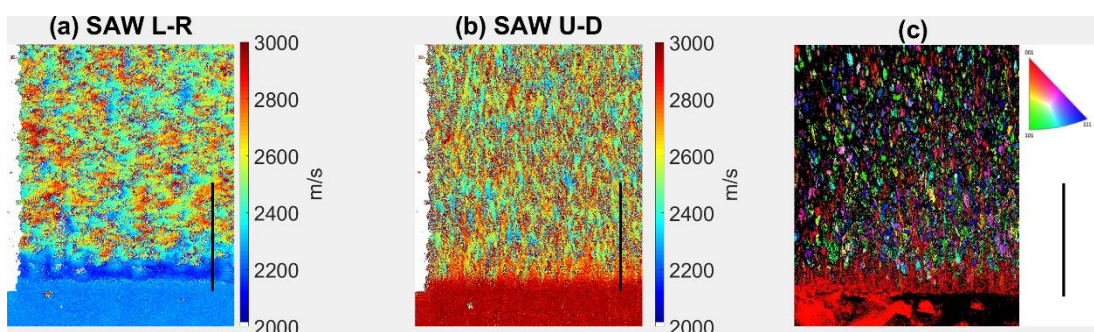


Figure 61 Images of SRAS acoustic data with the SAW in going left-right (a), up-down (b) and EBSD data (c) from the cross-section of the seed crystal sample. In the acoustic data, the small excess flat section towards the bottom left is intentionally included in this figure to indicate the end of the seed crystal and how anything above that point was part of the AM component. The start of the black 1 mm scale bar was aligned to this point.

The acoustic data presented in Figure 61 (a) and (b) shows how the first ~50 µm region within the AM section of the sample demonstrated the same SAW velocity as the seed crystal. The SAW was propagated in orthogonal directions to verify that this was real microstructure and not an artefact. The next ~100 µm region above the seed within the AM sample showed how

a majority of the velocities measured were low for L-R (blue) and high for U-D (red) mirroring the SAW velocity of the seed crystal.

The black region to the bottom right of the EBSD data in Figure 61 (c) is where no signal was detected and so could be ignored. This was due to the sample being uneven, which occurred during the polishing process, where each section (AM and seed) had a different wear rate. The EBSD scan was primarily focused on the interaction between seed crystal and AM sample. This data, similar to the SRAS acoustic data, showed how the AM section manufactured mirrored [001] crystal orientation of the seed crystal.

### 3.6.2.3. Discussion

#### Mechanical Defect Detection and Classification

The optical data in Figure 51 (a) showed several pores spread across the surface of the sample. The velocity data presented in Figure 51 (b) when closely inspected showed the same pores but were difficult to spot amongst the changes in colour due to the change in SAW velocity. This was expected as the optical data was used as a mask to filter the acoustic data. If there was no optical reflection measured, then there was no light on the detector and so no acoustic data was collected. When inspecting the velocity data further, there was a faint indication of the scan strategy used to build the part as seen in Figure 48. Narrow horizontal bands of low velocities (green-blue) and thick horizontal bands of high velocities (red-orange) could be observed. This however was not as clear or as obvious as it could be.

#### Detection

Focussing purely on the mechanical defects at this stage, following some thresholding of the optical data Figure 52 (a) illustrated how any surface defects detected in the SRAS optical data can be easily identified. Once individual surface pores were detected Figure 52 (b) illustrated the results of the spatial filtering methodology that can be applied in a shop floor environment. Using a predetermined spatial filter size – 1.25 mm square – regions with increased porosity could be instantly identified by a technician monitoring the AM system.

When comparing the photograph of the as-deposited sample in Figure 48 with the porosity clusters in Figure 52 (b) some correlation could be observed. The photograph in Figure 48 showed a protruding region along the top left to bottom right diagonal. The large porosity clusters in Figure 52 (b) were spread across the central belt of the sample. It is worth noting that the SRAS data came from the prepared (mechanically polished) surface of the sample in Figure 48. As part of the polishing process, several layers of material were removed. For this

reason, it could be assumed that the porosity detected in Figure 52 (a) were early signs that lead to the protrusion observed in Figure 48.

During the build process of the sample in Figure 48, a lot of balling was observed within the build chamber. This at the time was assumed to be due to increased moisture in the powder feedstock. This increased balling and potential moisture could have been the initial cause of the cluster of defects in Figure 52 (b) that led to the protrusion observed in Figure 48.

### Classification

The graphs in Figure 53 demonstrate the capability of SRAS data to not only detect but also classify the surface defects. The first point worth noting however was how the bar chart in Figure 53 (a) – no matter how small the bin size of the graph was – did not follow a normal distribution. Where in a naturally occurring dataset, you would expect the count relative to the size to gradually increase, peak at a median value and drop off as the size increased further. In this case, the pore count started high from 0-100  $\mu\text{m}^2$  and then dropped significantly for the 100-200  $\mu\text{m}^2$  bin and dropped further for the 200-300  $\mu\text{m}^2$  bin. This was due to the 10  $\mu\text{m}$  resolution of the SRAS optical data where all pores less than 100  $\mu\text{m}^2$  were counted within the 1<sup>st</sup> bin of 0-100  $\mu\text{m}^2$ . In a situation where the spatial resolution of the system was below the smallest pore size, a more normal distribution could be expected. Having this information, however, can help ensure parts meet the specification where for example a maximum pore size or count could not be exceeded.

The scatter plot in Figure 53 (b) illustrated the normalised roundness and aspect ratio of the detected pores. This was calculated using the equations discussed in section 2.3.1 and the data extracted from the individual pores detected in Figure 52 (a). The aim here was to differentiate between the cracks which would have a high aspect ratio and pores that would have a high roundness. The collection of points close to the top left corner of Figure 53 (b) showed that a majority of the defects on the surface of the sample were surface pores. This agreed with what can be visually observed in Figure 52 (a), where a vast majority of the detected defects were surface pores and very little cracking was observed. The lack of cracking on the sample was again reflected in Figure 53 (b) with only two points occupying the bottom right corner. In a similar manner to Figure 52 (b), the aim of Figure 53 (b) was to provide an easy-to-digest, visual illustration of the part being inspected. This could be used in a shop floor environment to understand the link between various types of defects and their cause. A good example of this would be gas pores (discussed in section 2.3.1) which are known to have a high circularity.

### Microstructural Classification

The acoustic data in Figure 51 (b) was difficult to understand for a shop floor user of such a system. Part of the reason for this was that AM grains are known to be in the region of  $\sim 25 \mu\text{m}$  – confirmed in the EBSD data presented in Figure 59 (b) – compared to the EMDA systems' spatial resolution for acoustic data was  $100 \mu\text{m}$ . This was due to its acoustic generation patch diameter being  $200 \mu\text{m}$ . Within the  $200 \mu\text{m}$  diameter generation patch, there were several individual grains. This meant that the velocity measured was an average of all of these individual grains.

Although it was clear that the current generation of smooth surface SRAS systems was unable to image individual grains on AM samples manufactured using SLM, there was still a vast amount of information that could be extracted from the obtained acoustic datasets. Using a predetermined spatial filter size –  $0.25 \text{ mm square}$  – the changes to the SAW velocities across the sample were enhanced and shown in Figure 54 (a). This illustrated the global change in SAW velocity better than in Figure 51 (b). Then using the mean velocity of the data set of  $2595 \text{ m/s}$  the filtered data was split into two regions as shown in Figure 54 (b), where high velocities were yellow and low velocities were blue. When compared to the photograph of the as-deposited surface of the sample in Figure 48 it was clear how the blue low regions in Figure 54 (b) corresponded to the thin raised walls between each of the scan rows, and the high velocities in yellow correspond to the thicker lowered bands across the sample. If the designed microstructure and its corresponding SAW velocities are known, then the methodology used for Figure 54 (b) can be applied in a shop floor environment. This would mean an operator monitoring the system can ensure the part being built matches the designed microstructure.

The methodology based on a watershed transform was developed on samples with large grains in an attempt to identify individual grains. The boundaries identified using this method on a large grain titanium sample are shown in Figure 55 (b). It was clear that this method required further optimisation before it could provide useful insights into such datasets. This was due to the relatively simple method of using the median of the velocity range to draw the grain boundaries. This essentially only identified a high and low region. The large grain velocity data in Figure 47 showed that this was not the case and that the individual grains had more subtle variations in their velocity.

The watershed transform applied to AM in Figure 56 (a) illustrated how small regions of local variation in SAW velocity can be identified. Although it was clear that this method was not

identifying individual grains, it helped outline a more local change in SAW velocity. Figure 56 (b) and (c) demonstrated across a small region how this was different to the dataset in Figure 54 (b). Unlike the large grain data previously discussed, the AM data have more drastic velocity gradients. This made the watershed methodology more suitable for acoustic datasets from AM samples. It was also worth noting that the watershed methodology used here maintained the spatial resolution of the acoustic data set. Although the use of this methodology is still to be fully realised, as the spatial resolution of new generations of SRAS systems improves, it stood as a useful mathematical tool to be used in the future.

### Further Microstructural Classification and Verification

Due to the lack of granular control over scan strategy in the AM system used, the part geometry was used to force changes in the scan strategy and thereby the part microstructure. Figure 57 illustrated how on the as-deposited surface of the sample, as the scan tracks decreased in length towards the end of each of the vertical bands, relatively smooth regions were observed (emphasized using the red triangles). The SRAS acoustic data from this sample, Figure 58 (b) showed regions of high velocity that matched the relatively smooth regions in Figure 57. Similarly the acoustic data in Figure 58 (b) peaks in the SAW velocity towards the end of each of the square islands. This was where the build laser had to decelerate and change direction. This meant that based on the energy density defined by Equation 6, as the scan speed decreased the energy density in that region increased (see section 2.4.7). This demonstrates the ability of SRAS to detect the change in component microstructure caused by the changes to the scan strategy. It was also worth noting how the optical data in Figure 58 (a) showed no correlation to the peaks in velocity found in Figure 58 (b), demonstrating how the acoustic data was completely decoupled from the microstructure of a component.

The next experiment aimed to directly compare and contrast the SRAS acoustic data and crystal orientation measured using EBSD – as this was the gold standard when it came to crystal orientation. The side-by-side comparison of the SAW velocity and EBSD crystal orientation in Figure 59 helped improve the understanding of the complementary data that can be obtained from both these systems. The EBSD data in Figure 59 (b) clearly showed horizontal bands of individual grains in green with a [101] crystal orientation. These were sized in the region of  $\sim 25 \mu\text{m}$ . When compared to the optical microscopy image of the as-deposited surface of the sample in Figure 57 the horizontal bands of [101] orientation grains aligned well with the longer scan lines. The tip of the triangle – the smooth region – showed a majority of the grain aligned to the [001] orientation, this was seen as a peak in the SAW

velocity in the SRAS acoustic data. Along the left-hand side of the triangle EBSD data, some grains were initially of a [101] orientation and switched to [001] orientation. This was mirrored in the SRAS data as a change from ~2500 m/s to ~3000 m/s. It was clear from the data in Figure 59 that based on the resolution of the current generation of SRAS instruments, it was unable to measure the SAW velocity of the individual grains within an AM component. It did however provide a good indication as to the changes in crystal orientation.

### Seed Crystal - Epitaxial Growth

Observing the optical data in Figure 60 (a) – from left to right – some vertical lines with subtle changes in intensity were observed. These started a third of the way across the sample. This was not linked to the samples being inspected. Instead, it was due to an ongoing issue where due to overheating, the green detection laser output power varied over time. This, in turn, varied the DC light return measured. Comparing this to the acoustic data in Figure 60 (b), it was clear that there was no correlatable variation in the acoustic data. The mean optical return in this data set was ~1.3 V. The vertical lines observed had a minimum value of ~1.1 V. Across the data sets in Figure 60, an optical return as low as 0.5 V provided valid acoustic data. This meant that the EMDA system was able to cope with a drop of up to ~60% in the reflected light before it had a significant effect on the measurement being carried out. This also showed how the optical and acoustic data were decoupled. Furthermore, it illustrated how robust the SRAS technique was, in that it was not affected by small changes to the optical return. As a final comment on the optical data in Figure 60 (a), the seed crystal at the bottom, showed an overall higher optical return when compared to the AM section. This was partly due to the uneven wear rates of the two materials, during the mechanical polishing process. The seed crystal was effectively polished more than the AM section. Another reason for this could have been the selective etching that occurred during the final stages of the polishing process where colloidal silica suspension fluid was used.

Focussing now on the use of a seed crystal to promote epitaxial growth within an SLM sample, it was difficult to quantify any effect when looking at both the optical and acoustic data in Figure 60. This was due to the relatively large region – 10 mm x 10 mm – that was inspected. For this reason, as shown in Figure 61 the SRAS inspection was focused on a small region with a much smaller 1 µm step size. To discount any effect of the SAW propagation direction, the sample was scanned with the SAW propagating in orthogonal directions(up-down and left-right). Within the two SRAS acoustic data sets, it was clear that the first ~50 µm of the AM section mirrored the SAW velocity of the seed crystal. When inspected using EBSD

– as presented in Figure 61 (c) – a similar behaviour was observed where the crystal orientation was mirrored by the first  $\sim 50\text{ }\mu\text{m}$  of the AM section.

Above the first  $50\text{ }\mu\text{m}$ , the SRAS data showed vertical dendritic structures that mirrored the seed crystal up to  $\sim 200\text{ }\mu\text{m}$  above the seed crystal. This was also observed in the EBSD data. The layer height used for this build was  $40\text{ }\mu\text{m}$  which meant that this region of influence due to the seed crystal was over several build layers high. Another observation within the EBSD data was the fact that through the AM section visually there was an increased number of grains orientated in the [001] orientation mirroring the seed crystal. Due to the relatively poor quality of the EBSD data, this could not be fully quantified. Once prompted it was possible to visually see a similar trend in the SRAS data where small patches of (low  $\sim 2000\text{ m/s}$  in the L-R and high  $\sim 3000\text{ m/s}$  in the U-D) similar velocity could be observed. This however was a very small visual observation and was difficult to quantify. Compared to the EBSD data in Figure 59 (b), the data in Figure 61 (b) contained more black – no data – regions. The reason for this was that the sample had a very uneven surface. This was due to the uneven wearing and selective etching of the two different materials discussed above. This made getting the entire sample in focus difficult. For this reason, the primary aim was to obtain the best data possible from the region between the seed crystal and AM sample.

### 3.6.3. Transition to Rough Surfaces

#### 3.6.3.1. Experiment Design

Following the experiments carried out on prepared surfaces, the focus was moved to the as-deposited surface of AM samples. One of the first challenges when inspecting as-deposited surfaces was surface roughness. For this reason as an initial step, a surface roughness comparator was inspected using the smooth surface EMDA system. This was used as a like-for-like comparison between the smooth surface and rough surface SRAS systems. The gradual change in surface roughness from  $0.025\text{ }\mu\text{m Ra}$  up to  $3.2\text{ }\mu\text{m Ra}$  of this sample allowed the smooth surface SRAS system to capture some data from the smooth sections, and tail off as the roughness increased.

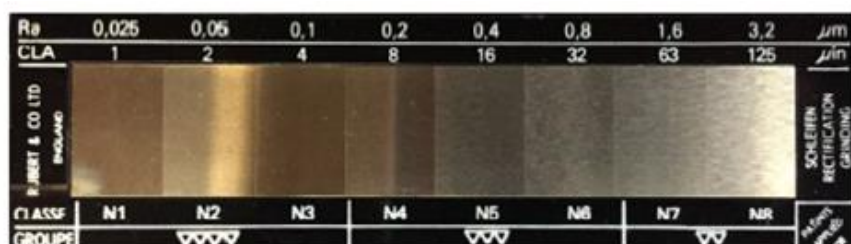


Figure 62 Photograph of Rubert & Co Ltd surface roughness comparator No 115. The varying surface roughness was manufactured using surface grinding and ranged from Ra  $0.025\text{ }\mu\text{m}$  to  $3.2\text{ }\mu\text{m}$ .

Following this, the SRAS-Qt system was used to inspect the same roughness comparator. This system was specifically designed and built around Quartet rough surface detector. Apart from the elements discussed in section 3.4.2.2 the biggest difference in the SRAS-Qt system when compared to the EMDA system was the move away from real-time scanning. Instead, to cope with the increased noise due to the surface roughness, this system averaged each data point.

### 3.6.3.2. Results

The data presented in Figure 63 row (a) illustrates how the measured velocity points decreased as the roughness increased. A similar behaviour was observed in the optical data in Figure 63 row (b) where the optical return decreased as the roughness increased. Finally, the signal amplitude presented in Figure 63 row (c) normalised as the roughness increased. The segments past  $0.4 \mu\text{m Ra}$  were not scanned due to the complete loss of useful data.

Table 14 SRAS System specifications for surface roughness comparator on EMDA

<b>Detector</b>	KED	<b>Spot size</b>	10 $\mu\text{m}$
<b>Wavelength</b>	23.37 $\mu\text{m}$	<b>Patch size</b>	200 $\mu\text{m}$
<b>Step size (x)</b>	10 $\mu\text{m}$	<b>Step size (y)</b>	10 $\mu\text{m}$
<b>Sample size (x)</b>	2 mm	<b>Sample size (y)</b>	2 mm
<b>Segments (x)</b>	200	<b>Segments (y)</b>	200

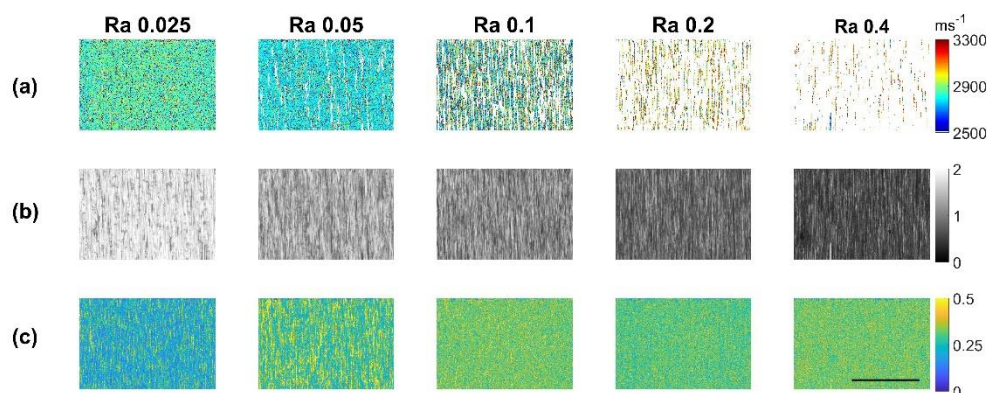


Figure 63 Images of SRAS data collected using the smooth surface EMDA system of the surface roughness comparator where the Ra value varied from 0.025-0.4  $\mu\text{m Ra}$  from left to right. Each of the rows showed (a) velocity, (b) optical and (c) signal amplitude. The black scale bar represents 1 mm.

The same roughness comparator was then scanned using the SRAS-Qt system. In this case Figure 64 row (a) shows the SRAS velocity measurement followed by row (b) which shows the signal amplitude. The use of a commercially available rough surface detector known as the Quartet meant that there was no optical DC return. SRAS data was obtained for the

surfaces between 0.05-1.6  $\mu\text{m}$  Ra. Due to the increased depth of focus on this system, the entire sample was scanned in one batch, whereas the data presented in Figure 63 from the smooth surface EMDA system required to be focused for each change in height between the surfaces.

Table 15 SRAS System specifications for surface roughness comparator on SRAS-Qt

<b>Detector</b>	Quartet	<b>Spot size</b>	30 $\mu\text{m}$
<b>Wavelength</b>	81.98 $\mu\text{m}$	<b>Patch size</b>	1000 $\mu\text{m}$
<b>Step size (x)</b>	200 $\mu\text{m}$	<b>Step size (y)</b>	100 $\mu\text{m}$
<b>Sample size (x)</b>	105 mm	<b>Sample size (y)</b>	2 mm
<b>Segments (x)</b>	525	<b>Segments (y)</b>	20

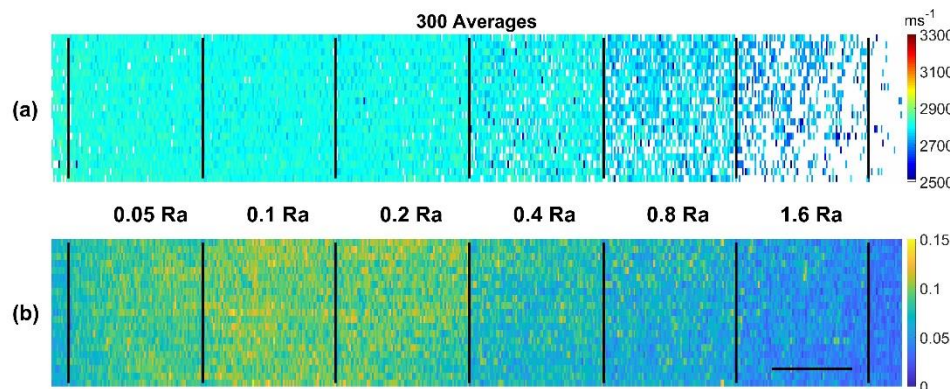


Figure 64 Images of SRAS data obtained using the rough surface SRAS-Qt system of the surface roughness comparator where (a) illustrates the acoustic data and (b) the signal amplitude. The Ra value varied from 0.05-1.6  $\mu\text{m}$  from left to right, with each segment separated using vertical lines. The black horizontal scale bar represents 10 mm.

### 3.6.3.3. Discussion

As an initial trial on rough surfaces, the surface roughness comparator in Figure 62 was inspected using the smooth surface EMDA system. It was clear in Figure 63 row (a) that as the surface roughness increased above  $\sim 0.1 \mu\text{m}$  Ra the optical return from the sample was not sufficient to produce reliable data. The small stripes of velocity presented from the 0.2-0.4  $\mu\text{m}$  Ra segments were when the optical return was seen to be sufficient (greater than 0.5 V). Anything below this optical threshold was considered to be noise.

The decrease in optical return was clearly illustrated in Figure 63 row (b), where, as the surface roughness increased a majority of the optical data dropped below 0.5 V. Figure 63 row (b) also showed subtle vertical striations. These were in fact real striations due to the surface grinding technique used to manufacture these surfaces. This again illustrated the increased optical resolution of this SRAS system and how on the smooth surfaces this effect

was decoupled from the acoustic data. Finally, Figure 63 row (c) illustrated the signal amplitude data from the varying surfaces. The matching striations to the optical were observed in this data. This was due to the peaks of the surface providing a better reflection than the troughs. Across the data sets from 0.1-0.4  $\mu\text{m}$  Ra the signal amplitude data showed no strong variations. This was due to the phenomena illustrated in Figure 40, where as the signal amplitude decreased, it was of a similar magnitude as the noise and so could not be distinguished.

The same sample was then inspected using the SRAS-Qt system. Due to the way this system was built around the Quartet rough surface detector, no true optical data was available. Instead, on all rough surface data sets using the SRAS-Qt system, the velocity was presented alongside the signal amplitude. It was clear from the acoustic data presented in Figure 64 row (a) that this system was able to provide reliable acoustic data up to surfaces  $\sim 1.6 \mu\text{m}$  Ra using 300 averages. Small dropouts in the acoustic data were observed at 1.6  $\mu\text{m}$  Ra and so the next segment of 3.2  $\mu\text{m}$  Ra was not inspected. The Quartet was specifically designed for industrial applications and so its typical use case involved some averaging. Due to an inherent limitation within the system, it was unable to provide reliable data using a single-shot measurement. As discussed in section 3.4.1.5 the number of averages used for an inspection was a compromise between signal quality, SNR and time.

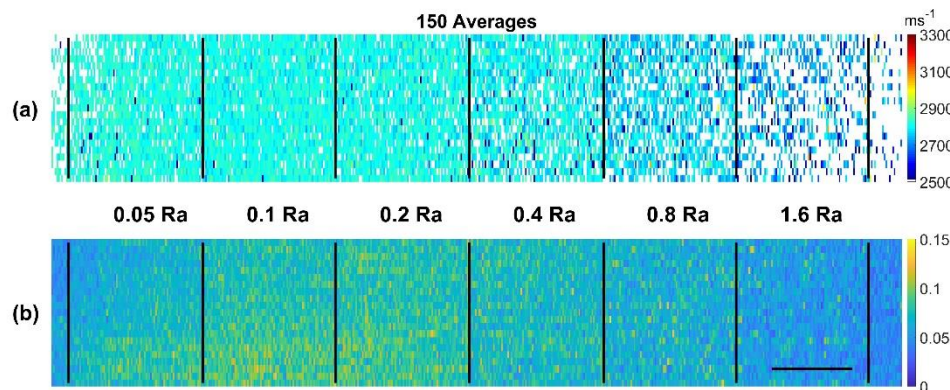


Figure 65 Images of SRAS data obtained using the rough surface SRAS-Qt system of the surface roughness comparator using 150 averages where (a) illustrates the acoustic data and (b) the signal amplitude. The black horizontal scale bar represents 10 mm.

Figure 65 illustrated the results that could be obtained with 150 averages. In this case, more dropouts in velocity data could be observed as low as 0.05  $\mu\text{m}$ . The data set in Figure 66 illustrated the effect 600 averages had on the results. No significant difference could be observed in the data set with 300 averages compared to that of 600 averages, but inherently the 600 averages data set took over double the time to acquire. For this reason, the 300

average data set in Figure 64 was seen to be the best compromise in terms of inspection time and data quality. This subject is discussed further in section 5.3.1.3.

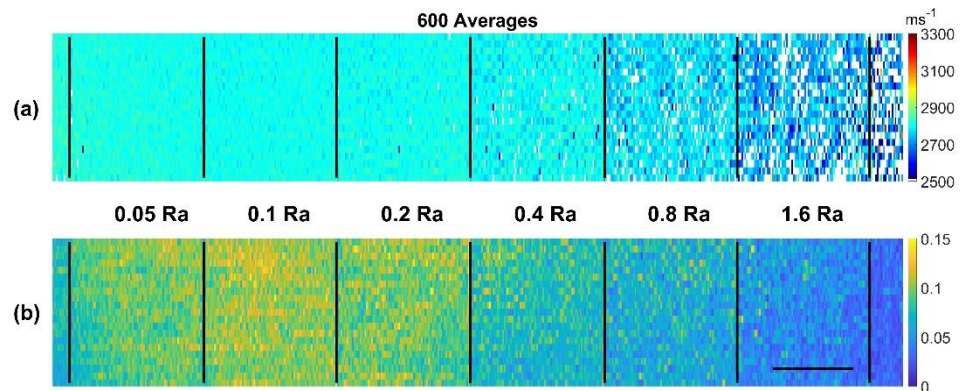


Figure 66 Images of SRAS data obtained using the rough surface SRAS-Qt system of the surface roughness comparator using 600 averages where (a) illustrates the acoustic data and (b) the signal amplitude. The black horizontal scale bar represents 10 mm.

### 3.6.4. SRAS on As-Deposited AM

#### 3.6.4.1. Experiment Design

Following the experiments on the surface roughness comparator, the following section discusses an experiment carried out on the top surface of a relatively large AM sample (discussed further in chapter 4) inspected using the SRAS-Qt system. This was manufactured using a Realizer SLM50 machine with AlSi10Mg powder. The scan strategy used to build this sample was a simple raster scan strategy as the main aim of this sample was to have intentionally positioned internal features, for the experiments carried out in chapter 4.

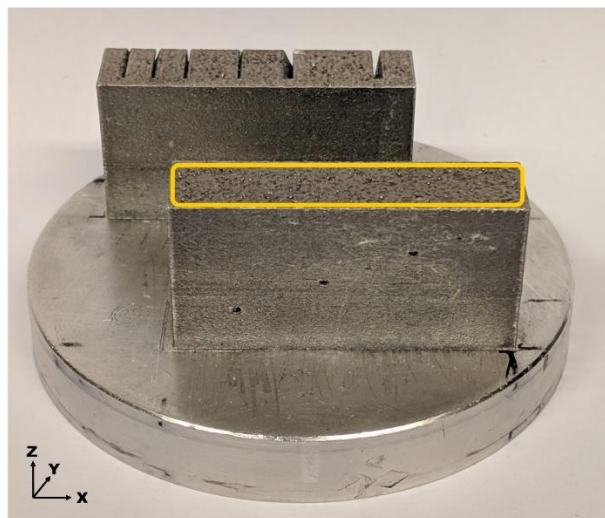


Figure 67 Photograph showing the sample used for the SRAS as-deposited surface trial where the yellow box illustrates the approximate region scanned using the SRAS-Qt system. The top rectangular surface of this sample was designed to be 40 mm x 10 mm.

Finally, as an extreme example of the surface variations found within AM components, the sidewall of an undeformed WAAM Ti64 sample was inspected using the SRAS-Qt system. The WAAM process, the method the samples were manufactured, followed by an in-depth analysis of SRAS data obtained from prepared samples was discussed in the literature [34]. The photograph in Figure 68 showed how on a small scale the surface of this sample appeared to be smooth and shiny. Whereas on a large scale, the apparent waviness of the surface presented an extreme challenge from an LU inspection perspective.

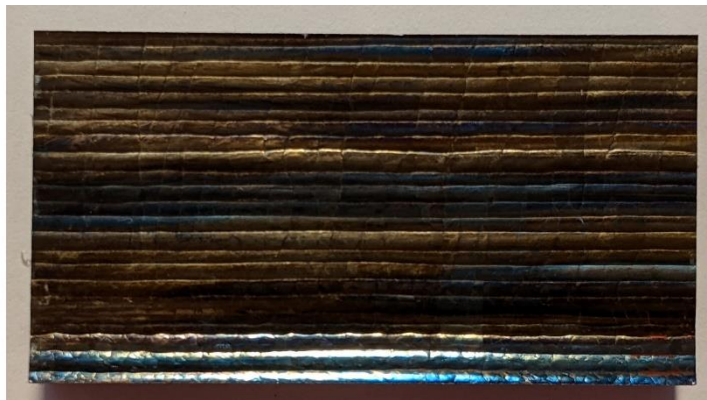


Figure 68 Photograph of the sidewall of an undeformed WAAM sample. The horizontal bands with changing colours were due to various thermal effects that occurred during the build. The subtle vertical lines were due to the large prior- $\beta$  grains. This sample was 40 x 20mm.

#### 3.6.4.2. Results

Figure 69 shows the data collected using the SRAS-Qt system from the as-deposited surface of the SLM sample in Figure 67. As the primary aim of this build was maximising bulk density, a simple raster scan strategy was used to build this part. This was reflected in the velocity data set in Figure 69 (a). Some data loss was observed in the top right and bottom left corners of the sample, due to a change in surface form across the sample (see section 5.3.1.1). This roll-off was also observed in the same positions of the signal amplitude data set in Figure 69 (b). On top of this clear striations can be seen in the signal amplitude data set, going from the top left to the bottom right. This pattern was not visible in a majority of the velocity data, except for the regions where the roll-off occurred, some faint striations can be observed.

Table 16 SRAS System specifications for large AM sample on SRAS-Qt

<b>Detector</b>	Quartet	<b>Spot size</b>	30 $\mu\text{m}$
<b>Wavelength</b>	81.98 $\mu\text{m}$	<b>Patch size</b>	1000 $\mu\text{m}$
<b>Step size (x)</b>	250 $\mu\text{m}$	<b>Step size (y)</b>	200 $\mu\text{m}$
<b>Sample size (x)</b>	40 mm	<b>Sample size (y)</b>	10 mm
<b>Segments (x)</b>	160	<b>Segments (y)</b>	50

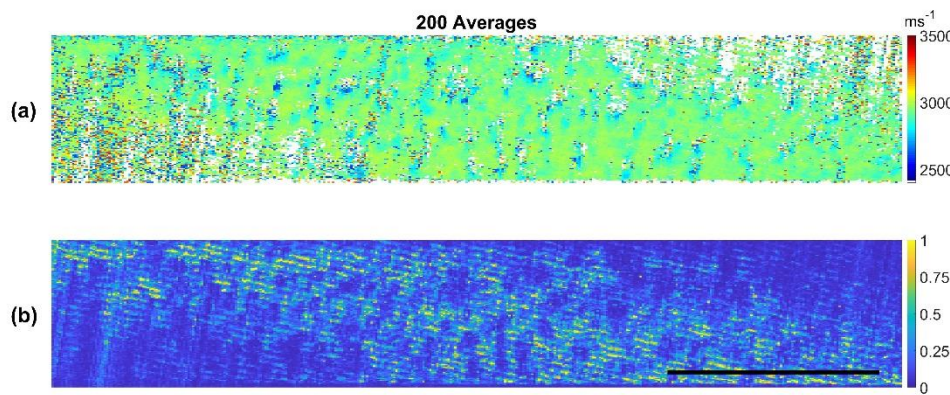


Figure 69 Images of SRAS data obtained using the rough surface SRAS-Qt system of the as-deposited surface of the large AM sample where (a) illustrates the acoustic data and (b) the signal amplitude. The black scale bar represents 10 mm.

Moving across from SLM to a different AM process, Figure 70 row (a) illustrates the velocity maps and signal amplitude obtained from the sidewall of an as-deposited WAAM sample. The two velocity maps, in this case, illustrate the SAW propagating in two orthogonal directions (up-down and left-right). In this figure, it was clear to see the large prior- $\beta$  grains growing vertically. Moving across the sample, the change in SAW velocity illustrated the presence of several grains with varying crystal orientations. The horizontal lines with drops in velocity and increased noise were due to a drop in optical return caused by the waviness of the sample surface, due to the layer-by-layer deposition process of WAAM. This phenomenon was more clearly visible in the signal amplitude data illustrated in Figure 70 row (b).

Table 17 SRAS System specifications for large AM sample on SRAS-Qt

<b>Detector</b>	Quartet	<b>Spot size</b>	30 $\mu\text{m}$
<b>Wavelength</b>	81.98 $\mu\text{m}$	<b>Patch size</b>	1000 $\mu\text{m}$
<b>Step size (x)</b>	100 $\mu\text{m}$	<b>Step size (y)</b>	100 $\mu\text{m}$
<b>Sample size (x)</b>	40 mm	<b>Sample size (y)</b>	15 mm
<b>Segments (x)</b>	400	<b>Segments (y)</b>	150

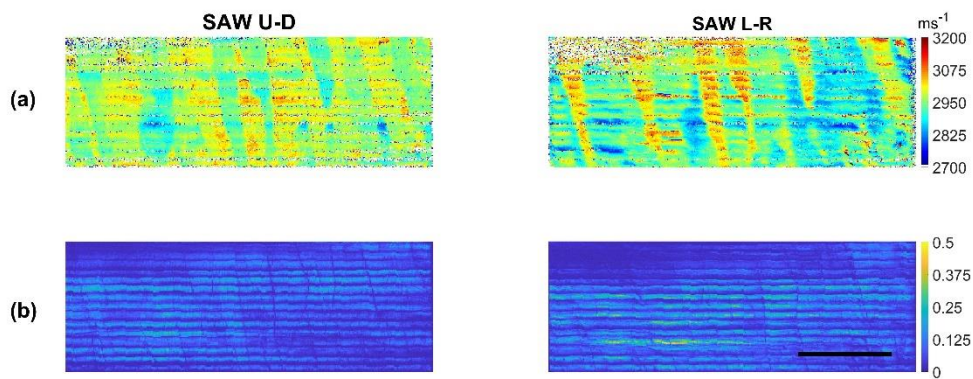


Figure 70 Images of SRAS data obtained using the rough surface SRAS-Qt system of the sidewall of an undeformed WAAM sample where row (a) showed the acoustic data and row (b) the signal amplitude. The black horizontal scale bar represents 10 mm.

#### 3.6.4.3. Discussion

The velocity map obtained off the as-deposited SLM sample in Figure 69 showed good velocity data across the entire surface of the sample. There was some loss of velocity data on the top right and bottom left of the sample. This was due to how uneven the top surface was. This change in height was outside the depth of focus the Quartet was capable of handling. This roll-off was also observed in the signal amplitude.

It was demonstrated in the previous sections that the smooth surface SRAS system was unable to resolve individual grains on AM samples manufactured using SLM. The SRAS-Qt system had an acoustic spatial resolution of 500  $\mu\text{m}$ , as its generation patch was 1 mm. For this reason, any variations detected using this system were more global changes to the microstructure similar to those seen in Figure 54 (a).

A series of short diagonal striations were observed in the corners of Figure 69 (a) along with noisy velocity data. These striations were more prominent across all of Figure 69 (b). This, in a similar manner to Figure 60 (a), was due to the power of the detection laser changing over time. This was assumed to be related to the temperature of the laser head, where it reduced its power output as the temperature increased. This variation in power showed no influence across the majority of the velocity data.

The two regions with low signal amplitude (top right and bottom left), showed increased noise in the acoustic data. This was due to a drop in optical return in these regions caused by the surface form of the sample (i.e. the surface sloping away). The lower optical return resulted in lower signal amplitude and thereby more noisy velocity data.

Due to the roughness of the as-deposited surface, more light was reflected away from the collection lens of the system, this meant that on the most challenging surfaces, the system

was close to the minimum limit of light required for the detector to function properly. This was not an issue in the smooth surface EMDA system as it only worked on optically smooth surfaces. Furthermore, the EMDA system had a reasonable amount of excess detection laser power which meant that it was less susceptible to such changes.

Now moving on to the more challenging surfaces of WAAM samples, It was clear that the waviness of the surface had a significant impact on the volume and quality of data collected. The dips in the surface visible in Figure 68 as horizontal lines, were due to the layer-by-layer deposition of the WAAM process. The drastic gradient in between each of these layers moved the reflected detection light cone away from the optical etendue of the detection system, this caused a loss of signal illustrated by the drop in signal amplitude in Figure 70 row (b). This in turn provided unreliable velocity which was filtered out.

Unlike the as-deposited SLM samples discussed above, the sidewall of the WAAM sample showed distinct changes to the SAW velocity in Figure 70 row (a). These changes corresponded to the large prior- $\beta$  grains observed on the prepared WAAM samples discussed in the literature [34]. As these grains were larger than 100  $\mu\text{m}$ , it meant that as discussed in section 3.3, SAW measurements from two orthogonals provided an understanding of the crystal orientation in these samples. Due to titanium having hexagonal crystals, it meant that the green areas in Figure 71 had the crystal orientated vertically, and red meant the crystal was orientated in the horizontal direction.

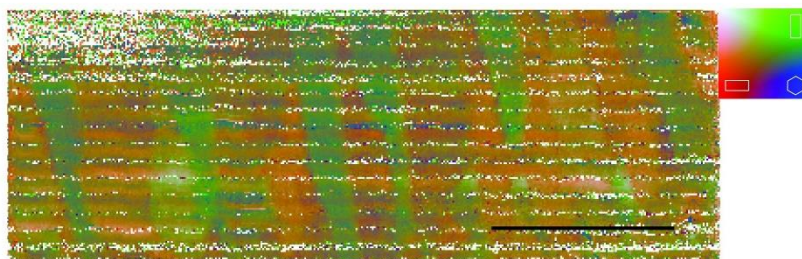


Figure 71 Vector map of the surface of a Ti64 WAAM sample, generated using SAW velocity data from two orthogonal directions ( $0^\circ$  and  $90^\circ$ ) where the RGB colours provide an idea of the crystal orientation.  
The black scale bar represents 10 mm.

## 3.7. Conclusion

This section summarises the conclusions drawn based on the work carried out within this chapter.

### 3.7.1. Calibration

Initially, the basic concepts of SRAS, how it works and how the systems are calibrated were presented. This was followed by a demonstration of the full capability of SRAS using a titanium sample with large grains. Here the optical, velocity and signal amplitude data sets obtained for a SRAS system was presented. The ability of SRAS to measure the SAW velocity of an individual grain on a sample with large grains was demonstrated.

### 3.7.2. SRAS on prepared AM

Using prepared AM samples, it was demonstrated how surface defects such as cracks and pores can be detected, measured and classified. This was due to the relatively high ( $\sim 10 \mu\text{m}$ ) optical resolution of the current generation smooth surface SRAS systems. This data was used to understand the cause of and identify regions with increased porosity.

Based on the current generation SRAS systems, it was clear that the grain size of SLM ( $\sim 25 \mu\text{m}$ ) was below the spatial resolution of the SRAS acoustic data. This meant that individual grains could not be imagined as they were on relatively large-grained samples. For this reason, several methodologies were developed to enhance the detected changes in microstructure.

The spatial filter method enhanced the global changes in the measured velocity which showed clear correlations with the scan strategy used to build the part. At a smaller scale, the watershed method was able to isolate local changes to SAW velocity. This method was geared towards the arrival of higher resolution SRAS systems that would be able to detect small clusters of grains with the same crystal orientation.

This was progressed further by specifically altering the scan strategy using the part geometry. The effect of short scan lines within the scan strategy was linked to the measurement of high SAW velocities (in the up-down direction) within the built part. This was correlated to a [001] crystal orientation using EBSD. This demonstrated the capability of SRAS to detect subtle changes to the scan strategies used to build the part and its effect on the crystal orientation.

As a final investigation into the capabilities of SRAS on prepared AM samples, the concept of epitaxial growth within SLM was explored. Using SRAS data it was shown that the AM

component built mirrored the crystal orientation of the seed crystal for the first few layers. This was verified using EBSD where the seed crystal and the first few layers of the AM sample had a [001] crystal orientation.

### 3.7.3. Transition to Rough Surfaces

Using the smooth surface SRAS system and a surface roughness comparator, the effect of surface roughness on the velocity, optical and signal amplitude was shown. It was clear that the capability of the smooth surface system was limited to a maximum of  $\sim 0.05 \mu\text{m Ra}$ . Using the rough surface SRAS system equipped with a Quartet detector, it was shown how the capability was extended to samples with a roughness of  $\sim 0.8 \mu\text{m Ra}$ . The detailed subject of surface roughness and its effect on an optical inspection is discussed further in section 5.3.1.3.

### 3.7.4. SRAS on as-deposited AM

The rough surface capability of SRAS was demonstrated using the as-deposited surface of an SLM sample and a SRAS system equipped with a Quartet detector. No change to the SAW velocity was detected due to the reduced resolution of the rough surface SRAS system and the small grain size of SLM. This however did demonstrate the capability of the SRAS-Qt system to inspect a surface with a surface roughness of  $0.44 \mu\text{m Ra}$ .

The further capability of SRAS was demonstrated using the as-deposited sidewall of a WAAM sample. In this case, it was clear that the small-scale roughness of  $0.069 \mu\text{m Ra}$  had no impact on the optical inspection taking place. Instead, the waviness of  $1.077 \text{ mm wavelength}$ , due to the build layers caused drops in the optical return and thereby SAW velocity measured. This is discussed further in section 5.3.1.2.

### 3.7.5. Summary

In summary, this chapter utilised the existing generation SRAS instruments to inspect both the prepared and the as-deposited surface of several SLM and one WAAM sample. It was shown that on the prepared surface of AM samples how surface defects down to  $\sim 10 \mu\text{m}$  could be detected, sized, counted and classified. It was clear that the resolution of the smooth surface SRAS system ( $\sim 100 \mu\text{m}$ ) was not low enough to detect individual AM grains ( $\sim 25 \mu\text{m}$ ). Two methodologies were developed to improve the detection of microstructure within AM samples. The spatial filter method successfully enhanced global changes within the component whilst the watershed method outlined the local changes to the microstructure. This was followed by the correlation of the microstructure changes detected

using SRAS with EBSD data. The final prepared surface experiment demonstrated the capability of SRAS to detect epitaxial growth within AM components. This was also verified using EBSD.

The transition to the as-deposited surface using the surface roughness comparator showed how the smooth surface SRAS system was limited to  $\sim 0.05 \mu\text{m}$  Ra. The capability of the rough surface SRAS-Qt system to inspect surfaces up to  $\sim 0.8 \mu\text{m}$  Ra was demonstrated. This was progressed further by inspecting the as-deposited surface of an SLM sample of  $0.44 \mu\text{m}$  Ra. Finally, the extremely challenging surface of a WAAM sample was inspected. This had a surface roughness of  $0.059 \mu\text{m}$  Ra and a waviness of  $1.067 \text{ mm}$  wavelength.

Due to the limitations of the AM processes used the samples inspected within this thesis were relatively small. The size of the samples that could be inspected using SRAS was only limited by the maximum travel of the translation stages used. This was partly demonstrated by the relatively large titanium sample of  $\sim 16 \text{ cm} \times 8 \text{ cm}$  in Figure 44.

Furthermore due to the nature of the defects within AM samples, combined with the other challenges found within AM the work, within this thesis was primarily focused on surface defects. Within the literature, however, Smith et al. and Brown et al. demonstrated the capability of SRAS to detect subsurface defects on AM components and the effects of machine induced grain distortion up to  $\sim 50 \mu\text{m}$  below the surface respectively [151], [184].

Although still early in its development, the literature reviewed in section 3.3.1 followed by the work carried out within this thesis demonstrated the capability of SRAS as an ideal candidate to be used as part of the in-process inspection of AM.

### 3.8. Future work

At the start of this chapter, a lot of work was carried out to demonstrate the capability of SRAS on the prepared surface of AM samples. The next logical step would be to progress this work onto the as-deposited surface of AM samples.

With this in mind, the following samples were designed to mimic various industrially relevant features. The bow tie sample in Figure 72 (left) aimed to mimic a relatively wide bottleneck section that would appear in a complex component. The heart pizza sample in Figure 72 (middle) was a combination of a triangle, square and circle, which was inspired by the unique microstructure observed in the triangle sample in Figure 59. Finally, the sample in Figure 72 (right) was designed to explore the effect of internal passages of various sizes and shapes.

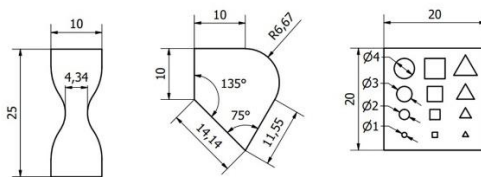


Figure 72 Schematic diagrams of bow tie sample to mimic a wide bottleneck (left), pizza heart sample to mimic a combination of various geometrical shapes (middle) and the various shaped passages sample to see the effect of narrowed regions around various geometrical samples (right).

The next set of samples designed were three cross-sections of a relatively small turbine or compressor blade found in a gas turbine engine. These were designed to mimic inspections taking place at three different stages of the build.

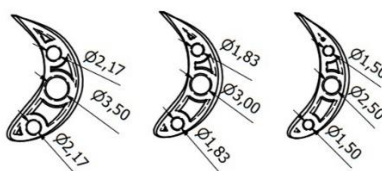


Figure 73 Schematic diagrams of three cross-sections of a small turbine or compressor blade, designed with a mostly thin-walled hollow structure and vertical cooling passages.

The final part was designed combining a range of ideas for thin walls with varying thicknesses and relative angles. These were combined into one sample to demonstrate the true capability of AM to manufacture components with extremely complex internal features. In tribute to the NDE technique used throughout this chapter, the sample was designed to spell out SRAS, as demonstrated in Figure 74. A preliminary data set off the as-deposited surface of this sample using the SRAS-Qt system was presented in Figure 45.

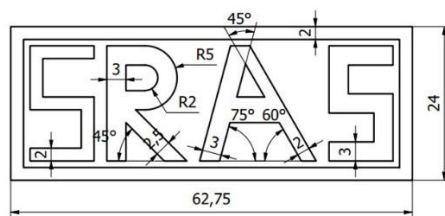


Figure 74 Schematic diagram of THE SRAS sample with several thin-walled internal structures with varying thickness and relative angles.

When manufacturing these samples, due to the influence of the scan strategy identified in previous sections of this chapter, two scan strategies were chosen. Two batches of the samples shown in Figure 72 were manufactured where one used a checkerboard/island scan strategy and the other used a simple meander/raster scan strategy. Evidence of this can be seen in Figure 75, on the samples manufactured using a checkerboard scan strategy, where square islands can be observed on the sample surface. Due to their complexity and thin walls, the samples in Figure 73 and Figure 74 were manufactured using a simple meander/raster scan strategy.

The future work planned for these samples was to be inspected using the SRAS-Qt system to detect changes to the SAW velocity and thereby microstructure caused by the changes to part geometry. The aim here was to further demonstrate the capability of SRAS as a technique for the in-process inspection of AM.

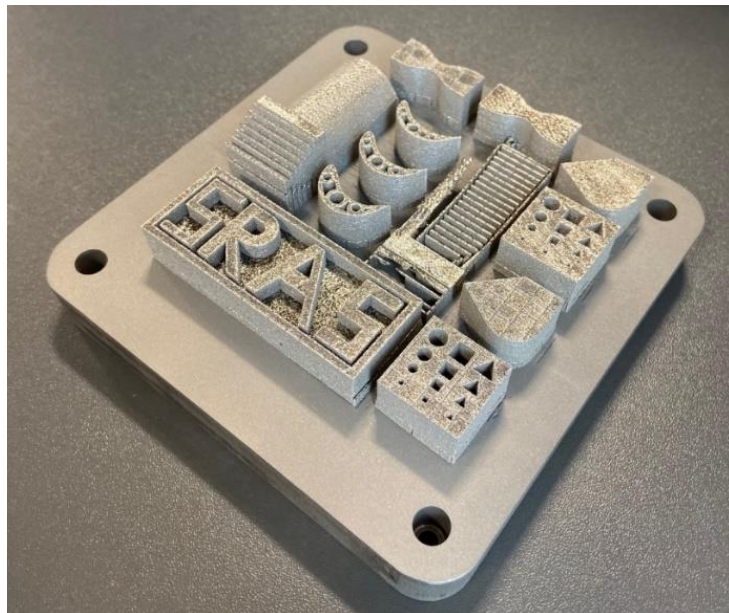


Figure 75 Image of samples manufactured for the further investigation of the capability of SRAS on the as-deposited surface of AM components.

The spatial resolution of the current generation rough surface SRAS systems was a limiting factor. Improving this would further improve the in-process inspection capability of SRAS. Another area that would require some improvement would be the SNR of the system when inspecting the as-deposited surface of AM samples. This could be achieved using a more focused (arcs focusing energy to the detection spot) generation pattern for the IR laser. For the same generation laser power, this would help improve the SAW amplitude detected. From a detection perspective, a higher power direction laser or detector with greater sensitivity could also improve the system SNR. Further improvements could be made by increasing the data acquisition rate of the system. This could be done by either the use of a higher repetition rate generation laser, faster mechanical scanning stage or the use of galvo mirrors and more optimised bespoke scanning software with adaptive resolution. Reducing the individual scan time would enable SRAS to move into the realm of real-time scanning in the future.

The SRAS technique is well-positioned to revolutionise the landscape of in-process inspection of AM processes. Its current limitations in terms of speed and resolution can be easily overcome with future generations of bespoke systems designed and built specifically for the in-process inspection of AM.

# **Chapter 4   Laser Induced Phased Arrays**

This chapter presents the work carried out using LIPA – an LU NDE technique used to detect internal features within metallic components proposed by Stratoudaki et al. [185]. This chapter initially outlines the need for and the difference between a LIPA and other LU inspections. It then discusses the theory behind LIPA and how it is implemented. Some initial LIPA results are presented and compared to both the CAD design of the part and the XCT data from the manufactured part. The work published by the author in Materials & Design, February 2020 forms the core results of this chapter [76].

## **4.1. Contributions to the Knowledge**

This chapter contributes to the knowledge by applying LIPA to additively manufactured components. It demonstrates the following capabilities and paves the way for new generations of in-process inspection techniques.

- Detection of internal features up to 26 mm deep inside an AM component.
- Detection of features with internal roughness.
- Measuring the geometrical accuracy (position) of internal features using LIPA data.

## **4.2. Introduction**

LIPA combines the concepts behind conventional phased arrays (see section 2.8.4) and LU (see section 2.9) to provide a completely non-contact and non-destructive NDE technique. This technique provides information regarding the cross-section of a given component and can be used to detect internal defects and or features. Within the CCM in section 2.10, Table

5, LIPA scored a relatively low score due to the literature having only shown evidence for its capability to detect one KPV – subsurface defects. In terms of integration, it was only considered an offline technique. However, as discussed in section 2.11, due to the non-contact and non-destructive nature of LU, LIPA had the same potential for implementation as part of an in-process inspection as the SRAS technique discussed in chapter 3. Furthermore, LIPA provided a complementary data set to SRAS which made them an excellent combination of LU techniques. This concept is discussed further in section 5.5.

When considering layer-by-layer processes such as AM, the ability to manufacture complex components with internal features comes with the burden of having to inspect them and ensure they are manufactured as designed. This is commonly carried out using post-manufacturing techniques such as XCT (see section 2.6.5) where high-energy electromagnetic rays are fired through the item being inspected onto a detector. The detected energy intensity is mapped as the part is rotated. These measured intensities are then combined using reconstruction algorithms, to create a 3D visualisation of the part being inspected. Compared to such an inspection, LIPA provides a relatively simple solution with the capability to image a slice across the sample.

Within this chapter, the potential for LIPA to be used as part of an in-process inspection is explored further. The capability of LIPA to detect internal features within an AM component manufactured using SLM is demonstrated. The further value of this dataset from a metrology point of view is explored.

### 4.3. Literature Review of Laser Ultrasonic Phased Arrays

The basic concept of laser ultrasonic phased arrays was initially proposed in 1968 by Lee et al. by spatially modifying a generation laser beam [186]. Based on this method, further work was carried out by Clark et al. to miniplate surface waves [187]. The SRAS technique discussed in chapter 3 was an evolution of this work. The next method considered was a temporal modification of a single laser pulse to steer the generated ultrasonic waves. Bruinsma et al. used individual fibres of different lengths as delay lines that steered the ultrasonic waves within the part being inspected [188]. Hopko et al. fabricated a fibre-based generation array with three individual elements, where each element consisted of seven 400 µm fibres [189]. This system was designed for generating ultrasound in the ablation regime for the real-time monitoring of weld quality [190]. The second method of temporal modification considered multiple laser sources. Murray et al. presented a 10 laser array capable of temporarily modifying a generation signal and demonstrated the capability of generating both a narrow

band surface wave and a steerable phased array [191]. Both the authors Murray and Noroy illustrated how the increase in signal amplitude was proportional to the number of elements [177], [192]. These methods, however, entailed extremely complex optical systems in the case of fibre-based systems and high costs in the systems that required multiple lasers.

An alternate method was the synthetic aperture focusing technique (SAFT) [193]. Here the generation and detection lasers were focused at the same point on the sample surface. As they are translated across the surface, the time domain waveforms are collected. These are summed for each point in the 2D imaging plane, based on the time delay  $t = 2d_i/v_L$  where  $d_i$  was the distance between the point in the 2D imaging plane and element  $i$  and  $v_L$  was the longitudinal wave velocity [194]. This method provided increased resolution when compared to conventional B scans. This was due to more information being collected from an array generation and detection, combined with the utilisation of the greater generation efficiency of longitudinal waves off-axis (see Figure 77) [195].

Stratoudaki et al. presented LIPA where both the generation and detection lasers were translated across the surface independently to capture the full matrix of generation and detection waveforms [185]. This was achieved using a simple experimental setup with two lasers. Capturing the full matrix meant that a wide range of imaging algorithms could be applied to the data set in post-processing. The authors used a version of the TFM algorithm which was adapted for LIPA and compared the results to simulated TFM, experimental SAFT and simulated SAFT. The results presented demonstrate how the TFM images were far superior to those generated using SAFT. The TFM images clearly showed indications from all of the features within the two samples inspected compared to the SAFT images where the indications were overshadowed by the noise. The sensitivity image showed a region with reduced sensitivity close to the back wall, away from the inspection surface at the centre of the array (see Figure 89). Consequently, this region of the TFM had increased noise. Although the array spacing was set based on a maximum frequency of 10 MHz. The authors were able to digitally filter the data for a wide range of frequencies below that. Using this method it was shown that the best SNR for this system was obtained in the region of 5 MHz.

The authors progressed this work further by correcting for the angular dependency of the generation and detection laser sources as part of the TFM [153]. By introducing two apodization terms the contributions from the generation and detection were weighted based on the directivity and sensitivity functions for each point in the 2D imaging plane. The apodized data presented showed improved SNR.

The work carried out within this chapter builds upon the LIPA technique discussed above to progress it towards becoming a useful and robust candidate for the in-process inspection of AM.

## 4.4. The Concept of LIPA

As discussed above Stratoudaki et al. presented the concept of LIPA where a phased array was artificially synthesised on the surface of the part being inspected [185]. This was carried out by individually collecting waveforms for each pair of generation elements  $N$  and detection elements  $M$  to form the  $N \times M$  array. This array is referred to as the full matrix and was discussed further within the context of conventional phased arrays in section 2.8.4.

		Generation							
		S <sub>11</sub>	S <sub>12</sub>	S <sub>13</sub>	S <sub>14</sub>	•	•	S <sub>1m</sub>	
Detection		S <sub>21</sub>	S <sub>22</sub>	S <sub>23</sub>	S <sub>24</sub>	•	•	S <sub>2m</sub>	
		S <sub>31</sub>	S <sub>32</sub>	S <sub>33</sub>	S <sub>34</sub>	•	•	S <sub>3m</sub>	
		S <sub>41</sub>	S <sub>42</sub>	S <sub>43</sub>	S <sub>44</sub>	•	•	S <sub>4m</sub>	
		•	•	•	•	•	•	•	
		•	•	•	•	•	•	•	
		S <sub>n1</sub>	S <sub>n2</sub>	S <sub>n3</sub>	S <sub>n4</sub>	•	•	S <sub>nm</sub>	

Figure 76 Image illustrating  $N$  number of generation elements and  $M$  number of detection elements that form the  $N \times M$  full matrix.

The collected full matrix is then imaged using TFM, which is an imaging algorithm where the focal laws are calculated for each point across the imaging plane/volume (this is typically done in a 2D imaging plane but can also be applied to a 3D imaging volume). The recorded signals are then time-shifted accordingly before they are summed for each point. This produces a 2D image where all points in the imaging plane are in focus [128]. This method assumes a flat geometry with a constant bulk wave velocity throughout the material. In the literature, Brown et al. discussed methods for carrying out ultrasonic phased array inspections on curved surfaces followed by Tant et al. who used time-of-flight data to approximate the locally anisotropic structure of a given material [196], [197].

The LIPA technique was presented as a couplant-free alternative to PAUT that was capable of inspecting areas with limited access, hazardous atmospheres, elevated temperatures and complex geometries [198], [199].

### 4.4.1. Laser Directivity and Sensitivity

LU generation is discussed in detail as part of section 2.9.1. In summary, a pulsed laser is focused onto the sample surface which causes local heating. This causes a thermal expansion and contraction which results in the generation of acoustic waves into the material. Most LU inspections use a laser spot that spreads the energy radially away from the centre. Within

these experiments, however, a line source was used to propagate the energy perpendicularly away from the line. This concept was illustrated elegantly by Millon et al. [150]. The angular dependence of the longitudinal wave amplitude  $G_L(\theta)$  and transverse wave amplitude  $G_T(\theta)$  from a laser generation source is calculated using Equation 13 and Equation 14 respectively [200]. In this case,  $C_L$  and  $C_T$  are longitudinal and transverse wave speeds respectively for the material being inspected. Within the thermoelastic regime, the ratio of radiated energy between transverse and longitudinal waves was 10:1 ( $k \sim 0.1$ ) [185]. For this reason, this experiment primarily focused on the use of transverse (shear) waves.

$$G_L(\theta) \propto \frac{\sin \theta \sin 2\theta (k^2 - \sin^2 \theta)^{1/2}}{2 \sin \theta \sin 2\theta (k^2 - \sin^2 \theta)^{1/2} + (k^2 - 2 \sin^2 \theta)^2} \quad \text{Equation 13}$$

$$G_T(\theta) \propto \frac{\sin 2\theta \cos 2\theta}{\cos^2 2\theta + 2 \sin \theta \sin 2\theta (k^2 - \sin^2 \theta)^{1/2}} \quad \text{Equation 14}$$

where

$$k = \frac{C_L}{C_T}$$

Laser detection is discussed in detail as part of section 2.9.1. In summary, a laser-based detection system is used to measure the out-of-plane displacement due to the ultrasonic waves within the sample. Unlike laser generation, the detection was heavily dependent on the surface texture of the part being inspected. Within the context of AM, this is discussed further in section 5.3.1. The sensitivity of a laser-based detection system for longitudinal waves  $D_L(\theta)$  and transverse  $D_T(\theta)$  waves is calculated using Equation 15 and Equation 16 respectively [201].

$$D_L(\theta) \propto \frac{\cos \theta (k^2 - \sin^2 \theta)}{F_0(\sin \theta)} \quad \text{Equation 15}$$

$$D_T(\theta) \propto \frac{\sin \theta (k^2 \sin^2 \theta - 1)^{1/2}}{F_0(k \sin \theta)} \quad \text{Equation 16}$$

where  $F_0(\xi) = (2\xi^2 - k^2)^2 - 4\xi^2(\xi^2 - 1)^{1/2}(\xi^2 - k^2)^{1/2}$

and  $\xi = \sin(\theta)$

Using the equations above the generation directivity (red) and detection sensitivity (green) to longitudinal and transverse waves are illustrated in Figure 77. It was clear that the longitudinal wave had a peak generation intensity at 60° from the vertical, compared to the transverse wave which peaked at ~30° from the vertical. Similarly, for detection, the longitudinal wave sensitivity peaked at 0° compared to the transverse wave which peaked at 36°.

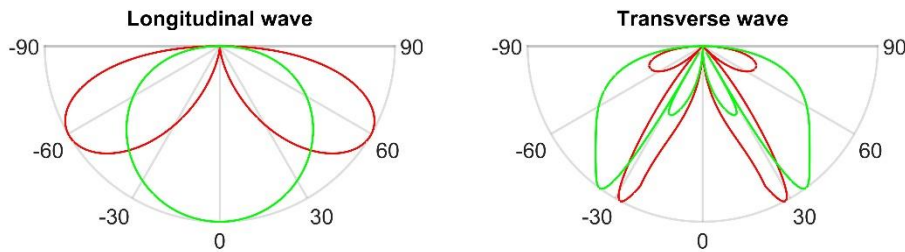


Figure 77 Polar plots of the generation directivity in red and detection sensitivity in green for the longitudinal and transverse waves where the radial axis illustrated the magnitude.

#### 4.4.2. Total Focusing Method for Laser Ultrasonics

TFM was originally developed for transducer-based phased arrays, with omnidirectional directivity. The LU generation directivity and detection sensitivity had an angular dependency as illustrated in Figure 77. Stratoudaki et al. discussed how the TFM algorithm has been adapted to account for this by introducing two apodization terms  $Z_g$  and  $Z_d$  [153]. The intensity of the TFM image,  $I(r)$ , is calculated using Equation 17.

$$I(r) = \sum_{g=1}^n \sum_{d=1}^n Z_g(\mathbf{r}) Z_d(\mathbf{r}) s_{gd}(t_{gd}(\mathbf{r})) \quad \text{Equation 17}$$

In this case, the double summation was over all of the generation  $g$  and detection  $d$  positions. The broadband excitation of LU meant that the data collected in the FMC contained information from all of the frequencies excited (see section 3.4.1.1) up to either the maximum frequency limited by the pulse width of the generation laser or the maximum frequency of the detector used.

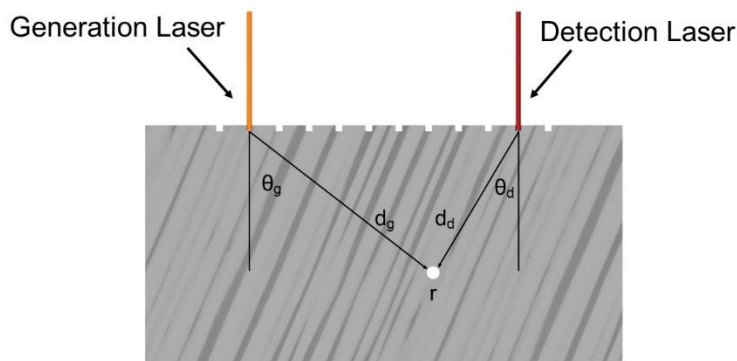


Figure 78 Schematic illustrating the target point ( $r$ ) within the 2D inspection plane, followed by the generation path length ( $d_g$ ) at an angle ( $\theta_g$ ) and the detection path length ( $d_d$ ) at an angle ( $\theta_d$ ).

The signal  $s_{gd}(t)$  was the digitally filtered time trace of the raw signals collected in the FMC. The time delay term ( $t_{gd}$ ) is calculated using Equation 18 for a transverse wave, where  $d_g(r)$  and  $d_d(r)$  are the respective distances of the generation and detection ray paths to the target point  $r$  within the inspection plane, illustrated in Figure 78.

$$t_{gd}(r) = \frac{d_g(r) + d_d(r)}{C_T} \quad \text{Equation 18}$$

The two apodization coefficients  $Z_g$  and  $Z_d$  were calculated using Equation 19 and Equation 20. In this case  $G_\alpha$  and  $D_\beta$  came from the directivity and sensitivity patterns in Figure 77 for laser generation and detection at angles  $\theta_g$  and  $\theta_d$  relative to the surface normal. Here the generation mode  $\alpha$  and detected mode  $\beta$  were substituted for longitudinal or transverse based on the wave mode used.

$$Z_g(r) = \frac{G_\alpha(\theta_g(r))}{[d_g(r)]^{1/2}} \quad \text{Equation 19}$$

$$Z_d(r) = \frac{D_\beta(\theta_d(r))}{[d_d(r)]^{1/2}} \quad \text{Equation 20}$$

The sensitivity within the 2D imaging plane is calculated using the following equation.

$$E(r) = \left| \sum_{d=1}^n \frac{G_\alpha(\theta_g(r))}{[d_g(r)]^{1/2}} \sum_{d=1}^n \frac{D_\beta(\theta_d(r))}{[d_d(r)]^{1/2}} \right| \quad \text{Equation 21}$$

Finally, the normalised image is obtained using the equation below.

$$N(r) = \frac{I(r)}{E(r)} \quad \text{Equation 22}$$

This provided a normalized TFM image with uniform sensitivity but non-uniform noise. This was due to the noise present in areas with low sensitivity getting amplified. This process is discussed further in the literature [185], [202].

## 4.5. Instrumentation

The nature of data acquisition required for FMC meant that both the generation and detection lasers needed to be translated freely across the surface of the sample being inspected. For this reason, unlike a majority of SRAS systems discussed in chapter 3, the sample was kept static and the generation and detection beams were translated independently. The generation laser used was an Inno Las Picolo1 ND:YAG IR (1064 nm) laser. This laser could go up to a 5 kHz repetition rate, with a maximum energy output of 80  $\mu\text{J}$ , maximum power of 400mW and a 0.8 ns pulse width. As discussed in section 4.4 the generation laser was focused into a line that was  $\sim 0.2$  mm wide and 5 mm tall.

The detection system used in this experiment was Polytech vibrometer with a 633 nm laser with an output power of < 1 mW. This system worked on the principle of laser doppler vibrometry as discussed in section 2.9.2.1 and was able to measure the out-of-plane displacement of the sample surface. This detector had an upper bandwidth limit of 24 MHz, which set the limit for the ultrasonic frequency captured. Due to the Polytech head being relatively small, it was directly mounted to a linear stage, which was used to translate the detection beam across the sample surface. The generation laser line was translated across the surface by mounting the final mirror and cylindrical lens on a linear stage. To accommodate the free movement of both the generation and detection lasers on the sample, the generation laser was incident on the sample surface at a slight angle of ~20°.

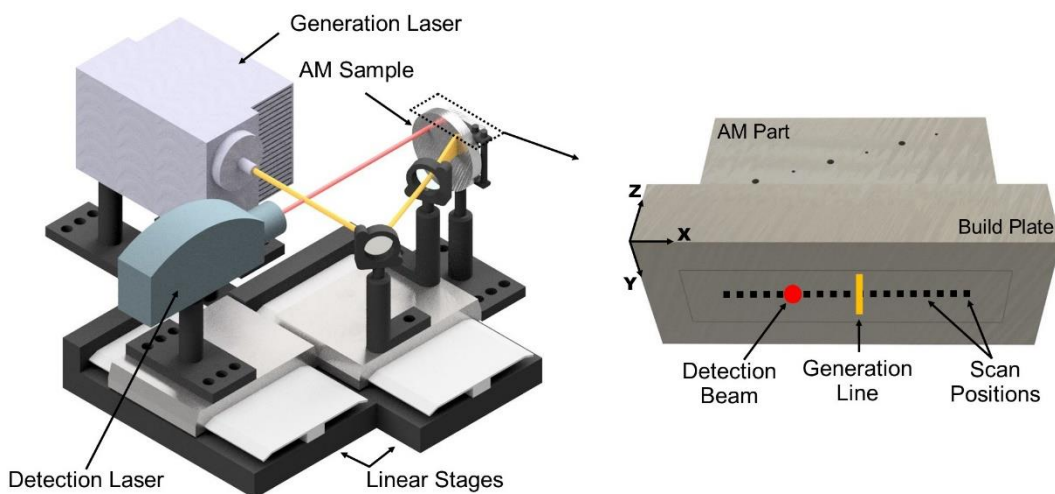


Figure 79 Schematic diagrams of the LIPA system (left) illustrating the IR generation laser, detection laser (Polytech vibrometer), linear stages used to translate the lasers across the sample surface and the AM sample. The underside of the AM sample (right) illustrating the generation line, detection beam and scan positions.

## 4.6. Methodology

This section discusses the sample design and how it was manufactured, followed by the experiment design and methodology used to inspect this sample using LIPA.

### 4.6.1. Sample Design and Manufacture

When designing the sample, the aim was to create internal features that mimic typical SLM characteristics such as internal surface roughness and backfilling. Mock side-drilled holes were chosen here to allow any unfused powder to drain out, as air-filled defects would provide better ultrasonic contrast than powder-filled cavities. The cylindrical shape of these holes provided the best case for demonstrating the potential of this ultrasonic method for defect detection. The uniform cross-section across the width was thought to give a clear indication of the location features in the XZ plane with very little influence from the Y

position. The features were sized to replicate internal features akin to cooling holes manufactured using processes such as SLM. The sample for this experiment was manufactured using the Realizer SLM50 AM platform and AlSi10Mg powder. This system was equipped with a 100 W CW laser at a wavelength of 1064 nm and had a usable build area of ~60 mm in diameter. This system was discussed further in section 3.5.

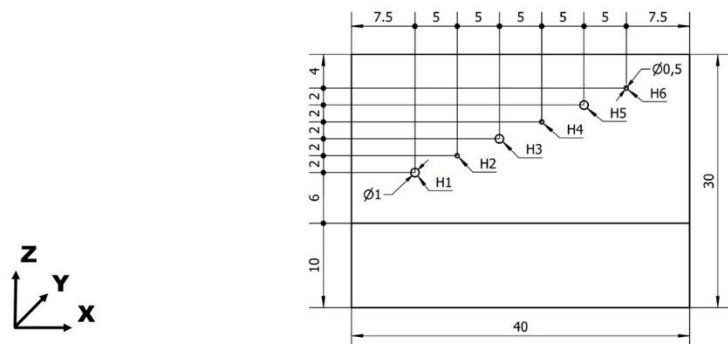


Figure 80 CAD drawing of the front elevation of the LIPA sample, illustrating the 10 mm thick build plate and AM sample that was 40 mm wide and 20 mm tall. The six holes were placed at an equal spacing of 2 mm on the Z-axis and 5 mm on the X-axis. The diameters of these holes alternated between 1 mm and 0.5 mm.

The sample was designed on top of the 10 mm thick Realizer build plate. Unlike other AM component inspections, this initial inspection was planned to be carried out on the underside of the build plate. To minimise the acoustic impedance mismatch, an aluminium alloy build plate was used alongside AlSi10Mg powder. The AM section of the sample was designed to be 20 mm tall, 40 mm wide and 10 mm thick. Within this section, six mock side-drilled holes were positioned at different depths. The first was 6 mm from the start of the AM section and the following holes were placed at increasing depths of 2 mm to each other. The holes were staggered along the X-axis with 5 mm between them, to avoid shadowing. The diameter of the holes was alternated between 1 mm and 0.5 mm. A pre-sinter scan strategy was used when building the parts to maximize the bulk density of the material, as described by Aboulkhair et al [203]. Once manufactured, the underside of the Realizer build plate had the threaded stub, used to screw into the AM system. This was milled away and the remaining flat surface was polished down to a mirror finish using the method discussed in section 3.5.1. This was to provide the best possible reflection for the detection laser. The manufactured sample is shown in Figure 81 where the 1 mm holes are clearly visible whereas the 0.5 mm holes are present but difficult to see.

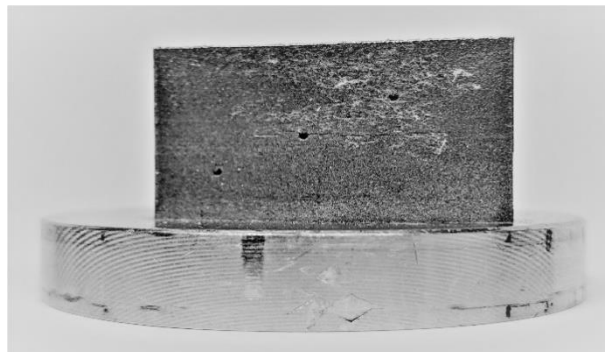


Figure 81 Picture of built LIPA AM sample on top of the 10 mm thick Realizer build plate. The three 1 mm holes are clearly visible whilst the 0.5 mm are difficult to identify. A small line of delamination can be observed about halfway up the AM section of this sample.

#### 4.6.2. Experiment Design

This experiment was approached in a slightly different manner to a majority of the other potential in-process inspections, reviewed in section 2.6. Instead of taking on the challenge of the surface roughness along with a wide variety of other challenges on the as-deposited side of an AM sample, this experiment was conceptualised to inspect the underside of the build plate. Figure 82 attempted to illustrate this concept where the build laser would be aimed at the top of the part being built. The LIPA system would be contained below the build plate, away from the harsh environments within the build chamber, and be free to carry out any inspection required without impeding the build.

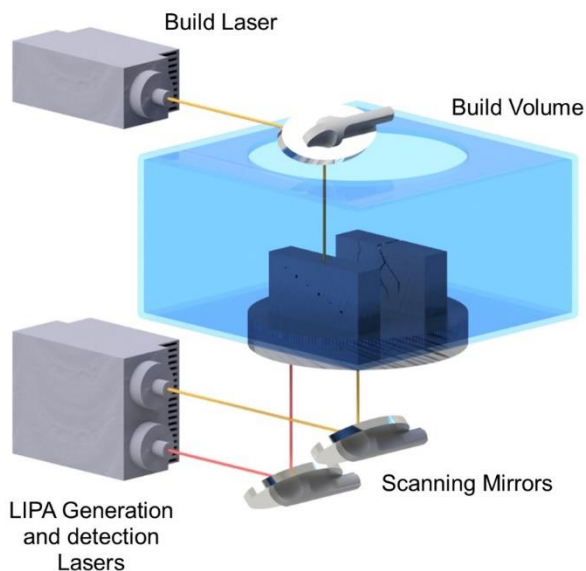


Figure 82 Schematic illustrating the build volume containing the part being built, the build laser aimed at the top of the part controlled using a scanning mirror, the LIPA generation and detection lasers, aimed at the underside of the part controlled using another pair of scanning mirrors.

With this concept in mind, a 1D LIPA with 129 elements was synthesised on the underside of the AM sample. As described in section 4.4 this was carried out using FMC where the

generation and detection lasers were scanned in turns. Once a row of signals where the position of the generation laser was varied was collected, the detection laser was incremented by the width of an element. This process was repeated for 129 elements to build up the  $129 \times 129$  element matrix required for FMC. Each waveform was obtained using 500 averages to improve the SNR. The element spacing was set to half the shear wave wavelength to avoid grating lobes, based on the Nyquist sampling criterion [204]. Using Equation 8, for a shear wave velocity of 3100 m/s in aluminium, at 8 MHz, the wavelength was calculated to be 387.6  $\mu\text{m}$ , based on this the element spacing was set to 194  $\mu\text{m}$ .

## 4.7. Results

The following section presents the results obtained from the LIPA system discussed above. This is followed by the XCT results collected to help verify the LIPA data.

As discussed in the experimental design above, the element spacing was set to provide a maximum frequency of 8 MHz. An initial test data set was obtained using a small array of 21 elements. The non-normalised TFM datasets from this test array is presented in Figure 83. Due to the broadband nature of LU, and as discussed in section 4.4, a bandpass filter was applied to the data in the frequency domain to maximise the SNR. Based on the seeded defect diameters of between 0.5-1 mm the digital filtering was used to process the data with centre frequencies between 2-5 MHz with a bandwidth of 50% for each centre frequency. These images have a non-uniform sensitivity and uniform noise.

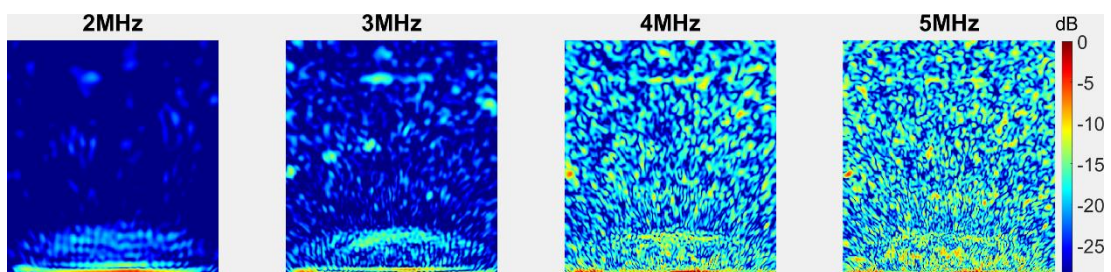


Figure 83 TFM images using a small test array of 21 elements presented at centre frequencies of 2,3,4 and 5 MHz using transverse (shear) waves for generation and detection. These images were obtained directly from the TFM imaging Equation 17 and have not been normalised, and have a non-uniform sensitivity and uniform noise.

Based on the initial results in Figure 83 it was clear that some indication of the seeded defects could be observed in the 3 MHz data set. For this reason, all of the following LIPA data was presented at 3 MHz with 100% bandwidth at -40 dB. This was because, at 3 MHz, the wavelength for the shear wave was calculated to be 1 mm and was assumed to be well suited to detect the seeded defects within the part of 0.5-1 mm in diameter. The noise that appeared at higher frequencies was assumed to be due to several factors such as the

backscatter from the internal structures and the reduced energy and penetration depth as discussed in section 2.8.3.

Figure 84 shows the normalised TFM image where the bandwidth was limited to -10 dB to enhance the indications from the seeded defects. This normalised image has a uniform sensitivity but non-uniform noise. This was because, in the regions where the sensitivity was low (Figure 89), the noise was effectively amplified. The LU generation simultaneously excited both bulk and surface acoustic waves. This meant that there was a cross-talk region where the surface wave signals appeared along with the shear wave. In the LIPA results presented in Figure 84, this was observed in the first ~5 mm, which was still within the thickness of the 10 mm build plate. As there were no features of interest in this area, the effect of this cross-talk on the inspection taking place was negligible. The LIPA data in Figure 84 showed clear indications of holes 1-4 and 6 with a faint indication from hole 5 which was blended in with the noise. It was worth noting that the presence of this cluster of noise in the centre top region of the results figure did have the capability to trigger false positives.

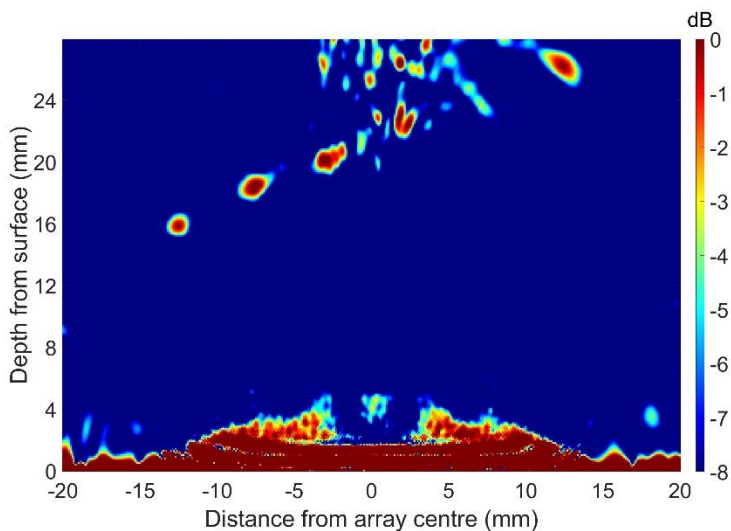


Figure 84 Normalised TFM image obtained using a 129-element array with an element spacing of 194  $\mu\text{m}$  and a centre frequency of 3 MHz using transverse (shear) waves for generation and detection.

Unlike previous work presented in the literature using LIPA – where the features detected were precision-machined into the part being inspected – this part was manufactured using AM, so the internal dimensions of the part could not be guaranteed to be the same as they were in the CAD. For this reason, XCT data was obtained at a voxel size of 30  $\mu\text{m}$  to verify the internal geometry of the AM part.

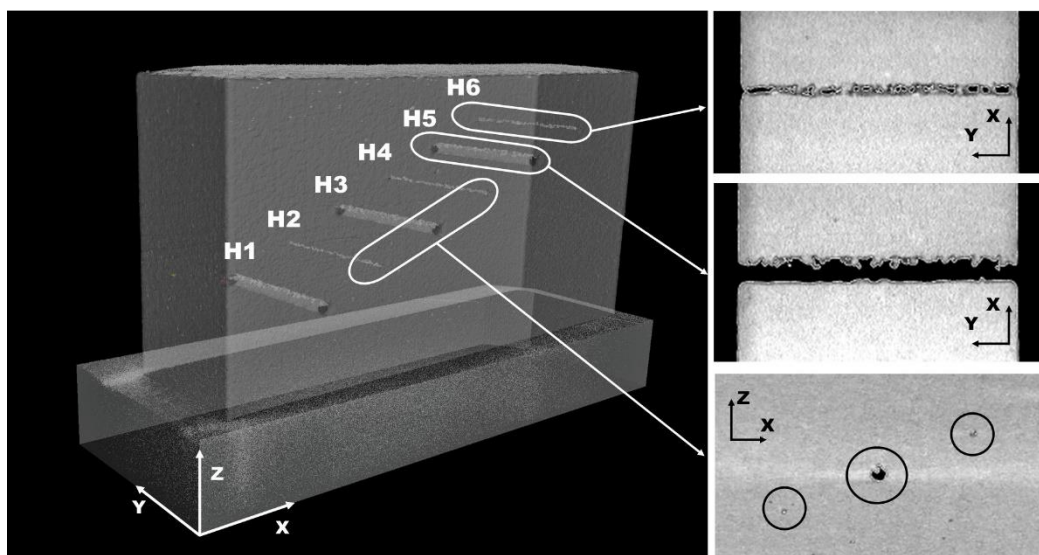


Figure 85 XCT data of the entire sample (left), with detailed vertical cross-sections of H6 (top right), H5 (middle right) and orthogonal cross-sections of H4, H3 and H2 (bottom right).

The XCT data presented in Figure 85 illustrates how the cross-section of the larger hole H5, expected to be 1 mm in diameter, was clear all the way through with some evident internal surface roughens. The smaller 0.5 mm diameter H6 hole showed some evidence of backfilling with a lot more internal roughness where some segments looked like they bridged the holes. The orthogonal cross-section of H4, H3 and H2 demonstrated a different perspective of the same phenomenon. This was similar to the picture of the built sample in Figure 81.

#### 4.8. Discussion

The results presented in Figure 84 showed how LIPA was capable of detecting nested features within AM components. The XCT data presented in Figure 85 verified the presence of these internal features. As part of an in-process inspection, however, the capability to size and measure these would elevate LIPA to a higher level when viewed as part of the CCM in section 2.10, Table 5.

Extracting measurements from one slice of the XCT data was considered inaccurate due to the aggressive internal roughness of the features. For this reason, the entire volume of the part was considered. As illustrated in Figure 86, best-fit cylinders were constructed inside each of the mock side-drilled holes. This method considered the entire length of the holes and averaged out the effect of the internal surface roughness, making the measured centre of the holes a surface-independent feature. This method also provided a diameter measurement that considered the entire length of the hole.

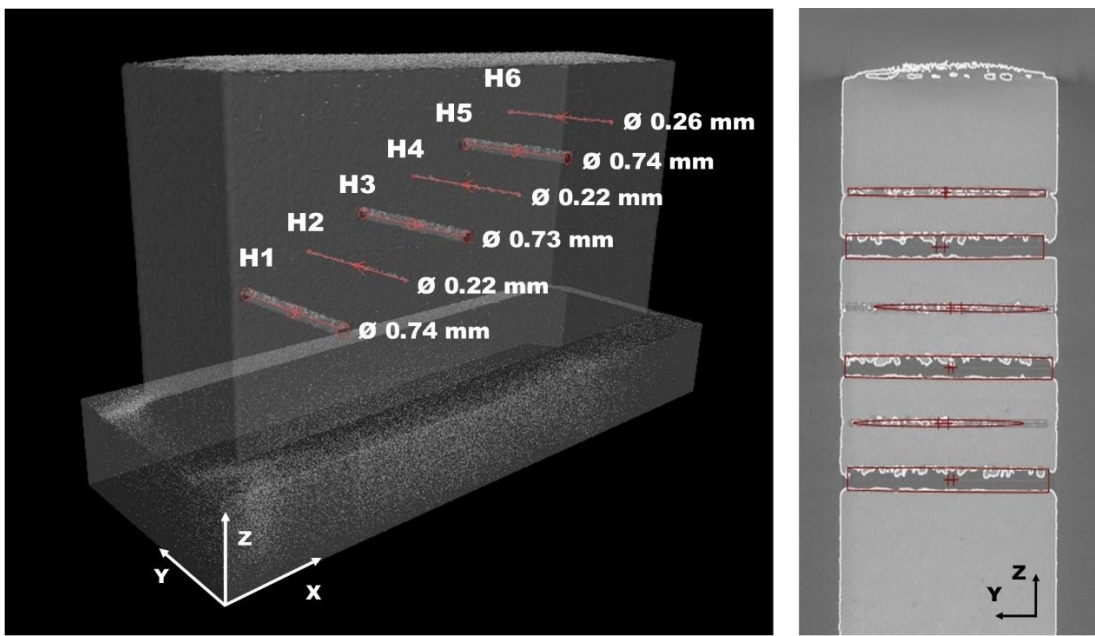


Figure 86 XCT data of the entire sample with the best-fit cylinders in red used for the diameter and position measurements (left) alongside the vertical cross-sections of all six holes superimposed onto one plane showing how the best-fit cylinders in red followed the internal part geometry (right).

On top of the diameters, the XCT data also provided location information of the holes, within the part volume. As there were no other obvious features that could be used to reference the measurements within the LIPA data in Figure 84, the position of H1 is considered as the origin (0,0) and used to measure the relative positions of the following holes. In the CAD drawing shown in Figure 80, the hole diameters alternated between 1 mm and 0.5 mm whilst the horizontal X-axis spacing was set to 5 mm and vertical Z-axis spacing was set to 2 mm. The XCT measurements in Table 18 showed how in terms of positioning the AM part was within  $\sim 0.1$  mm on the Z-axis and within  $\sim 0.5$  mm of the CAD on the X-axis. The hole diameters however were all undersized by up to  $\sim 0.28$  mm.

Table 18 Measurements extracted from the XCT data of the AM sample in millimetres.

Hole No	Diameter	Position X	Position Z	$\Delta X$	$\Delta Z$
1	0.74	0	0	0	0
2	0.22	4.98	2.00	4.98	2.00
3	0.73	9.96	3.96	4.97	1.95
4	0.22	14.90	6.06	4.95	2.10
5	0.74	19.88	8.02	4.97	1.97
6	0.26	24.87	10.12	4.99	2.10

When sizing the indications from the LIPA data, a combination of the -6 dB drop and the method developed for the SRAS data in section 3.6.2 to detect and size mechanical defects

were used. A -6 dB drop was used to define the outer perimeter of the indications as illustrated in Figure 87. This was followed by further image processing where object analysis was used to individually identify each indication and its distinct properties such as the area, diameter and position.

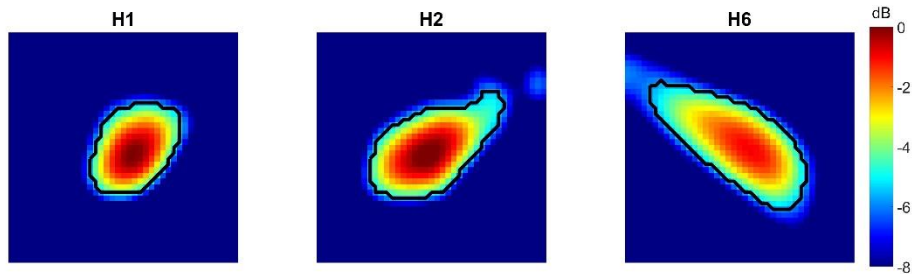


Figure 87 Three zoomed images of the H1, H2 and H6 form the LIPA data illustrating the premier outline obtained using the -6 dB method used to obtain the position and location of the indications.

The features H1, H2 and H6 were chosen to be presented as examples in Figure 87 as they were the clearest indications in the LIPA data presented in Figure 84. The features H3, H4 and H5 were distorted due to the noise in the top centre region of the LIPA dataset. The data presented in Table 19 shows how compared to the dimensions in the CAD, the measured diameters were oversized by ~1.1 mm in the most extreme case of H6. Similarly, the measured positioning of the holes had variations of up to ~0.7 mm on the Z-axis and ~1.1 mm on the X-axis.

Table 19 Measurements extracted from the LIPA data of the AM sample in millimetres.

Hole No	Diameter	Position X	Position Z	$\Delta X$	$\Delta Z$
<b>1</b>	1.04	0.00	0.00	0.00	0.00
<b>2</b>	1.36	4.90	2.50	4.90	2.50
<b>3</b>	1.41	9.80	4.30	4.90	1.80
<b>4</b>	1.36	14.60	7.00	4.80	2.70
<b>5</b>	1.38	18.70	9.10	4.10	2.10
<b>6</b>	1.60	24.80	10.30	6.10	1.20

Due to the inherent changes that occurred during the AM build process, it was unfair to compare the measurements obtained using LIPA to the values from the CAD. For this reason, Table 20 compares the measurement data from XCT, now used at a datum, to the measurements from the LIPA data.

Table 20 The difference in measurements between the XCT data and LIPA data.

Hole No	$\Delta$ Diameter	$\Delta\Delta X$	$\Delta\Delta Z$
1	0.30	0.00	0.00
2	1.14	0.08	-0.50
3	0.68	0.07	0.15
4	1.14	0.15	-0.60
5	0.64	0.87	-0.13
6	1.34	-1.11	0.90

It was clear that the LIPA technique was unable to accurately size the holes. This was due to the wavelength of the shear wave at a frequency of 3 MHz being  $\sim 1$  mm. The holes that were sized to be between 0.5 and 1 mm in diameter were measured using XCT to be about 0.22 and 0.73 mm. This meant that they were close to the diffraction limit of  $0.5 \lambda$  which made accurate sizing and characterisation difficult [205], [206]. Furthermore as seen in the XCT data in Figure 85 and Figure 86, it was clear that the holes were not a consistent diameter all the way through. Instead, they consisted of extremely rough internal surfaces and in some cases physically bridged across the holes.

More accurate defect classification could be carried out by comparing the predicted and measured scattering coefficients, but this was outwith the scope of this project and covered in the literature [207]. More optimized data acquisition and imaging of the individual defects would also aid the sizing and classification of these features as discussed by Lukacs et al. [208].

Now considering the position measurements between XCT and LIPA, it was clear that the LIPA technique was able to detect the positions of the holes H1, H2, H3 and H4 within  $\sim 0.15$  mm in the X-axis and  $\sim 0.6$  mm in the Z-axis. As illustrated in Figure 88 the methodology applied to identify the positions of the holes, misidentified H5, shown by the black circle. It however is clear that there was some indication in the region where H5 was expected to be when considering the white circle for the XCT measured position for H5 in Figure 88. The misidentification was due to the noise amplitude in that region giving a slightly higher amplitude than that of the actual hole. Similarly, H6 which as manufactured was a 0.26 mm diameter hole, provided one of the biggest indications in the LIPA data and was measured to have a diameter of 1.34 mm.

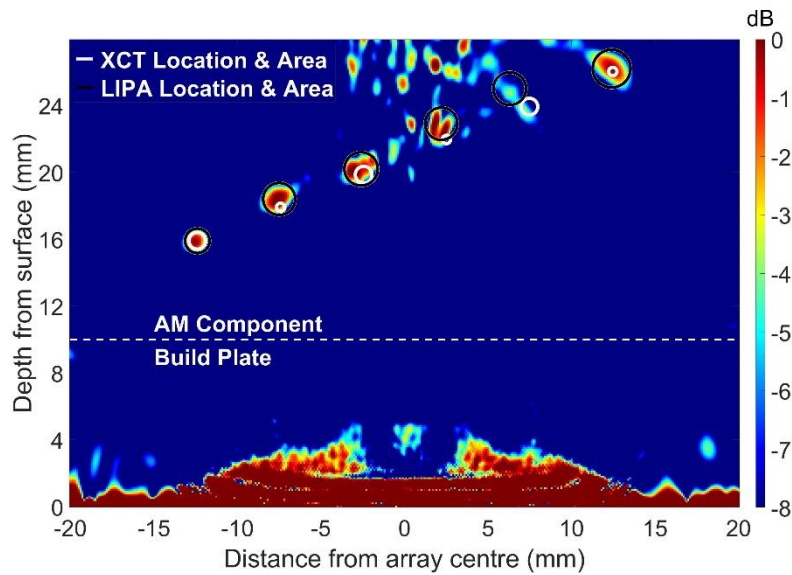


Figure 88 Image of LIPA TFM data with an overlay of the build plate and AM component, where the black circles represent LIPA indications and white circles show the hole locations detected using XCT. The diameter of both sets of circles is proportional to the area measured.

Based on Equation 21 the image presented in Figure 89 illustrated the expected amplitude from a perfect point target as a function of position. This was due to the directivity and sensitivity of the generation and detection lasers illustrated in Figure 77. The region above 20 mm in the centre of the array in blue shows how there was a drop sensitivity. This effectively created a blind spot where due to the drop in sensitivity the noise was amplified.

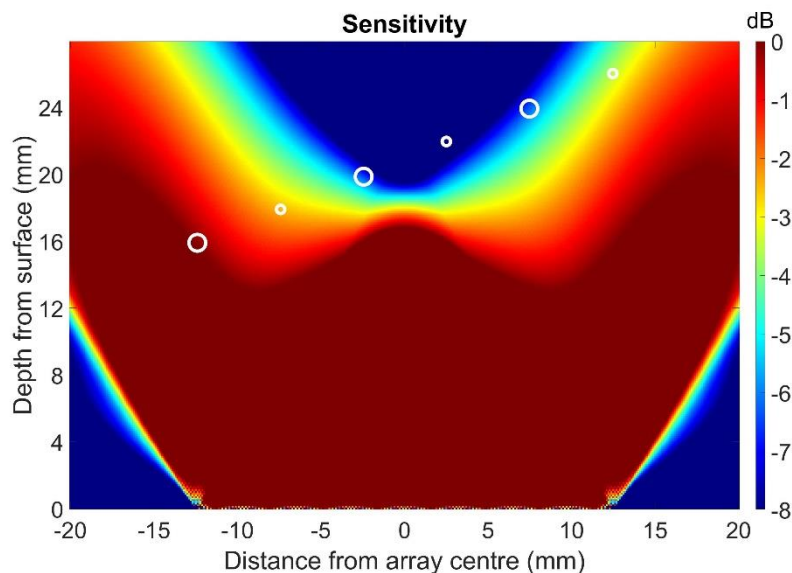


Figure 89 Image of LIPA sensitivity map due to the directivity and sensitivity patterns of the laser-generated and detected shear waves showing the expected amplitude from a perfect point target as a function of position. The white circles show the hole locations detected using XCT.

This was the reason why a prominent cluster of noise was observed in the LIPA data in Figure 84, around the indications of H3, H4, H5 and H6. These lay in the region of relatively low sensitivity, compared to H1 and H2. Especially in the case of the position measurement of

H5, reduced sensitivity and increased noise was part of the reason why the location was incorrectly identified. In the case of H6, the indication was oversized for this same reason. As a method of overcoming this, Lukacs et al. presented an optimised methodology referred to as selective matrix capture (SMC) [208]. Here the author's used prior knowledge from a large array, as presented in this thesis, to create a more optimised array for the detection of the various defects and features, based on the directivity and sensitivity patterns in Figure 77.

Due to the nature of XCT, although it was a good technique for the verification of LIPA data, it was not a like-for-like comparison. For this reason, a conventional PAUT probe at 10 MHz with 128 elements was used to collect the dataset presented in Figure 90. Not seen in the LIPA data the PAUT data was able to detect a band of microporosity in the region just above the build plate. This was caused by the steep thermal gradients that typically occur at the start of a build. The PAUT also picked up another region  $\sim$ 18 mm into the component. This was delamination that was visible on the sidewall of the built part in Figure 81. This data set provided a snapshot of the capability of the future generation LIPA systems.

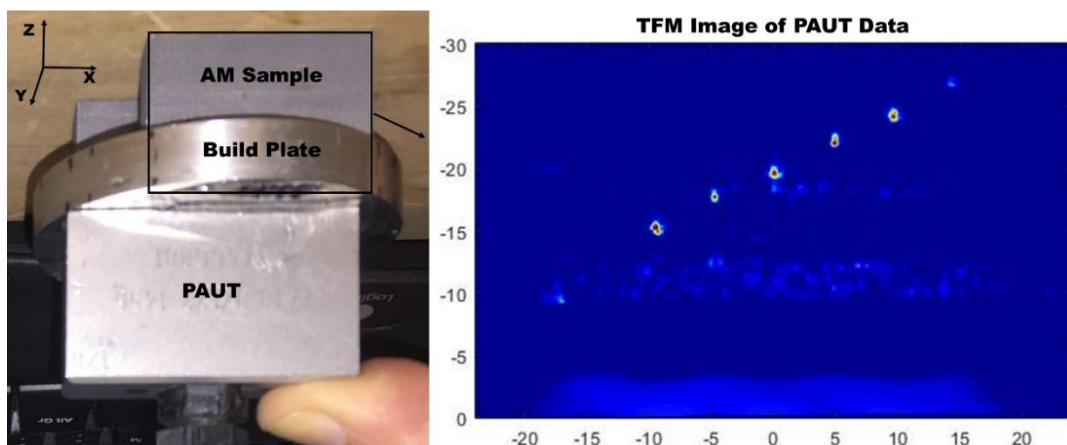


Figure 90 Experimental setup of PAUT probe placed on the underside of the build plate (left). TFM data from the AM sample clearly illustrates all six through holes with a lower intensity indication from the furthest away feature at 26 mm (right).

#### 4.9. Conclusion

This section summarises the conclusions drawn based on the work carried out within this chapter.

It was initially demonstrated that the LIPA technique was capable of providing cross-sectional information from an AM sample, obtained in a non-contact, non-destructive manner. This was followed by the capability to detect features as small as 0.22 mm in diameter with a significant amount of internal roughness.

LIPA data, when compared to XCT, demonstrated the capability to successfully locate nested features within a given component up to 26 mm deep and to an accuracy of  $\sim$ 0.5 mm.

The current generation LIPA was unable to accurately size the detected features due to the limitations in SNR. This could be solved using a wider array with more elements, higher power generation and detection lasers and the use of other combinations of wave modes.

The current generation of LIPA data acquisition is relatively slow. The data presented above took close to 3 hours to acquire. The use of higher repetition rate generation lasers would directly impact the data acquisition time. Higher power detection lasers along with more sensitive detectors would also reduce the number of averages required and thereby reduce the total time required for the inspection.

Finally, the conventional PAUT data presented showed the future potential for LIPA. As the inspection resolution increases, data acquisition and processing time decreases and rough surface capabilities develop further, LIPA is well-positioned to provide extremely valuable inspection capabilities as part of an in-process inspection of AM.

## 4.10. Future work

This chapter demonstrated the capability of LIPA to detect internal features up to 26 mm below the sample surface, in a non-destructive non-contact manner. This work however was carried out on the prepared underside of the AM sample. The next step as part of the progression towards an in-process inspection would be carrying out the same inspection on the rough/as-deposited side of the AM sample. This would require the design and build of a new system equipped with a rough surface laser ultrasonic detector. Such a system could then carry out and improve on the work carried out within this chapter.

This chapter demonstrated the ability of LIPA to detect and position several features within the component. Following this, the aim was to investigate further the limitations of this capability. The following sample was designed and manufactured using AM to explore the limitations of the current generation LIPA systems.

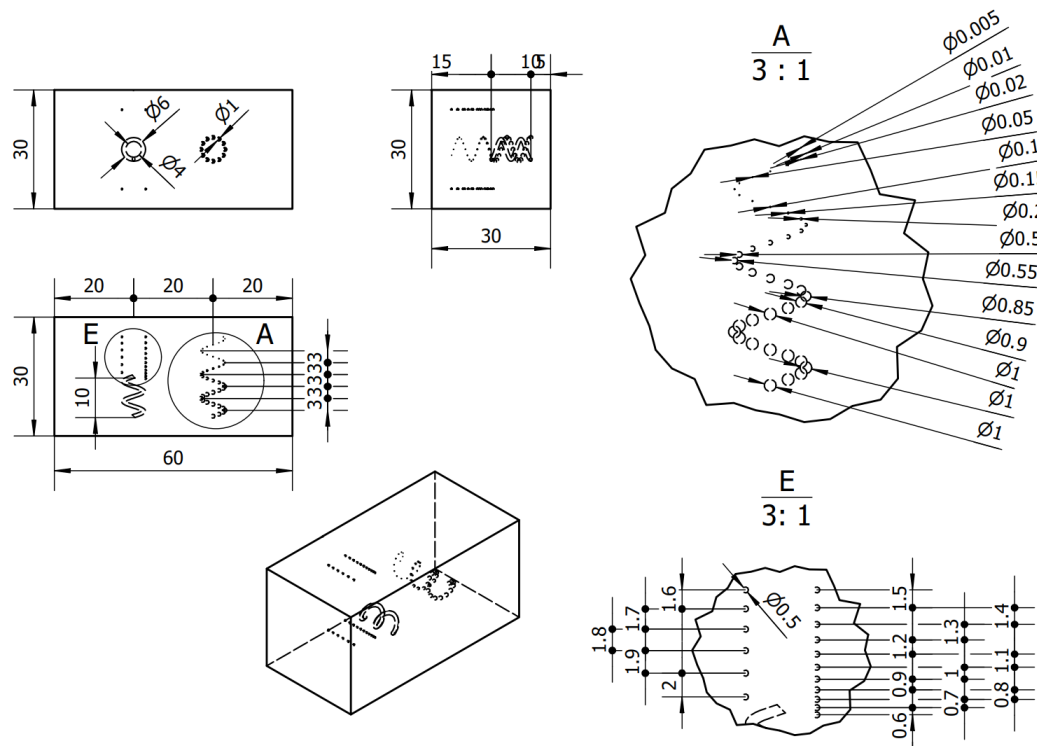


Figure 91 Schematic diagram of AM sample designed to investigate further capabilities of the LIPA system to detect internal features within AM samples.

The first set of features aimed to quantify and then go on to challenge the minimum detectable defect size of LIPA. Illustrated using the exploded view A in Figure 91 a range of spherical features were embedded into the design. These ranged from 0.005-1 mm and were positioned in a spiral pattern. The next set of features aimed to quantify the minimum detectable defect spacing by placing several spherical features at horizontal spacings ranging from 0.6-2 mm.

This sample was designed so that the features can be detected from both the as-deposited side (top) and prepared/polished side (bottom). This meant that the capabilities of LIPA can be pushed further in terms of detectable defect size, depth and spacing when inspecting the bottom/polished side. This work can then be transferred into an as-deposited capability by inspecting the top /as-deposited side.

Following further work on the as-deposited surface of AM samples, a new generation of LIPA systems could be designed to be incorporated into an AM machine to carry out an in-process inspection. This combined with improvements in resolution, penetration depth and acquisition time make LIPA an extremely useful non-contact NDE technique for the in-process inspection of AM to detect defects and features embedded deep within a component being built.

# **Chapter 5 Challenges of In-Process Inspection**

Within the context of the two laser ultrasound techniques discussed in chapters 3 & 4, it was clear that there is a wide range of challenges to be addressed as part of an in-process inspection of AM. This chapter discusses a range of practical variables encountered during AM processes and the impact on LU measurements, starting with the effect of elevated temperatures. It then addresses the effect of surface texture and the various ways an LU system can be adapted to deal with this challenge.

As identified in section 2.5 the inspection time formed a significant segment of the overall time to manufacture a part. The time required to inspect the entire volume of an AM sample using SRAS is modelled and considered as part of this chapter. Finally, this chapter discusses the similarities between the SRAS and LIPA techniques and presents the concept of a hybrid system. The aim here is to demonstrate the value of the complementary datasets from these two techniques, within the context of an in-process inspection. This chapter addresses each of these individual challenges as part of a short self-contained discussion.

## **5.1. Contributions to the Knowledge**

This chapter contributes to the knowledge by addressing several challenges that need to be overcome to carry out an in-process inspection of AM using LU processes such as SRAS and LIPA.

- The effect of elevated temperature due to AM processes is modelled using a relatively simple method. Its effect on the ultrasonic velocity is understood.

- The complex problem of as-deposited surface roughness is broken down into three key features, surface form, waviness and surface roughness. Methods of adapting an optical system to cope with such problems are discussed.
- The time required to carry out a full volumetric inspection of an AM component using an LU system is calculated. This is then presented as a multiple of the build time and tied to reality with the time required for an XCT inspection.
- A novel design for a hybrid system that combines LIPA and SRAS is presented.

## 5.2. Temperature

As illustrated in Figure 17 (page 32), to carry out a true on-line inspection of AM the build and inspection need to be carried out simultaneously. This requires the inspection to take place whilst the powder bed is still at an elevated temperature. As discussed in section 2.1.11 the SLM process works by translating a heat source (a laser) across a substrate (the powder bed). This process is similar in principle to welding processes which are well understood and studied in the literature [59]–[63]. Within the scope of this thesis, Rosenthal's solution for the temperature distribution of a moving heat source across a semi-infinite plate as shown in Equation 1 (page 21) is used. This is applied to an SLM process using the parameters in Table 21.

Table 21 Parameters used in Equation 1 model the temperature distribution of an SLM powder bed.

<b>Initial Temperature</b>	$T_0$	20	°C
<b>Laser power</b>	$q$	400	W
<b>Thermal conductivity (powder)</b>	$k$	50	W/(mK)
<b>Density</b>	$\rho$	8190	kg/m <sup>3</sup>
<b>Laser scanning speed</b>	$v$	0.01	m/s
<b>Heat capacity</b>	$C_p$	435	J/(kg K)

The temperature distributions in Figure 92 show how in the region close to the melt pool (where the temperature is capped at a maximum of 1500°C) the thermal gradients over time and distance are extremely steep. This meant that taking an accurate temperature measurement was not feasible. Whereas further behind the heat source the temperature gradient was lower and more stable.

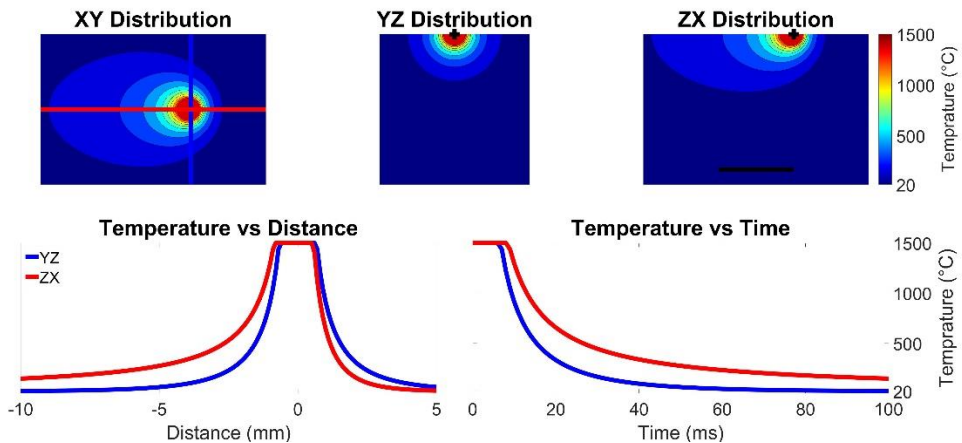


Figure 92 Images of temperature distribution in the XY, YZ and ZX planes with two graphs illustrating the temperature distribution vs distance and time.

With respect to the SRAS technique discussed in chapter 3, for a given material (NiAl alloy in this case) the elastic constants at elevated temperatures from 350-1300 K are available in the literature and presented in Table 22 [209]. These elastic constants are used in the forward model discussed by Li in the literature to calculate the expected SAW velocity at all crystal orientations as plotted in Figure 93 [169].

Table 22 Elastic constants  $C_{11}$ ,  $C_{12}$  and  $C_{44}$  for NiAl 12.69% at temperatures between 350-1300 K [209]

T(K)	$C_{11}$	$C_{12}$	$C_{44}$
350	233.2	155.7	116.7
400	231.3	155.1	115.3
450	229.4	154.4	113.8
500	227.1	153.3	112.4
550	225.2	152.7	111
600	223.7	152.4	109.6
650	221.7	151.8	108
700	219.9	151.2	106.4
750	217.6	150.3	104.8
800	216.3	150.4	103.3

T(K)	$C_{11}$	$C_{12}$	$C_{44}$
850	214.4	150.9	101.7
900	212.7	149.7	100
950	210.5	149	98.1
1000	209.2	149.3	96.2
1050	206.8	148.5	94.4
1100	204.2	147.5	92.6
1150	202.3	147.3	91
1200	200.4	147	89.2
1250	201.1	149.5	87.5
1300	197.9	147.8	85.6

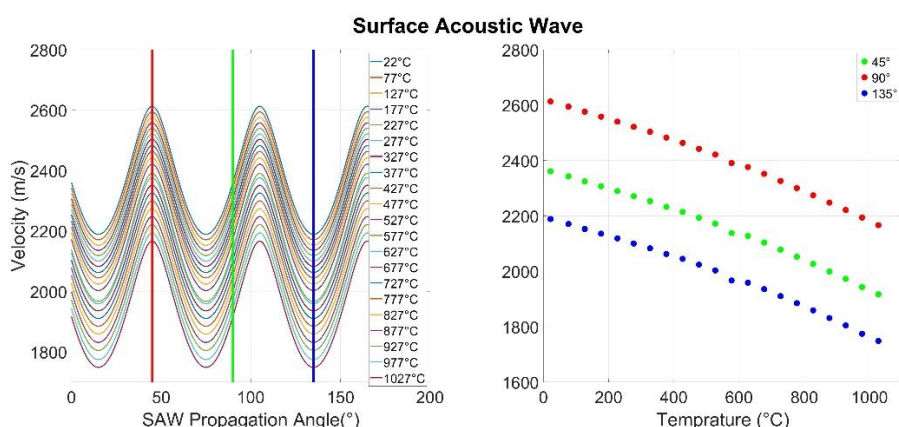


Figure 93 Plots of SAW velocity for the [1 1 1] crystal orientation of a NiAl alloy calculated using the forward model discussed by Li in the literature using the elastic constants at temperatures between 350-1300 K [169], [209].

Similarly considering the LIPA technique discussed in chapter 4, the bulk wave velocity for this specific NiAl alloy can be calculated using the model discussed by Li for a range of elevated temperatures [209] [169].

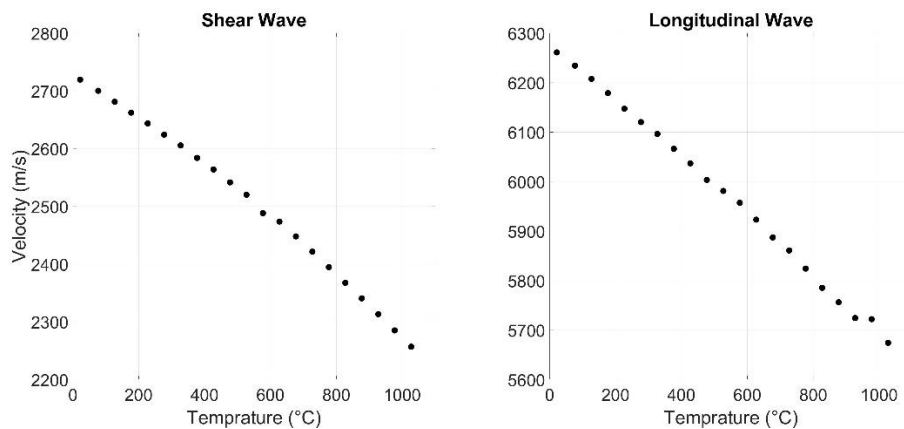


Figure 94 Plots of Bulk Wave velocities for a NiAl alloy calculated using the forward model discussed by Li in the literature using the elastic constants at temperatures between 350-1300 K [169], [209].

The data presented in Figure 93 and Figure 94 illustrate how the SAW and bulk wave velocity of a given material is affected by a change in temperature. This meant that, within the context of an in-process LU inspection, if the temperature of the point at which the inspection is taking place can be measured, then the effect on the measurement due to the elevated temperature can be calibrated out of the collected data.

Another approach to this would be to delay the inspection relative to the build laser source. Due to steep thermal gradients in SLM, as illustrated in Figure 92, a short delay of the inspection would give enough time for the inspection region to cool down to a more manageable temperature. Although this would add a short delay to the inspection taking place, it would drastically simplify the inspection process and require less temperature calibration and post-processing

In practice, the most feasible solution would be a combination of these two solutions where there would be a short delay between the build and the inspection, to avoid the steep thermal gradients. Then the measured temperature is used to calibrate the effect of the surface temperature on the inspection.

### 5.3. Surface Texture

The surface texture of AM samples poses a significant challenge for an in-process inspection. This was clear from the as-deposited AM samples presented in Figure 67 and Figure 68 and from the data presented in section 3.6.4.

When considering the surface of an AM sample, three distinct surface properties can be identified. These are separated using different cut-off lengths, also referred to as the correlation length [210]. The cut-off length is a method of filtering out various features from a surface profile based on their length scale. The plots in Figure 95 are obtained using surface metrology data from the as-deposited surface of the SLM sample in Figure 106 (left). This data was collected using an Alicona Infinite Focus Microscope (which worked using focus variation as discussed in section 2.6.2). The data was processed using the MountainsMap 9, a software by Digital Surf, which is the gold standard for surface texture analysis [211].

The unfiltered surface profile of this sample is shown using the blue line. A cut-off length of 1 mm is used here to extract the surface form (red line). Then next cut-off length of 0.025 mm was used to separate the waviness (green line) from the surface roughness (pink line). This cut-off length was in line with ISO 4288-1996 for these types of surfaces and is discussed to a greater detail in the literature [210], [212]. The length and magnitude of the cut-off length used varies on a case-by-case basis. In geography for example the surface form could be in the kilometre range whilst the waviness could be in the metre range.

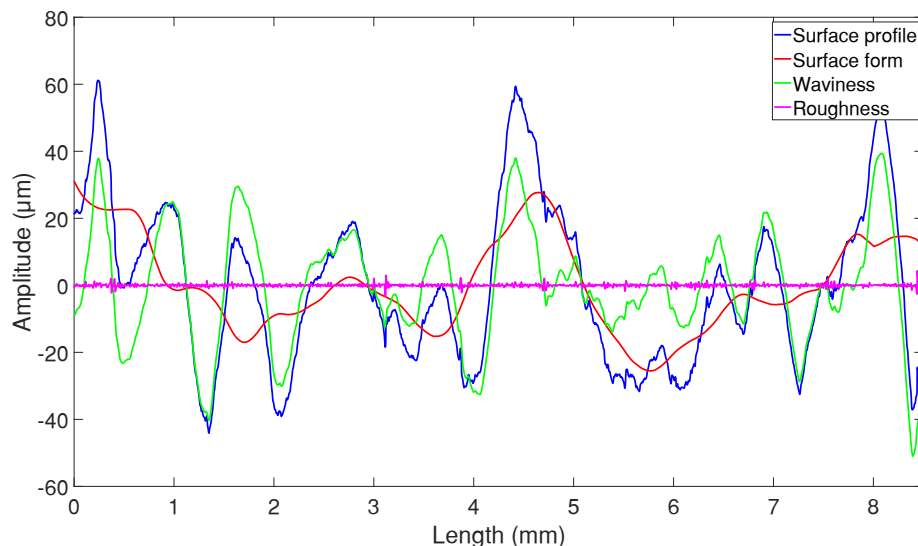


Figure 95 Plots illustrating the various types of surface texture that can be extracted from a surface profile based on the cut-off length used. The surface profile shown using the blue line is off the as-deposited surface of an SLM sample. The surface form is extracted using a cut-off length of 1 mm and presented using the red line. The waviness and roughness are separated using a cut-off length of 0.025 mm and are shown using the green and pink lines respectively.

The following sections initially discuss the effect surface texture has on LU detection, followed by the effect on LU generation. Due to the available equipment and the aims of this engineering doctorate, it only considered laser-based generation and detection.

### 5.3.1. Effect on Laser Ultrasonic Detection

This section considers the three surface texture properties identified above: surface form, waviness and roughness, typically found on AM samples and their effect on LU detection. Section 2.9.1 discussed the various detectors that could be used to detect LU signals off optically rough surfaces. The following section only considers the effect surface texture has on the front end/collection aperture, from an optical detection point of view of an LU system for the in-process inspection of AM. This is because when less light is collected by the system, less light is focused on the detector. This in turn reduces the amplitude of the measured signal.

#### 5.3.1.1. Surface form

Sometimes referred to as topography, surface form on AM samples can be observed visually as a change in height of the sample surface. Within AM changes to the surface form are typically caused by defects that occur during the build, or distortions due to the build process. The sample in Figure 96 (left) showed a diagonal protrusion which was caused by a cluster of pores that occurred during the build. On the top surface of the sample in Figure 96 (right) it can be observed how the external perimeter of all the letters along with the outer and inner perimeter of the bounding rectangle is elevated from the rest of the sample surface. These regions warped during the build which resulted in this change to the surface form.



Figure 96 Photographs of two SLM samples. Circle AM sample with protrusion due to a cluster of defects that occurred during the build (left). SRAS letters sample where the external perimeters of all the letters and the bounding box are elevated as a consequence of the AM build process (right).

When considered as part of an LU system, this is a relatively simple problem to solve and compensate for. Changes to surface form are primarily seen by an optical system as a change in height of the sample or part being inspected. This results in the incident beam being defocused. This affected the LU detection in several ways, the first was the change in the size of the detection spot. If the spot was too large, it would not be sensitive to the generated acoustic waves. Similarly, the change in height would change the characteristics of the reflected cone of light returning to the collection aperture, where any lost light would reduce the detected signal amplitude.

A variety of autofocusing methods have been discussed in the literature to translate the optical system or sample along the optical axis to solve this [213]. These systems, however, do not account for the change in surface angle or slope. They only account for the change in surface height. For this reason, the following section discusses the effect of surface waviness. Due to the magnitude in height and how widespread the effect of the surface form was it was typically removed as part of the first steps of processing surface metrology data.

The focus variation surface metrology technique discussed in section 2.6.2 is a good example of autofocus as an integral part of the system. The basic principle of autofocus relies on implementing some image processing to check if an image was in focus, then using a mechanical stage to translate the sample or the entire inspection system, along the optical axis. This process is then repeated until the focus is maximised. Changes to surface form were typically greater than 10 µm (see Figure 95 and Figure 108)

### 5.3.1.2. Waviness

Waviness in most cases can be observed visually. A change in the surface form only accounts for the change in the vertical height of a sample. Waviness takes into account the change in slope or angle of a given surface. Within AM, waviness is typically caused by a combination of build parameters and the manufacturing process itself. The sample in Figure 97 shows several horizontal and four distinct vertical lines. These were caused by the SLM scan strategy used to build the part. The use of a different scan strategy can negate or minimise this effect – Figure 96 (right) and Figure 106 (left) are examples of parts made using a raster scan strategy with no visible waviness. Figure 106 (right) is the sidewall of a WAAM sample where the horizontal lines corresponded to the build layers used to manufacture the part. Due to the linear motion of the deposition head, each scan track cooled and solidified in a domed shape. This meant when the next layer was deposited, the new layer bulged out at the bottom and domed at the top, causing waviness of the sidewall.

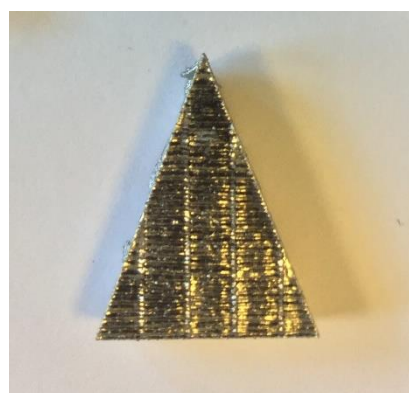


Figure 97 Photograph the triangle AM sample with repeating vertical and horizontal lines, caused by the scan lines of the SLM process used to build the part.

The impact of the waviness of a surface on an LU inspection is relatively simple to understand. Based on the law of reflection, the incident ray and reflected ray have the same angle to the surface normal. As the angle of the surface and thereby surface normal changes, the angle of the reflected ray can be calculated. Assuming an optically smooth surface, this means that for a given range of sample waviness amplitudes and wavelengths, the range of reflecting ray angles can be calculated. Figure 98 illustrates the behaviour of the reflected ray off a smooth surface (left) compared to a wavy surface (middle) and a rough surface (right).

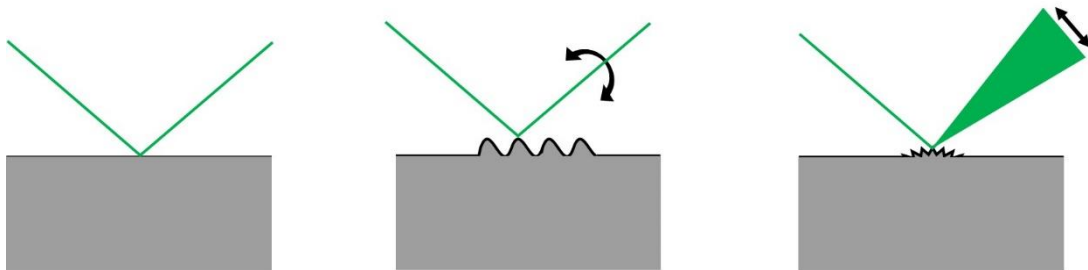


Figure 98 Diagrams illustrating how light reflects off a smooth surface (left), a wavy surface (middle) and a rough surface (right).

The schematic in Figure 99 shows how a lens with a diameter  $D$  and focal length  $f$  coped with a single point on the surface of a sample that was inclined by the angle  $\alpha$ . This resulted in the perpendicular green beam being reflected off the sample surface towards the lens at an angle  $\theta$  where  $\theta = 2\alpha$ . Looking at this diagram it is clear that a lens with a large diameter and short focal length would be able to cope with surfaces with a greater inclination to the horizontal.

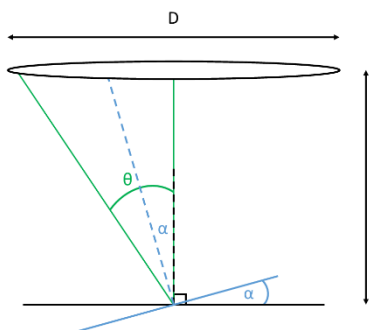


Figure 99 Schematic showing the lens with diameter  $D$  and focal length  $f$  with a surface angled by  $\alpha$  where the incident green laser beam is reflected at an angle  $\theta$  to the surface normal.

If we specifically consider the SRAS-Qt system used in section 3.6.4. The final optic in this system was a 25 mm diameter lens with a focal length of 35 mm. Based on these dimensions using trigonometry we can calculate the maximum acceptance angle of the reflected ray,  $\theta$  to be  $19.65^\circ$ . Based on this, the theoretically maximum acceptable surface angle  $\alpha$  for this system was calculated to be  $\sim 10^\circ$ .

This relatively simple methodology can be applied to a range of simulated sample surfaces. The theoretical sample surface was modelled as a sine wave with a range of amplitudes between 1-50  $\mu\text{m}$  and wavelengths between 0.1-2 mm. Based on that, the absolute mean surface angle was calculated and presented using the RGB colour scale in Figure 100. This plot showed how the wavelength had a significant impact on the mean surface angle. It was clear that longer wavelengths resulted in a low mean surface angle.

The mean wavelength and amplitude of one SLM and three WAAM samples were measured using surface metrology and presented as coloured dots in Figure 100. Compared to the theoretical maximum surface angle,  $\alpha$  of  $\sim 10^\circ$ , it was clear that all four samples had a much higher mean surface angle. Based on the SRAS results presented in section 3.6.4, however, it was clear that the SRAS-Qt system was able to measure these samples. This is discussed further in the following section within the context of surface roughness.

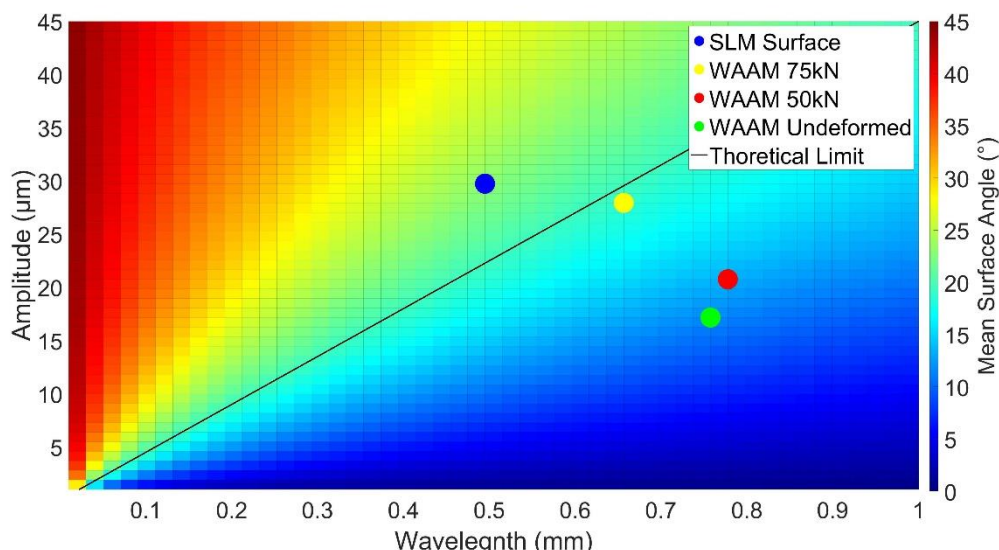


Figure 100 Plot showing the mean surface angle calculated for a range of waviness profiles with varying amplitude and wavelength. The mean angle of the sample surface is presented using the colour bar. The wavelength and amplitude obtained from surface metrology for an SLM and three WAAM samples are presented using the coloured dots.

### 5.3.1.3. Roughness

Surface roughness can be observed visually but cannot be quantified by the human eye. In a shop-floor environment, surface roughness comparators (Figure 62 and Figure 101) are used where the surfaces are compared using touch. The surface roughness of a part is typically caused by the manufacturing process itself. For example, in casting the surface roughness of the part mirrors that of the cast or mould used. In machined parts, the surface roughness consists of traces of the last tool and tool path used. This can be seen in the vertical milling and turning columns of the surface roughness comparator in Figure 101. Similarly, in AM the

surface roughness is a consequence of the manufacturing process. The as-deposited surface on typical SLM samples varies from  $\sim 1.5 \mu\text{m Ra}$  to a maximum of  $\sim 16 \mu\text{m Ra}$  [96].

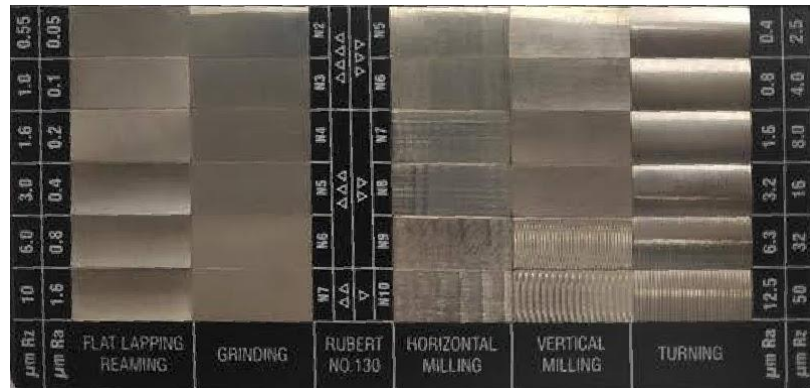


Figure 101 Photograph of Rubert & Co Ltd surface roughness comparator No 130 showing a wide range of machined surfaces with varying surface roughness values.

The surface roughness has a significantly greater impact on an LU inspection when compared to surface form and waviness. This is because as light reflects off an optically rough surface it results in a diffused field that is difficult to predict as shown in Figure 98 (right). This can be explained by considering a beam of light as a bundle of individual rays. In this case, each ray of light follows the law of reflection and reflects relative to the angled surface it encounters. As the surface roughness increases (Figure 111 and Figure 113), these individual rays reflect in more random directions. This causes the diffused reflection seen off the SLM sample surface in Figure 102. This field is made up of individual rays of light known as speckles. In this case, the green laser beam emitted from a Bossa-Nova Tempo LU detector is reflected off the as-deposited surface of an SLM sample. The reflected cone light (the diffused field) can be seen in the region around the large lens of the Tempo but also on the blue panel section to the right of the lens.

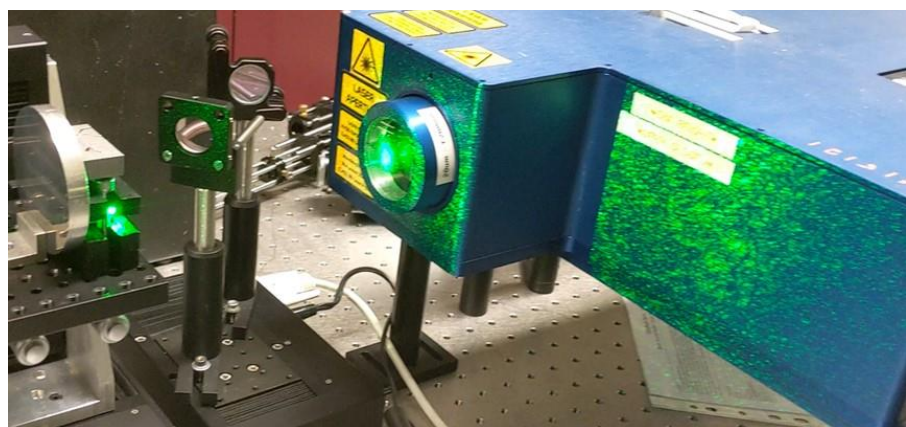


Figure 102 Photograph showing the reflected speckle pattern of a green laser off the as-deposited surface of an SLM sample.

Within the context of the as-deposited surface of AM samples, the properties of this diffused field can be influenced by a wide range of parameters, such as the AM process and build strategy used. Measuring and or calculating the specific diffused fields of light from various as-deposited AM surfaces is outside the scope of this thesis. Instead, the experiment below is carried out to understand the diffused field of the samples used within this thesis.

### Diffused Field

In this experiment, a green laser pointer is aimed at three different surfaces, which helped visualise their diffused field. This experiment used the reflection from a compact disc (CD) – popular in the 90's – which was assumed to be an optically smooth surface. It then used the sidewall of a WAAM sample, which was known to be wavy but relatively smooth, with a surface roughness of  $0.06 \mu\text{m Ra}$ . Finally, it used the as-deposited surface of an SLM sample, with a surface roughness of  $0.44 \mu\text{m Ra}$ .

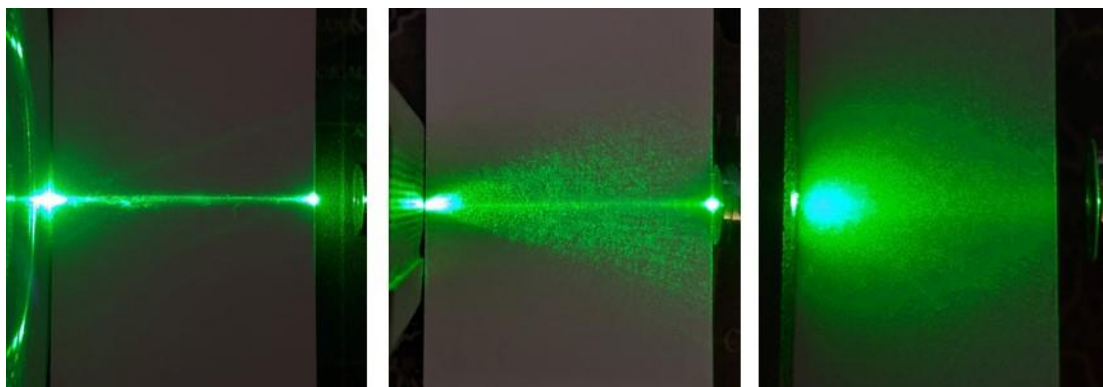


Figure 103 Photographs of a green laser reflected off the surface of a CD, used as an optically smooth surface (left), the sidewall of a WAAM sample used as a relatively smooth but wavy surface (middle) and the as-deposited surface of an SLM sample used as a rough surface (right).

Figure 103 illustrates how the optically smooth surface of the CD exhibited specular reflection, where the light reflected predictably as a single beam back to the laser pointer. The WAAM sidewall reflected the light towards the laser pointer in a diffused cone of  $\sim 40^\circ$ . Finally, the SLM sample surface provided a wide diffused field of light in the direction of the laser pointer. This diffused field of light meant that less light was reflected back into the collection aperture.

One practical method of compensating for this was increasing the power of the detection laser. As an example, the smooth surface EMDA system had a detection laser power of 420 mW compared to the rough surface SRAS-Qt which used a 1500 mW laser. This increased power meant that more light was incident on the sample surface and even though a lot of it was scattered due to the surface roughness, the light that returned into the collection aperture was sufficient to obtain a signal. This in itself came with other compromises. To

remain in the non-destructive regime the detection spot diameter needed to be increased. The EMDA system detection spot was 10  $\mu\text{m}$  compared to the SRAS-Qt system which had a 30  $\mu\text{m}$  detection spot. This had a knock-on effect on the spatial resolution of the system as discussed in section 3.4.1.4.

It was also worth considering the effect of increased laser power on the SNR of the system. The SNR of a given system does not scale indefinitely with the laser power as it is fundamentally limited by the photon noise which increases with the square root of the laser power [139]. This can be shown using Equation 23 where  $h$  is Plank's constant,  $\nu$  is the frequency,  $\eta$  is the quantum efficiency,  $\Delta f$  was the bandwidth and  $W_o$  is the laser power.

$$\left[ \frac{\text{Signal}}{\text{Noise}} \right]_{\max} = \left( \frac{\eta W_o}{4h\nu\Delta f} \right)^{1/2} \quad \text{Equation 23}$$

This experiment also helped explain some of the data points in Figure 100. The waviness and amplitude for the SLM sample lay above the theoretical maximum surface angle of  $\sim 10^\circ$ . However, that was based on the assumption that the reflection was a single beam of light from a locally smooth surface. Figure 103 showed how this was not the case, which meant due to the local roughness of the surface the reflected light formed a cone with a diameter  $d$  as shown in Figure 104. As the diameter of this cone increased based on the surface roughness, it effectively increased the angle from which data could be collected from a given sample surface. This explained how although the data points from the SLM sample were above the theoretical maximum surface angle of  $\sim 10^\circ$ , they could still be inspected using the SRAS-Qt system.

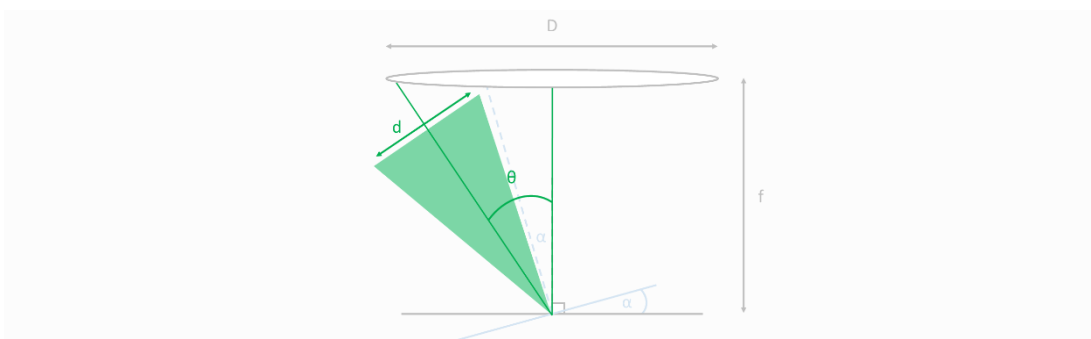


Figure 104 Modified schematic showing how the incident green laser beam is reflected at an angle  $\theta$  to the surface normal but in this case with a cone of light with diameter  $d$ .

Another method of improving the signal was averaging. This was initially discussed in section 3.4.1.5 but is considered in the context of optically rough surfaces in the following section.

### Signal Averaging

This is used as a method to improve the SNR of acoustic signals. SNR is a qualitative measure of how good a signal from a given system is relative to the noise floor of that system. In conventional ultrasonics, the SNR is defined as the intensity ratio between the acoustic reflections from a defect compared to the background reflections classed as “noise” [214]. Within a SRAS experiment, the SNR in dB is calculated using the equation below as the ratio between signal amplitude and noise amplitude.

$$SNR_{dB} = 20 \log 10 \left( \frac{A_{Signal}}{A_{Noise}} \right) \quad \text{Equation 24}$$

In the next experiment, eight segments of the surface roughness comparator in Figure 62 and the top surface of the SLM sample Figure 67 were scanned using the SRAS-Qt system. This system was specifically designed to carry out a SRAS inspection on samples with rough surfaces (see section 3.4.2.2). As part of this experiment, the time window collected was double the length compared to that in Figure 46. This meant that alongside the SAW packet, a segment of the noise in the system was collected. This was used to calculate the SNR. These relatively small 10 mm square area scans were carried out with 25 averages, all the way up to 16000 averages for each data point. The relationship between SNR and the number of averages is well understood and can be seen in Figure 105. As the number of averages increases, any random noise in the data is removed and the signal amplitude is increased. This can also be seen in the form of a SAW packet in Figure 42.

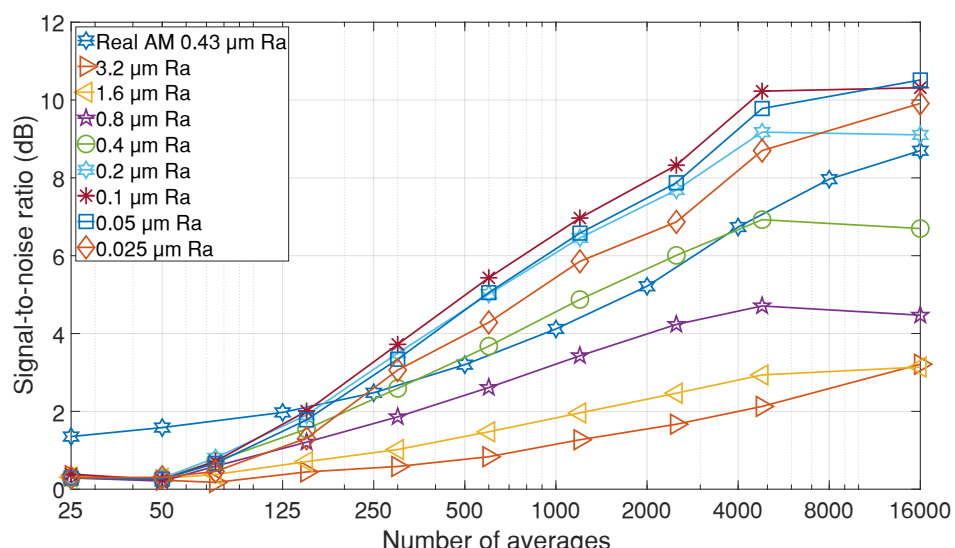


Figure 105 Graph showing the relationship between the number of averages and SNR for surfaces with varying surface roughness.

Visually the as-deposited surface of the SLM sample in Figure 106 (left) had a much rougher surface compared to all of the segments in the surface roughness comparator. Based on the data in Figure 105 however, the trend of the SLM sample – denoted using the dark blue line with a six-pointed start – lay in between 0.2 and 0.4  $\mu\text{m}$  Ra surface roughness samples. This was consistent with the fact that the measured surface roughness of the SLM sample was 0.43  $\mu\text{m}$  Ra. This combined with diffused field experiment above illustrated how the surface texture of a given sample was a multifaceted problem that could not be expressed using a single number such as Ra.

#### 5.3.1.4. Surface Texture Case Studies

This section aims to quantify using surface metrology data, the effect changes to surface texture had on two SRAS data sets obtained from the SLM sample in Figure 106 (left) and WAAM sample in Figure 106 (right) using the rough surface SRAS-Qt system.

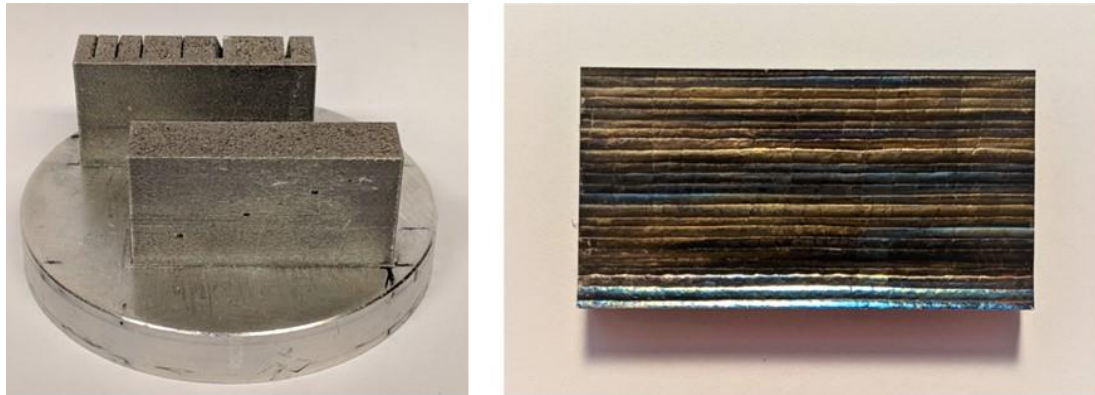


Figure 106 Photographs of two AM samples, manufactured using SLM where the as-deposited top surface was 40 x 10 mm (left) and WAAM where the entire sample surface was 40 x 20 mm (right). These are used as examples of the different effects surface texture has on an LU inspection.

The first effect due to surface texture can be observed in the SLM data in Figure 107 (left). The top right and bottom left corners show a drop in both signal amplitude and an increased noise in the velocity data. This was caused by a change in the surface form, where the outer edges of the rectangular SLM sample was warped during the build. This was a relatively large change across the entire sample and so was not picked up by the small 5 mm square surface metrology data sets – illustrated in Figure 107 (left) using the black box. This effect was also obvious on the outer perimeters of SRAS letters in Figure 96 (Right). A similar phenomenon can be observed in the top left corner of the WAAM data in Figure 107 (right). Just like the SLM sample this manifested as a drop in signal amplitude and increased noise in the velocity data. The primary method of compensation for such changes in surface form is the use of an autofocus system as discussed in section 5.3.1.1. As these large changes in surface form affected the sample from a more global perspective they could not be seen in the relatively

small surface metrology data set. For this reason, they will not be addressed in the following section.

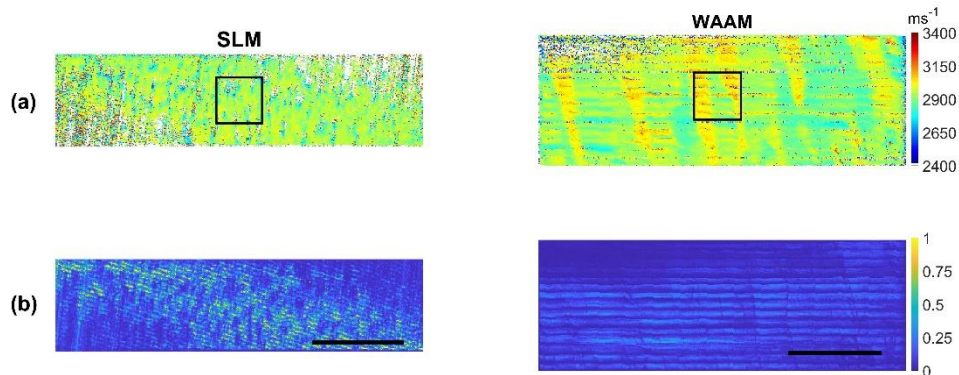


Figure 107 SRAS data was obtained using the rough surface SRAS-Qt system off the as-deposited surface of the SLM sample (left) and WAAM sample (right). Row (a) represents the SAW velocity data whilst row (b) shows the signal amplitude. The black boxes identify the small 5 mm square region from which the surface metrology data was obtained. The black horizontal scale bar represents 10 mm.

The following sections individually discuss the effect surface texture had on the SLM and WAAM datasets presented in Figure 107. These effects are correlated to the sample surfaces using the surface metrology data collected from the small 5 mm square region illustrated using the black boxes in Figure 107.

### Wire Arc Additive Manufacturing

Considering the WAAM data in Figure 107 (right) the most prominent effect due to surface texture was the drops in signal amplitude. This was due to the waviness that could be observed in Figure 106 (right) which was due to the horizontal lines caused by the layer-by-layer deposition process.

The blue line in Figure 108 represents a single line profile extracted from the surface metrology data for this WAAM sample. Using a cut-off length of 1 mm the surface form is extracted and shown using the red line. This is followed by the waviness shown using the green line which was separated from the surface roughness by a cut-off length of 25 µm. Due to the large change in height of the surface form, the relatively smaller changes due to the surface roughness, illustrated using the pink line cannot be seen clearly in Figure 108. For this reason, the surface roughness of the WAAM sample was plotted independent of the waviness and surface form and presented in Figure 111.

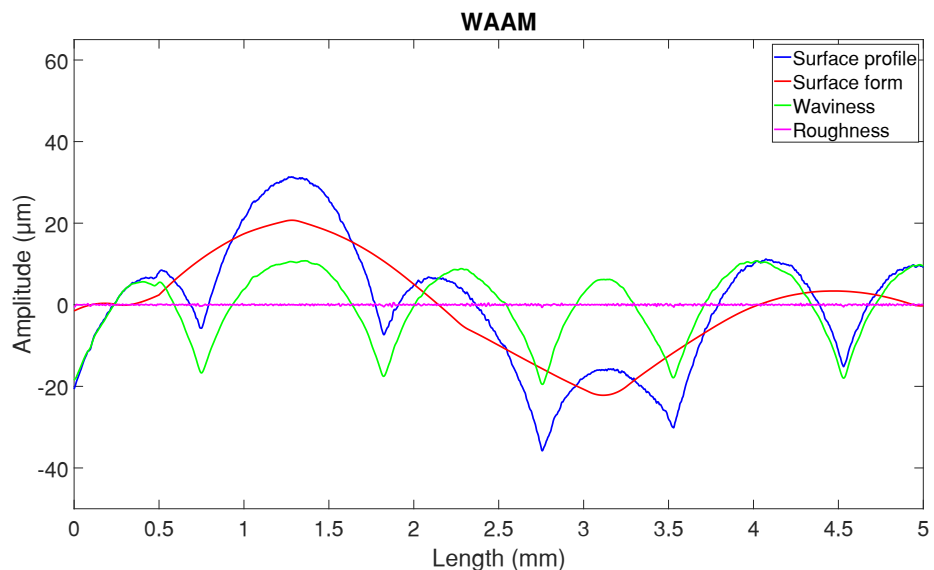


Figure 108 Graphs showing the surface metrology data from the WAAM sample sidewall where the blue line shows the surface profile, the red line shows the surface form extracted using a cut-off length of 1 mm, the green line is the waviness and the pink line is the surface roughness separated using a cut-off length of 25  $\mu\text{m}$ .

This waviness correlates to the loss in the signal amplitude of the WAAM sample in Figure 107 (right). Based on the discussion in section 5.3.1.2 the maximum acceptable surface angle  $\alpha$  for the SRAS-Qt system was calculated to be  $\sim 10^\circ$ . The method in section 5.3.1.2 is applied to the waviness data from Figure 108 to calculate the surface angle presented in Figure 109. Based on this, the regions around the troughs had steep surface angles – the repeating ‘M’ pattern in Figure 109 – which meant that the reflected detection laser beam did reflect into the collection aperture.

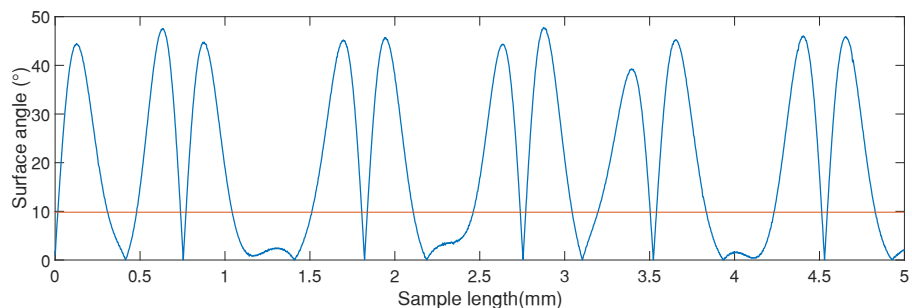


Figure 109 Graph showing the absolute surface angle  $\alpha$  relative to the horizontal plane, calculated based on the surface waviness of the WAAM sample. The red line represents  $\sim 10^\circ$  which was the theoretical limit of detection for the SRAS-Qt system.

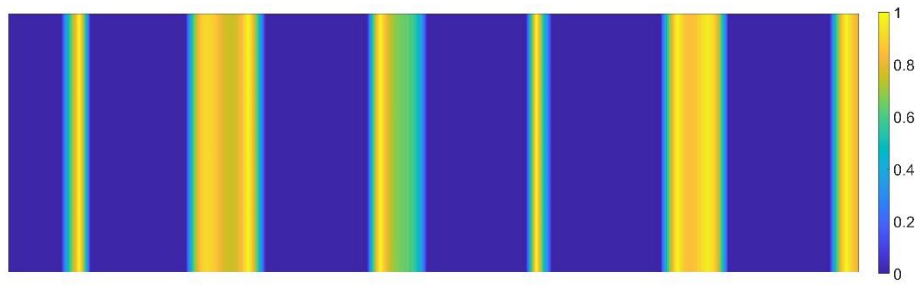


Figure 110 Plot showing simulated signal amplitude for the WAAM sample surface. The colour bar is used to represent the simulated signal which was proportional to the surface gradient.

Based on the surface angle of the sample and the known  $\sim 10^\circ$  limit of the SRAS-Qt system, the theoretical signal amplitude in Figure 110 is calculated. The signal amplitude is plotted to be proportional to the surface angle in Figure 109. Comparing this to the signal amplitude and SAW data in Figure 107 (right), it was clear that there were wider bands of good data collected by the SRAS-Qt system.

The greater quantity of data in Figure 107 (right) compared to Figure 110 can be explained by the surface roughness shown in Figure 111 and the diffused light experiment carried out as part of section 5.3.1.3. The surface roughness of the WAAM sample was measured to be  $0.06 \mu\text{m Ra}$ . The presence of this surface roughness on the WAAM sidewall meant that the light was reflected in a cone of  $\sim 40^\circ$  as shown in Figure 103 (middle). This meant that at surface angles greater than the calculated  $\sim 10^\circ$  some light still returned to the collection aperture of the system. This also helped explain how, although the wavelength and amplitude of the WAAM sample waviness were above the theoretical limit in Figure 100, they still provided reliable data.

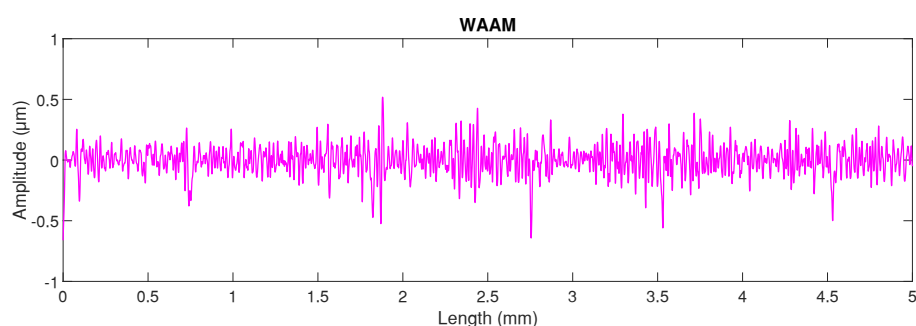


Figure 111 Graph showing the height variation of the WAAM sample surface due to the surface roughness, where the effect of surface form and waviness was removed.

Finally, it is worth noting that apart from the slight loss of signal in the top left corner of Figure 107 (right), the surface form identified by the red line in Figure 108, appeared to have no significant impact on the SRAS data collected from the sidewall of the WAAM sample. This meant that the change in surface form across the WAAM sample – between  $+20$  and  $-22 \mu\text{m}$  – was within the range the SRAS-Qt system could cope with.

### Selective Laser Melting

The signal amplitude in Figure 107 (left) had some diagonal striations, this was due to a thermal issue causing the detection laser power to vary over time and was discussed further in section 3.6.4. For this reason, it is not addressed in this section.

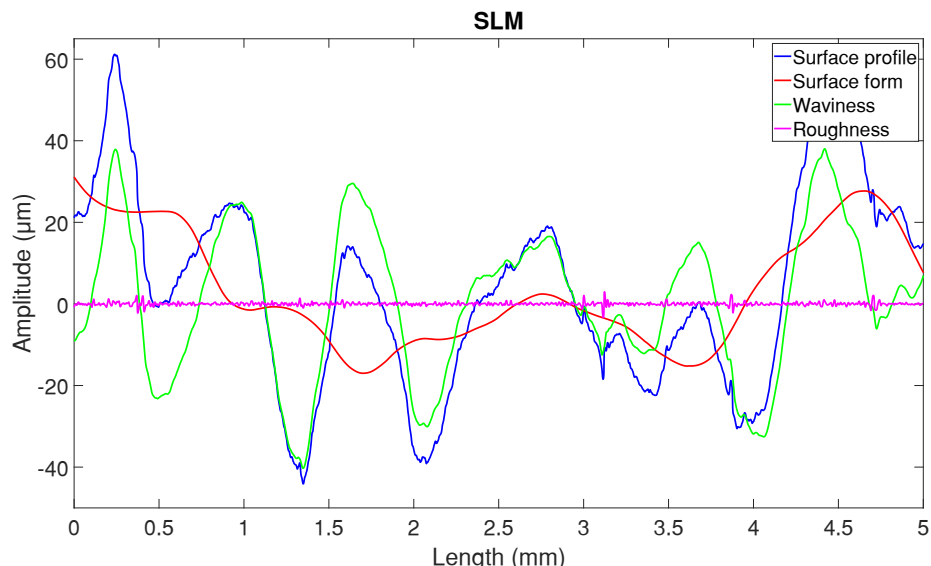


Figure 112 Graphs showing the surface metrology data from the SLM sample where the blue line shows the surface profile, the red line shows the surface form extracted using a cut-off length of 1 mm, the green line is the waviness and the pink line is the surface roughness separated using a cut-off length of 25  $\mu\text{m}$ .

The velocity data as a whole in Figure 107 (left) seemed to be clustered together and separated by vertical segments of noise. This is mirrored in the signal amplitude where vertical lines of low signal amplitude can be seen. Considering this in the context of the surface metrology data in Figure 112, the surface form (red line) clearly showed a dip in the middle and peaks at either end. This was compounded by the fact that waviness (green line) rode on top of the surface form. This meant that the surface peaks (blue line) at either end of the surface metrology dataset in Figure 112 were much higher than those in the middle. This high amplitude, long wavelength waviness could be used to explain the clusters of data seen in Figure 107 (left).

The dip in the middle of the surface form data (red line) was also consistent with the reasoning for the loss of data in the top right and bottom left of the SLM sample. This could be a small-scale representation of how the perimeter of the sample was warped. Due to how small the surface metrology data was compared to the total sample surface, this was difficult to quantify but could be observed when visually inspecting the sample.

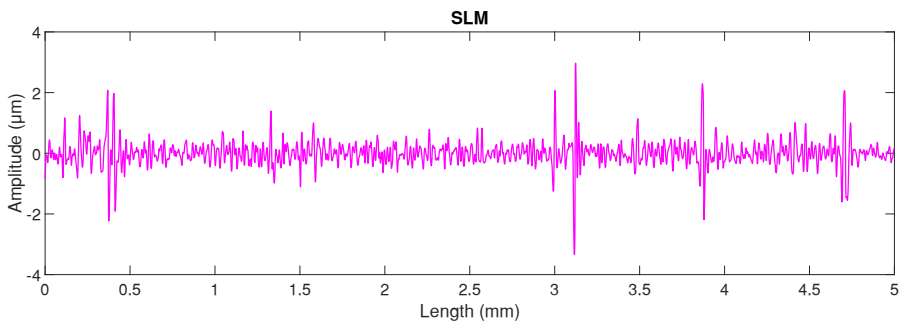


Figure 113 Graph showing the height variation of the SLM sample surface due to the surface roughness, where the effect of surface form and waviness was removed.

Comparing the surface metrology data for the WAAM sample in Figure 108 and the SLM sample in Figure 112, it was clear that the SLM sample had a more challenging surface to inspect based on surface form and waviness amplitude. The WAAM surface was more consistent and predictable, whereas the SLM surface appeared to have random variations in the surface that made it difficult to predict and compensate for.

The pure surface roughness of the SLM sample as seen in Figure 113 was again more random and had a higher magnitude when compared to the WAAM sample surface roughness in Figure 111. This resulted in a much wider diffused field of light as seen in Figure 103 (right). Similar to the WAAM sample, although the wavelength and amplitude of the SLM sample placed it above the calculated limit in Figure 100, the large diffused field due to the surface roughness meant that a sufficient amount of light from the detection laser made it back to the collection aperture, which provided reliable data.

### 5.3.2. Effect on Laser Ultrasonic Generation

Considering only the generation of ultrasound, Ruiz and Nagy presented the effect shot-peened aluminium samples had on the dispersion of SAW compared to smooth aluminium samples [215]. This experiment used a transducer and wedge to generate the SAW, while a Fabry-Perot interferometer was used to detect the SAW. The authors showed the effect on the SAW velocity due to the surface roughness increased at higher frequencies. This effect was reduced significantly as the samples were heat-treated for an hour at temperatures ranging from 150-325 °C. The higher temperature heat-treated samples showed a relatively lower effect on the SAW at higher frequencies. This was because the top surface of the sample recrystallised faster at elevated temperatures during the heat treatment. This effectively removed any residual stress due to the shot-peening process.

Bakre et al. carried out three different experiments to investigate the effect of surface roughness on laser generation, laser detection and SAW propagation [216]. The experiment focusing purely on laser generation was carried out where the SAW was detected using a

transducer on the smooth surface of the sample. Then using a slit mask, narrow-band SAWs were generated on three levels of surface roughness. This was achieved using various emery paper grit sizes – 60 for high roughness, 150 for low roughness and 1500 for smooth. The data presented in Figure 114 shows how as the surface roughness increased, a higher amplitude in the SAW packet was observed. This was due to the thermal energy of the generation laser being absorbed better by the rough surface. This effect is discussed in greater detail by Bergström et al. in the literature [217].

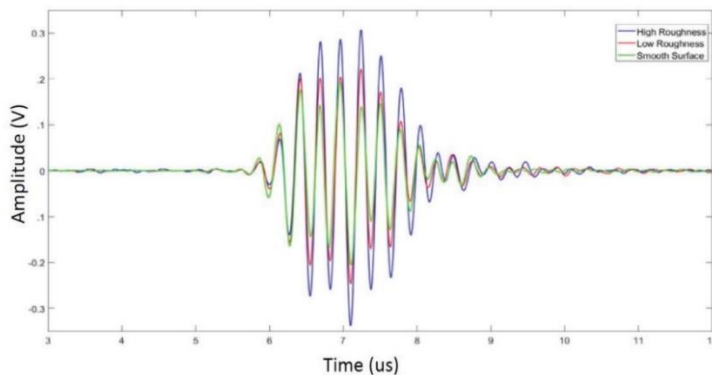


Figure 114 Plots showing three A-scans of SAW packets generated using a combination of 532 nm generation laser and a slit mask on three different surfaces and detected using a transducer [216].

In a similar manner to the surface texture case studies in section 5.3.1.4, the SRAS-Qt system is used to further investigate the effect surface texture had on SRAS inspection taking place. As concluded in the section above, surface form – and to a certain extent waviness – had a similar effect on the generation which could be addressed by the use of an autofocus system. For this reason, within the context of the generation of a SRAS inspection, only the effect of surface roughness is considered.

In a similar manner to the experiments carried out by Ruiz and Nagy [215], the SAW velocity was measured across eight 10 mm square segments of the surface roughness comparator in Figure 62 with varying surface roughness. Based on the results presented in section 3.6.3.3 all eight sections were scanned using 300 averages and the mean SAW velocity is presented in Figure 115.

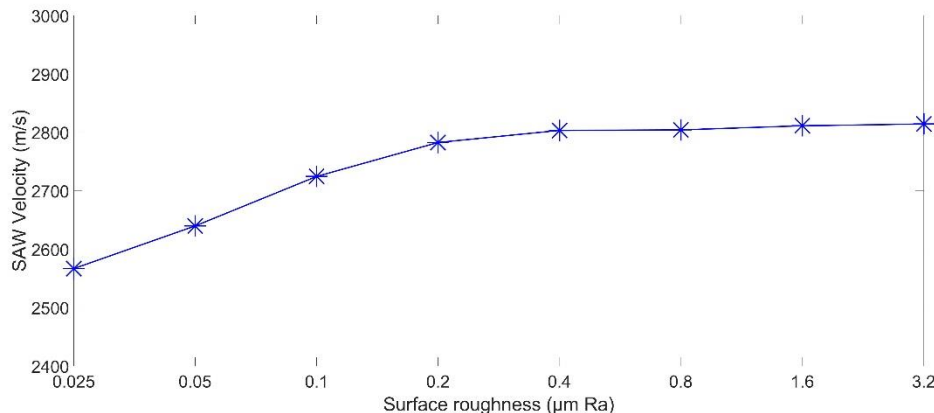


Figure 115 Plot showing the effect of surface roughness on the measured SAW velocity using the SRAS-Qt system with 300 averages.

These results showed a trend that was the opposite of what was observed by Ruiz and Nagy. The results presented by Ruiz and Nagy showed how SAW velocity decreased when going from the smooth to the shot-peened samples [215]. The results in Figure 115 however showed how the SAW velocity increased as the roughness increased. The primary reason for this was the fact that the SRAS-Qt systems detection arm was more affected by the surface roughness compared to the generation. This meant that as the roughness increased, the increased noise in the data (see Figure 64) appeared as high velocities. This skewed the calculated mean SAW velocity presented in Figure 115. Another reason was the fact that the shot-peened samples had some residual stress which affected the SAW velocity. The experiments carried out by Bakre, Ruiz and Nagy isolated either the laser detection or generation by using a transducer for one and a laser for the other. This allowed for a more objective experiment that only considered the effect surface roughness had on the generation of ultrasound. In the case of a SRAS inspection, this was not practical, as the laser generation and detection were a fundamental part of the NDE technique.

### 5.3.3. Conclusion

Based on the points discussed above, it is clear that the surface texture of an AM sample is a complex and multifaceted problem and no single number could be used to classify a given surface. The effect on an LU inspection varied based on the different types of surface texture prevalent on the sample surface. Considering the design of a system capable of carrying out an in-process inspection of AM, it was important to combine all the requirements identified above to cope with the surface form, waviness and roughness of the sample being inspected.

Section 5.3.1.1 discussed how for a sample with relatively large changes in surface form, an autofocus system would be required. This could be implemented as either the entire

instrument being translated towards or away from the sample being inspected or a lens in the system that could be moved to correct the focus.

The next point discussed was the effect of waviness, where the reflected beam of the detection laser moved relative to the surface normal. The methodology used to plot Figure 100 provided an initial indication of the effect of waviness on an LU inspection. However, it was clear that the effect of waviness was closely tied in with the surface roughness of the sample.

The effect of surface roughness could initially be compensated for with an LU detector specifically designed for rough surfaces - as discussed in section 2.9.1. However, for an overall system built for the in-process inspection of AM, some further considerations needed to be given. The simple experiment in section 5.3.1.3 showed how a rough surface resulted in a diffused cone of light which meant that less light was reflected into the collection aperture. It was initially discussed how this could be compensated for by increasing the laser power, but this had a knock-on effect on the spatial resolution due to the damage threshold of the material being inspected. It also showed how this did not linearly scale due to the limitations of photon noise. The next method discussed was signal averaging, but this had the consequence of increased time for the total inspection.

A positive consequence of the surface roughness on the samples being inspected was the fact that it allowed SRAS inspections to be carried out on surfaces that were technically outside the capability of the SRAS-Qt system according to Figure 100. The diffused cone of light reflected off the sample surface meant that for an angled surface greater than the calculated angle  $\alpha$ , part of the cone of light was still reflected into the collection aperture, as shown in Figure 104. This alongside the increased detection laser power of the SRAS-Qt system meant that a sufficient amount of light was reflected onto the detector to carry out a reliable SRAS inspection.

Finally, touching on the surface roughness and the generation of a SRAS system. It was clear based on the literature that the presence of surface roughness allowed for slightly more efficient LU generation. Within the context of a SRAS inspection, however, the greater problem was still the effect on the detection, and the effect due to surface roughness on the generation was minimal.

The conclusion here was that designing one system to cope with a wide range of surface texture parameters was difficult and involved several compromises. Instead, if the specific inspection case was known, the points discussed above could be used to tailor the inspection

system to the expected surface texture. This would provide the best possible instrument geared towards the specific in-process inspection scenario.

## 5.4. Time

Chapter 1 brought attention to the need for in-process NDE for the further development of AM as a technology. Section 2.5 illustrated how the time taken to carry out an inspection was an important segment of the total time required to build a component using AM. As illustrated in Figure 17, due to the lack of AM platforms capable of carrying out a true on-line inspection, the build and inspection happened sequentially. This is referred to as an in-line inspection. This meant that the total time to build a part was comparable to conventional manufacturing and was the sum of the total time to build and the total time to inspect the part.

The following section aims to calculate the time required to carry out a SRAS inspection of the entire volume of an AM part being built. This calculation is based on a 10 mm cube built using a Realizer SLM50 (see section 3.5). The total build time for this sample based on a 20  $\mu\text{m}$  layer height was 60 minutes.

When carrying out a full volumetric SRAS inspection, it was important to consider which factors affected the inspection time. The first factor was the repetition rate of the generation laser, which defined how often an inspection could take place. This was followed by the spatial and vertical resolution of the inspection, which defined the quality of the collected data. The final factor considered was the speed of the stages used to translate the sample or the inspection system. As these were relatively fast and varied based on how the system was designed and implemented, they are not considered as part of this calculation. In terms of LU detection, section 5.3.1.3 discussed the need for and effect of signal averaging. For this reason, it is also considered.

For a single layer, the spatial resolution was a function of the generation wavelength and patch size. The reasoning behind some of these decisions was discussed in greater detail in section 3.4.1.4. In this case, the number of fingers  $N$  was set to 10 to limit the number of variables going into the calculation as this was a good compromise for velocity resolution (see figure Figure 40). The wavelength of the inspection  $\lambda$  was set between 20-100  $\mu\text{m}$ . The patch size was the product of the number of fringes and the wavelength. The step size was set to half the patch size to allow for good coverage across the sample surface and oversampling. This step size was used to divide the length  $X$  and width  $Y$  of the sample surface to calculate the total number of points. The scan time for a single layer was then

calculated based on a range of generation laser repetition rates  $R_r$  between 1 and 5000 Hz. The number of inspection layers was calculated by dividing the sample height  $Z$  by the wavelength  $\lambda$ . This was because the SAW is sensitive to up to a wavelength in terms of depth. This number of inspections was used to multiply the scan time for a single layer to calculate the total volumetric scan time. This calculation for total scan time is simplified and presented in Equation 25.

$$\text{volume scan time} = \frac{(4XYZ)}{R_r N^2 \lambda^3} \quad \text{Equation 25}$$

Based on this methodology the theoretical time taken to inspect the complete volume of the 10 mm cube sample is presented in Figure 116 as a multiple of the build time using the RGB scale bar.

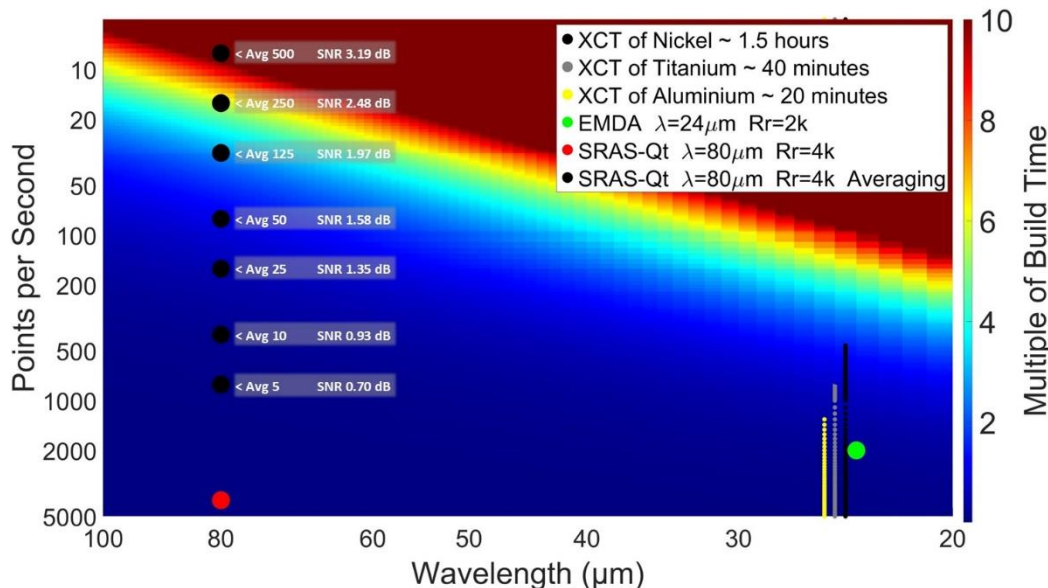


Figure 116 Plot showing the time taken to inspect the entire volume of a given sample, as a multiple of the build time using the RGB scale.

To put the total time taken to inspect the sample into context, the time required to XCT this sample is also plotted in Figure 116 as black, grey and yellow dotted lines for Nickel, Titanium and Aluminium respectively. Although the information obtained from XCT and SRAS is very different, it is used to help give context to this figure as a volumetric inspection technique commonly used in the aerospace industry. The XCT inspection times are for a 25  $\mu\text{m}$  voxel size and are based on quotes from the MTC in Coventry.

It was clear that the time required to XCT the sample was comparable to the time required to inspect the entire volume of this sample using the smooth surface EMDA system (green

dot) at a wavelength of 24 µm, which took 0.23 times the build time. This however was not realistic considering the surface texture of as-deposited AM as discussed in section 5.3.

Considering the SRAS-Qt system which was specifically designed to inspect rough samples, the theoretical time to inspect the entire volume with no averaging was calculated to be 2 times the total build time. This looked relatively short as shown by the red dot in Figure 116. This was due to the larger wavelength meaning that each collected data point covered more area and a greater penetration depth which meant fewer intermediate layer inspections were required. The SRAS-Qt system also had a laser with a higher repetition rate of 4000 Hz compared to the EMDA system at 2000 Hz. This, however, was not realistic because to cope with the surface texture of as-deposited AM samples, some signal averaging was required. Based on the SNR data for an as-deposited SLM sample in Figure 105, for a 10 mm cube, the black dots in Figure 116 are plotted for a range of averages. Each point was also annotated with the number of averages and the expected SNR based on Figure 105.

Based on the data presented in section 3.6.4.2, Figure 69, it was clear that for an SLM sample ~200 averages on the SRAS-Qt system provided a good compromise between acceptable SNR and total inspection time. Considering this in the context of the SNR graph in Figure 105 and the inspection time plot in Figure 116, 250 averages provided a realistic data point for the full volumetric of an SLM sample. This would theoretically take 6.5 times the total build time which was ~6.5 hours at an SNR of ~2.48 dB.

At this stage, it was worth considering if inspecting an AM sample on every layer would be truly necessary. Instead, an inspection could be carried out every 2<sup>nd</sup>, 10<sup>th</sup> or 50<sup>th</sup> layer. This point is illustrated in Figure 117 where the plot from Figure 116 is simplified by using the effective points per second (*effective points per second = points per second / number of averages*). The three plots shown in Figure 117 are for carrying out a full volume inspection for a 10 mm cube sample but instead of every layer, the inspection would take place every 50<sup>th</sup>, 10<sup>th</sup> and 2<sup>nd</sup> layer.

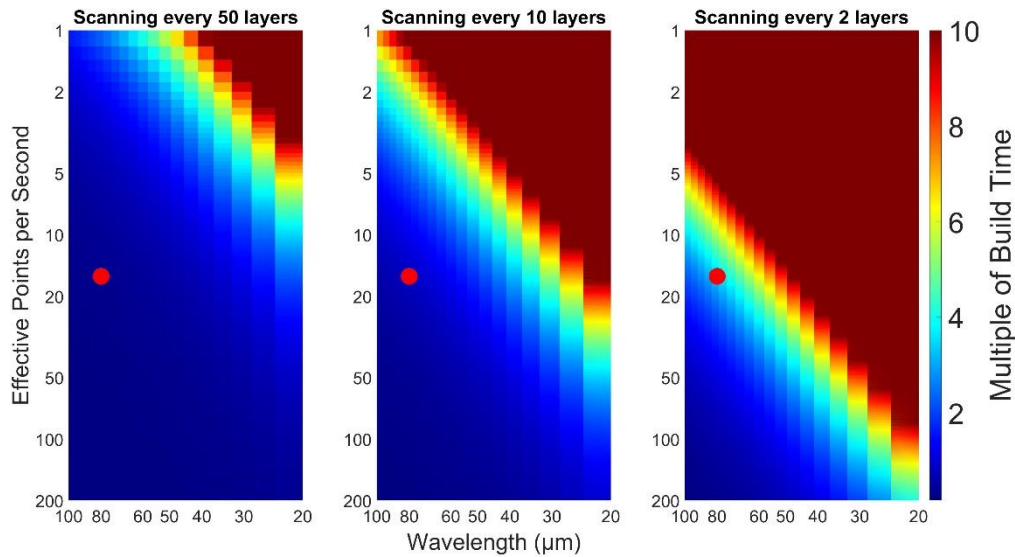


Figure 117 Simplified time plots for carrying out an inspection every 50, 10 and 2 layers with the effective points per second accounting for averaging. The RGB scale shows the total time as a multiple of the build time.

In this case, the SRAS-Qt system at a generation laser repetition rate of 4000 Hz, performing 250 averages resulted in an effective inspection rate of 16 points per second. The total inspection time resulted in 0.13, 0.66 and 3.34 multiples of the build time respectively for inspecting every 50<sup>th</sup>, 10<sup>th</sup> and 2<sup>nd</sup> layer, shown using the red dot in Figure 117.

Based on the theoretical plots in Figure 117 it was clear that the inspection time was heavily dependent on: the inspection laser repetition rate, the number of inspections required, the desired SNR and the spatial and depth resolution of the data collected. In addition to this, the calculations above did not account for the delay in processing and saving the data, the speed and inherent delay in the mechanical stages used along with other practical limitations when it came to high-speed inspections. It is also worth noting that the methodology above was developed specifically for a SRAS inspection.

The plots above provide an initial indication of the theoretical time required for a full volumetric inspection using SRAS. They also highlight how the total inspection time could be shortened by reducing the overall noise in the system and increasing the sensitivity of the detections which would result in higher SNR and therefore require less averaging. Another way of shortening the inspection time would be to increase the generation laser repetition rate. Finally, the most important factors were found to be the total number of inspections and the spatial resolution. This means that if the inspection strategy was adapted based on the expected defects or part complexity, the total inspection time relative to the build time could be reduced drastically.

## 5.5. Integration

The following section looks at the potential integration of SRAS and LIPA into a hybrid system. When considering the base elements required for a SRAS and LIPA system, as illustrated in Figure 118, it was clear that both systems shared a lot of common elements. In terms of generation, both systems used a 1064 nm pulsed generation laser. SRAS required a mask to create fringes and a lens to image the mask onto the sample surface, whilst LIPA used a cylindrical lens to convert the columnated IR beam into a line on the sample surface. For detection, as discussed in section 3.4.2.2, the rough surface SRAS system used a Quartet LU detector. In the literature, Lukacs et al. presented data from a LIPA system that used a newer version of the same Quartet LU detector [218].

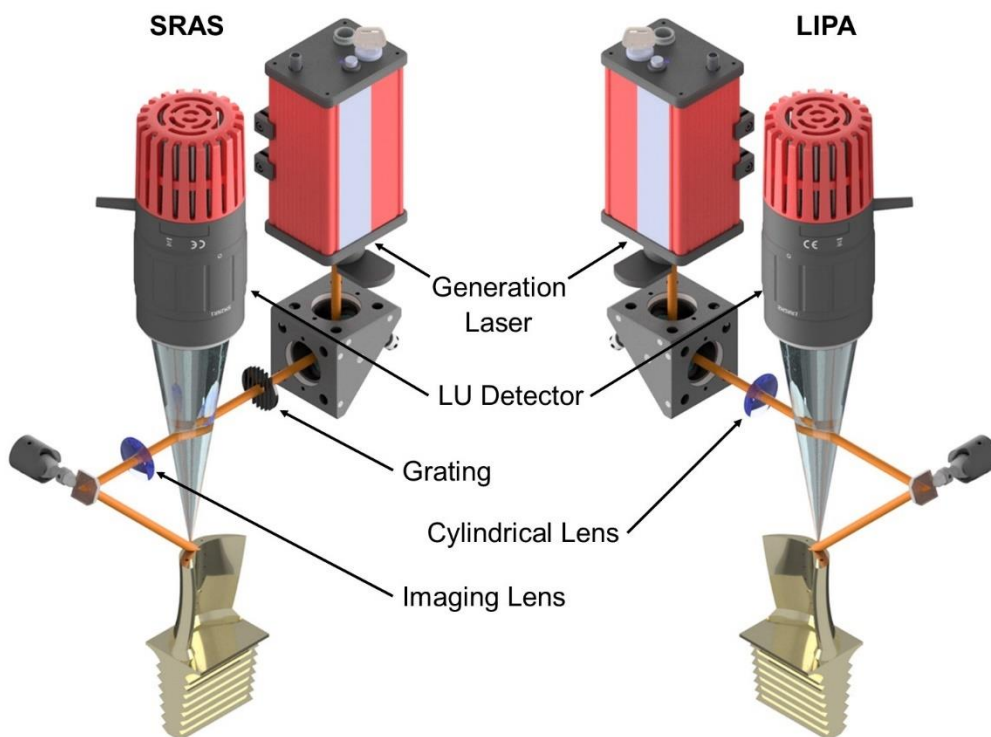


Figure 118 Simplified schematic diagrams of SRAS (right) and LIPA (left) systems, showing how both systems share a generation laser and LU detector.

This showed the similarities between the two NDE techniques from an optical system design point of view. Now from a data point of view Figure 119 illustrated what the combination of SRAS and LIPA datasets would look like if they were obtained from the same sample. From an in-process perspective, based on the data presented in chapters 3 and 4, a hybrid inspection of this nature could provide a vast amount of useful information. The SRAS data provided an understanding of the microstructure of the top surface of the part whilst the LIPA data provided information regarding any internal features or defects within the part.

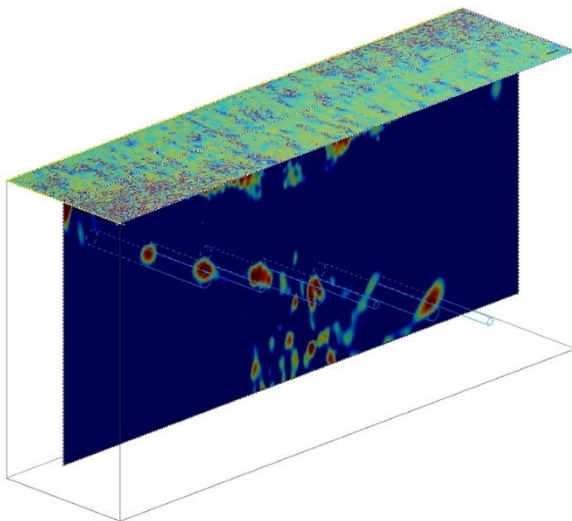


Figure 119 Composite image combining the CAD wireframe of an AM sample with the data from the SRAS and the LIPA superimposed.

Some future work in this area involves designing and building one optical system capable of carrying out both a SRAS and LIPA inspection. Such a system would have several practical challenges. This first would be integrating a motorised element to remove the mask and lens required for SRAS and replace it with the lens required for LIPA. In terms of the SRAS inspection, the entire sample would need to be translated to inspect the entire sample surface. For a simple SRAS system, the generation and detection beams do not need to be translated independently. For LIPA, however, the generation and detection lasers need to be translated independently. This can be achieved using galvo scanning mirrors which were also capable of providing a step-up in scanning speed. The integration of such a hybrid system as part of an in-process inspection of AM has the potential to revolutionise the landscape of the future generations of AM systems. The ability to obtain several datasets regarding the component microstructure using SRAS combined with the cross-sectional information obtained using LIPA would be an unparalleled result in the field of in-process NDE.

## 5.6. Conclusion

This section summarises the conclusions drawn based on the work carried out within this chapter.

Due to the nature of AM, carrying out an in-process inspection came with a wide range of challenges. These were identified in the previous chapters to be the elevated temperature of the as-deposited surface of the sample, its surface texture and the time required to carry out an inspection.

Within this chapter, the challenge of the elevated temperature was addressed by using a simple Rosenthal's solution for temperature distribution to model the surface temperature around the melt pool and sample surface. Figure 92 showed how in the region close to the melt pool the temperature gradient was extremely steep. This meant that it was difficult to obtain an accurate temperature measurement. Figure 92, however, also showed how ~5 mm or ~40 ms behind the melt pool the temperature was more stable. The forward model discussed by Li in the literature showed how the surface and bulk wave velocities of a given material can be calculated using the elastic constants from the literature for elevated temperatures. Any effect on the inspection due to the elevated temperature can be calibrated by using a combination of temperature measurement and the modelled wave velocity.

When inspecting the as-deposited surface of AM, Figure 95 showed how the surface texture was a complex problem. Section 5.3 showed how based on the cut-off length used, the surface texture can be separated into surface form, waviness and surface roughness. The following sections discuss how various aspects of a given optical system can be modified to deal with these challenges.

This was initially discussed from the detection point of view of an LU system. The relatively large change in height due to surface form could be compensated for using an autofocus system. The waviness presented a more complex problem that required some consideration to be given from an optical design point of view. In an ideal situation, a large collection aperture with a short focal length could be used to focus the maximum amount of light onto the detector. Figure 99 illustrated how for a known optical system, the theoretically maximum acceptable surface angle can be calculated. Based on this Figure 100 illustrated how this could be plotted for a range of sample waviness amplitudes and wavelengths.

The surface roughness presented the greatest challenge due to it reflecting the light in a diffused cone as demonstrated in Figure 102 and Figure 103. From one point of view, this was a positive. It meant that due to the wider defused field of light, as shown in Figure 104, when the mean surface angle was greater than the theoretical maximum acceptable surface angle, some light from the edge of the reflected cone was collected by the system and focused on the detector. In most cases, however, the increased surface roughness meant less light as reflected onto the detector and so increased noise in the system. Two methods of compensating for this were by increasing the detection laser power and averaging the signal over time. Figure 105 illustrated how the SNR was directly affected by the surface roughness

and improved by the number of averages taken. These effects were discussed further as part of the case studies in 5.3.1.4 using WAAM and SLM samples. Finally, this section also discussed the effect on laser generation due to the surface roughness.

The next section of this chapter carried out a theoretical calculation for the time required to inspect the entire volume of an AM sample using SRAS. The basis for this was carrying out a SRAS inspection at a given wavelength across the entire 2D surface of the sample, then dividing the height of the part by the wavelength for the number of layer inspections required. This was based on the assumption that the sensitivity of surface waves was up to wavelength in depth. The total volume scan time was presented as a multiple of the build time. Using the current generation SRAS system built to inspect rough surfaces, this worked out as 6.5 times the build time. This was progressed further to calculate the time required to carry out an inspection every 2<sup>nd</sup>, 10<sup>th</sup> and 50<sup>th</sup> layer. This worked out as 3.34, 0.66 and 0.13 times the build time. This puts into context how principles such as adaptive resolution would be required when considering SRAS as in an in-process inspection.

The final section of this chapter discussed the unique concept of a hybrid LU system. The aim here was to combine the surface microstructure capabilities of SRAS with the subsurface defect detection capabilities of LIPA. The combination of these techniques could provide an extremely valuable T-shaped data set as presented in Figure 119.

In summary, this chapter first showed how the challenge of surface temperature during an in-process inspection could be overcome, if the inspection had a slight delay, or took place away from the melt pool. This was further progressed by modelling the behaviour of the SAW and bulk waves. This showed that if the surface temperature was measured accurately, its effect could be calibrated. This was followed by the challenge of the various aspects of surface texture. This chapter showed how changes in surface form, waviness and surface roughness could be accounted for by making considerations for the specific inspection case at an optical design stage. The theoretical calculation of the inspection time showed the total time required for the full volumetric inspection, followed by highlighting the importance of considering the depth and volume of information collected. Finally, the concept of a hybrid LIPA and SRAS system stood as a simple and elegant solution to obtain both subsurface and surface information of an AM component being built.

## **Chapter 6 Conclusions**

This thesis sets out to identify and develop the capabilities of one or more NDE techniques to carry out an in-process inspection of advanced manufacturing processes such as AM. It addresses some of the challenges faced by such NDE techniques when carrying out an in-process inspection of AM. This chapter presents a summary of the main findings and conclusions from the previous chapters along with their impact on future generations of in-process inspection systems for AM.

Chapter 1 outlines the industrial motivation and need for advanced manufacturing processes such as AM within the aerospace industry. The ability to manufacture components with complex geometries that cannot be manufactured using conventional manufacturing processes such as milling and casting is particularly appealing. The two case studies that followed outlined the need for NDE of safety-critical components used within the aerospace sector. These case studies focus on incidents caused by undesirable microstructure within components which highlight the need for NDE techniques capable of detecting such anomalies. The research motivation shows how layer-by-layer AM processes are well suited for in-process NDE where several intermediate layer inspections can be combined to build a digital twin of the part being built.

Chapter 2 briefly discusses a wide range of AM processes before focussing on SLM due to its capability to manufacture complex components using metallic powders suitable for aerospace applications. This is followed by a detailed discussion of a wide range of defects that commonly occur in AM components such as cracks, pores and undesirable microstructure. The early detection of such defects is pivotal for the progress of AM within

the manufacturing industry. These defects arise partly due to the stochastic nature of the build process and the relative lack of knowledge and experience in the coupled nature of the process parameters. Additionally, the nature of the parts that are manufactured using AM processes can be extremely complex which makes a post-manufacture inspection very challenging. This chapter also outlines several KPVs of SLM, such as surface and subsurface defects, scan strategy, laser power, scan speed, hatch spacing and energy density.

Although a change in the part microstructure is not typically classified as a defect, changes in the microstructure have a direct impact on the part performance. For this reason, the capability to detect changes to microstructure is considered alongside the KPV of SLM. It then goes on to review the literature that detected changes to and aimed to control the AM component microstructure.

NDE is discussed within the context of AM where terms such as off-line, on-line and in-line are defined. The sections that follow discuss the theory behind and review the literature for a wide range of NDE techniques used for both the in-process and the post-manufacture inspection of AM. Throughout this review, it is evident there is a distinct lack of in-process NDE techniques capable of inspecting both the component microstructure and any defects embedded within the component. It also brings forward the fact that the in-process inspection of AM presents a wide range of challenges such as the confined nature of the build chamber, elevated temperature and the surface texture of the parts being built.

The CCM in Table 5 ranks each of the reviewed NDE techniques against the KPV identified for SLM. This highlights the capabilities and limitations of each of the NDE techniques and helped select the most suitable techniques for further investigation. Following this, it is clear that thermographic NDE ranks the highest, even without the capability to detect changes to component microstructure and defects embedded deep within the component. It also, however, lacks future space for innovation due to the technique already being deployed as part of an in-process inspection. For this reason, the next suitable candidate, an LU technique known as SRAS is chosen. This is due to its non-contact, non-destructive nature and its ability to detect changes to KPV such as laser scan strategy, laser power, surface defects and changes to component microstructure. SRAS however has a distinct lack of capability to detect defects embedded within a given component. Looking further up the CCM in Table 5 LIPA is another NDE technique that combines the advantages of LU with the capability to detect features or defects embedded deep within a given component. This is advantageous due to the capability of AM to manufacture extremely complex components which meant

that in some cases, sections of the component that are accessible during the layer-by-layer build process could not be accessed for a post-manufacture inspection.

Chapter 3 is a detailed study into the capabilities of SRAS to detect a range of defects and changes to the microstructure of samples manufactured using AM processes such as SLM. This chapter initially outlines the concept and theory behind SRAS followed by a literature review of its use within the field of AM. It goes on to discuss the SRAS instrument in a modular manner to outline how adaptable the SRAS technique is for the specific inspection taking place. To be considered for an in-process inspection of AM, SRAS needs to demonstrate its capability in three key areas. The ability to detect defects, the ability to detect changes to part microstructure and carry out an inspection on the as-deposited surface of an AM component.

Several experiments are carried out on the prepared/smooth surface of samples manufactured using AM to demonstrate the capability of SRAS to detect and classify surface defects and changes to the part microstructure. The first set of experiments initially focuses on the detection and classification of mechanical defects such as cracks and pores. The two rich data streams (optical and acoustic) obtained following a SRAS inspection are used to generate a binary data set. This is processed to obtain information such as the position, area, perimeter, major and minor axis lengths of the detected defects. This information is used to help classify the detected defects and understand their causes. Obtaining this information as part of an in-process inspection would aid a repair strategy or prevent further defects using closed-loop feedback.

The next set of experiments demonstrates the capability of SRAS to detect changes to AM component microstructure. Two methodologies are developed to enhance the detected changes to microstructure using SRAS data. The first uses a spatial filter to bring forward more global changes in the microstructure of an AM part. The second uses a watershed transform to identify more local changes. This is followed by two further experiments that use part geometry and a seed crystal to encourage changes in the part microstructure.

The latter half of chapter 3 focuses on transitioning the smooth surface capabilities of SRAS to the as-deposited/rough surface of AM samples. This is initially done using a surface roughness comparator where the surface roughness increases from 0.025-3.2  $\mu\text{m}$  Ra. The smooth surface EMDA system was only able to cope with ~0.1  $\mu\text{m}$  Ra. The rough surface SRAS-Qt system was able to cope with a roughness of ~0.8  $\mu\text{m}$  Ra using 300 averages. Following this, the SRAS-Qt system is used to inspect the as-deposited surface of an SLM

sample. No large changes to the part microstructure can be observed, however, small changes to the surface microstructure were visible. This is due to the typical grain size of SLM ( $\sim 25 \mu\text{m}$ ) being below the spatial resolution of the SRAS-Qt system. To work around the spatial resolution limitations and demonstrate the capability of SRAS as a technique, the sidewall of a WAAM sample is inspected. This dataset shows clear indications of the large prior- $\beta$  grains on the sidewall of the WAAM sample. These two experiments show how the rough surface SRAS-Qt system can inspect the challenging surfaces of SLM and WAAM.

This presents SRAS as a viable candidate to be considered as part of an in-process inspection for AM processes such as SLM and WAAM. It shows how the work carried out as part of this engineering doctorate helped progress the technique further by extracting valuable information out of the data collected from the current generation SRAS systems. It also develops methodologies that could be used alongside future generations of higher resolution SRAS systems as part of an in-process inspection.

Chapter 4 is a detailed study into the capabilities of LIPA to detect nested features and/or defects in components manufactured using AM. It initially outlines the basic principles behind a laser phased array along with a literature review that investigates the history of such systems. This is followed by the principles and theory behind the current generation LIPA system.

The experiment carried out in this chapter focuses on demonstrating the capability of LIPA to not only detect the presence of internal features but also locate them and attempt to size them. The non-contact, non-destructive nature of LIPA means that the ability to image the cross-section of an AM component is another unique inspection that could be carried out as part of an in-process inspection of AM. From one perspective this means that the internal features of a complex component could be monitored for geometrical accuracy as the part is being built. From another perspective, any defects detected at an earlier stage could aid the decision-making process in terms of restarting the build or attempting a repair, reducing overall costs and build time. Previously such an inspection could only be carried out post-manufacture using XCT. Some of the current limitations of LIPA are the capability to inspect the as-deposited surface of AM and the data acquisition speed. Both of these can be addressed in future generations of LIPA systems with the use of rough surface detectors and faster scanning stages or galvo mirrors. LIPA is a relatively new NDE technique especially when it comes to its implementation for AM. Data acquisition methods such as SMC, combined with spatial encoding for generation and parallel detection mean that LIPA has a

lot of untapped potential to improve its acquisition speed. With further development over the coming years, LIPA can progress towards real-time in-process inspections of AM processes such as SLM and WAAM.

Chapter 5 address a range of challenges a laser-based inspection would have to overcome when carrying out an in-process inspection of AM. These are the elevated temperature of the inspection surface, the surface texture of the as-deposited surface and the time required to carry out an inspection. This chapter also considers the concept of a hybrid system that combines the capability of both LIPA and SRAS.

To carry out an in-process inspection of SLM, the NDE system needs to cope with the elevated temperature of the build chamber and powder bed. This is to minimise any delay between the build and inspection. A simple mathematical model is used to demonstrate the temperature around an SLM melt pool and show how the region close to the melt laser has a steep thermal gradient. This makes measuring the surface temperature and carrying out an inspection in this region impractical. The model shows that at a short distance behind the melt laser the temperature is more stable (lower temperature gradient) and could be measured accurately. Following this, the effect of elevated temperature on the SAW and bulk waves are modelled. This shows how if the temperature where the inspection was taking place can be measured, its effect on the SAW and bulk waves can be compensated for. This is an initial step towards an in-process inspection to allow an in-line inspection (where the build is paused for the inspection to take place) to be carried out. Such an in-line inspection would then pave the way for an on-line inspection where there is no impact on the build time.

The next section of chapter 5 focuses on the effective surface texture has on an LU inspection. Due to the extreme amount of energy used to melt metallic powders and wires as part of an AM process, the surface texture is an inherent challenge for the in-process inspection of any AM process. The surface texture appeared to have a minimal effect on laser generation, so this section focuses primarily on the effect of surface texture on laser detection. The surface texture of a given component is an extremely complex multifaceted problem and so is broken down into three distinct properties: surface form, waviness, and surface roughness. The surface form is separated from the surface profile using a cut-off length of 1 mm. This accounts for the large overall changes in the surface height of a given sample. In an optical system, this can be compensated for, by using an autofocus system. The waviness of a surface is commonly caused by the AM build process or specific build parameters. This causes the

reflected beam of light to sway left and right. Compensating for this involves considerations at an optical design stage. The use of large diameter lenses with a shorter focal length allows a system to cope with an increased sample waviness wavelength and amplitude. Finally, the surface roughness of a given sample is separated from the waviness using a cut-off length of 0.025 mm. The effect of roughness means that the light reflected off the sample surface forms a diffused cone of light. This requires the rough surface detectors discussed in chapter 2. This cone effectively expands the operating window for the maximum waviness wavelength and amplitude a system could cope with, as some light is still focused onto the detector. Using surface metrology data from SLM and WAAM samples, each of these effects of surface texture is discussed further within the context of optical detection as part of the two case studies in chapter 5. This shows how the challenges presented by the as-deposited surface of SLM and WAAM could be overcome by, knowing the various properties of the surface and considering them at the design stage of the optical system.

The next challenge discussed in chapter 5 is the time required to carry out an in-process inspection. The end goal for an in-process inspection of AM would be the on-line inspection of an AM build taking place, where there is no impact on the total build time whatsoever, effectively providing an inspection for free. In practice, however, the current and next-generation systems will only be able to carry out an in-line inspection, where the build is paused for a short period to carry out this inspection. For this reason, it is important to understand the time required to carry out such an inspection.

This section develops a methodology to calculate the time required to inspect the entire volume of a 10 mm cube AM sample, using SRAS. This total inspection time is presented as a multiple of the build time. The total inspection time is put into context using the time required for an XCT inspection of the same sample manufactured using various materials. Further context is given to this theoretical calculation by plotting the equivalent total inspection time for the rough surface SRAS-Qt system which worked out as 6.5 times the total build time. This is followed by the question “Was an inspection required on every build layer?”. The same method is used to model the time required to carry out an inspection every 2<sup>nd</sup>, 10<sup>th</sup> and 50<sup>th</sup> layer, which provides a total inspection time of 3.34, 0.66 and 0.13 multiples of the build time respectively. This shows how alongside improvements in spatial resolution, rough surface capability and faster, more optimised scanning, an in-process SRAS system is capable of inspecting the full volume of a part with minimal interruption to the build process. It also paves the way for future generations of in-line and on-line SRAS systems to be integrated into AM build platforms.

The final section of chapter 5 explores the concept of a hybrid LU system that combines the surface inspection capabilities of SRAS with the subsurface inspection capability of LIPA. The similarities of the base elements used by both LU systems mean that the design of a hybrid system only requires the changing of two elements to carry out the two different inspections. The combination of the two data sets obtained from these systems, alongside their future in-process inspection capabilities has the potential to provide very useful information regarding complex components built using layer-by-layer processes such as SLM and WAAM.

AM does not yet have the track record and depth of knowledge that traditional manufacturing processes such as milling and casting have. This means that they are prone to defects and errors which limit their implementation in the manufacturing industry. For this reason, assurances around part integrity are required for AM to become a fully-fledged manufacturing technique. This engineering doctorate utilises the unique opportunity layer-by-layer AM processes provided for carrying out an in-process inspection. The capabilities of the two LU techniques known as SRAS and LIPA have been investigated within this thesis due to their non-contact and non-destructive nature. Both these LU techniques are capable not only of providing useful information about the part being built but also informing the AM system as a means of process control. Once fully implemented, such an in-process inspection will be able to collect information from within the part to construct a digital twin of the part being built. This information can also be used in a closed-loop feedback system which would remove the need for post-manufacture inspections and result in the ultimate goal of zero defect parts.

# Bibliography

- [1] Rolls-Royce, “Rolls-Royce celebrates 50th anniversary of Power-by-the-Hour,” *Rolls-Royce Website*, 2012. <http://www.rolls-royce.com/media/press-releases/yr-2012/121030-the-hour.aspx> (accessed Feb. 20, 2017).
- [2] M. Cohen, “Power by the hour: Can paying only for performance redefine how products are sold and serviced,” *Wharton School of the University of Pennsylvania*, 2007. <http://knowledge.wharton.upenn.edu/article/power-by-the-hour-can-paying-only-for-performance-redefine-how-products-are-sold-and-serviced/> (accessed Feb. 21, 2017).
- [3] D. Appleyard, “Powering up on powder technology,” *Metal Powder Report*, vol. 70, no. 6, pp. 285–289, 2015, doi: 10.1016/j.mprp.2015.08.075.
- [4] L. Vinet and A. Zhedanov, “A ‘missing’ family of classical orthogonal polynomials,” *Journal of Physics A: Mathematical and Theoretical*, vol. 44, no. 8, pp. 10–12, 2011, doi: 10.1088/1751-8113/44/8/085201.
- [5] D. Herzog, V. Seyda, E. Wycisk, and C. Emmelmann, “Additive manufacturing of metals,” *Acta Materialia*, vol. 117, pp. 371–392, 2016, doi: 10.1016/j.actamat.2016.07.019.
- [6] B. P. Conner *et al.*, “Making sense of 3-D printing: Creating a map of additive manufacturing products and services,” *Additive Manufacturing*, vol. 1, pp. 64–76, 2014, doi: 10.1016/j.addma.2014.08.005.
- [7] S. Singamneni, Y. LV, A. Hewitt, R. Chalk, W. Thomas, and D. Jordison, “Additive Manufacturing for the Aircraft Industry: A Review,” *Journal of Aeronautics & Aerospace Engineering*, vol. 08, no. 01, p. 215, Feb. 2019, doi: 10.35248/2168-9792.19.8.215.
- [8] “Hydraulic manifold for aerospace redesigned for additive manufacturing with MTC, part-1,” *Gen3D*, 2021. [https://gen3d.com/news-and-articles/hydraulic-manifold-for-aerospace-redesigned-for-additive-manufacturing-part-2/?utm\\_content=170544006&utm\\_medium=social&utm\\_source=linkedin&hss\\_channel=lcp-33258515](https://gen3d.com/news-and-articles/hydraulic-manifold-for-aerospace-redesigned-for-additive-manufacturing-part-2/?utm_content=170544006&utm_medium=social&utm_source=linkedin&hss_channel=lcp-33258515) (accessed Jul. 01, 2021).

- [9] Z. Wang, Y. Zhang, and A. Bernard, "A constructive solid geometry-based generative design method for additive manufacturing," *Additive Manufacturing*, vol. 41, no. January, p. 101952, May 2021, doi: 10.1016/j.addma.2021.101952.
- [10] M. Pietropaoli, R. Ahlfeld, F. Montomoli, A. Ciani, and M. D'Ercole, "Design for Additive Manufacturing: Internal Channel Optimization," *Journal of Engineering for Gas Turbines and Power*, vol. 139, no. 10, pp. 1–8, 2017, doi: 10.1115/1.4036358.
- [11] A. Stevenson, "A cost model of part consolidation for additive manufacturing . EngD thesis , University of Nottingham . A Cost Model of Part Consolidation for Additive Manufacturing," University of Nottingham, 2018.
- [12] Metal-AM, "New GE plant to assemble world's first passenger jet engine with additive manufactured fuel nozzles," *Inovar Communications Ltd*, 2014. <https://www.metal-am.com/new-ge-plant-to-assemble-worlds-first-passenger-jet-engine-with-additive-manufactured-fuel-nozzles/> (accessed Oct. 08, 2020).
- [13] General Electric, "New manufacturing milestone: 30,000 additive fuel nozzles," *GE Additive*, 2018. <https://www.ge.com/additive/stories/new-manufacturing-milestone-30000-additive-fuel-nozzles%0Ahttps://www.ge.com/additive/blog/new-manufacturing-milestone-30000-additive-fuel-nozzles> (accessed Oct. 08, 2020).
- [14] Safran, "Successful first flight of LEAP-powered Airbus A320neo, with Safran engines and systems," *Safran-Group*, 2015. [https://www.safran-group.com/media/20150519\\_successful-first-flight-leap-powered-airbus-a320neo-safran-engines-and-systems](https://www.safran-group.com/media/20150519_successful-first-flight-leap-powered-airbus-a320neo-safran-engines-and-systems) (accessed Oct. 08, 2020).
- [15] Airbus, "Airbus A350-1000 Trent XWB-97 engine begins flight-test campaign on A380 flying-test-bed," *Airbus press release*, 2015. <https://www.airbus.com/newsroom/press-releases/en/2016/11/first-a350-1000-successfully-completes-first-flight.html> (accessed Apr. 14, 2020).
- [16] Airbus, "First A350-1000 successfully completes first flight," *Airbus press release*, 2016. <https://www.airbus.com/newsroom/press-releases/en/2015/11/airbus-a350-1000-trent-xwb-97-engine-begins-flight-test-campaign-on-a380-flying-test-bed.html> (accessed Feb. 20, 2017).
- [17] S. Nathan, "Rolls-Royce breaks additive record with printed Trent-XWB bearing," *The Engineer*, 2015. <https://www.theengineer.co.uk/issues/june-2015-digi-issue/rolls->

- royce-breaks-additive-record-with-printed-trent-xwb-bearing/ (accessed Apr. 14, 2020).
- [18] M. Sivak, D. J. Weintraub, and M. Flannagan, "Nonstop Flying Is Safer Than Driving," *Risk Analysis*, vol. 11, no. 1, pp. 145–148, Mar. 1991, doi: 10.1111/j.1539-6924.1991.tb00584.x.
  - [19] P. Johnston and R. Harris, "The Boeing 737 MAX Saga: Lessons for Software Organizations," *Software Quality Professional*, vol. 21, no. 3, pp. 4–12, 2019.
  - [20] National Transportation Safety Board, "Aircraft accident report - United airlines flight 232 McDonnell Douglas DC-10-10, NTSB/AAR-90/06," *Aircraft Accident Report*, pp. 1–126, 1990.
  - [21] France-BEA, "Accident to the AIRBUS A380-861 equipped with Engine Alliance GP7270 engines registered F-HPJE operated by Air France on 30 September 2017 in cruise over Greenland (Denmark)," *Bureau d'Enquêtes et d'Analyses pour la sécurité de l'aviation civile*, no. September, 2020.
  - [22] France-BEA, "Investigation Report - Accident to the AIRBUS A380-861," 2020.
  - [23] S. Pattnaik, D. B. Karunakar, and P. K. Jha, "Developments in investment casting process - A review," *Journal of Materials Processing Technology*, vol. 212, no. 11, pp. 2332–2348, 2012, doi: 10.1016/j.jmatprotec.2012.06.003.
  - [24] M. Hirsch *et al.*, "Targeted rework strategies for powder bed additive manufacture," *Additive Manufacturing*, vol. 19, no. November, pp. 127–133, 2018, doi: 10.1016/j.addma.2017.11.011.
  - [25] T. Moritz and S. Maleksaeedi, "Additive manufacturing of ceramic components," in *Additive Manufacturing: Materials, Processes, Quantifications and Applications*, Elsevier, 2018, pp. 105–161. doi: 10.1016/B978-0-12-812155-9.00004-9.
  - [26] S. Morales-Planas, J. Minguela-Canela, J. Lluma-Fuentes, J. A. Travieso-Rodriguez, and A. A. García-Granada, "Multi Jet Fusion PA12 manufacturing parameters for watertightness, strength and tolerances," *Materials*, vol. 11, no. 8, pp. 1–11, 2018, doi: 10.3390/ma11081472.
  - [27] N. Link and R. Semiat, "Ink drop motion in wide-format printers. I. Drop flow from Drop-On-Demand (DOD) printing heads," *Chemical Engineering and Processing: Process Intensification*, vol. 100, pp. 1–10, 2016, doi: 10.1016/j.cep.2015.11.016.

- Process Intensification*, vol. 48, no. 1, pp. 68–83, 2009, doi: 10.1016/j.cep.2008.02.005.
- [28] M. Hudspeth, “Rapid prototyping,” in *Catalyst*, vol. 24, no. 2, Elsevier, 2007, pp. 44–46. doi: 10.1016/B978-0-12-382038-9.00014-4.
- [29] S. Rahmati, “Direct Rapid Tooling,” in *Comprehensive Materials Processing*, vol. 10, Elsevier Ltd, 2014, pp. 303–344. doi: 10.1016/B978-0-08-096532-1.01013-X.
- [30] M. Zenou and L. Grainger, “Additive manufacturing of metallic materials,” in *Additive Manufacturing: Materials, Processes, Quantifications and Applications*, Elsevier, 2018, pp. 53–103. doi: 10.1016/B978-0-12-812155-9.00003-7.
- [31] S. Ocylok, E. Alexeev, S. Mann, A. Weisheit, K. Wissenbach, and I. Kelbassa, “Correlations of melt pool geometry and process parameters during laser metal deposition by coaxial process monitoring,” *Physics Procedia*, vol. 56, no. C, pp. 228–238, 2014, doi: 10.1016/j.phpro.2014.08.167.
- [32] A. Gasser, G. Backes, I. Kelbassa, A. Weisheit, and K. Wissenbach, “Laser Additive Manufacturing,” *Laser Technik Journal*, vol. 7, no. 2, pp. 58–63, 2010, doi: 10.1002/latj.201090029.
- [33] S. W. Williams, F. Martina, A. C. Addison, J. Ding, G. Pardal, and P. Colegrove, “Wire + Arc additive manufacturing,” *Materials Science and Technology (United Kingdom)*, vol. 32, no. 7, pp. 641–647, May 2016, doi: 10.1179/1743284715Y.0000000073.
- [34] P. Dryburgh *et al.*, “Spatially resolved acoustic spectroscopy for integrity assessment in wire–arc additive manufacturing,” *Additive Manufacturing*, vol. 28, no. April, pp. 236–251, 2019, doi: 10.1016/j.addma.2019.04.015.
- [35] S. H. Masood, “Advances in Fused Deposition Modeling,” in *Comprehensive Materials Processing*, vol. 10, Elsevier Ltd, 2014, pp. 69–91. doi: 10.1016/B978-0-08-096532-1.01002-5.
- [36] A. Mostaghimi *et al.*, “Rapid prototyping and clinical testing of a reusable face shield for health care workers responding to the COVID-19 pandemic,” *medRxiv*, 2020, doi: 10.1101/2020.04.11.20061960.
- [37] M. Wilhelm, K. D. Wissenbach, and A. D. Gasser, “Patent : DE19649865C1 - Shaped body especially prototype or replacement part production,” *DE Patent*, 1996.

- [38] D. Gu, "Laser Additive Manufacturing (AM): Classification, Processing Philosophy, and Metallurgical Mechanisms," in *Laser Additive Manufacturing of High-Performance Materials*, Springer Berlin Heidelberg, 2015, pp. 15–71. doi: 10.1007/978-3-662-46089-4\_2.
- [39] S. Sanchez *et al.*, "Powder Bed Fusion of nickel-based superalloys: A review," *International Journal of Machine Tools and Manufacture*, vol. 165, p. 103729, Jun. 2021, doi: 10.1016/j.ijmachtools.2021.103729.
- [40] T. G. Spears and S. A. Gold, "In-process sensing in selective laser melting (SLM) additive manufacturing," *Integrating Materials and Manufacturing Innovation*, vol. 5, no. 1, pp. 16–40, 2016, doi: 10.1186/s40192-016-0045-4.
- [41] M. Mani, S. Feng, B. Lane, A. Donmez, S. Moylan, and R. Fesperman, "Measurement science needs for real-time control of additive manufacturing powder-bed fusion processes," *Additive Manufacturing Handbook: Product Development for the Defense Industry*, vol. 8036, no. September, pp. 629–676, 2017, doi: 10.1201/9781315119106.
- [42] T. Kurzynowski, E. Chlebus, B. Kuźnicka, and J. Reiner, "Parameters in selective laser melting for processing metallic powders," in *High Power Laser Materials Processing: Lasers, Beam Delivery, Diagnostics, and Applications*, Feb. 2012, vol. 8239, p. 823914. doi: 10.1117/12.907292.
- [43] M. V Elsen, *Complexity of selective laser melting: a new optimisation approach*. Phd. Department of Mechanical Engineering. 2007.
- [44] D. D. Gu, W. Meiners, K. Wissenbach, and R. Poprawe, "Laser additive manufacturing of metallic components: Materials, processes and mechanisms," *International Materials Reviews*, vol. 57, no. 3, pp. 133–164, May 2012, doi: 10.1179/1743280411Y.0000000014.
- [45] M. Wang, B. Song, Q. Wei, Y. Zhang, and Y. Shi, "Effects of annealing on the microstructure and mechanical properties of selective laser melted AlSi7Mg alloy," *Materials Science and Engineering A*, vol. 739, pp. 463–472, Jan. 2019, doi: 10.1016/j.msea.2018.10.047.
- [46] F. Trevisan *et al.*, "On the selective laser melting (SLM) of the AlSi10Mg alloy: Process, microstructure, and mechanical properties," *Materials*, vol. 10, no. 1, 2017, doi: 10.3390/ma10010076.

- [47] Renishaw, “In625-0402 powder for additive manufacturing,” 2001. <http://resources.renishaw.com/en/download/data-sheet-alsi10mg-0403-400-w-powder-for-additive-manufacturing--73122>
- [48] M. J. Donachie, *Titanium: A Technical Guide*, vol. 99, no. 5. 2012.
- [49] S. Liu and Y. C. Shin, “Additive manufacturing of Ti6Al4V alloy: A review,” *Materials and Design*, vol. 164, p. 107552, Feb. 2019, doi: 10.1016/j.matdes.2018.107552.
- [50] Don. Pieris, “Advanced Gas Turbine Concepts,” 2015.
- [51] B. Sarre, S. Flouriot, G. Geandier, B. Panicaud, and V. De Rancourt, “Mechanical behavior and fracture mechanisms of titanium alloy welded joints made by pulsed laser beam welding,” in *Procedia Structural Integrity*, 2016, vol. 2, pp. 3569–3576. doi: 10.1016/j.prostr.2016.06.445.
- [52] P. Law, “Lockheed SR-71 Propulsion System P&W J58 Engine ( JT11D-20 ),” 1991.
- [53] C. Laboratories, *Development of Explosive-Welding Techniques for Fabrication of Regeneratively Cooled Thrust Chambers for Large-Rocket- Engine Requirements*. 1971.
- [54] Haynes International, “Principal Features HASTELLOY ® X alloy,” vol. 06002, no. 2, 2019.
- [55] D. F. Paulonis and J. J. Schirra, “Alloy 718 at Pratt & Whitney - Historical perspective and future challenges,” *Proceedings of the International Symposium on Superalloys and Various Derivatives*, vol. 1, pp. 13–23, 2001, doi: 10.7449/2001/superalloys\_2001\_13\_23.
- [56] “Inconel 718 Tech Data.”
- [57] X. Z. Jin, “Study on the Fresnel absorption and multiple reflections in a conical keyhole,” *Hunan Daxue Xuebao/Journal of Hunan University Natural Sciences*, vol. 31, no. 6, pp. 32–37, 2004.
- [58] B. Lane, S. Moylan, E. P. Whitenton, and L. Ma, “Thermographic measurements of the commercial laser powder bed fusion process at NIST,” *Rapid Prototyping Journal*, vol. 22, no. 5, pp. 778–787, 2016, doi: 10.1108/RPJ-11-2015-0161.
- [59] T. W. Eagar and N. S. Tsai, “Temperature Fields Produced By Travelling Distributed Heat Sources.,” *Welding Journal*, vol. 62, no. 12, pp. 154–155, 1983.

- [60] A. P. Mackwood and R. C. Crafer, "Thermal modelling of laser welding and related processes: A literature review," *Optics and Laser Technology*, vol. 37, no. 2, pp. 99–115, Mar. 2005, doi: 10.1016/j.optlastec.2004.02.017.
- [61] A. V. Gusarov, I. Yadroitsev, P. Bertrand, and I. Smurov, "Heat transfer modelling and stability analysis of selective laser melting," *Applied Surface Science*, vol. 254, no. 4, pp. 975–979, 2007, doi: 10.1016/j.apsusc.2007.08.074.
- [62] J. Winczek, A. Modrzycka, and E. Gawrońska, "Analytical description of the temperature field induced by laser heat source with any trajectory," *Procedia Engineering*, vol. 149, no. June, pp. 553–558, 2016, doi: 10.1016/j.proeng.2016.06.704.
- [63] Y. Yang, M. F. Knol, F. van Keulen, and C. Ayas, "A semi-analytical thermal modelling approach for selective laser melting," *Additive Manufacturing*, vol. 21, pp. 284–297, 2018, doi: 10.1016/j.addma.2018.03.002.
- [64] H. Gu *et al.*, "Multi-physics modelling of molten pool development and track formation in multi-track, multi-layer and multi-material selective laser melting," *International Journal of Heat and Mass Transfer*, vol. 151, p. 119458, 2020, doi: 10.1016/j.ijheatmasstransfer.2020.119458.
- [65] M. Kirka, R. Bansal, and S. Das, "Recent progress on scanning laser epitaxy: A new technique for growing single crystal superalloys," *20th Annual International Solid Freeform Fabrication Symposium, SFF 2009*, pp. 799–806, 2009.
- [66] R. Bansal, R. Acharya, J. J. Gambone, and S. Das, "Experimental and theoretical analysis of scanning laser epitaxy applied to nickel-based superalloys," *22nd Annual International Solid Freeform Fabrication Symposium - An Additive Manufacturing Conference, SFF 2011*, pp. 496–503, 2011.
- [67] M. Grasso and B. M. Colosimo, "Process defects and in situ monitoring methods in metal powder bed fusion: A review," *Measurement Science and Technology*, vol. 28, no. 4, p. 044005, 2017, doi: 10.1088/1361-6501/aa5c4f.
- [68] A. J. Nathan and A. Scobell, "How China sees America," *Foreign Affairs*, vol. 91, no. 5, pp. 1689–1699, 2012, doi: 10.1017/CBO9781107415324.004.

- [69] I. Maskery *et al.*, “Quantification and characterisation of porosity in selectively laser melted Al-Si10-Mg using X-ray computed tomography,” *Materials Characterization*, vol. 111, pp. 193–204, 2016, doi: 10.1016/j.matchar.2015.12.001.
- [70] H. C. Pavanati, A. M. Maliska, A. N. Klein, and J. L. R. Muzart, “Comparative study of porosity and pores morphology of unalloyed iron sintered in furnace and plasma reactor,” *Materials Research*, vol. 10, no. 1, pp. 87–93, 2007, doi: 10.1590/S1516-14392007000100019.
- [71] B. M. Sharratt, “Non-Destructive Techniques and Technologies for Qualification of Additive Manufactured Parts and Processes: A Literature Review,” *Department of National Defence of Canada*, vol. 55, no. March, pp. 95–100, 2015.
- [72] T. Mukherjee, W. Zhang, and T. DebRoy, “An improved prediction of residual stresses and distortion in additive manufacturing,” *Computational Materials Science*, vol. 126, pp. 360–372, 2017, doi: 10.1016/j.commatsci.2016.10.003.
- [73] L. N. Carter, C. Martin, P. J. Withers, and M. M. Attallah, “The influence of the laser scan strategy on grain structure and cracking behaviour in SLM powder-bed fabricated nickel superalloy,” *Journal of Alloys and Compounds*, vol. 615, pp. 338–347, 2014, doi: 10.1016/j.jallcom.2014.06.172.
- [74] M. F. Zäh and S. Lutzmann, “Modelling and simulation of electron beam melting,” *Production Engineering*, vol. 4, no. 1, pp. 15–23, Feb. 2010, doi: 10.1007/s11740-009-0197-6.
- [75] D. Gu and Y. Shen, “Balling phenomena in direct laser sintering of stainless steel powder: Metallurgical mechanisms and control methods,” *Materials and Design*, vol. 30, no. 8, pp. 2903–2910, 2009, doi: 10.1016/j.matdes.2009.01.013.
- [76] D. Pieris *et al.*, “Laser Induced Phased Arrays (LIPA) to detect nested features in additively manufactured components,” *Materials and Design*, vol. 187, p. 108412, Feb. 2020, doi: 10.1016/j.matdes.2019.108412.
- [77] S. Tsopanos *et al.*, “The influence of processing parameters on the mechanical properties of selectively laser melted stainless steel microlattice structures,” *Journal of Manufacturing Science and Engineering, Transactions of the ASME*, vol. 132, no. 4, pp. 0410111–04101112, 2010, doi: 10.1115/1.4001743.

- [78] A. Du Plessis, I. Yadroitsev, I. Yadroitsava, and S. G. Le Roux, "X-Ray Microcomputed Tomography in Additive Manufacturing: A Review of the Current Technology and Applications," *3D Printing and Additive Manufacturing*, vol. 5, no. 3, pp. 227–247, Sep. 2018, doi: 10.1089/3dp.2018.0060.
- [79] X. Zhou *et al.*, "3D-imaging of selective laser melting defects in a Co-Cr-Mo alloy by synchrotron radiation micro-CT," *Acta Materialia*, vol. 98, pp. 1–16, 2015, doi: 10.1016/j.actamat.2015.07.014.
- [80] J. P. Kruth, L. Froyen, J. Van Vaerenbergh, P. Mercelis, M. Rombouts, and B. Lauwers, "Selective laser melting of iron-based powder," in *Journal of Materials Processing Technology*, Jun. 2004, vol. 149, no. 1–3, pp. 616–622. doi: 10.1016/j.jmatprotec.2003.11.051.
- [81] S. Catchpole-Smith, N. Aboulkhair, L. Parry, C. Tuck, I. A. Ashcroft, and A. Clare, "Fractal scan strategies for selective laser melting of 'unweldable' nickel superalloys," *Additive Manufacturing*, vol. 15, pp. 113–122, 2017, doi: 10.1016/j.addma.2017.02.002.
- [82] B. Vandenbroucke and J. P. Kruth, "Selective laser melting of biocompatible metals for rapid manufacturing of medical parts," in *17th Solid Freeform Fabrication Symposium, SFF 2006*, 2006, pp. 148–159.
- [83] M. Hirsch *et al.*, "Assessing the capability of in-situ nondestructive analysis during layer based additive manufacture," *Additive Manufacturing*, vol. 13, pp. 135–142, 2017, doi: 10.1016/j.addma.2016.10.004.
- [84] K. V. Gogolinskii and V. A. Syasko, "Actual metrological and legal issues of non-destructive testing," in *Journal of Physics: Conference Series*, 2019, vol. 1379, no. 1, p. 12045. doi: 10.1088/1742-6596/1379/1/012045.
- [85] P. M. Clifford, "The international vocabulary of basic and general terms in metrology," *Measurement*, vol. 3, no. 2, pp. 72–76, 1985, doi: 10.1016/0263-2241(85)90006-5.
- [86] K. H. Goh, N. Phillips, and R. Bell, "The applicability of a laser triangulation probe to non-contacting inspection," *International Journal of Production Research*, vol. 24, no. 6, pp. 1331–1348, 1986, doi: 10.1080/00207548608919807.

- [87] S. Carmignato and E. Savio, "Traceable volume measurements using coordinate measuring systems," *CIRP Annals - Manufacturing Technology*, vol. 60, no. 1, pp. 519–522, Jan. 2011, doi: 10.1016/j.cirp.2011.03.061.
- [88] P. I. Stavroulakis and R. K. Leach, "Invited Review Article: Review of post-process optical form metrology for industrial-grade metal additive manufactured parts," *Review of Scientific Instruments*, vol. 87, no. 4, p. 041101, Apr. 2016, doi: 10.1063/1.4944983.
- [89] B. Zhang, J. Ziegert, F. Farahi, and A. Davies, "In situ surface topography of laser powder bed fusion using fringe projection," *Additive Manufacturing*, vol. 12, pp. 100–107, 2016, doi: 10.1016/j.addma.2016.08.001.
- [90] P. Keller and R. Mendricky, "Parameters influencing the precision of slm production," *MM Science Journal*, vol. 2015, no. OCTOBER, pp. 705–710, Oct. 2015, doi: 10.17973/MMSJ.2015\_10\_201540.
- [91] S. Afazov *et al.*, "A methodology for precision additive manufacturing through compensation," *Precision Engineering*, vol. 50, pp. 269–274, Oct. 2017, doi: 10.1016/j.precisioneng.2017.05.014.
- [92] "Sensofar Metrology technology - Multiple techniques."
- [93] R. Danzl, F. Helml, and S. Scherer, "Focus variation - A robust technology for high resolution optical 3D surface metrology," *Strojnicki Vestnik/Journal of Mechanical Engineering*, vol. 57, no. 3, pp. 245–256, 2011, doi: 10.5545/sv-jme.2010.175.
- [94] M. Conroy and J. Armstrong, "A comparison of surface metrology techniques," *Journal of Physics: Conference Series*, vol. 13, pp. 458–465, 2005, doi: 10.1088/1742-6596/13/1/106.
- [95] R. Su, Y. Wang, J. Coupland, and R. Leach, "On tilt and curvature dependent errors and the calibration of coherence scanning interferometry," *Optics Express*, vol. 25, no. 4, p. 3297, Feb. 2017, doi: 10.1364/oe.25.003297.
- [96] G. Strano, L. Hao, R. M. Everson, and K. E. Evans, "Surface roughness analysis, modelling and prediction in selective laser melting," *Journal of Materials Processing Technology*, vol. 213, no. 4, pp. 589–597, Apr. 2013, doi: 10.1016/j.jmatprotec.2012.11.011.

- [97] D. M. Shah and A. Cetel, "Evaluation of PWA1483 for Large single crystal IGT Blade Applications," pp. 295–304, 2012, doi: 10.7449/2000/superalloys\_2000\_295\_304.
- [98] J. A. Kanko, A. P. Sibley, and J. M. Fraser, "In situ morphology-based defect detection of selective laser melting through inline coherent imaging," *Journal of Materials Processing Technology*, vol. 231, pp. 488–500, 2016, doi: 10.1016/j.jmatprotec.2015.12.024.
- [99] S. Keaveney, A. Shmeliov, V. Nicolosi, and D. P. Dowling, "Investigation of process by-products during the Selective Laser Melting of Ti6Al4V powder," *Additive Manufacturing*, vol. 36, p. 101514, Dec. 2020, doi: 10.1016/j.addma.2020.101514.
- [100] Renishaw Plc., "InfiniAM Central – remote process monitoring for AM systems Introduction," *Report*, 2017. <http://resources.renishaw.com/en/details/data-sheet-renam-500q--99032>
- [101] L. J. Jiang *et al.*, "A perspective on medical infrared imaging," *Journal of Medical Engineering and Technology*, vol. 29, no. 6. Taylor & Francis, pp. 257–267, Dec. 01, 2005. doi: 10.1080/03091900512331333158.
- [102] J. R. Speakman and S. Ward, "Infrared thermography: principles and applications," 1998.
- [103] Á. H. Herraiz, A. P. Marugán, and F. P. G. Márquez, "A review on condition monitoring system for solar plants based on thermography," in *Non-Destructive Testing and Condition Monitoring Techniques for Renewable Energy Industrial Assets*, 2019, pp. 103–118. doi: 10.1016/B978-0-08-101094-5.00007-1.
- [104] M. Islam, T. Purtonen, H. Piili, A. Salminen, and O. Nyrhilä, "Temperature profile and imaging analysis of laser additive manufacturing of stainless steel," *Physics Procedia*, vol. 41, pp. 835–842, 2013, doi: 10.1016/j.phpro.2013.03.156.
- [105] H. Krauss, C. Eschey, and M. F. Zaeh, "Thermography for monitoring the selective laser melting process," in *23rd Annual International Solid Freeform Fabrication Symposium - An Additive Manufacturing Conference, SFF 2012*, 2012, pp. 999–1014.
- [106] R. R. Carlton and A. M. Adler, "Radiographic film," *Principles of radiographic imaging: an art and a science CN - WN200 C285p 2013*, 2013. <https://www.nde-ed.org/EducationResources/CommunityCollege/Radiography/EquipmentMaterials/radiographicfilm.htm> (accessed Apr. 29, 2020).

- [107] A. Thompson, I. Maskery, and R. K. Leach, "X-ray computed tomography for additive manufacturing: A review," *Measurement Science and Technology*, vol. 27, no. 7, p. 72001, Jun. 2016, doi: 10.1088/0957-0233/27/7/072001.
- [108] J. Mireles, S. Ridwan, P. A. Morton, A. Hinojos, and R. B. Wicker, "Analysis and correction of defects within parts fabricated using powder bed fusion technology," *Surface Topography: Metrology and Properties*, vol. 3, no. 3, 2015, doi: 10.1088/2051-672X/3/3/034002.
- [109] F. H. Kim, H. Villarraga-Gómez, and S. P. Moylan, "Inspection of embedded internal features in additively manufactured metal parts using metrological x-ray computed tomography," in *Proceedings - ASPE/euspen 2016 Summer Topical Meeting: Dimensional Accuracy and Surface Finish in Additive Manufacturing*, 2016, no. June, pp. 191–195.
- [110] C. L. A. Leung, S. Marussi, R. C. Atwood, M. Towrie, P. J. Withers, and P. D. Lee, "In situ X-ray imaging of defect and molten pool dynamics in laser additive manufacturing," *Nature Communications*, vol. 9, no. 1, pp. 1–9, 2018, doi: 10.1038/s41467-018-03734-7.
- [111] W. J. Sames, F. A. List, S. Pannala, R. R. Dehoff, and S. S. Babu, "The metallurgy and processing science of metal additive manufacturing," *International Materials Reviews*, vol. 61, no. 5, pp. 315–360, 2016, doi: 10.1080/09506608.2015.1116649.
- [112] M. de Assumpção Pereira-da-Silva and F. A. Ferri, "Scanning Electron Microscopy," in *Nanocharacterization Techniques*, Elsevier Inc., 2017, pp. 1–35. doi: 10.1016/B978-0-323-49778-7.00001-1.
- [113] S. Nishikawa and S. Kikuchi, "Diffraction of cathode rays by calcite [4]," *Nature*, vol. 122, no. 3080. Nature Publishing Group, p. 726, 1928. doi: 10.1038/122726a0.
- [114] A. T. Polonsky, M. P. Echlin, W. C. Lenthe, R. R. Dehoff, M. M. Kirka, and T. M. Pollock, "Defects and 3D structural inhomogeneity in electron beam additively manufactured Inconel 718," *Materials Characterization*, vol. 143, pp. 171–181, Sep. 2018, doi: 10.1016/j.matchar.2018.02.020.
- [115] C. Körner, H. Helmer, A. Bauereiß, and R. F. Singer, "Tailoring the grain structure of IN718 during selective electron beam melting," *MATEC Web of Conferences*, vol. 14, p. 08001, 2014, doi: 10.1051/matecconf/20141408001.

- [116] D. J. Browne, “Modelling Columnar and Equiaxed Growth,” 2002.
- [117] R. R. Dehoff *et al.*, “Site specific control of crystallographic grain orientation through electron beam additive manufacturing,” *Materials Science and Technology (United Kingdom)*, vol. 31, no. 8, pp. 931–938, 2015, doi: 10.1179/1743284714Y.0000000734.
- [118] R. R. Dehoff, M. M. Kirka, F. A. List, K. A. Unocic, and W. J. Sames, “Crystallographic texture engineering through novel melt strategies via electron beam melting: Inconel 718,” *Materials Science and Technology (United Kingdom)*, vol. 31, no. 8, pp. 939–944, 2015, doi: 10.1179/1743284714Y.0000000697.
- [119] J. Raplee *et al.*, “Thermographic Microstructure Monitoring in Electron Beam Additive Manufacturing,” *Scientific Reports*, vol. 7, no. October 2016, p. 43554, 2017, doi: 10.1038/srep43554.
- [120] B. de Mayo, *The Everyday Physics of Hearing and Vision*. Morgan & Claypool Publishers, 2015. doi: 10.1088/978-1-6270-5675-5.
- [121] M. Schanz and M. Schanz, “Wave propagation,” *Wave Propagation in Viscoelastic and Poroelastic Continua*, 2001. <https://www.nde-ed.org/EducationResources/CommunityCollege/Ultrasonics/Physics/wavepropagation.htm> (accessed Oct. 02, 2020).
- [122] “Speed of Sound in Solids and Metals,” *Engineering ToolBox*, 2004. [https://www.engineeringtoolbox.com/sound-speed-solids-d\\_713.html](https://www.engineeringtoolbox.com/sound-speed-solids-d_713.html) (accessed May 28, 2021).
- [123] K. V. Jata, T. Kundu, and T. A. Parthasarathy, “An Introduction to Failure Mechanisms and Ultrasonic Inspection,” in *Advanced Ultrasonic Methods for Material and Structure Inspection*, Wiley-ISTE, 2010, pp. 1–42. doi: 10.1002/9780470612248.ch1.
- [124] D. Royer and D. Clorennec, “Theoretical and Experimental Investigation of Rayleigh Waves on Spherical and Cylindrical Surfaces,” 2008.
- [125] P. Aryan, A. Kotousov, C. T. Ng, and B. S. Cazzolato, “Lamb wave characterisation and damage imaging for isotropic plate-like structures using 3D laser vibrometry,” in *Recent Advances in Structural Integrity Analysis - Proceedings of the International Congress (APCF/SIF-2014)*, Elsevier, 2014, pp. 585–589. doi: 10.1533/9780081002254.585.

- [126] J. Krautkraemer, H. Krautkraemer, and W. Sachse, *Ultrasonic Testing of Materials*, vol. 51, no. 1. Berlin: Springer-Verlag, 1984. doi: 10.1115/1.3167589.
- [127] M. Redwood, *Rayleigh and Lamb waves*, vol. 5, no. 4. New York: Plenum Press, 1967. doi: 10.1016/0041-624x(67)90079-0.
- [128] C. Holmes, B. W. Drinkwater, and P. D. Wilcox, "Advanced post-processing for scanned ultrasonic arrays: Application to defect detection and classification in non-destructive evaluation," *Ultrasonics*, vol. 48, no. 6–7, pp. 636–642, 2008, doi: 10.1016/j.ultras.2008.07.019.
- [129] J. Zhang, B. Drinkwater, and P. D. Wilcox, "Comparison of ultrasonic array imaging algorithms for nondestructive evaluation," *IEEE Transactions on Ultrasonics, Ferroelectrics, and Frequency Control*, vol. 60, no. 8, pp. 1732–1745, 2013, doi: 10.1109/TUFFC.2013.2754.
- [130] Ö. Oralkan *et al.*, "Capacitive micromachined ultrasonic transducers: Next-generation arrays for acoustic imaging?," *IEEE Transactions on Ultrasonics, Ferroelectrics, and Frequency Control*, vol. 49, no. 11, pp. 1596–1610, Nov. 2002, doi: 10.1109/TUFFC.2002.1049742.
- [131] C. Holmes, B. W. Drinkwater, and P. D. Wilcox, "Post-processing of the full matrix of ultrasonic transmit-receive array data for non-destructive evaluation," *NDT and E International*, vol. 38, no. 8, pp. 701–711, 2005, doi: 10.1016/j.ndteint.2005.04.002.
- [132] H. Rieder, A. Dillhöfer, M. Spies, J. Bamberg, and T. Hess, "Online Monitoring of Additive Manufacturing Processes Using Ultrasound 2 . Additive Manufacturing and Quality Assurance Considerations 3 . Ultrasonic Process Monitoring," *Proceedings of the 11th European Conference on Non-Destructive Testing*, vol. 1, no. Ecndt, pp. 2194–2201, 2014.
- [133] H. Rieder, M. Spies, J. Bamberg, and B. Henkel, "On- and Offline Ultrasonic Inspection of Additively Manufactured Components," *19th World Conference on Non-Destructive Testing 2016*, pp. 1–8, 2016.
- [134] A. Chabot, N. Laroche, E. Carcreff, M. Rauch, and J. Y. Hascoët, "Towards defect monitoring for metallic additive manufacturing components using phased array ultrasonic testing," *Journal of Intelligent Manufacturing*, vol. 31, no. 5, pp. 1191–1201, 2020, doi: 10.1007/s10845-019-01505-9.

- [135] Y. Javadi *et al.*, "Continuous monitoring of an intentionally-manufactured crack using an automated welding and in-process inspection system," *Materials and Design*, vol. 191, p. 108655, 2020, doi: 10.1016/j.matdes.2020.108655.
- [136] C. Kim, H. Yin, A. Shmatok, B. C. Prorok, X. Lou, and K. H. Matlack, "Ultrasonic nondestructive evaluation of laser powder bed fusion 316L stainless steel," *Additive Manufacturing*, vol. 38, no. November 2020, p. 101800, 2021, doi: 10.1016/j.addma.2020.101800.
- [137] C. B. Scruby and L. E. Drain, *Laser Ultrasonics*, 1st Editio. Bristo: Adam Hilger, 1990. doi: 10.1201/9780203749098.
- [138] A. M. Aindow, R. J. Dewhurst, and S. B. Palmer, "Laser-generation of directional surface acoustic wave pulses in metals," *Optics Communications*, vol. 42, no. 2, pp. 116–120, Jun. 1982, doi: 10.1016/0030-4018(82)90378-9.
- [139] D. Scruby, C.B L.E, *Laser Ultrasonics Techniques and Applications*, vol. 1, no. 1. 1990.
- [140] J. P. Monchalin, "Optical Detection of Ultrasound," *IEEE Transactions on Ultrasonics, Ferroelectrics, and Frequency Control*, vol. 33, no. 5, pp. 485–499, 1986, doi: 10.1109/T-UFFC.1986.26860.
- [141] M. Polyanskiy, "Refractive Index Info," *RefractiveIndex.info*, 2015. <https://refractiveindex.info/> (accessed Jul. 21, 2021).
- [142] A. D. Rakić, "Algorithm for the determination of intrinsic optical constants of metal films: application to aluminum," *Applied Optics*, vol. 34, no. 22, p. 4755, Aug. 1995, doi: 10.1364/ao.34.004755.
- [143] P. B. Johnson and R. W. Christy, "Optical constants of the noble metals," *Physical Review B*, vol. 6, no. 12, pp. 4370–4379, 1972, doi: 10.1103/PhysRevB.6.4370.
- [144] J. Ke, C. Duan, W. Yi, and C. Yan, "Application of an adaptive two-wave mixing interferometer for detection of surface defects," *2016 Progress In Electromagnetics Research Symposium, PIERS 2016 - Proceedings*, pp. 2142–2146, 2016, doi: 10.1109/PIERS.2016.7734892.
- [145] B. Pouet, S. Breugnot, and P. Clémenceau, "An innovative interferometer for industrial laser ultrasonic inspection," *AIP Conference Proceedings*, vol. 760, no. 2005, pp. 273–280, 2005, doi: 10.1063/1.1916688.

- [146] R. L. Whitman and A. Korpel, "Probing of Acoustic Surface Perturbations by Coherent Light," *Applied Optics*, vol. 8, no. 8, p. 1567, 1969, doi: 10.1364/ao.8.001567.
- [147] S. D. Sharples *et al.*, "The SKED: Speckle knife edge detector," in *Journal of Physics: Conference Series*, 2014, vol. 520, no. 1, p. 012004. doi: 10.1088/1742-6596/520/1/012004.
- [148] G. Davis, K. Balasubramaniam, S. Palanisamy, R. Nagarajah, and P. Rajagopal, "Additively manufactured integrated slit mask for laser ultrasonic guided wave inspection," *International Journal of Advanced Manufacturing Technology*, vol. 110, no. 5–6, pp. 1203–1217, 2020, doi: 10.1007/s00170-020-05946-y.
- [149] S. K. Everton, P. Dickens, C. Tuck, and B. Dutton, "Identification of sub-surface defects in parts produced by additive manufacturing, using laser generated ultrasound," *Materials Science and Technology Conference and Exhibition 2016, MS and T 2016*, vol. 1, pp. 141–148, 2016.
- [150] C. Millon, A. Vanhoye, A. F. Obaton, and J. D. Penot, "Development of laser ultrasonics inspection for online monitoring of additive manufacturing," *Welding in the World*, vol. 62, no. 3, pp. 653–661, 2018, doi: 10.1007/s40194-018-0567-9.
- [151] R. J. Smith, M. Hirsch, R. Patel, W. Li, A. T. Clare, and S. D. Sharples, "Spatially resolved acoustic spectroscopy for selective laser melting," *Journal of Materials Processing Technology*, vol. 236, pp. 93–102, 2016, doi: 10.1016/j.jmatprotec.2016.05.005.
- [152] M. Hirsch *et al.*, "Meso-scale defect evaluation of selective laser melting using spatially resolved acoustic spectroscopy," *Proceedings of the Royal Society A: Mathematical, Physical and Engineering Sciences*, vol. 473, no. 2202, p. 20170194, 2017, doi: 10.1098/rspa.2017.0194.
- [153] T. Stratoudaki, Y. Javadi, W. Kerr, P. D. P. D. P. D. Wilcox, D. Pieris, and M. Clark, "Laser induced phased arrays for remote ultrasonic imaging of additive manufactured components," *NDT 2018 - 57th Annual Conference of the British Institute of Non-Destructive Testing*, pp. 174–182, 2018.
- [154] J. Zhang *et al.*, "Laser ultrasonic imaging for defect detection on metal additive manufacturing components with rough surfaces," *Applied Optics*, vol. 59, no. 33, p. 10380, 2020, doi: 10.1364/ao.405284.

- [155] J. Singh *et al.*, "Component shape optimisation for enhanced non-destructive testing," *Materials and Design*, vol. 195, p. 109041, 2020, doi: 10.1016/j.matdes.2020.109041.
- [156] R. J. Dewhurst and Q. Shan, "Optical remote measurement of ultrasound," *Measurement Science and Technology*, vol. 10, no. 11. Institute of Physics Publishing, pp. 139–168, Nov. 01, 1999. doi: 10.1088/0957-0233/10/11/201.
- [157] R. Patel *et al.*, "Imaging material texture of as-deposited selective laser melted parts using spatially resolved acoustic spectroscopy," *Applied Sciences (Switzerland)*, vol. 8, no. 10, p. 1991, Oct. 2018, doi: 10.3390/app8101991.
- [158] G. Davis, R. Nagarajah, S. Palanisamy, R. A. R. Rashid, P. Rajagopal, and K. Balasubramaniam, "Laser ultrasonic inspection of additive manufactured components," *International Journal of Advanced Manufacturing Technology*, vol. 102, no. 5–8, pp. 2571–2579, 2019, doi: 10.1007/s00170-018-3046-y.
- [159] Y. Javadi *et al.*, "Ultrasonic phased array inspection of a Wire + Arc Additive Manufactured (WAAM) sample with intentionally embedded defects," *Additive Manufacturing*, vol. 29, no. July, p. 100806, Oct. 2019, doi: 10.1016/j.addma.2019.100806.
- [160] A. Bauereiß, T. Scharowsky, and C. Körner, "Defect generation and propagation mechanism during additive manufacturing by selective beam melting," *Journal of Materials Processing Technology*, vol. 214, no. 11, pp. 2522–2528, 2014, doi: 10.1016/j.jmatprotec.2014.05.002.
- [161] S. D. Sharples, M. Clark, and M. G. Somekh, "Spatially resolved acoustic spectroscopy for fast noncontact imaging of material microstructure," *Optics Express*, vol. 14, no. 22, p. 10435, 2006, doi: 10.1364/oe.14.010435.
- [162] Don. Pieris *et al.*, "Spatially Resolved Acoustic Spectroscopy Towards Online Inspection of Additive Manufacturing," *Insight - Non-Destructive Testing and Condition Monitoring*, vol. 61, no. 3, pp. 132–137, Mar. 2019, doi: 10.1784/insi.2019.61.3.132.
- [163] W. J. Sames, K. A. Unocic, R. R. Dehoff, T. Lolla, and S. S. Babu, "Thermal effects on microstructural heterogeneity of Inconel 718 materials fabricated by electron beam melting," *Journal of Materials Research*, vol. 29, no. 17, pp. 1920–1930, 2014, doi: 10.1557/jmr.2014.140.

- [164] Y. S. Lee and W. Zhang, "Modeling of heat transfer, fluid flow and solidification microstructure of nickel-base superalloy fabricated by laser powder bed fusion," *Additive Manufacturing*, vol. 12, pp. 178–188, Oct. 2016, doi: 10.1016/j.addma.2016.05.003.
- [165] M. Gäumann, S. Henry, F. Cléton, J. D. Wagnière, and W. Kurz, "Epitaxial laser metal forming: Analysis of microstructure formation," *Materials Science and Engineering A*, vol. 271, no. 1–2, pp. 232–241, Nov. 1999, doi: 10.1016/s0921-5093(99)00202-6.
- [166] I. Aniekan Essienubong, O. Ikechukwu, P. O. Ebunilo, and E. Ikpe, "Material Selection for High Pressure (HP) Turbine Blade of Conventional Turbojet Engines," *American Journal of Mechanical and Industrial Engineering*, vol. 1, no. 1, pp. 1–9, 2016, doi: 10.11648/j.ajmie.20160101.11.
- [167] S. D. Sharples, "All-Optical Scanning Acoustic Microscope Thesis submitted to The University of Nottingham for the degree of Doctor of Philosophy , May 2003 Contents," *Scanning*, no. May, 2003.
- [168] R. J. Smith, W. Li, J. Coulson, M. Clark, M. G. Somekh, and S. D. Sharples, "Spatially resolved acoustic spectroscopy for rapid imaging of material microstructure and grain orientation," *Measurement Science and Technology*, vol. 25, no. 5, p. 55902, 2014, doi: 10.1088/0957-0233/25/5/055902.
- [169] W. Li, "Laser Ultrasonic Method for Determination of Crystallographic Orientation of Large Grain Metals by Spatially Resolved Acoustic Spectroscopy ( SRAS )," University of Nottingham, 2012.
- [170] W. Li *et al.*, "Orientation characterisation of aerospace materials by spatially resolved acoustic spectroscopy," in *Journal of Physics: Conference Series*, 2014, vol. 520, no. 1, pp. 1–6. doi: 10.1088/1742-6596/520/1/012017.
- [171] S. D. Sharples, M. Clark, and M. G. Somekh, "All-optical adaptive scanning acoustic microscope," *Ultrasonics*, vol. 41, no. 4, pp. 295–299, Jun. 2003, doi: 10.1016/S0041-624X(02)00461-4.
- [172] D. Clark, S. D. Sharples, and D. C. Wright, "Development of online inspection for additive manufacturing products," *Insight: Non-Destructive Testing and Condition Monitoring*, vol. 53, no. 11, pp. 610–613, 2011, doi: 10.1784/insi.2011.53.11.610.

- [173] P. Dryburgh *et al.*, "Spatially resolved acoustic spectroscopy for texture imaging in powder bed fusion nickel superalloys," *AIP Conference Proceedings*, vol. 2102, no. May, p. 020004, 2019, doi: 10.1063/1.5099708.
- [174] A. F. Mark, W. Li, S. Sharples, and P. J. Withers, "Comparison of grain to grain orientation and stiffness mapping by spatially resolved acoustic spectroscopy and EBSD," *Journal of Microscopy*, vol. 267, no. 1, pp. 89–97, 2017, doi: 10.1111/jmi.12550.
- [175] S. O. Achamfufo-Yeboah, R. A. Light, and S. D. Sharpies, "Optical detection of ultrasound from optically rough surfaces using a custom CMOS sensor," *Journal of Physics: Conference Series*, vol. 581, no. 1, p. 012009, 2015, doi: 10.1088/1742-6596/581/1/012009.
- [176] R. Smith, S. Sharples, W. Li, M. Clark, and M. Somekh, "Orientation imaging using spatially resolved acoustic spectroscopy," *Journal of Physics: Conference Series*, vol. 353, no. 1, p. 012003, 2012, doi: 10.1088/1742-6596/353/1/012003.
- [177] M. H. Noroy, D. Royer, and M. Fink, "The laser-generated ultrasonic phased array: Analysis and experiments," *Journal of the Acoustical Society of America*, vol. 94, no. 4, pp. 1934–1943, 1993, doi: 10.1121/1.407516.
- [178] A. Gebhardt, F. M. Schmidt, J. S. Höller, W. Sokalla, and P. Sokalla, "Additive Manufacturing by Selective Laser Melting: The realizer desktop machine and its application for the dental industry," in *Physics Procedia*, 2010, vol. 5, no. PART 2, pp. 543–549. doi: 10.1016/j.phpro.2010.08.082.
- [179] F. Martina, J. Mehnen, S. W. Williams, P. Colegrove, and F. Wang, "Investigation of the benefits of plasma deposition for the additive layer manufacture of Ti–6Al–4V," *Journal of Materials Processing Technology*, vol. 212, no. 6, pp. 1377–1386, Jun. 2012, doi: 10.1016/J.JMATPROTEC.2012.02.002.
- [180] "AM Sample Preparation for SRAS and EBSD - Applied Optics Wiki," *Optics and photonics wiki*. [http://optics.eee.nottingham.ac.uk/wiki/AM\\_Sample\\_Preparation\\_for\\_SRAS\\_and\\_EBSD](http://optics.eee.nottingham.ac.uk/wiki/AM_Sample_Preparation_for_SRAS_and_EBSD) (accessed Dec. 21, 2020).
- [181] "How to clean a sample prior to lithography - Applied Optics Wiki," *Optics and photonics wiki*.

- [http://optics.eee.nottingham.ac.uk/wiki/How\\_to\\_clean\\_a\\_sample\\_prior\\_to\\_lithography](http://optics.eee.nottingham.ac.uk/wiki/How_to_clean_a_sample_prior_to_lithography) (accessed Dec. 21, 2020).
- [182] R. Patel, W. Li, R. J. Smith, S. D. Sharples, and M. Clark, "Orientation imaging of macro-sized polysilicon grains on wafers using spatially resolved acoustic spectroscopy," *Scripta Materialia*, vol. 140, pp. 67–70, 2017, doi: 10.1016/j.scriptamat.2017.07.003.
- [183] K. Harris and J. B. Wahl, "Improved Single Crystal Superalloys, CMSX-4®(SLS)[La+Y] and CMSX-486®, 2004.
- [184] M. Brown *et al.*, "Non-destructive detection of machining-induced white layers through grain size and crystallographic texture-sensitive methods," *Materials and Design*, vol. 200, p. 109472, Feb. 2021, doi: 10.1016/j.matdes.2021.109472.
- [185] T. Stratoudaki, M. Clark, and P. Wilcox, "Laser induced ultrasonic phased array using Full Matrix Capture data acquisition and Total Focusing Method," in *Optics Express*, Sep. 2017, vol. 24, no. 19. doi: 10.1364/oe.24.021921.
- [186] R. E. Lee and R. M. White, "Excitation of surface elastic waves by transient surface heating," *Applied Physics Letters*, vol. 12, no. 1, pp. 12–14, 1968, doi: 10.1063/1.1651832.
- [187] M. Clark, S. D. Sharples, and M. G. Somekh, "Diffractive acoustic elements for laser ultrasonics," *J Acoust Soc Am*, vol. 107, no. 6, pp. 3179–3185, 2000, doi: 10.1121/1.429345.
- [188] A. J. A. Bruinsma and J. A. Vogel, "Ultrasonic noncontact inspection system with optical fiber methods," *Applied Optics*, vol. 27, no. 22, p. 4690, 1988, doi: 10.1364/ao.27.004690.
- [189] S. N. Hopko, I. C. Ume, and D. S. Erdahl, "Development of a flexible laser ultrasonic probe," *Journal of Manufacturing Science and Engineering, Transactions of the ASME*, vol. 124, no. 2, pp. 351–357, 2002, doi: 10.1115/1.1379369.
- [190] B. Mi and C. Ume, "Real-time weld penetration depth monitoring with laser ultrasonic sensing system," *Journal of Manufacturing Science and Engineering, Transactions of the ASME*, vol. 128, no. 1, pp. 280–286, 2006, doi: 10.1115/1.2137747.
- [191] T. W. Murray, J. B. Deaton, and J. W. Wagner, "Experimental evaluation of enhanced generation of ultrasonic waves using an Array of Laser Sources," *Ultrasonics*, vol. 34, no. 1, pp. 69–77, Mar. 1996, doi: 10.1016/0041-624X(95)00090-P.

- [192] M. H. Noroy, D. Royer, and M. A. Fink, "Shear-Wave Focusing with a Laser-Ultrasound Phased-Array," *IEEE Transactions on Ultrasonics, Ferroelectrics, and Frequency Control*, vol. 42, no. 6, pp. 981–988, 1995, doi: 10.1109/58.476540.
- [193] P. W. Lorraine, R. A. Hewes, and D. Drolet, "High Resolution Laser Ultrasound Detection of Metal Defects," in *Review of Progress in Quantitative Nondestructive Evaluation*, Springer US, 1997, pp. 555–562. doi: 10.1007/978-1-4615-5947-4\_73.
- [194] A. Blouin, D. Levesque, C. Neron, D. Drolet, and J.-P. Monchalin, "Improved resolution and signal-to-noise ratio in laser-ultrasonics by SAFT processing," *Optics Express*, vol. 2, no. 13, p. 531, 1998, doi: 10.1364/oe.2.000531.
- [195] D. Lévesque, A. Blouin, C. Néron, and J. P. Monchalin, "Performance of laser-ultrasonic F-SAFT imaging," *Ultrasonics*, vol. 40, no. 10, pp. 1057–1063, 2002, doi: 10.1016/S0041-624X(02)00256-1.
- [196] R. H. Brown, J. Dobson, S. G. Pierce, B. Dutton, and I. Collison, "Quantifying performance of ultrasonic immersion inspection using phased arrays for curvilinear disc forgings," *AIP Conference Proceedings*, vol. 1806, no. February, pp. 1–8, 2017, doi: 10.1063/1.4974591.
- [197] K. M. M. Tant, E. Galetti, A. J. Mulholland, A. Curtis, and A. Gachagan, "Effective grain orientation mapping of complex and locally anisotropic media for improved imaging in ultrasonic non-destructive testing," *Inverse Problems in Science and Engineering*, vol. 28, no. 12, pp. 1694–1718, Jun. 2020, doi: 10.1080/17415977.2020.1762596.
- [198] L.-S. Wang, J. S. Steckenrider, and J. D. Achenbach, "A Fiber-Based Laser Ultrasonic System for Remote Inspection of Limited Access Components," Springer US, Boston, MA, 1997. doi: 10.1007/978-1-4615-5947-4\_67.
- [199] M. Dubois, M. Militzer, A. Moreau, and J. F. Bussière, "New technique for the quantitative real-time monitoring of austenite grain growth in steel," *Scripta Materialia*, vol. 42, no. 9, pp. 867–874, Apr. 2000, doi: 10.1016/S1359-6462(00)00305-5.
- [200] L. R. F. Rose, "Point-source representation for laser-generated ultrasound," *Journal of the Acoustical Society of America*, vol. 75, no. 3, pp. 723–732, Aug. 1984, doi: 10.1121/1.390583.

- [201] G. F. Miller, H. PURSEY, and T. R. Society, "The field and radiation impedance of mechanical radiators on the free surface of a semi-infinite isotropic solid," *Proceedings of the Royal Society of London. Series A. Mathematical and Physical Sciences*, vol. 223, no. 1155, pp. 521–541, May 1954, doi: 10.1098/rspa.1954.0134.
- [202] T. Stratoudaki, M. Clark, and P. D. Wilcox, "Adapting the full matrix capture and the total focusing method to laser ultrasonics for remote non destructive testing," *IEEE International Ultrasonics Symposium, IUS*, pp. 3–6, 2017, doi: 10.1109/ULTSYM.2017.8092864.
- [203] N. T. Aboulkhair, N. M. Everitt, I. Ashcroft, and C. Tuck, "Reducing porosity in AlSi10Mg parts processed by selective laser melting," *Additive Manufacturing*, vol. 1, pp. 77–86, 2014, doi: 10.1016/j.addma.2014.08.001.
- [204] S. C. Wooh and Y. Shi, "Optimum beam steering of linear phased arrays," *Wave Motion*, vol. 29, no. 3, pp. 245–265, Apr. 1999, doi: 10.1016/s0165-2125(98)00039-0.
- [205] J. Zhang, B. W. Drinkwater, and P. D. Wilcox, "The use of ultrasonic arrays to characterize crack-like defects," *Journal of Nondestructive Evaluation*, vol. 29, no. 4, pp. 222–232, 2010, doi: 10.1007/s10921-010-0080-6.
- [206] A. A. Maznev and O. B. Wright, "Upholding the diffraction limit in the focusing of light and sound," *Wave Motion*, vol. 68, pp. 182–189, 2017, doi: 10.1016/j.wavemoti.2016.09.012.
- [207] L. Bai, A. Velichko, A. T. Clare, P. Dryburgh, D. Pieris, and B. W. Drinkwater, "The effect of distortion models on characterisation of real defects using ultrasonic arrays," *NDT and E International*, vol. 113, no. March, Jul. 2020, doi: 10.1016/j.ndteint.2020.102263.
- [208] P. Lukacs, T. Stratoudaki, P. Wilcox, M. Clark, and A. Gachagan, "Optimisation of data acquisition and processing for laser induced ultrasonic phased arrays," in *Proceedings of Meetings on Acoustics*, 2019, vol. 38, no. 1, p. 30015. doi: 10.1121/2.0001170.
- [209] S. V. Prikhodko, J. D. Carnes, D. G. Isaak, and A. J. Ardell, "Elastic constants of a Ni-12.69 at. % Al alloy from 295 to 1300 K," *Scripta Materialia*, vol. 38, no. 1, pp. 67–72, 1997, doi: 10.1016/S1359-6462(97)00448-X.

- [210] W. R. Chang, M. Hirvonen, and R. Grönqvist, "The effects of cut-off length on surface roughness parameters and their correlation with transition friction," *Safety Science*, vol. 42, no. 8, pp. 755–769, Oct. 2004, doi: 10.1016/j.ssci.2004.01.002.
- [211] "MountainsMap® surface analysis software for profilometers." <https://www.digitalsurf.com/software-solutions/profilometry/> (accessed Aug. 10, 2021).
- [212] "Cut-offs and the Measurement of Surface Roughness :: Spectrum Metrology." <https://www.spectrum-metrology.co.uk/surface-roughness/theory.php> (accessed Apr. 07, 2021).
- [213] Y. Zhang *et al.*, "Autofocus System and Evaluation Methodologies: A Literature Review," *Sensors and Materials*, vol. 30, no. 5, pp. 1165–1174, 2018, doi: 10.18494/SAM.2018.1785.
- [214] Iowa State University, "Nondestructive Evaluation Physics: Signal-to-Noise Ratio." <https://www.nde-ed.org/Physics/Waves/signaltonoise.xhtml> (accessed Apr. 06, 2021).
- [215] A. Ruiz and P. B. Nagy, "Laser-ultrasonic surface wave dispersion measurements on surface-treated metals," *Ultrasonics*, vol. 42, no. 1–9, pp. 665–669, Apr. 2004, doi: 10.1016/j.ultras.2004.01.045.
- [216] C. Bakre, M. Hassanian, and C. Lissenden, "Influence of surface roughness from additive manufacturing on laser ultrasonics measurements," in *AIP Conference Proceedings*, 2019, vol. 2102, p. 20009. doi: 10.1063/1.5099713.
- [217] D. Bergström, J. Powell, and A. F. H. Kaplan, "The absorption of light by rough metal surfaces-A three-dimensional ray-tracing analysis," *Journal of Applied Physics*, vol. 103, no. 10, 2008, doi: 10.1063/1.2930808.
- [218] P. Lukacs *et al.*, "Remote Ultrasonic Imaging of a Wire Arc Additive Manufactured Ti-6Al-4V Component Using Laser Induced Phased Array," *IEEE International Instrumentation and Measurement Technology Conference*, pp. 1–6, May 2021, doi: 10.1109/I2MTC50364.2021.9459823.